# Optical Dosimetry and Treatment Planning for Photodynamic Therapy

by

Timothy M. Baran

Submitted in Partial Fulfillment of the

Requirements for the Degree

Doctor of Philosophy

Supervised by Thomas Foster

The Institute of Optics

Arts, Sciences and Engineering

Edmund A. Hajim School of Engineering and Applied Sciences

University of Rochester

Rochester, NY

2013

*To Andrea*

# Biographical Sketch

Timothy Baran was born in Buffalo, NY. He attended Rensselaer Polytechnic Institute, and graduated with a Bachelor of Science degree in Electrical and Computer & Systems Engineering in 2007. He began doctoral studies in Optics at the University of Rochester in 2007. He pursued his research in optical spectroscopy and photodynamic therapy under the direction of Thomas Foster.

The following publications were a result of work conducted during doctoral study:

T.M. Baran, B.R. Giesselman, R. Hu, M.A. Biel and T.H. Foster. Factors influencing tumor response to photodynamic therapy sensitized by intratumor administration of methylene blue. *Lasers Surg Med* **42**, 728-735 (2010).

T.M. Baran and T.H. Foster. New Monte Carlo model of cylindrical diffusing fibers illustrates axially heterogeneous fluorescence detection: simulation and experimental validation. *J Biomed Opt* **16**, 085003 (2011).

T.M. Baran and T.H. Foster. Fluence rate-dependent photobleaching of intratumorally-administered Pc 4 does not predict tumor growth delay. *Photochem Photobiol* **88**, 1273-1279 (2012).

T.M. Baran, J.D. Wilson, S. Mitra, J.L. Yao, E.M. Messing, D.L. Waldman and T.H. Foster. Optical property measurements establish the feasibility of photodynamic therapy as a minimally invasive intervention for tumors of the kidney. *J Biomed Opt* **17**, 098002 (2012).

# Acknowledgments

This thesis is the culmination of many years' work, and would not have been possible without the support of a number of individuals who I would like to thank here.

First and foremost, I would like to thank my advisor, Professor Thomas Foster. I am extremely grateful for the large amount of time and effort that Professor Foster invested in my graduate work, and the amount of scientific freedom that I was given to explore a wide variety of topics. His excitement for the work was inspiring and his deep knowledge of the field has provided me with a strong foundation for a future in scientific research. I feel privileged to have worked with Professor Foster.

I would also like to thank current and former members of the Foster group who I had the pleasure of working with: Soumya Mitra, Andrew Soroka, Steve Hupcher, Tammy Lee, William Cottrell, Jeremy Wilson, Jarod Finlay, Michael Fenn, and Adnan Hirad. Soumya was a source of knowledge and advice in everything related to experimental work, and was invaluable to the completion of the studies presented in this thesis. I shared an office with Andrew and Steve, and they were a great help in developing new ideas and critically analyzing experiments. Tammy was instrumental in my introduction to the lab, and taught me a number of things about system design and data analysis that directly contributed to the work shown here. William designed the spectroscopy probe that was used to do interstitial optical property recovery and Jeremy collected the diffuse reflectance data that were used to recover kidney optical properties. A number of the ideas for optical property recovery were inspired by Jarod's graduate work in the Foster lab. Michael was an undergraduate student that contributed to Monte

Carlo modeling of the interstitial spectroscopy probe, and helped me to explore a number of possible alternative schemes. Adnan was a rotation student that helped with the early work related to doxorubicin fluorescence detection.

I am also grateful to two former technicians in our laboratory, Ben Giesselman and Katie Hamm. Ben and Katie were both crucial in cell culture, maintenance of animals, and in the daily operations of the lab. In my early days in the lab, Ben taught me a number of experimental techniques that I now use routinely. He also directly contributed to the methylene blue study outlined in Chapter 2. Katie performed a large amount of the preliminary work that led to the Pc 4 study shown in Chapter 2 and taught me cell culture and animal handling techniques.

This work would also not have been possible without a number of key collaborators. The methylene blue used in the study shown in Chapter 2 was provided by Dr. Merrill Biel of the Minneapolis ENT Research Foundation. Dr. Biel was also extremely helpful in providing clinical perspectives on photodynamic therapy. The statistical analysis for this study was performed by Rui Hu, of the Department of Biostatistics and Computational Biology at the University of Rochester Medical Center. The Pc 4 used in the photobleaching study detailed in Chapter 2 was graciously provided by Malcolm Kenney of Case Western Reserve University. I would also like to acknowledge the support of funding from the National Institutes of Health, the American Society for Laser Medicine and Surgery, and the Institute of Optics and Department of Imaging Sciences at the University of Rochester.

I could not consider these acknowledgments complete without expressing my gratitude to my friends and fellow Institute of Optics students Mick Brown and Adam Heiniger. They have been great friends, and have given me an outlet for the trials and tribulations of graduate school. I consider myself lucky to have made the journey with them.

Finally, I would like to thank my parents, Richard and Frances Baran, and my wife, Andrea, for their love and support. From an early age, my parents encouraged a love of math, science, and engineering in me. They taught me to think big, while being mindful of the challenges that face our world. Andrea has been my rock and a constant source of inspiration, motivation, and comfort. Without her love and patience, I truly could not have done this.

# Abstract

Accurate dosimetry and treatment planning for photodynamic therapy (PDT) require knowledge of tissue optical properties and models of light propagation. We present techniques, based on reflectance and fluorescence spectroscopy, to examine these problems using analytical approximations and Monte Carlo (MC) simulations.

We begin with studies that monitored PDT in mouse models using reflectance and fluorescence spectroscopy. In the first, spectroscopy informed the optimization of treatment parameters for methylene blue PDT, with dependencies on injection vehicle, drug-light interval, and fluence found. In the second, fluorescence photobleaching during Pc 4 PDT was examined for correlation to tumor response. Irradiance-dependent photobleaching was demonstrated, but was not predictive of tumor response.

Next we outline the graphics processing unit enhanced MC model that was used to simulate light propagation in tissue. We demonstrate a number of source models that were used in subsequent experiments.

We then focus on the recovery of optical properties from diffuse reflectance measurements by examining two studies. In the first study, diffuse reflectance measurements were made at the surface of human kidneys to extract optical properties, which were then used in MC simulations of interstitial PDT. We found that the optical properties measured make PDT feasible in human kidneys. We then examined the interstitial recovery of optical properties using a custom optical probe. This recovery was based on a MC model of the probe used, with a mean error of 6.5% in the determination of absorption.

We examined fluorescence detection by cylindrical diffusing fibers using a MC model. This model predicted heterogeneous fluorescence detection, which was verified experimentally.

Recovery of intrinsic fluorescence from point, interstitial measurements was demonstrated. This technique did not require *a prori* knowledge of the tissue optical properties, and was used to determine these values. Mean error of fluorophore concentration recovery was 12%, while mean error for background absorption was 23%.

Finally, we demonstrate a treatment planning modality for interstitial PDT based on clinical imaging, optical spectroscopy, and MC simulations. This allows for individualized therapy based on the patient's anatomy and optical properties. We demonstrate optimization of diffuser placement, and show results for determination of deposited dose.

# Contributors and Funding Sources

This work was supervised by a dissertation committee consisting of Professor Thomas Foster (advisor) of the Institute of Optics and Departments of Imaging Sciences, Biomedical Engineering, and Physics & Astronomy, Professor Andrew Berger of the Institute of Optics and the Department of Biomedical Engineering, Professor Thomas Brown of the Institute of Optics, and Professor Jarod Finlay of the Department of Radiation Oncology at the University of Pennsylvania. The spectroscopy system depicted in chapter 2 was based on a design by Tammy Lee, and the statistical analysis of results for the methylene blue study was performed by Dr. Rui Hu. Methylene blue was provided by Dr. Merrill Biel of the Minneapolis ENT Research Foundation, and Pc 4 was provided by Malcolm Kenney of Case Western Reserve University. The diffuse reflectance data from excised kidneys detailed in chapter 4 were collected by Dr. Jeremy Wilson. The interstitial reflectance spectroscopy probe outlined in chapters 3 and 4 was designed by Dr. William Cottrell. Clinical CT data in chapter 7 were provided by Dr. Daryl Nazareth of the Radiation Medicine Department at the Roswell Park Cancer Institute. All other work covered in this dissertation was completed independently by Timothy Baran. Funding support was provided by grants CA68409 and CA55791 from the National Institutes of Health, a student research grant from the American Society for Laser Medicine and Surgery, and a grant from the Fischer Fund in the University of Rochester Medical Center's Department of Imaging Sciences.

# Table of Contents

# List of Tables

# List of Figures

# List of Symbols

| Symbol | Meaning |
|---|---|
| $\delta$ | Characteristic light propagation distance |
| $\mu_a$ | Absorption coefficient |
| $\mu_s$ | Scattering coefficient |
| $\mu_s'$ | Reduced scattering coefficient |
| $\mu_t$ | Total attenuation coefficient |
| $\mu_{eff}$ | Effective attenuation coefficient |

# Chapter 1

# Introduction

This thesis focuses on optical techniques related to the monitoring and planning of photodynamic therapy (PDT). A brief introduction to PDT is included in order to motivate these topics. In order to accurately create treatment plans and evaluate the outcome of PDT, knowledge of tissue optical properties and models of light propagation in tissue are required. Brief reviews of these topics are provided, as well as an overview of the remaining chapters of the thesis.

## 1.1 Photodynamic Therapy

Photodynamic therapy is an emerging cancer therapy that has been an active area of research since the 1970s[1]. PDT relies on the combination of photosensitizer, light, and molecular oxygen in order to create a photochemical reaction that leads to the destruction of malignant tissue. The mechanism of action for PDT is shown in Figure 1.1.

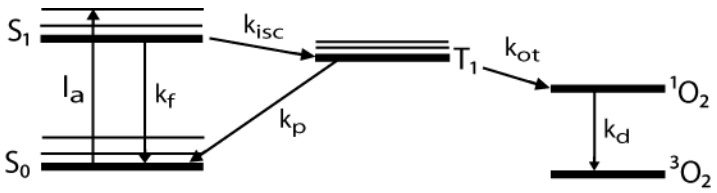


**Figure 1.1** Jablonski diagram illustrating PDT mechanism

The photosensitizer begins in the singlet ground state, $S_0$. In this state, the photosensitizer is inactive, and will generally not lead to damage to the surrounding tissue. Upon excitation by the treatment light at the rate $I_a$, the photosensitizer is promoted to its first excited singlet state, $S_1$. From this first excited state, the

photosensitizer can decay to the ground state non-radiatively or by fluorescence at a rate $k_f$. This intrinsic fluorescent property of many photosensitizers can be exploited for treatment monitoring, and will be expanded upon below. From the excited state, the photosensitizer can also undergo intersystem crossing at a rate $k_{isc}$ to the excited triplet state, $T_1$. This triplet state is longer lived than the excited singlet state and allows for the photosensitizer to come into contact with ground state oxygen. This allows for energy transfer to oxygen at rate $k_{ot}$, which promotes ground state triplet oxygen to excited singlet oxygen. Alternatively, the triplet state photosensitizer can decay to its ground state non-radiatively or via phosphorescence at a rate $k_p$. The excited singlet oxygen can also decay to its ground state non-radiatively or via phosphorescence at a rate $k_d$ [2]. This phosphorescence has a wavelength of 1270 nm, and detection of it has been used as a measure of the singlet oxygen generated by PDT[3].

Singlet oxygen is the major compound which causes cell killing in PDT. Interaction of singlet oxygen with cellular components leads to damaging of cell membranes, lysosomes, mitochondria, and nuclei, which leads to cell and tumor necrosis[4]. Some photosensitizers that localize to certain organelles, often the mitochondria or lysosomes, can also trigger apoptosis[5], which leads to less local inflammation and a reduction in damage to nearby healthy tissue. These singlet oxygen mediated reactions are referred to as Type II reactions. Type I reactions can also occur, which involve radical species of the photosensitizer as well as alternative forms of excited oxygen. These Type I reactions are generally less pronounced than the dominant Type II mechanism. However, there are some photosensitizers for which this Type I

reaction is the dominant mechanism and accounts for most of the photodynamic damage[6].

In a typical PDT treatment, the photosensitizer is first administered to the patient. There is then a waiting period during which the photosensitizer localizes to the tumor, referred to as the drug-light interval. After the drug-light interval, treatment light of a specific wavelength is applied to the tumor and photodynamic action occurs. Common factors that are adjusted are the total fluence delivered to the tumor and the rate at which this fluence is delivered (i.e. optical power).

PDT has traditionally been used to treat superficial malignancies, such as those of the skin or in areas, such as the throat, that are readily accessible to surface illumination[7]. Recently, there has been interest in using PDT to treat bulky tumors that are located deep within the body by the insertion of optical fibers. This is referred to as interstitial PDT, or iPDT. iPDT has been used in humans to treat many types of cancer, including obstructing esophageal[8] and bronchial cancer[9], prostate[10, 11], cholangiocarcinoma[12], glioma[13], and large tumors of the head and neck[14, 15]. This configuration creates a number of challenges that are not apparent in treatment of superficial malignancies.

## 1.2 Optical Monitoring of PDT

Unlike therapies such as ionizing radiation, there is no easily-calculable dose metric for PDT. The outcome of therapy is tied to a combination of photosensitizer concentration, light dose delivered, and local oxygen concentration. Thus, a number of techniques have been developed to monitor the progression of PDT during treatment. One of these

consists of a straightforward measurement of fluence in the treated tissue during PDT. To achieve this, one or more optical probes are inserted into the tumor, and possibly the surrounding normal tissue. The fluence detected by these probes is monitored continuously or at discrete intervals in order to quantify the light being delivered[16]. This information can then be used to adjust the duration of illumination in order to achieve a certain light dose, which can lead to improved clinical outcomes.

Another technique used to monitor PDT is reflectance spectroscopy. With this method, treatment is briefly interrupted in order to inject interrogation light into the tissue, either at a single wavelength or over a broad band. Light is then detected at one or more positions in order to deduce information about the tissue, such as the oxygen saturation[17]. Whereas the measurement of fluence seeks to determine the light dose being delivered to tissue, reflectance spectroscopy seeks to examine factors such as the local oxygen and photosensitizer concentrations. For example, Busch *et al* examined the change in hemoglobin concentration due to PDT using reflectance spectroscopy[18]. They found that PDT led to a decreased hemoglobin concentration in the tumor.

As mentioned previously, many photosensitizers are naturally fluorescent. This allows for measurements of photosensitizer fluorescence to be made during treatment, which can provide information on the photosensitizer concentration and production of singlet oxygen. The determination of photosensitizer concentration by fluorescence spectroscopy has been investigated by a number of research groups[19]. Photosensitizer fluorescence can also be used to examine photosensitizer photobleaching. Photobleaching is the process by which the photosensitizer is destroyed by interactions

with singlet oxygen or other radicals produced by PDT[20]. This destruction of photosensitizer leads to a decrease in fluorescence, which can be measured and quantified during PDT. Since photobleaching can be mediated by reactive oxygen species, it has been speculated that changes in photosensitizer fluorescence could be tied to PDT outcome. This has been shown to be the case for the prodrug aminolevulinic acid (ALA), which is metabolized into protoporphyrin IX (PpIX). A correlation between PpIX photobleaching and tumor response was shown in rat models of Barrett's esophagus[21] and ovarian cancer[22], and in humans with actinic keratoses, Bowen's disease, and basal cell carcinoma[23]. A correlation between photobleaching and tumor outcome has also been shown for the silicon phthalocyanine photosensitizer Pc 4, in the context of a mouse model of breast cancer[24].

## 1.3 Monte Carlo Simulation of Light Propagation in Tissue

Due to the variable and turbid nature of biological tissue, standard methods for the calculation of light propagation cannot be used, except under certain rare conditions[25]. For this reason, statistical methods are used that reduce the propagation of light to the handling of absorption and scattering in the presence of bulk optical properties. The most prominent of these methods is the Monte Carlo (MC) simulation, which depends upon the use of random number generators and large quantities of propagated photons in order to generate accurate results. In MC simulations, light generated at a source is divided into discrete photons or photon packets. Each of these undergoes absorption, scattering, and transmission and reflection at material boundaries. These phenomena are handled in a statistical fashion based on the optical properties of the tissue, with random number

generators used to provide statistically independent photon paths. If a sufficient number of photons are run, MC simulation provides very accurate results. The accuracy of MC simulation has been demonstrated multiple times[26, 27], and MC is treated as the "gold standard" for simulation of light propagation in biological tissue. A number of MC codes are freely available, including MCML by Wang *et al*[28].

Due to the independent nature of individual photon runs, MC simulations are ideally suited for parallel-programming techniques. In particular, MC simulations can utilize the parallel computing power of the modern graphics processing unit (GPU). GPUs were originally designed for use in computer graphics, and are therefore efficient at performing a large number of computations in parallel. A number of GPU-based MC codes exist, capable of representing layered samples[29], three dimensional samples with voxels[30], and three dimensional samples with a triangular mesh[31]. However, these codes all utilize sources that are in contact with the tissue surface.

## 1.4 Optical Property Recovery

Light propagation through tissue can largely be described using two processes, absorption and scattering. At wavelengths relevant to PDT, absorption in biological tissue is largely due to hemoglobin and water[32], and provides a fundamental limit on the depth to which light can penetrate in tissue. In the case of PDT, the photosensitizer absorption may also play a large part and needs to be accounted for in the case of certain photosensitizers. The presence of many index of refraction mismatches in tissue leads to the scattering of light. Due to the turbid nature of biological tissue, scattering is generally the dominant effect and leads to the diffuse nature of light propagation in tissue. Absorption and

scattering are represented by the coefficients $\mu_a$ and $\mu_s$, respectively, with units of inverse length. These coefficients represent the bulk optical properties of tissue, with $\mu_a$ corresponding to the inverse of the absorption mean free path (MFP) and $\mu_s$ corresponding to the inverse of the scattering MFP. These mean free paths are the average distance over which a photon must propagate before encountering an absorption or scattering event.

As can be expected, the exact values of $\mu_a$ and $\mu_s$ in tissue can have a large effect on the area or volume that receives a particular light dose. It is therefore desirable to determine these values for a given patient. This is often accomplished by use of MC simulations. Kienle and Patterson used a scaled MC method in order to determine tissue optical properties from time- and radially-resolved reflectance measurements[33]. This scaling method allows detected light from a reference simulation to be scaled based on a new set of optical properties, which does not require repeated simulations. The optical properties of a sample can then be determined by fitting measured data with scaled MC simulation data. This scaling method was also utilized by Palmer and Ramanujam in order to recover optical properties over a wide range of absorption and scattering coefficients[34]. A similar method was demonstrated by Kumar and Vasu, using perturbation MC instead of scaling[35]. Under this scheme, changes in optical properties are assumed to be a perturbation of the optical properties from a known reference simulation. This method has the benefit of working for low-scattering objects.

Even with the use of GPU-accelerated codes, MC simulations can still require a significant amount of computation time. Therefore, a number of analytical

approximations for light propagation in tissue have been developed. The bulk of these approximations rely upon the radiative transport equation,

$$\nabla \cdot (L\hat{s}) + \frac{1}{c}\frac{\partial L}{\partial t} = -\mu_t L + \mu_s \int p(\hat{s}, \hat{s}')L(\vec{r}, \hat{s}')d\omega' + \varepsilon(\vec{r}, \hat{s}) , \qquad (1.1)$$

which treats light propagation as an energy transport problem, rather than as the propagation of waves[36]. Here, $L$ is the radiance, $\hat{s}$ is the direction of light propagation, $c$ is the speed of light, $\mu_t$ is the total attenuation coefficient ($\mu_t \equiv \mu_a + \mu_s$), $\mu_s$ is the scattering coefficient, $p$ is the scattering phase function, and $\varepsilon$ is the source function. Except under a very limited set of conditions, this equation cannot be solved directly. Therefore, a number of approximations have been created that expand the terms in the equation as summations of basis functions. The most commonly used approximations are the diffusion and $P_3$ approximations, which expand the terms to first and third order, respectively[37]. The $P_3$ approximation will be examined in greater detail in chapter 4 of this thesis.

By solving the diffusion or P3 approximations for a given set of boundary and source conditions, the optical properties of a tissue sample can be determined. This has largely been done in the case of surface-contact light sources and detectors, due to the simpler boundary conditions. A number of studies have demonstrated accurate recovery of optical properties in surface-contact geometry. In particular, Hull and Foster showed recovery of optical properties to within 10% for source-detector separations as small as 0.43 mm and albedos as low as 0.59[37]. For the case of interstitial geometry, there has been less work done. Most interstitial schemes rely on calibration with a library of tissue-simulating phantoms[38, 39], or on having multiple implanted fibers with which to

perform spectroscopy[40, 41]. In scenarios where only a single fiber can be inserted, such as in the treatment of cholangiocarcinoma, a scheme that utilizes only a single fiber probe is desirable.

## 1.5 Treatment Planning for PDT

As mentioned previously, the outcome of a PDT treatment depends heavily on the patient's anatomy and optical properties. Sparing of healthy tissue surrounding the treated region is also important, particularly in delicate regions such as the prostate[42]. In these areas, damage to surrounding healthy tissue can result in significant side effects for the patient. Therefore, it is crucial to create treatment plans that deliver the required dose to malignant tissue while minimizing damage to healthy tissue.

The creation of these treatment plans depends on a number of factors. The first of these is knowledge of the patient's anatomy. This is typically achieved via non-optical imaging, using magnetic resonance imaging (MRI) or x-ray computed tomography (CT). These imaging modalities allow for the determination of the volume to be treated, as well as the identification of vulnerable healthy tissues. Unlike in the planning of ionizing radiation therapy, data from CT scans cannot be used directly to calculate therapeutic doses delivered to patients. For this, knowledge of the patient optical properties is also required. This can be achieved with a number of methods, some of which were outlined in the previous section. Treatment planning also requires a model of light propagation in tissue. Commonly MC simulations are used, but approximations to the radiative transport equation have also been used to determine the light dose.

A number of schemes exist for treatment planning in PDT. Swartling *et al* demonstrated a PDT dose planning system for prostate cancer utilizing trans-rectal ultrasound images of the treatment volume and diffuse reflectance measurements made using the treatment fibers [43]. Ultrasound images were used to generate a 3D model of the prostate and surrounding tissues. Diffuse reflectance measurements, combined with a diffusion model of light propagation, were used to determine the effective attenuation coefficient in the treatment volume. This was then used to adjust the duration of illumination in order to achieve a threshold light dose determined in previous studies**.** Davidson *et al* used a finite element model of light diffusion, coupled with measured optical properties in order to create individualized treatment plans[44]. Based on calculated fluence deposition in tissue, they were able to calculate the combined light-drug dose to the tumor and found a correlation between this dose and tumor response. Altschuler *et al* examined the optimization of position, length, and strength of light source in PDT of the prostate using the Cimmino feasibility algorithm and a diffusion approximation of light transport[45]. They found that they were able to improve coverage of the tumor region, while sparing surrounding healthy tissue. These studies make it clear that a good treatment planning system for PDT requires knowledge of the patient's anatomy and optical properties, a model of light transport in tissue, and a means of optimizing the number, placement, and strength of light sources.

## 1.6 Overview of Thesis

In chapter 2, two schemes for the monitoring of PDT during treatment are presented. These schemes rely on reflectance and fluorescence spectroscopy in order to evaluate the effects of various factors on the outcome of PDT. This chapter serves as a segue into the more rigorous examinations of tissue optical properties that follow in subsequent chapters.

In chapter 3, the GPU-based MC code that was developed is discussed in detail. A number of source models that were created are outlined, each of which is designed to interface with a specific experimental application.

Chapter 4 focuses on the recovery of optical properties in both surface-contact and interstitial geometries. The first piece focuses on a study of kidney optical properties using a surface contact probe and the $P_3$ approximation to the radiative transport equation. The $P_3$ approximation is outlined in further detail, and the fitting of experimental data is shown. The implications of changing optical properties are also examined. The second piece focuses on the interstitial recovery of optical properties using a custom optical probe. The details of the fitting process are outlined, and the accuracy of the method is shown in a number of tissue-simulating phantoms.

An examination of the MC model of cylindrical diffusing fibers developed in chapter 3 is provided in chapter 5. Model-based predictions of heterogeneous fluorescence detection are explored, and experimental verification is provided. Application of the model to the design of such fibers is also discussed.

In chapter 6, a method for the recovery of intrinsic fluorescence and background optical properties from a single interstitial source and detector is developed. This scheme, also based on the $P_3$ approximation, allows for correction of distortions to fluorescence spectra created by background optical properties. This further allows for accurate recovery of the fluorophore and background absorber concentrations in an interstitial geometry, as demonstrated by experiments in tissue-simulating phantoms.

The MC simulation work and optical property recovery are brought together in chapter 7 in the context of treatment planning for iPDT. Clinical CT images are integrated with optical property measurements in order to generate a model of light delivery for iPDT. The effects of changing optical properties are examined, and algorithms to optimize the number and placement of sources for iPDT are provided.

Chapter 8 consists of conclusions drawn from the thesis, as well as possible future directions for the work. In the appendix, a clinical laser system for PDT is demonstrated.

# Chapter 2

# Optical Monitoring of Photodynamic Therapy

## 2.1 Introduction

As mentioned in Chapter 1, doses delivered by PDT cannot be pre-computed in a straightforward fashion, as in other treatment modalities such as radiotherapy. We therefore generally describe the PDT dose in terms of a drug-light product that depends upon the photosensitizer concentration and the treatment light field[46]. The light dose is affected by the source strength, duration of irradiation, and the optical properties of the tissue being treated. Here we refer to the source strength as the fluence rate, measured in mW per unit area for the case of surface illumination. Combined with the duration of irradiation, this fluence rate yields a total light dose in units of J per unit area. As is to be expected, the volume over which this light dose is distributed is strongly influenced by the tissue optical properties. In the wavelength range used for PDT, optical properties can vary significantly both inter- and intra-patient, resulting in differing treatment fields from the same total administered light dose. A thorough description of the spectroscopic recovery of tissue optical properties is provided in chapter 4. Here we focus on methods to monitor the progression of PDT in the context of these differing optical properties.

A number of studies have been done to monitor the light dose delivered during PDT. This is typically done by the addition of detection fibers that measure fluence over time. In the surface geometry, this is accomplished by detectors placed remotely from the source at the surface of the treatment volume. van Veen *et al* demonstrated a

treatment source for PDT of the nasopharyngeal cavity that incorporated detectors for determination of fluence and fluence rate[47]. They observed a reduction in fluence rate during treatment, which they hypothesize to be due to treatment-induced changes in tissue optical properties. In the interstitial geometry, additional detection fibers are inserted into the tumor mass in order to monitor the fluence. Yu *et al* used isotropic detector fibers to monitor the delivery of fluence in PDT of the prostate[16]. These measurements were used to track fluence delivery during the treatment, and to determine the total light dose to particular regions of the prostate. Davidson *et al* also used isotropic detector fibers in order to monitor the light dose delivered in PDT of prostate cancer[44].

The other key component of the delivered photodynamic dose is the photosensitizer concentration. In a typical PDT treatment, the photosensitizer is administered either systemically or via intra-tumor injection. Some time is then allowed to pass, known as the drug-light interval, before treatment light is delivered. Following systemic delivery, this drug-light interval has been shown to improve photosensitizer concentration in the tumor relative to the surrounding healthy tissue[48], and allows for the distribution of the photosensitizer in the tumor to become more homogeneous. Due to differences in circulation and the tumor micro-environment between patients, the drug concentration within the tumor can vary between subjects, even with the same total injected dose. There is therefore a need to determine the photosensitizer concentration in order to accurately determine the drug-light dose that a patient receives.

There are a number of ways to do this using reflectance and fluorescence spectroscopy. Due to the fluorescent nature of most photosensitizers, measured

fluorescence can be used to determine photosensitizer concentration. Finlay *et al* measured the concentration of Motexafin Lutetium during interstitial PDT of the prostate[19]. They found the photosensitizer concentration to be heterogeneous within single patients, and noted significant variability between patients. These techniques require correction of detected fluorescence for background optical properties, which is covered in detail in chapter 6. The absorption of photosensitizers can also be used to determine drug concentration, as has been demonstrated previously[49-51]. In particular, Bai *et al* demonstrated that the concentration of the photosensitizer Pc 4 before PDT, determined by reflectance spectroscopy, was correlated with tumor growth delay[24]. This illustrates the need for determination of photosensitizer concentration before delivery of treatment light.

As mentioned in chapter 1, the major reactive intermediate that causes cell destruction in PDT is singlet oxygen[4]. Although we speak about the photodynamic dose in terms of the drug-light product, the real determinant of tumor cell destruction is the production of singlet oxygen. Singlet oxygen is weakly phosphorescent at 1270 nm, and the emission of this phosphorescence has been studied in an effort to determine singlet oxygen production during PDT[3, 52, 53]. However, these techniques are vulnerable to low signal-to-noise ratios, and require complex and expensive instrumentation[32]. Therefore, singlet oxygen production is often monitored indirectly.

The most common method for this is through examination of the photobleaching of sensitizer fluorescence. For some photosensitizers, the singlet oxygen that is responsible for destruction of tumor cells also leads to irreversible destruction of the

sensitizer. This can be monitored by fluorescence spectroscopy, and has been shown to correlate with fluence rate[54, 55]. There have also been studies done that show strong correlations between fluorescence photobleaching and tumor response [21-23], indicating that this measurement indeed provides information on singlet oxygen generation. However, this is only true of certain photosensitizers, particularly for the prodrug amino-levulinic acid (ALA) which is metabolized into protoporphyrin IX (PpIX). As will be shown later in this chapter, there exist sensitizers for which the photobleaching of fluorescence is not correlated with tumor response.

Another method for monitoring of singlet oxygen generation involves the examination of reflectance spectra. These collected reflectance spectra can be used to determine the relative concentrations of oxy- and deoxyhemoglobin, since the absorption of hemoglobin depends upon the binding of oxygen. The generation of singlet oxygen requires the consumption of ground state, molecular oxygen, which can lead to the de-oxygenation of hemoglobin in the treatment field. The oxygen saturation of hemoglobin can then be used as an indicator of singlet oxygen generation and tumor outcome. Interpretation of this information can be challenging, as reduced oxygen saturation can also indicate treatment-induced reduction of blood flow to a volume. Wang *et al* studied the correlation between hemoglobin oxygen saturation and tumor response in a mouse model[56]. They found that the change in hemoglobin oxygen saturation during PDT was significantly correlated with survival, indicating that a decrease in oxygenation can be used as a metric of the photodynamic dose delivered. Spectroscopic determination of oxy- and deoxyhemoglobin concentrations is discussed further in chapter 4.

This chapter focuses on two studies that examined optical monitoring of PDT in mouse models. In the first, we demonstrate the ways in which spectroscopy can inform the selection of treatment parameters using reflectance and fluorescence. The main goal of this study was to determine the optimal treatment parameters for methylene blue mediated PDT, in which spectroscopy played a major role. In the second study, we examine the photobleaching of the photosensitizer Pc 4, and its relation to the fluence rate during treatment. This photobleaching is then analyzed in the context of tumor response.

## 2.2 Monitoring of methylene blue mediated PDT by fluorescence and reflectance spectroscopy

### 2.2.1 Introduction

A key component of PDT is the photosensitizer. In this study[57], we investigated methylene blue (MB), an FDA-approved phenothiazine dye that is generally used to treat methemoglobinemia [58] and has been used successfully to stain intestinal metaplasia in Barrett's esophagus[59] and in the stomach to guide endoscopic biopsy[60]. It is inexpensive and is routinely available in hospital pharmacies. MB is also well known to be photodynamically active. Several studies have shown that MB mediated PDT (MB-PDT) can effectively inactivate viruses[61] and destroy bacteria[62]. Additionally, MB-PDT has been shown to be effective in destroying tumors in mice[63-65]. In humans, MB-PDT has been used to treat superficial tumors of the bladder[66], esophageal carcinomas[67], melanoma[68], and Kaposi's sarcoma[69] with no reported toxicities.

Because it is biochemically modified to a colorless form[70], there is little if any systemic photosensitivity associated with MB.

Despite the potential advantages of MB and the opportunities presented by its FDA status, widespread availability, and low cost, there have not been systematic investigations of the effects of various treatment parameters on MB-PDT in animal models. Therefore, the intention in this study was to evaluate some of the factors that may influence the outcome of MB-PDT in a tumor model. The variables that we examined were drug-light interval, delivery vehicle, and fluence. Because MB is typically administered via direct intratumor injection, short drug-light intervals may be exploited without sacrificing selectivity. The vehicle in which the photosensitizer is delivered may also have an impact on the outcome of the treatment insofar as it influences the homogeneity of intratumor distribution. Orth *et al*[65] described inhomogeneous intratumor distribution of MB following injection using an aqueous vehicle. In previous studies with the photosensitizer Pc 4, we demonstrated relatively uniform distributions with a Cremophor-ethanol-saline injection vehicle[71]. Finally, the fluence is another obvious factor influencing the treatment outcome. Anticipating an eventual clinical trial, we chose to limit the total treatment time from injection to the end of irradiation to approximately two hours. This constrained the maximum fluence for a given irradiance. The comparison of these factors was accomplished through a combination of spectroscopic studies *in vitro* and *in vivo*, imaging of MB fluorescence in freshly excised tumors, and long term tumor control trials in an intradermal murine tumor model.

### 2.2.2 Methods

#### 2.2.2.1 Tumor model

Intradermal (ID) mouse mammary EMT6 tumors were initiated on the backs of female BALB/c mice by ID injection of $10^6$ cells. Tumor growth was monitored daily. For a period of approximately 2 weeks prior to PDT and spectroscopy, mice were fed a chlorophyll-free diet prepared using the recipe of Holmes *et al*[72]. Tumors were treated when volumes reached approximately 25 – 40 $mm^3$. All experiments were conducted according to the institutional guidelines of the University of Rochester Medical Center and approved by the University Committee on Animal Resources.

#### 2.2.2.2 Photosensitizer administration and light treatment

Sterile, clinical grade MB (10 mg/mL, American Regent, Shirley, NY) was obtained from the pharmacy at Strong Memorial Hospital, University of Rochester. This was diluted 1:20 in deionized water to obtain a 500 µg/mL aqueous injection vehicle. A 5% ethanol-5% Cremophor-90% saline solution (Cremophor vehicle) containing the same 500 µg/mL concentration of MB was created by diluting 50 µL of the sterile MB stock in 850 µL of 0.9% saline and adding this to 100 µL of a 1:1 solution of Cremophor and ethanol. Either the water or the Cremophor vehicle was administered in a 35 µL dose via intratumor (IT) injection at a single site using a 29-gauge needle. Either immediately (0 drug-light interval) or after 1 h, 667 nm PDT treatment light from a diode laser (Power Technology, Alexander, AR) was delivered at 60 $mW/cm^2$ using the off-surface delivery probe shown in Figure 2.1. Fluences of 240 or 480 $J/cm^2$ were delivered, and the total treatment time (from MB injection to the end of irradiation) was constrained to approximately 2 h.

Irradiation was interrupted every 60 J/cm$^2$ (16 min 40 s) for approximately 6 s in order to perform spectroscopy as described immediately below. Control animals received the same 35 μL IT injection of MB with either the water or Cremophor vehicle but were not irradiated.

### 2.2.2.3 Light Delivery and Spectroscopic Measurements

Treatment light, excitation light for fluorescence spectroscopy, and broadband white light for reflectance spectroscopy were delivered to the surface of the tumor via a custom, off-surface probe shown in Figure 2.1.

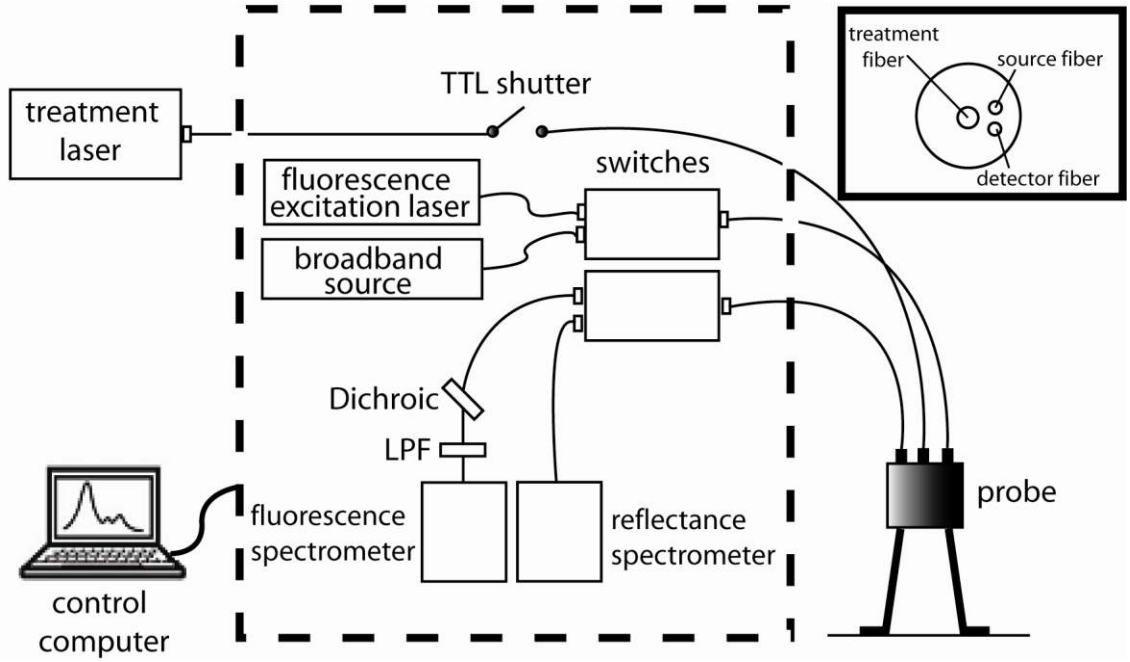


**Figure 2.1** Schematic of PDT treatment and spectroscopy system. Switches, sources, and spectrometers are computer controlled. A 664 nm long pass filter and a 669 nm dichroic mirror are used to filter out the excitation source in the fluorescence detection arm. Inset shows schematic of probe for delivery of treatment light, fluorescence excitation, and broadband white light and collection of spectra. The probe is not drawn to scale. Reproduced from [57].

The probe consisted of a central GRIN-terminated fiber for delivery of treatment light and two SMA-terminated fibers, one of which served as a source for delivery of fluorescence excitation and broadband light while the other collected fluorescence and reflectance from the tumor. During a treatment session, PDT irradiation was interrupted every 60 J/cm$^2$ with a computer controlled in-line shutter (Mikropack, Ostfildern, Germany), and fluorescence excitation and broadband light were routed sequentially via an optical switch (Piezosystem Jena, Hopedale, MA) to the source fiber of the probe. Fluorescence excitation was performed with 639 nm light from a diode laser (Oz Optics, Ottawa, Ontario, Canada). The broadband reflectance source was a tungsten-halogen lamp (Avantes, Broomfield, CO). Fluorescence and reflectance spectra were acquired by dedicated, TE-cooled, 16 bit spectrometers (B & W Tek, Newark, DE) using integration times of 5 and 0.5 s, respectively. The fluorescence detection path included a dichroic mirror (FF669-Di01, Semrock, Rochester, NY) and a long pass filter (LP02-664RU, Semrock) as shown in Figure 2.1. The source and detector fibers of the probe interrogated an overlapping 3 mm-diameter area at the center of the treatment field. A custom LabVIEW program (National Instruments, Austin, TX) controlled the sequence of PDT irradiation and spectral acquisitions.

**2.2.2.4 Spectral processing and analysis**

Spectra were corrected by subtracting the background and then dividing by the measured, wavelength-dependent system response. Backgrounds were taken before each mouse was treated by integrating dark signals for the durations described above. System responses were acquired by reflecting the light from a NIST-traceable lamp (Model # LS-

1-CAL, Ocean Optics, Dunedin, FL) off of a diffuse reflectance standard (Part # WS-1, Ocean Optics) into the probe collection fiber. The measured spectrum was then background subtracted and divided by the known lamp spectrum to obtain the system response. Fluorescence spectra were further corrected for the effects of tissue optical properties by dividing the fluorescence by reflectance spectra measured in the same wavelength range and in the same geometry[73].

After fluorescence spectra were acquired and corrected, they were fit using a singular value decomposition (SVD) algorithm based on the work of Press *et al.*[74]. The two basis spectra shown in Figure 2.2a were used in the fits. The first was the monomeric MB fluorescence spectrum, determined by measuring the fluorescence emission of 3.1 μM MB in a commercial fluorometer (Varian Eclipse, Palo Alto, CA). The sample was prepared in a 1:10 dilution of 10% Liposyn (Abbott Laboratories, North Chicago, IL) in deionized water in order to more closely replicate conditions *in vivo*. The other basis was created in order to fit the long wavelength, dimeric fluorescence. This was done by slowly increasing the concentration of MB from 3 to approximately 200 μM and acquiring fluorescence spectra as shown in Figure 2.2b.

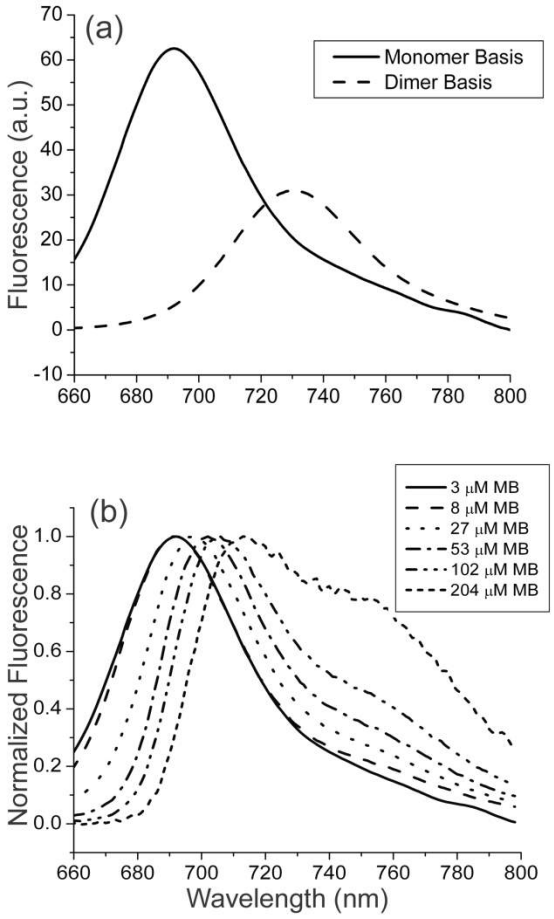


**Figure 2.2** (a) Bases used for SVD fitting, as determined by cuvette measurements made in a commercial fluorometer. Amplitude scaling is arbitrary and meant to illustrate relative contributions of bases to overall SVD fitting. (b) Normalized fluorescence spectra of MB measured in a commercial fluorometer illustrate shifted peak wavelength and growing contribution of long wavelength components with increasing MB concentration. Reproduced from [57].

The spectra were then normalized to their maximum value and shifted so their maxima aligned. The lowest concentration spectrum was then subtracted from the highest concentration spectrum in order to isolate the long wavelength fluorescence. This difference was then fitted with a Gaussian in order to generate the dimer basis spectrum. In addition to the basis spectra, a series of 61 Fourier terms was also used in fitting to

account for unknown possible contributions to the measured fluorescence *in vivo*. These Fourier terms were given a smaller weight in the fitting in order to favor the basis spectra.

Fitting followed the SVD scheme found in MATLAB (Mathworks, Natick, MA). However, the basis functions were allowed to shift a few nanometers in either direction in order to account for apparent absorption-induced changes in fluorescence that were not corrected by the division by reflectance.

**2.2.2.5 Imaging MB fluorescence in freshly excised EMT6 tumors**

Freshly excised tumors from several mice were sectioned in half and imaged using a stereofluorescence microscope (Model SMZ1500, Nikon Instruments Inc., Melville, NY) to assess intratumor distribution of MB. Mice were given an IT injection of 35 µL of 500 µg/mL MB in either the water or Cremophor vehicle. They were then immediately sacrificed and the tumors excised. Tumors were then sliced in half and placed on the stage of the microscope. Imaging was performed using 639 nm laser excitation (Oz Optics, Ottawa, Ontario, Canada), routed to the microscope with a liquid light guide, and a custom filter cube optimized for MB (Micro Video Inst., Avon, MA). Images were acquired using a 12-bit Photometrics CoolSNAPHQ CCD (Roper Scientific, Inc., Trenton, NJ). An image of a homogeneous methylene blue solution served as a system response function, and each subsequent image was divided by this image to eliminate non-uniformities due to illumination and collection optics. Image analysis was performed using the Surface Plot tool in ImageJ (NIH; URL: http://rsb.info.nih.gov/ij/).

#### 2.2.2.6 Tumor response assay and statistics

Tumor dimensions along three axes were measured daily following PDT. The tumor volume was computed assuming an ellipsoidal shape. Mice were removed from the study if the tumor grew to twice the volume measured at the time of irradiation. Cures were defined as no palpable tumor 90 days after PDT. Uni- and multivariate statistical analysis of tumor responses was performed using a Cox proportional hazards model implemented in the R package survival (http://cran.r-project.org/web/packages/survival/index.html). Model selection in the multivariate analysis was done using an Akaike information criterion (AIC).

### 2.2.3 Results

Fluorescence and reflectance spectra were acquired from MB-sensitized EMT6 tumors *in vivo* immediately before, at defined intervals during, and immediately after irradiation. Measured fluorescence spectra were fit with an SVD algorithm and two basis spectra, as described in section 2.2.2.4. The results of this fitting can be seen in Figure 2.3. Figure 2.3a shows a representative fit to a spectrum acquired immediately after IT injection of 500 μg/mL MB in the water vehicle. The spectrum is fit well with a superposition of the monomer and dimer bases. In this case the dimer/monomer ratio was 0.26, but there was considerable tumor-to-tumor variation in this pre-irradiation ratio. The fluorescence spectrum of the same tumor after irradiation with 480 J/cm$^2$ is shown in Figure 2.3b. The overall fluorescence magnitude is increased relative to the pre-irradiation spectrum, and there is an increased contribution of the dimer basis to the fit. In this tumor, the post-irradiation dimer/monomer ratio increased to 0.52, but this also was not a general trend.

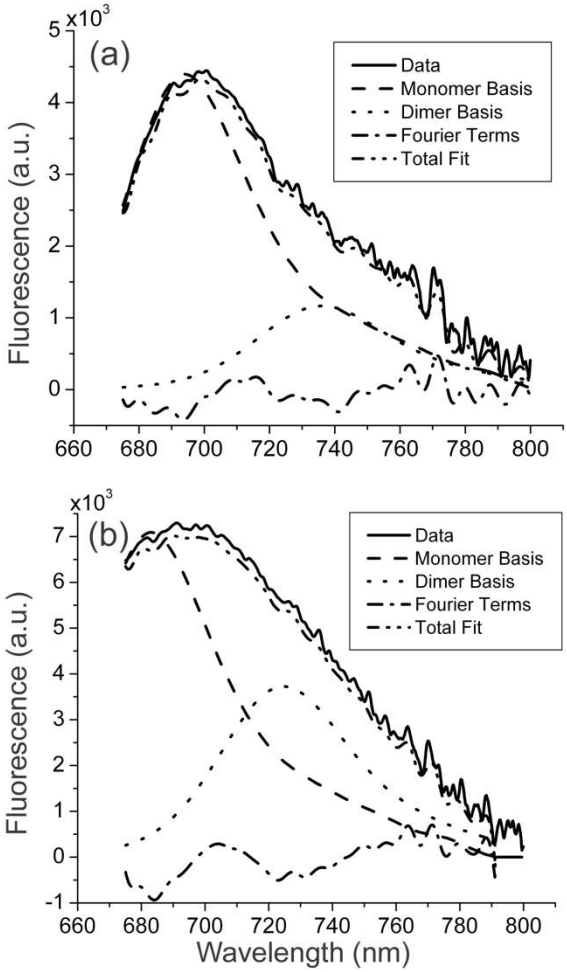


**Figure 2.3** Results of SVD fitting of a representative fluorescence spectrum taken from the same EMT6 tumor *in vivo* (a) immediately after IT injection of MB but before delivery of treatment light and (b) after conclusion of PDT (480 J/cm$^2$) under identical acquisition conditions, illustrating the increased magnitude of fluorescence and an increased presence of dimer fluorescence induced by irradiation. Reproduced from [57].

Figure 2.4a shows a series of fluorescence spectra acquired *in vivo* from a tumor that received a 35 µL IT injection of 500 µg/mL MB in the Cremophor vehicle. Fluorescence was measured every 15 minutes after injection for a period of two hours in the absence of irradiation. As can be seen, the measured fluorescence decreases

monotonically after injection during this interval. Figure 2.4b summarizes this trend in mice monitored for a period of one hour, after which seven mice were irradiated with 667 nm light at 60 mW/cm$^2$.

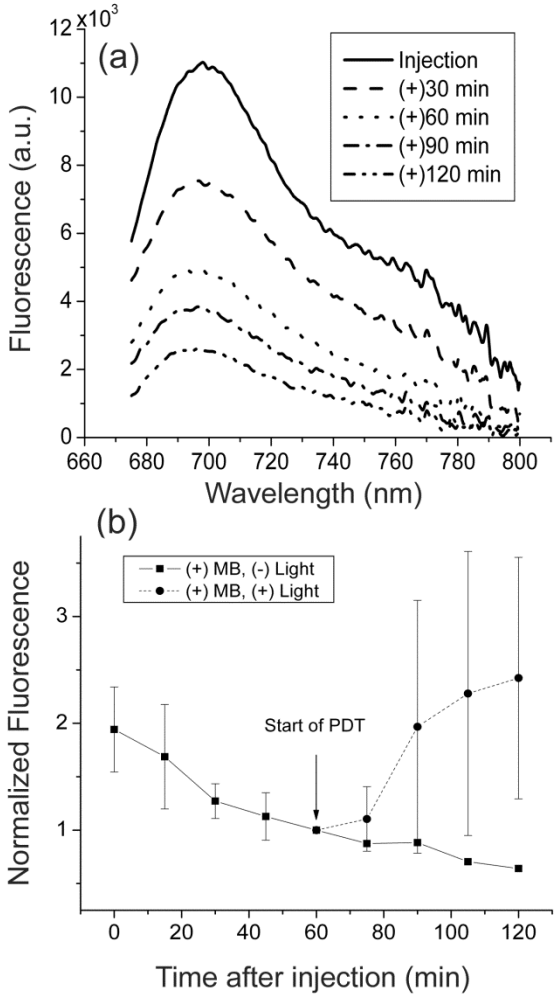


**Figure 2.4** (a) MB fluorescence spectra *in vivo* at various times following IT administration of MB in a 5% EtOH, 5% Cremophor, 90% saline vehicle. Excitation wavelength was 639 nm. (b) Magnitude of MB fluorescence before and during PDT, normalized to the onset of irradiation. All mice received 35 µL of 500 µg/mL of MB in Cremophor based vehicle. Irradiated mice (n=7) received 240 J/cm$^2$, 60 mW/cm$^2$ at 667 nm. MB fluorescence in mice not irradiated (n=2) continued to decrease from 60 to 120 min after injection. Reproduced from [57].

In the irradiated mice, the amplitude of MB fluorescence was progressively restored and in some cases exceeded the pre-irradiation levels, while fluorescence from the un-irradiated tumors continued to decrease. This irradiation-induced increase suggests that the measured loss of fluorescence during the dark interval is not the result of clearance of MB from the tumor. Rather, it likely originates in the biochemical modification to a colorless form as described by DiSanto and Wagner[70].

To assess the intratumor distribution of MB following IT injection at a single site, mice were sacrificed immediately after injection, tumors were excised, sectioned in half, and placed on the stage of the stereofluorescence microscope. Representative images and image analysis are shown in Figure 2.5 for the Cremophor (a, c) and water (b, d) injection vehicles. Tumors injected using the Cremophor vs. water vehicle show a greater degree of MB fluorescence homogeneity. Image analysis revealed that fluctuations in pixel intensities were more pronounced (6- vs. ~2.5-fold) in tumors injected with the water vehicle. Nearly 10% of the pixels in the "aqueous" image were below a threshold set at twice the background counts measured from control tumors under identical image acquisition conditions. In the "Cremophor" images, less than 0.5% of pixels were below this threshold.

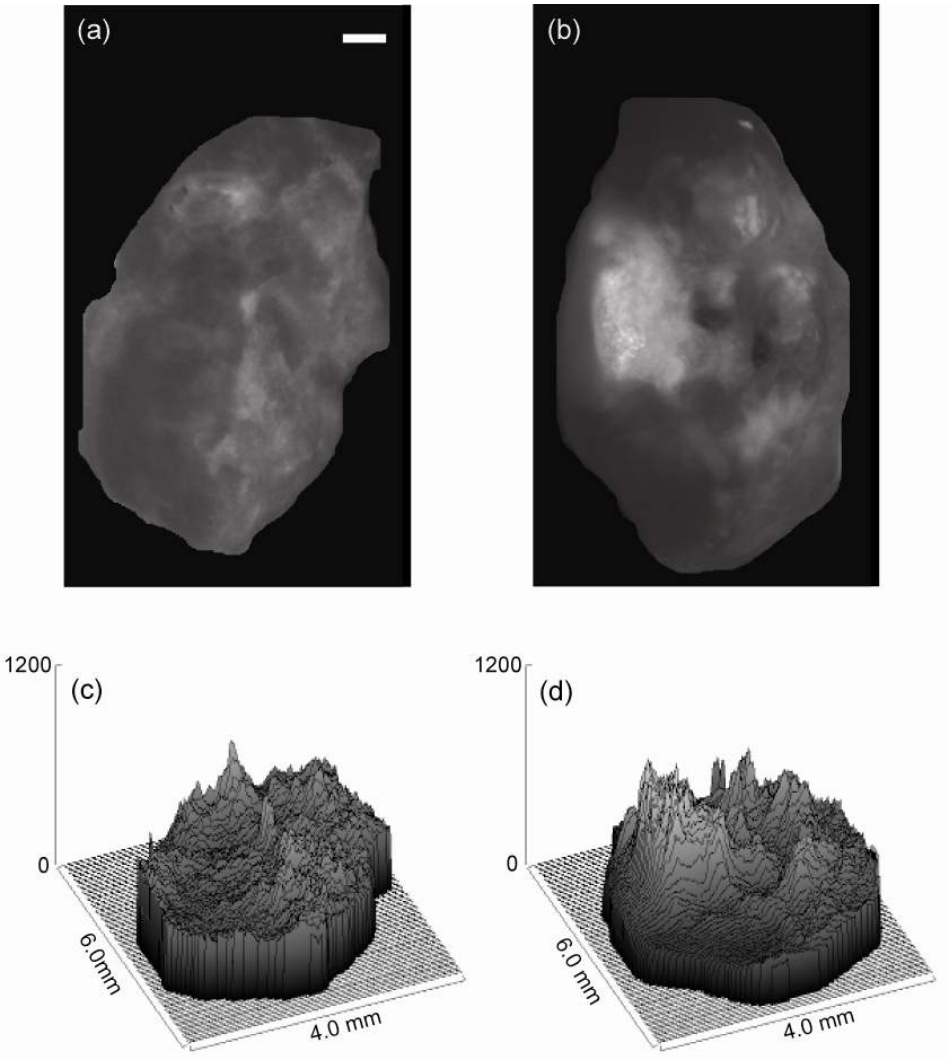


**Figure 2.5** MB fluorescence images of freshly sectioned EMT6 tumors acquired immediately after IT administration of 500 µg/mL MB in the Cremophor (a) and water (b) injection vehicles. (c) and (d) are surface plots of pixel intensities from (a) and (b), respectively. The scale bar is 0.5 mm. Reproduced from [57].

Results of the tumor control studies are illustrated in the Kaplan-Meier plots of Figure 2.6. As described in section 2.2.2.6, tumor volume doubling was the end point used as a measure of treatment failure. Cures were defined as no evidence of tumor 90 days after PDT. All mice received the same 35 µL injection of 500 µg/mL MB administered in either the water or Cremophor vehicle. In addition to injection vehicle,

we investigated responses to 480 vs. 240 J/cm$^2$ fluence. Based on anticipated clinical constraints, we limited the duration of the procedure (from time of injection to end of irradiation) to approximately 2 hours. Thus, we evaluated protocols in which irradiation was initiated immediately after sensitizer injection in order to deliver the maximum fluence within this 2 hour interval. Among these protocols, the most successful combined the Cremophor vehicle, a zero drug-light interval, and a fluence of 480 J/cm$^2$. A long-term cure rate of 55% (5 of 9) was achieved under these conditions. Univariate statistical analysis of all of the protocols using a Cox proportional hazards model revealed that increased fluence ($p=0.00042$), decrease in the drug-light interval ($p=0.0013$), and the use of a Cremophor vs. water vehicle ($p=0.009$) were all statistically significant predictors of long-term tumor response, with p-values $< 0.05$ for each of these treatment parameter comparisons. From a multivariate Cox proportional hazards analysis and model selection based on AIC, a combination of increased fluence ($p=0.001$) and use of the Cremophor vehicle ($p=0.027$) emerged as the best predictor of treatment outcome ($p < 0.05$).

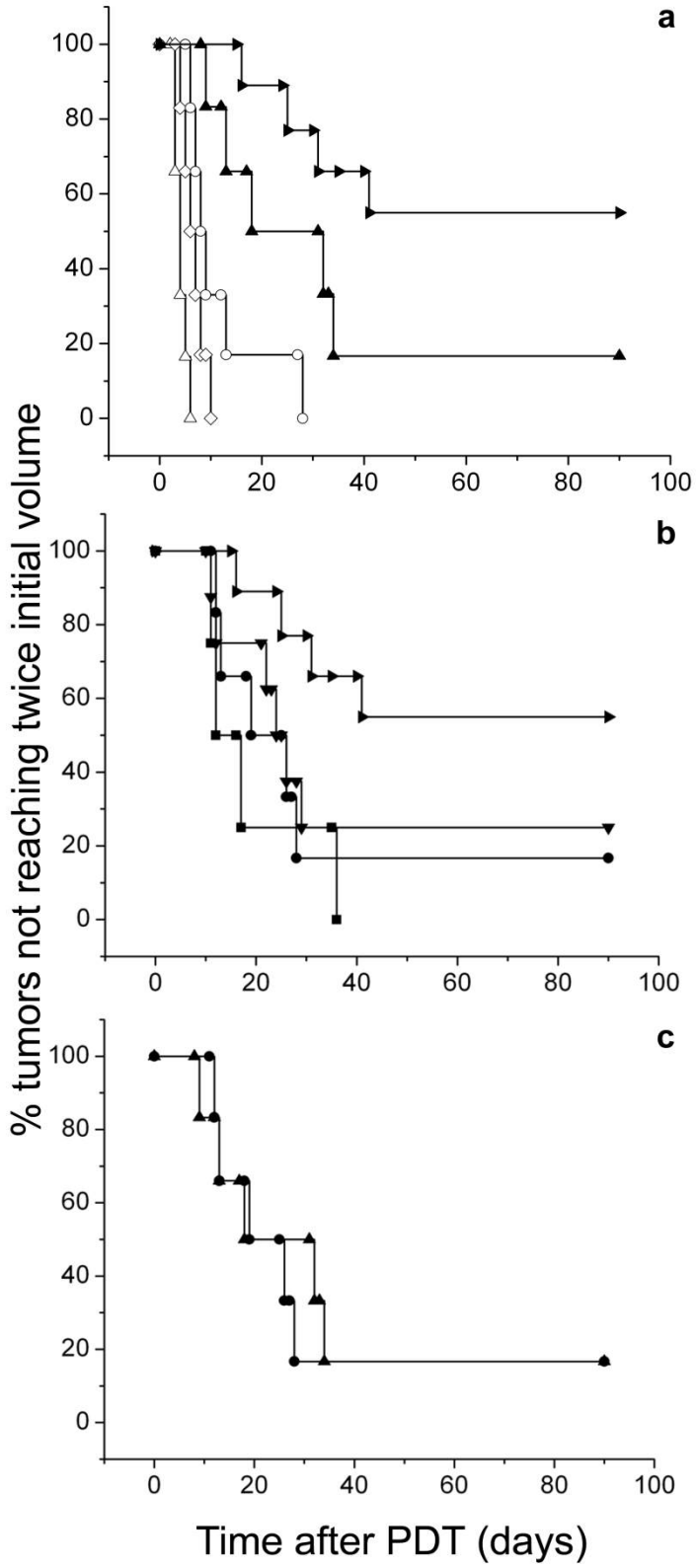
a
b
c
% tumors not reaching twice initial volume
Time after PDT (days)
0
20
40
60
80
100

**Figure 2.6** Kaplan-Meier curves illustrating effects of (a) fluence, (b) sensitizer delivery vehicle, and (c) drug-light interval on response of EMT6 tumors to methylene-blue PDT *in vivo*. (a) (Δ) Drug and irradiation free control (n=6); (◊) Drug only control, water vehicle (n=6); (○) Drug only control, Cremophor vehicle (n=6); (▲) Cremophor vehicle, 0 drug-light interval, 240 J/cm$^2$ (n=6); (►) Cremophor vehicle, 0 drug-light interval, 480 J/cm$^2$ (n=9); (b) (■) Water vehicle, 1 h drug-light interval, 240 J/cm$^2$ (n=5); (●) Cremophor vehicle, 1 h drug-light interval, 240 J/cm$^2$ (n=6); (▼) Water vehicle, 0 drug-light interval, 480 J/cm$^2$ (n=10); (►) Cremophor vehicle, 0 drug-light interval, 480 J/cm$^2$ (n=9); (c) (●) Cremophor vehicle, 1 h drug-light interval, 240 J/cm$^2$ (n=6); (▲) Cremophor vehicle, 0 drug-light interval, 240 J/cm$^2$ (n=6). Reproduced from [57].

As mentioned above, reflectance spectra were also acquired before, during, and immediately after PDT. In addition to allowing for correction of the fluorescence spectra, reflectance provides a measure of tissue optical properties. Figure 2.7 shows a series of three reflectance spectra taken *in vivo* from the same tumor prior to injection of MB, immediately after injection but before the start of irradiation, and immediately post-irradiation with 480 J/cm$^2$.

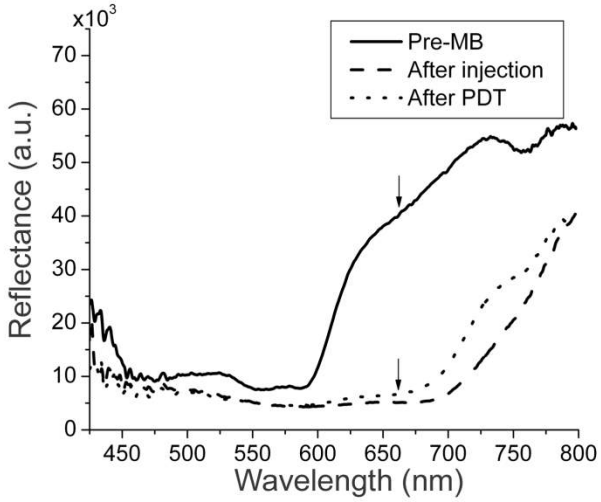


**Figure 2.7** Reflectance spectra measured from an EMT6 tumor before IT injection of MB, immediately after injection (500 μg/mL, 35 μL), and immediately after irradiation with 480 J/cm$^2$. Post injection spectrum shows decreased reflectance (*i.e.* increased absorption) at the treatment wavelength (arrow) and negligible irradiation-induced increase in reflectance. Reproduced from [57].

Particularly noteworthy is the greatly reduced reflectance (*i.e.* higher absorption) at the 667 nm treatment wavelength from the presence of MB. After irradiation only a modest increase in reflectance is observed. Thus MB at this injection concentration significantly increases tissue absorption at the PDT treatment wavelength, and this will be a factor in treatment planning for larger tumors.

### 2.2.4 Discussion

Our experiments investigated effects of intratumor sensitizer delivery vehicle, the drug-light interval, and the fluence as factors capable of influencing the response of tumors to MB-PDT *in vivo*. Results illustrate that indeed attention to each of these treatment variables contributes to long term tumor control in this model. Specifically, the Cremophor vs. water vehicle, a 0 vs. 1 h drug-light interval, and increased fluence all independently predicted for reduced survival hazard.

Effects of the drug-light interval in intratumor MB-PDT have not been reported previously. The reduction of MB to a colorless form *in vivo* probably precludes systemic administration, but our fluorescence spectroscopy results, presented in Figure 2.4, show for the first time that a progressive loss of MB fluorescence occurs even after direct intratumor injection. This may provide a rationale for a very short drug light interval. As shown also in Figure 2.4, however, the MB fluorescence is restored in response to irradiation. Our statistical analysis suggests that even with this restoration, there is an advantage to a 0 vs. 1-h drug-light interval. In the case of intratumor sensitizer administration, long drug-light intervals are not needed in order to achieve selectivity. It is still desirable of course to allow enough time for the sensitizer to distribute throughout

the tumor volume. The images of Figure 2.5 show that this happens almost immediately after injection of a 35 µL volume, indicating that fluid pressure as opposed to passive diffusion drives the rapid transport of MB. Finally, in the anticipated clinical setting, it is desirable to limit the total treatment time. The 0 drug-light interval enables delivery of the maximum fluence in a given treatment duration. Taking all of this into account, if treatment time is constrained, a protocol including an efficient vehicle and the shortest possible drug-light interval will provide the highest fluence and the greatest efficacy. Other factors, specifically treatment irradiance and the use of more than one PDT treatment, which were evaluated by Orth *et al*[65], have not been considered here but may certainly contribute, as well.

The *in vivo* fluorescence and reflectance spectra shown in Figure 2.3**,** Figure 2.4**,** and Figure 2.7 are, to the best of our knowledge, the first such data to be reported in the literature. As illustrated in Figure 2.3, MB fluorescence from tumors could be fit consistently using a superposition of the two basis spectra shown in Figure 2.2. These bases were constructed from cuvette measurements over a wide range of MB concentrations and are attributed to monomer and dimer/aggregated forms. Tumor spectra generally contained contributions from both species, and it was not unusual for their relative contributions to change in response to PDT, as was the case for the tumor represented in Figure 2.3. There was, however, considerable heterogeneity in the pre-irradiation dimer/monomer ratio extracted from fits to spectra. Further, no significant trends were discernible in the dimer/monomer ratio changes induced by irradiation. In the case shown in Figure 2.3, the amplitudes of both the monomer and the dimer

contributions to the spectrum increased in response to irradiation, thereby ruling out a simple interpretation based on a shifting equilibrium between monomers and aggregates. MB is capable of complex chemistry, which is reflected in the following equations[75],

$$2\mathrm{MB} \underset{\longleftarrow}{\xrightarrow{K_D}} (\mathrm{MB})_2 \tag{2.1}$$

$$(\mathrm{MB})_2 \xrightarrow{k_1} \mathrm{MB}\cdot + \mathrm{MB}\cdot^{2+} \tag{2.2}$$

$$\mathrm{MB}\cdot + \mathrm{O}_2 \xrightarrow{k_2} \mathrm{O}_2^{-\bullet} + \mathrm{MB} \tag{2.3}$$

where equation 2.1 represents the equilibrium between MB monomers (MB) and dimers, $(MB)_2$, with equilibrium constant $K_D$. Equation 2.2 represents the creation of MB radicals from ground state dimers at a rate $k_1$ proportional to the laser excitation, with $MB\cdot$ and $MB\cdot^{2+}$ indicating the semi-reduced and semi-oxidized radical forms, respectively. Finally, Equation 2.3 represents the formation of superoxide, $O_2^{-\bullet}$, and ground state MB monomer at the rate $k_2$ from the semi-reduced MB radical in the presence of molecular oxygen. Thus, the creation and dissociation of aggregates *in vivo* is likely to be a complex process, especially in the presence of heterogeneous and possibly dynamic tumor oxygen concentrations. The interpretation of MB fluorescence before, during, and after PDT is therefore a rich area for further study. As indicated in equations 2.2 and 2.3, it is entirely likely that Type I processes contribute to tumor destruction with MB-PDT.

Finally, the reflectance spectra shown in Figure 2.7 reveal an important aspect of PDT performed with relatively high intratumor concentrations. MB at the concentration injected in our study significantly attenuates the transmission of 667 nm treatment light,

indicated by the vertical arrows in the figure. This attenuation is not appreciably reduced by irradiation-induced photodegradation of MB. This effect on tumor optical properties will have to be taken into account in treatment planning.

## 2.3 Analysis of Pc 4 photobleaching by fluorescence spectroscopy

### 2.3.1 Introduction

One of a number of second-generation photosensitizers, the silicon phthalocyanine Pc 4 ($HOSiPcOSi(CH_3)_3(CH_2)_3N(CH_3)_2$) was developed in the laboratory of Malcolm Kenney at Case Western Reserve University. Its synthesis and structure have been reported previously[76], and its history has been reviewed[77]. It has been evaluated in humans to treat cutaneous T-cell lymphoma and a variety of other cutaneous neoplasms in phase 1 clinical trials at Case Western Reserve University[77-79]. Our laboratory has previously demonstrated increased effectiveness of Pc 4-photodynamic therapy (PDT) in mice using intratumor vs. systemic injection of the photosensitizer with short drug-light intervals[71]. This study also showed recovery of Pc 4 fluorescence 24 hours after PDT, which we interpreted as an indication of initially aggregated Pc 4 monomerizing following the bleaching of a fraction of the locally-injected sensitizer population. Thus it appeared that intratumor injection had resulted in excess Pc 4 under the conditions of those experiments.

Most photosensitizers undergo irreversible photobleaching in response to irradiation during PDT[20]. Since photobleaching can be mediated by reactive oxygen species, it has often been speculated that the loss of photosensitizer fluorescence could be used to predict dose deposition and therefore the outcome of PDT. A number of studies

have been carried out with various photosensitizers in order to examine this possibility. As mentioned previously, the most promising results have been reported for the prodrug ALA, which is metabolized into PpIX. A correlation between PpIX photobleaching and tumor response has been shown in a rat model of Barrett's esophagus[21], a rat model of ovarian cancer[22], and in humans with actinic keratoses, Bowen's disease, and basal cell carcinoma[23]. In all cases, high PpIX bleaching was associated with a strong response to PDT. However, the ability of fluorescence photobleaching to predict tumor outcome at the level of an individual animal or patient was not explored in these studies.

In the case of Pc 4, work in tumor cell monolayers and very low fluences demonstrated an increase in sensitizer fluorescence in response to irradiation[80]. However, this phenomenon has not been observed *in vivo*, where several studies have shown that Pc 4 does indeed bleach in response to irradiation [24, 71, 81]. Whether a correlation between photobleaching dynamics and tumor response exists for Pc 4 has not been thoroughly examined. A link between Pc 4 concentration before irradiation, assessed using reflectance spectroscopy, and tumor response was shown in a study by Bai *et al*[24]. That work demonstrated that pre-PDT Pc 4 concentration at the tumor could be used as a predictor of outcome for individual animals. They also noted a correlation between total Pc 4 photobleaching and tumor response.

In this study[82], we explored the relationship between spectroscopic measurements made during PDT and tumor response in individual tumor-bearing mice. If established, such a relationship would allow prediction of treatment response in individual patients, thereby enabling earlier intervention in those cases where PDT is

likely to fail. To do this, we examined tumor response to Pc 4-PDT at 100 J/cm$^2$ using either 50 or 150 mW/cm$^2$ and a whole-body photosensitizer concentration of 0.03 mg/kg administered by IT injection. Fluorescence and reflectance spectra were collected before, during, and after PDT in order to quantify the photobleaching of Pc 4 in response to irradiation. The relationship between photobleaching and tumor response was examined for individual animals within both treatment groups and as a pooled group. Correlation between photobleaching and tumor growth delay was found to be statistically insignificant in all cases.

### 2.3.2 Methods

#### 2.3.2.1 Tumor model

ID mouse mammary EMT6 tumors were initiated on the backs of female BALB/c mice by ID injection of $10^6$ cells. Tumor growth was monitored every 2-3 days. For a period of approximately 2 weeks prior to PDT and spectroscopic measurements, mice were fed a chlorophyll-free diet prepared using the recipe of Holmes *et al*[72]. Tumors were treated when volumes reached approximately 100 mm$^3$. All experiments were conducted according to the institutional guidelines of the University of Rochester Medical Center and approved by the University Committee on Animal Resources.

#### 2.3.2.2 Photosensitizer administration and light treatment

Powdered Pc 4 was obtained from Dr. Malcolm Kenney at Case Western Reserve University, and was prepared as described previously[83]. Pc 4 was dissolved in a 1:1 solution of ethanol and Cremophor (Cremophor® EL, Sigma-Aldrich, St. Louis, MO) to create a stock solution at a concentration of 2.1 mg/mL. This stock solution was diluted

at a ratio of 1:9 in a 1:1 solution of ethanol and Cremophor, and then further diluted at a ratio of 1:9 in 0.9% saline. This series of dilutions yielded a Pc 4 concentration of 0.021 mg/mL, in a solution consisting of 90% saline, 5% ethanol, and 5% Cremophor. A fresh stock solution of Pc 4 was created on each day for which PDT was delivered.

Prior to light treatment, 35 µL of 0.021 mg/mL Pc 4 was delivered by IT injection at a single site using a 29 gauge needle. Given an average mass of 25 g for mice used in the study, this resulted in a whole body Pc 4 concentration of 0.03 mg/kg. In our experience with this injection vehicle[57, 71], this procedure results in relatively uniform distribution of photosensitizer throughout tumors of this size. Immediately after drug administration, 667 nm PDT treatment light from a diode laser (Power Technology, Alexander, AR) was delivered at either 50 or 150 mW/cm$^2$. The fluence delivered was fixed at 100 J/cm$^2$. Irradiation was interrupted at pre-defined points for approximately 3 seconds in order to perform spectroscopy as described below. Drug-only control animals were given the same Pc 4 injection but were not irradiated, while drug-free controls received neither Pc 4 nor irradiation.

**2.3.2.3 Light delivery and spectroscopic measurements**

Treatment light, excitation light for fluorescence, and broadband white light for reflectance were delivered to the surface of the tumor using the system shown in Figure 2.1. During a treatment session, PDT irradiation was interrupted at pre-defined fluences with a computer controlled in-line shutter (Mikropack) and fluorescence excitation and broadband light were routed sequentially via an optical switch (Piezosystem Jena). Fluorescence excitation was performed with 639 nm light from a diode laser (Oz Optics,

Ottawa, Ontario, Canada) filtered by a band-pass filter (Z635/20x, Chroma Technology, Bellows Falls, VT). The broadband source was a tungsten-halogen lamp (Avantes). Fluorescence and reflectance spectra were acquired by dedicated, TE-cooled, 16 bit spectrometers (B&W Tek, Newark, DE) using integration times of 2 and 0.5 seconds, respectively. Spectra were captured before, during, and immediately after PDT, as well as 24 hours post-PDT. The fluorescence detection path included a long pass filter (HQ645LP, Chroma). The source and detector fibers on the probe interrogated an overlapping area at the center of the treatment field with a diameter of 3 mm. A custom LabVIEW program (National Instruments) controlled the sequence of PDT irradiation and spectral acquisition.

**2.3.2.4 Spectral processing and analysis**

Spectra were corrected by background subtraction and division by a measured, wavelength-dependent system response, as described in section 2.2.2.4. Fluorescence spectra were further corrected for the effects of tissue optical properties by dividing the fluorescence by reflectance spectra measured in the same wavelength range and geometry[73]. Effects of PDT-induced changes in optical properties at the fluorescence excitation wavelength were accounted for by dividing the emission spectrum by the measured reflectance at this wavelength raised to the power 0.88. This empirical, probe-specific correction factor was derived from measurements in tissue simulating phantoms, as reported previously[54].

After fluorescence spectra were acquired and corrected, they were fit using a singular value decomposition (SVD) algorithm based on the work of Press *et al* [74].

The basis spectrum used in fitting was acquired by measuring the fluorescence emission of 0.3 μM Pc 4 in a 5% ethanol, 5% Cremophor, 90% saline solution using a commercial fluorometer (Varian Eclipse, Palo Alto, CA). Fitting followed the SVD scheme found in MATLAB (Mathworks, Natick, MA). The Pc 4 basis was allowed to shift a few nanometers in either direction in order to account for environment-induced changes in fluorescence that were not corrected by the division by reflectance. A Fourier series was used to fit small contributions of unknown origin to the measured fluorescence spectra[54].

In order to quantify Pc 4 photobleaching, the magnitude of the Pc 4 basis returned by SVD fitting of fluorescence was plotted against fluence, normalized to the magnitude of the Pc 4 basis immediately prior to irradiation. A single exponential model of photobleaching was then fit to the degradation of fluorescence,

$$F(d) = F_0 e^{-kd} + F_B \tag{2.4}$$

where $F(d)$ is the fitted Pc 4 fluorescence at a given fluence, $d$ (J/cm$^2$), $F_0$ is the fluorescence prior to irradiation, $k$ is the photobleaching decay constant, and $F_B$ is a term representing background fluorescence[84]. Fitting was performed using the MATLAB curve fitting toolbox (Mathworks).

#### 2.3.2.5 Tumor response

Tumor dimensions along three axes were measured every 2-3 days following PDT. The tumor volume was computed assuming an ellipsoidal shape. Mice were removed from the study if the tumor grew to a volume twice that measured immediately before PDT.

#### 2.3.2.6 Statistical analysis

Comparison of photobleaching between the treatment groups was performed using a two-sample paired t-test at each measured fluence point (Origin 7, OriginLab, Northampton, MA). Statistical analysis of tumor doubling times was performed using the same test. The correlations between tumor doubling and photobleaching or reflectance were analyzed by calculating Spearman's rank correlation coefficients. The coefficients calculated were tested for significance using the test statistic,

$$t = r\sqrt{\frac{n-2}{1-r^2}} \tag{2.5}$$

where $n$ is the sample size and $r$ is the Spearman rank correlation coefficient. Statistical significance was determined by comparing the t value to a Student's t-distribution with n-2 degrees of freedom[74].

### 2.3.3 Results

Fluorescence and reflectance were acquired from Pc 4-sensitized EMT6 tumors *in vivo* before, during, and immediately after irradiation. Typical fluorescence and reflectance spectra are shown in Figure 2.8.

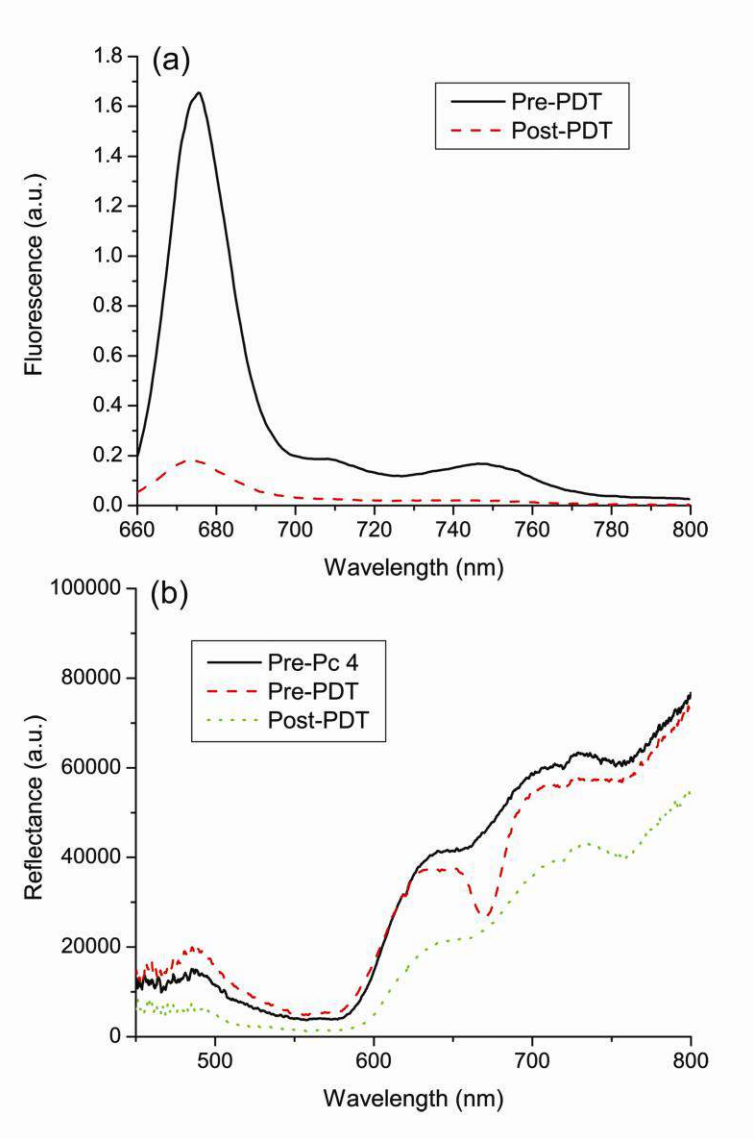


**Figure 2.8** Representative (a) fluorescence and (b) reflectance spectra taken *in vivo* from the same EMT6 tumor illustrate photobleaching of Pc 4 in response to PDT. The pre-Pc 4 reflectance spectrum was taken before administration of Pc 4 and pre-PDT spectra were taken immediately after IT injection of 0.03 mg/kg Pc 4. Post-PDT spectra were taken immediately after conclusion of irradiation (100 J/cm$^2$). Both sets of spectra were background subtracted and corrected for the wavelength-dependent system response. Fluorescence spectra were additionally divided by the corresponding reflectance spectra. Reproduced from [82].

The effect of Pc 4 absorption is evident in the reflectance spectra, with reflectance decreasing markedly around 667 nm after administration of the photosensitizer. Pc 4 photobleaching is visible in both fluorescence and reflectance spectra, with both the magnitude of Pc 4 fluorescence and the relative reduction of reflectance at 667 nm decreasing in response to irradiation. SVD fitting was performed on all fluorescence spectra, using a Pc 4 basis as described above. A typical SVD fit is shown in Figure 2.9.

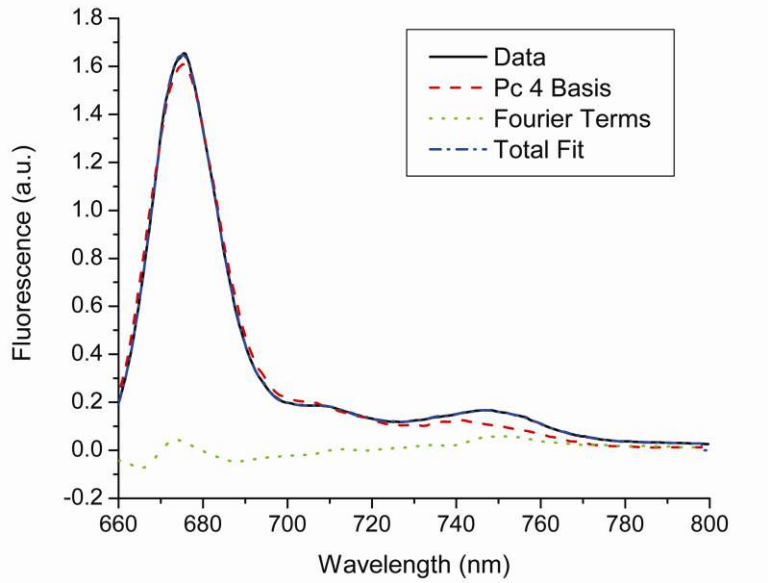


**Figure 2.9** Results of SVD fitting of a representative fluorescence spectrum taken *in vivo* after IT injection of 0.03 mg/kg Pc 4, but before delivery of treatment light. The Pc 4 basis was created by measuring 0.3 µM Pc 4 in solution using a commercial fluorometer. A 61-term Fourier series was used to fit unknown contributions to the fluorescence. Reproduced from [82].

The spectrum is fit well with the Pc 4 basis, as indicated by the relatively small magnitude of the Fourier terms in the overall fit.

Spectra were also acquired 24 hours after irradiation. The results of this are shown for a representative tumor in Figure 2.10.

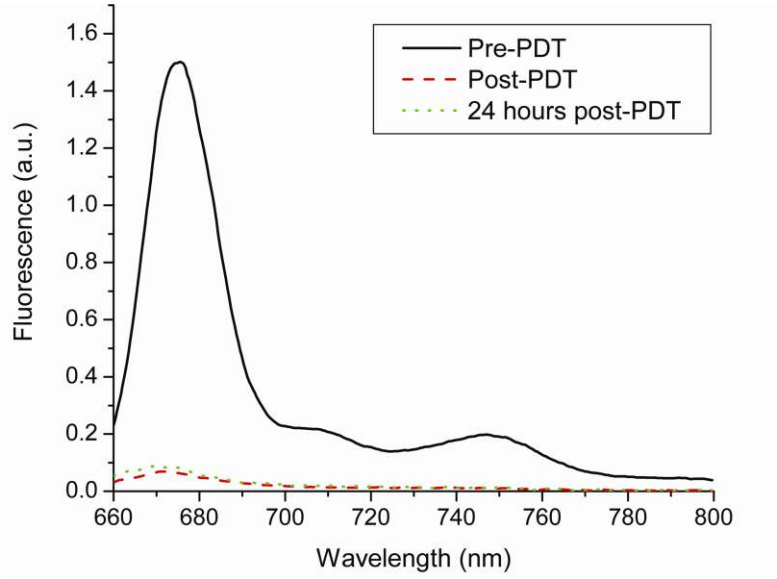


**Figure 2.10** Representative fluorescence spectra collected from the same EMT6 tumor *in vivo* before, immediately after, and 24 hours after irradiation (100 J/cm$^2$), as indicated in the legend. All spectra were collected under the same excitation and detection conditions, corrected for background and system response, and divided by the corresponding reflectance spectrum. Reproduced from [82].

As can be seen in the figure, the magnitude of Pc 4 fluorescence is essentially unchanged from immediately after to 24 hours after irradiation. The lack of fluorescence recovery, which we observed with a ten-fold higher injected Pc 4 concentration(5), suggests that a fluence of 100 J/cm$^2$ effectively consumes an intratumorally-administered whole-body drug dose of 0.03 mg/kg.

Pc 4 photobleaching was quantified by examining the amplitude of the Pc 4 fluorescence basis returned by SVD fitting, normalized to its amplitude measured immediately before irradiation. A representative bleaching curve for one mouse is shown in Figure 2.11.

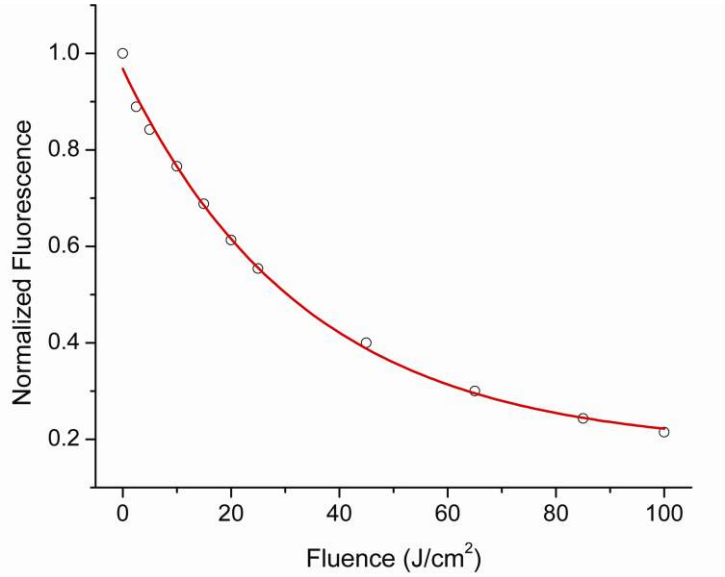


**Figure 2.11** Photobleaching of Pc 4 fluorescence measured *in vivo* during delivery of 667 nm treatment light at 50 mW/cm$^2$. Open circles represent the fit coefficient of the Pc 4 basis obtained from SVD fitting, normalized to the magnitude at the beginning of PDT. The solid line corresponds to a single exponential fit to the measured photobleaching, as shown in Equation 2.4. Reproduced from [82].

In this case, the open circles represent Pc 4 fluorescence measured during irradiation at 50 mW/cm$^2$. The solid line shown is the result of fitting Equation 2.4 to the measured data. The quality of the fit is good, indicating that Equation 2.4 is an appropriate empirical model in this case.

Average photobleaching curves were also generated for the two treatment groups. The results of this are shown in Figure 2.12.

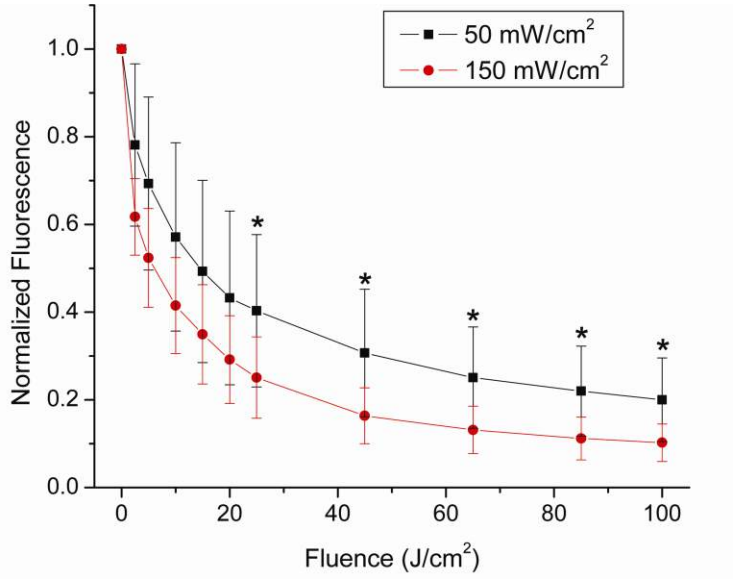


**Figure 2.12** Degradation of Pc 4 fluorescence due to photobleaching of Pc 4 in response to irradiation at (■) 50 mW/cm$^2$ (n=5) or (●) 150 mW/cm$^2$ (n=5), normalized to pre-PDT fluorescence. The increased rate of photobleaching at 150 mW/cm$^2$ was found to be significant with a significance level of $p<0.1$. The points marked with an asterisk (*) are fluences for which the difference between fluence rates was significant with a significance level of $p<0.05$. Error bars are standard deviations of measurements made in n=5 tumors for each group. Reproduced from [82].

Both photobleaching curves are the result of averaging the data from the five animals in each group, and the error bars are the standard deviations. Qualitatively, Pc 4 appears to photobleach more rapidly as a function of fluence for the fluence rate of 150 vs. 50 mW/cm$^2$. Photobleaching curves were compared on a point-by-point basis using a two-sample paired t-test, with the null hypothesis being that the two treatment groups had the same mean. All of the points, with the exception of the normalized pre-PDT value, were found to be significantly different at a significance level of $p<0.1$. At a significance level of $p<0.05$, only the points marked with an asterisk in Figure 2.12 were shown to be significantly different.

The results of Pc 4 PDT on tumor regrowth are shown in Figure 2.13.

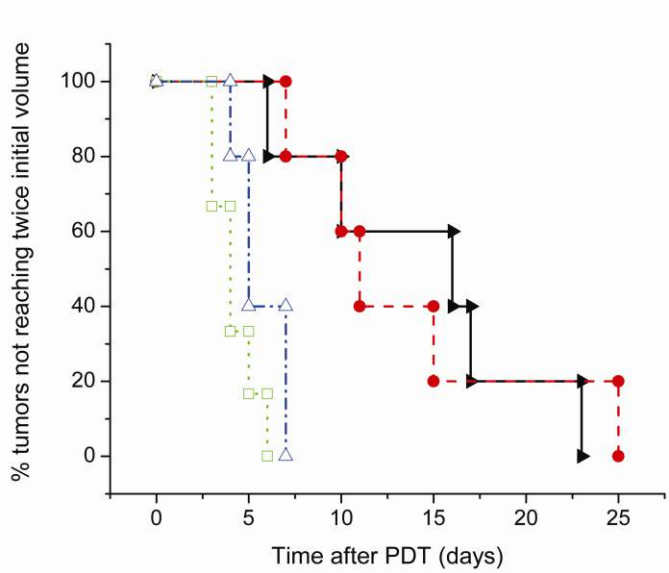


**Figure 2.13** Kaplan-Meier curves illustrating the effects of fluence rate on response of EMT6 tumors to Pc 4-PDT *in vivo*. Curves shown are (□) drug and irradiation free control (n=6); (Δ) 0.03 mg $kg^{-1}$ Pc 4, drug only control (n=5); (►) 0.03 mg $kg^{-1}$ Pc 4, 50 mW/$cm^2$, 100 J/$cm^2$ (n=5); (●) 0.03 mg $kg^{-1}$ Pc 4, 150 mW/$cm^2$, 100 J/$cm^2$ (n=5). The effect of PDT on tumor growth delay was significant when compared to the effect of drug alone (50 mW/$cm^2$, p = 0.019; 150 mW/$cm^2$, p = 0.036; combined, p = 0.014). The effect of fluence rate on tumor growth delay between treatment groups was not found to be significant (p = 0.857). Reproduced from [82].

As described in the section 2.3.2.5, animals were removed from the study when their tumor grew to twice its pre-PDT volume. All mice, with the exception of drug-free controls, received the same intratumor injection of 35 µL of 0.021 mg/mL Pc 4 in a 5% ethanol, 5% Cremophor, 90% saline vehicle, corresponding to a whole-body dose of 0.03 mg/kg. As can be seen, no tumors were cured as a result of Pc 4-PDT with this drug concentration, although there was significant tumor growth delay compared to the control cases. Using a paired t-test, the effect of PDT treatment was shown to be statistically significant compared to animals that received Pc 4 without irradiation (50 mW/$cm^2$, p = 0.019; 150 mW/$cm^2$, p = 0.036; combined, p = 0.014). Pc 4 administration alone had a

modest effect on tumor growth compared to drug-free controls ($p = 0.063$). Irradiance (50 vs. 150 mW/cm$^2$) had no significant effect on tumor growth delay ($p = 0.857$).

Pc 4 photobleaching curves were fit using Equation 2.4. In order to examine the relation between photobleaching and tumor growth delay, the reciprocal of the fitted *k* value from Equation 2.4 was plotted against tumor doubling time for each animal. The results of this are shown in Figure 2.14.

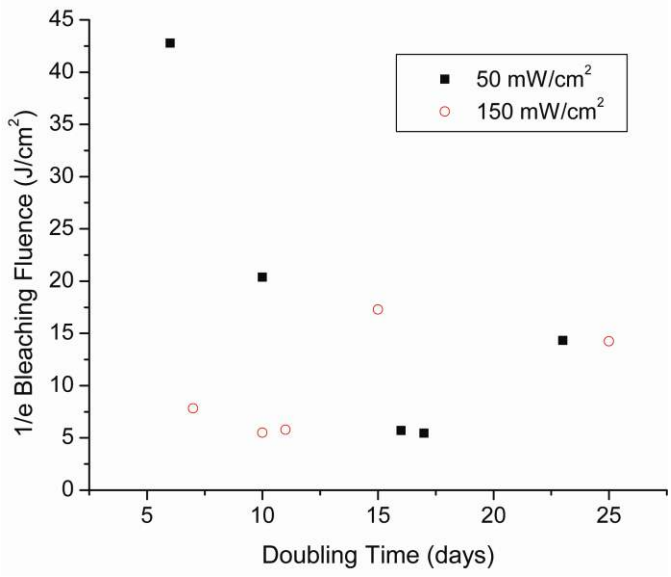


**Figure 2.14** Relationship between tumor doubling time and the fluence at which Pc 4 fluorescence photobleaches to 1/e of its pre-PDT value for irradiation at fluence rates of (■) 50 mW/cm$^2$ and (○) 150 mW/cm$^2$. Both treatment groups received 100 J/cm$^2$ of irradiation. For the treatment groups taken individually, no significant correlation was found between doubling and bleaching (50 mW/cm$^2$, p=0.188; 150 mW/cm$^2$, p=0.308). For the data taken as a whole, there was also no significant correlation found between doubling and bleaching (p=0.977). Reproduced from [82].

The relationship between doubling time and the fluence at which Pc 4 photobleaches to 1/e of its initial value was examined using Spearman's rank correlation coefficient. Probability values were calculated using Equation 2.5, and these were then converted to p values by treating the calculated values as coming from a Student's t-distribution with n-

2 degrees of freedom. When all PDT-treated mice were combined into one data set, no correlation was found between tumor volume doubling time and the 1/e bleaching fluence, assuming 8 degrees of freedom for the underlying Student's t-distribution ($p = 0.977$). When the mice were grouped by treatment irradiance, interesting but relatively weak associations were identified. The Spearman coefficients were $r = -0.7$ for the 50 mW/cm$^2$ treatment group and $r = 0.6$ for the 150 mW/cm$^2$ treatment group. The negative value of the Spearman coefficient for the 50 mW/cm$^2$ group indicates that there is a decreasing monotonic trend between tumor doubling and the 1/e bleaching fluence, while the positive value for the 150 mW/cm$^2$ group indicates an increasing monotonic trend. These trends were not statistically significant at a $p<0.05$ level, but exhibited p-values of 0.188 and 0.308 for the 50 and 150 mW/cm$^2$ treatment groups, respectively.

Reflectance spectra were also examined for correlation with tumor doubling times. The method followed was the same as that used in the photobleaching analysis, but the metric used was the total measured reflectance at 667 nm before irradiation. This wavelength was chosen because it corresponds to the peak absorption for Pc 4. The results of this analysis are shown in Figure 2.15.

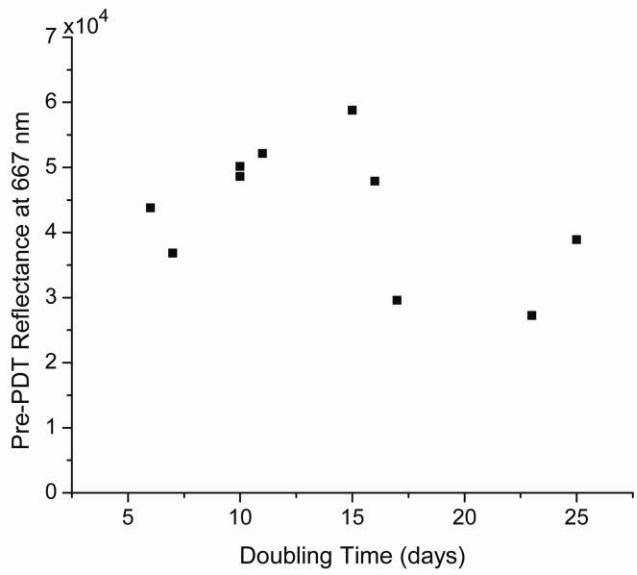


**Figure 2.15** Relationship between tumor doubling time and pre-PDT reflectance at 667 nm for all treated animals. Treatment groups were combined because the reflectance measurements being examined were made prior to irradiation. No significant correlation was found between doubling and pre-PDT reflectance at 667 nm (p=0.354). Reproduced from [82].

Since the metric being used was reflectance prior to irradiation, the data from both treatment groups were combined. The Spearman coefficient was calculated to be $r$ = -0.3283. Again using the test statistic given in Equation (2) and assuming a Student's t-distribution with 8 degrees of freedom, no significant correlation was shown between tumor doubling time and measured reflectance at 667 nm prior to irradiation (p = 0.354).

### 2.3.4 Discussion

Our experiments have shown that Pc 4 bleaches to a significant extent in response to irradiation with a fluence of 100 J/cm$^2$. For both 50 and 150 mW/cm$^2$ fluence rates, approximately 80-90% of Pc 4 photobleached during irradiation. Previous studies done in clinical trials of Pc 4-PDT for cutaneous T-cell lymphoma by our research group showed only 30% bleaching at 100 J/cm$^2$, with a fluence of 200 J/cm$^2$ increasing bleaching to approximately 50%[81]. This study was done at a different photosensitizer concentration than the current study, and Pc 4 was applied topically rather than by IT injection. We therefore conclude that the increased degree of Pc 4 photobleaching observed in the current study is a function of the photosensitizer concentration and the intralesion distribution. Compared to other clinically relevant photosensitizers, particularly PpIX and Photofrin, however, Pc 4 is relatively photostable. For example, Finlay *et al* demonstrated approximately 80% bleaching of initial Photofrin fluorescence *in vivo* in rat skin in response to only 9 J/cm$^2$ of irradiation at 514 nm[85], and for ALA-PpIX in the same system, a similar 80% bleaching fluence was reported[54]. Boere *et al* showed approximately 70% bleaching of PpIX for those animals that responded to PDT with a fluence of 50 J/cm$^2$ and approximately 40% bleaching for those that did not[21].

Under the conditions of our experiments, Pc 4 bleached more rapidly with respect to fluence at an irradiance of 150 vs. 50 mW/cm$^2$. To the best of our knowledge, this is the first such observation with any PDT photosensitizer. Lower irradiances have generally been associated with more efficient photobleaching of PpIX[54, 55, 86, 87], which has been hypothesized to result from a reduced consumption of molecular oxygen.

The bleaching of Photofrin *in vivo* exhibited no irradiance dependence[85]. Thus, with the results of this study, all possible irradiance dependencies have been observed experimentally, once again underscoring the complexity of fluorescence-based PDT dosimetry and the need to evaluate each photosensitizer separately.

In our experiments, no improvement in tumor outcome was shown for the 150 $mW/cm^2$ treatment group, even though bleaching was more efficient at this irradiance. When the tumor responses from both protocols were pooled, neither did we find any significant correlation between Pc 4 bleaching and time to tumor doubling. We conclude that monitoring of Pc 4 photobleaching is unlikely to be a useful predictor of individual tumor response to Pc 4-PDT *in vivo*. When the 50 and 150 $mW/cm^2$ treatment groups were analyzed separately, weak but intriguing associations were suggested. At the lower irradiance, there was a trend toward improved tumor response with increased photobleaching. On the other hand, tumor growth delays in response to irradiation at 150 $mW/cm^2$ tended to be increased with decreased loss of Pc 4 fluorescence. One may speculate that these trends, although not statistically significant, suggest interesting differences in photochemistry *in vivo* under these different treatment conditions.

We found no correlation between the total reflectance at 667 nm measured immediately before irradiation and tumor doubling time. This is in apparent disagreement with results reported by Bai *et al* [24], who demonstrated a significant relationship ($p < 0.001$) between pre-irradiation Pc 4 concentration and tumor growth delay using a calibrated measurement to convert the area under a measured absorbance curve to Pc 4 concentration. A number of differences exist between the current study and

that reported by Bai *et al*, which may account for this disagreement. Most importantly, Bai *et al* administered Pc 4 via tail-vein injection, whereas we used an intratumor injection, almost certainly resulting in different Pc 4 concentrations and intratumor distributions. We note that the tumors studied by Bai *et al* were also larger than those used in the current study, with a mean tumor volume of 315.3 $mm^3$ versus 115.3 $mm^3$. We did not achieve any cures in either treatment group. In contrast, a previous study by our group showed a >70% cure rate for Pc 4-PDT using IT injection of a 10-fold higher (0.3 mg/kg) sensitizer dose[71]. In that previous study, we noted that Pc 4 fluorescence at the treated site recovered completely 24 hours after irradiation, suggesting to us that aggregated Pc 4 was monomerizing after the bleaching of a fraction of the initial concentration. It therefore seemed reasonable to evaluate a lower injected drug concentration. From Figure 2.10, it can be seen that there is no recovery of Pc 4 fluorescence after irradiation in the current study, indicating that aggregation is not taking place and that the drug is being nearly completely consumed. However, the tumor responses indicate that the 10-fold reduction was too much and that an intermediate IT concentration is likely optimal.

There are a number of possible interpretations for why Pc 4 photobleaching does not predict tumor growth delay in individual animals. More generally, given these data it may be useful to consider the nature of the problem we are asking spectroscopy to address. We offer the following simple picture. We begin by asking, for a typical response to PDT, what is the volume of tumor spared by treatment relative to that

sampled by spectroscopy? Assuming that tumor cells surviving PDT replicate at their pre-treatment rate, we may express the number of these cells as,

$$N(t) = N(t_0)e^{k_G(t-t_0)} \tag{2.6}$$

where $N$ is the tumor volume in $mm^3$, $t$ is time in days, $t_0$ is day of treatment, and $k_G$ is an empirically-determined growth rate constant. In our case, $k_G$ is 0.1663 $days^{-1}$ based on control tumor growth data. Using this growth rate, the average pre-irradiation tumor volume of 115 $mm^3$, and an average tumor doubling time of 14 days after PDT, we can estimate that approximately 80% of the tumor volume was destroyed by PDT. For the longest observed doubling time of 25 days, this figure increases to 97% of tumor volume destroyed. In these cases, in order for spectroscopy to predict outcome it would be necessary for it to discern differences in fluorescence signals originating from small (20 – 3% in these examples) volumes of tissue. For longer doubling times corresponding to more effective treatments, the fraction of the tumor that spectroscopy would need to report grows even smaller. Because these small populations of surviving cells are likely distributed throughout the tumor volume as microscopic foci, the prediction of tumor response based on volume-averaged fluorescence spectroscopy measurements appears daunting.

# Chapter 3

# Monte Carlo Simulation of Light Propagation in Turbid Media using GPUs

## 3.1 Introduction

As discussed in chapter 2, the treatment light field generated during PDT can have a large effect on the outcome of treatment. Given knowledge of the tissue's optical properties, this light field can be represented by analytical approximations to the radiative transport equation, as will be discussed in chapter 4, or by the use of Monte Carlo (MC) simulations. Analytical approximations require certain assumptions about the behavior of light, and therefore are constrained to specific sets of optical properties. The solution is also highly sensitive to geometry, especially at the boundaries of the tissue. It is therefore attractive to consider MC simulations.

MC simulation of light propagation treats light as a series of photons or photon packets that undergo absorption, scattering, and transmission and reflection at boundaries. Each of these phenomena is handled statistically, based on the optical properties of the sample. If enough photons are run, MC simulation can provide very accurate results. This accuracy has been demonstrated many times[27, 88], and MC is treated as the "gold standard" for simulation of light propagation in tissue. MC simulation has been used extensively in the modeling of light propagation in tissue. There are a number of publically available codes, including MCML by Wang *et al*[28].

One disadvantage of MC simulation as compared to analytical approximations is the long run-times of the simulations. For typical optical properties and sufficient number of photons, a MC simulation can sometimes take hours or days[89]. This places significant limitations on the use of MC in clinical applications, where results are desired in a matter of minutes or seconds. In order to combat this computational overhead, some research groups have begun to utilize the graphics processing unit (GPU) to speed up simulation. GPUs were originally designed for use in computer graphics, and are therefore very efficient at performing large calculations in parallel. Since each of the individual photon runs within a MC simulation is independent of the others, MC is an ideal candidate for GPU-acceleration. Alerstam *et al* demonstrated a GPU-based version of the MCML code, with a speed-up of 1000x compared to simulations run on a single CPU core[29]. For complex, 3D samples, Fang and Boas demonstrated a speed-up of 75-300x using a voxel-based representation[30], while Ren *et al* showed up to a 10x speed-up using a mesh-based representation[31].

In this chapter, we present a GPU-based Monte Carlo framework based on a voxel representation of a 3D tissue sample. Section 3.2 covers the principles of Monte Carlo simulation and outlines the specific steps that were taken to run the code on GPU. In section 3.3, the creation of a number of source and detector MC models that correspond to experimental conditions is covered. These models are more rigorous than previous ones, and attempt to more closely replicate experimental conditions.

## 3.2 GPU-accelerated Monte Carlo model of light propagation

### 3.2.1 Principles of Monte Carlo simulation

Wang *et al* provides an excellent overview of the basic principles of MC simulation[28], which will be outlined here. As previously stated, MC simulation reduces light propagation in tissue to absorption, scattering, and interactions with boundaries. A representation of the MC framework is shown in Figure 3.1.

MC codes are typically divided into analog and variance reduction schemes. In analog MC, light propagation is represented with discrete photons, with absorption events eliminating the photon. These can be computationally expensive, with each photon path requiring launch calculations and tracking. This burden is reduced with variance reduction MC codes, which represent light as photon packets consisting of a collection of individual photons propagating over the same path. This reduces computational overhead, and improves signal-to-noise by propagating multiple photons over the same path. In variance reduction MC, absorption events therefore reduce the weight of the photon packet, rather than eliminating the photon. This weight is set to one at launch, and is reduced at each absorption event following

$$W_{out} = W_{in} \frac{\mu_s}{\mu_a + \mu_s}, \tag{3.1}$$

where $W_{out}$ is the photon packet weight after the absorption event, $W_{in}$ is the photon packet weight before absorption, $\mu_a$ is the local absorption coefficient, and $\mu_s$ is the local scattering coefficient.

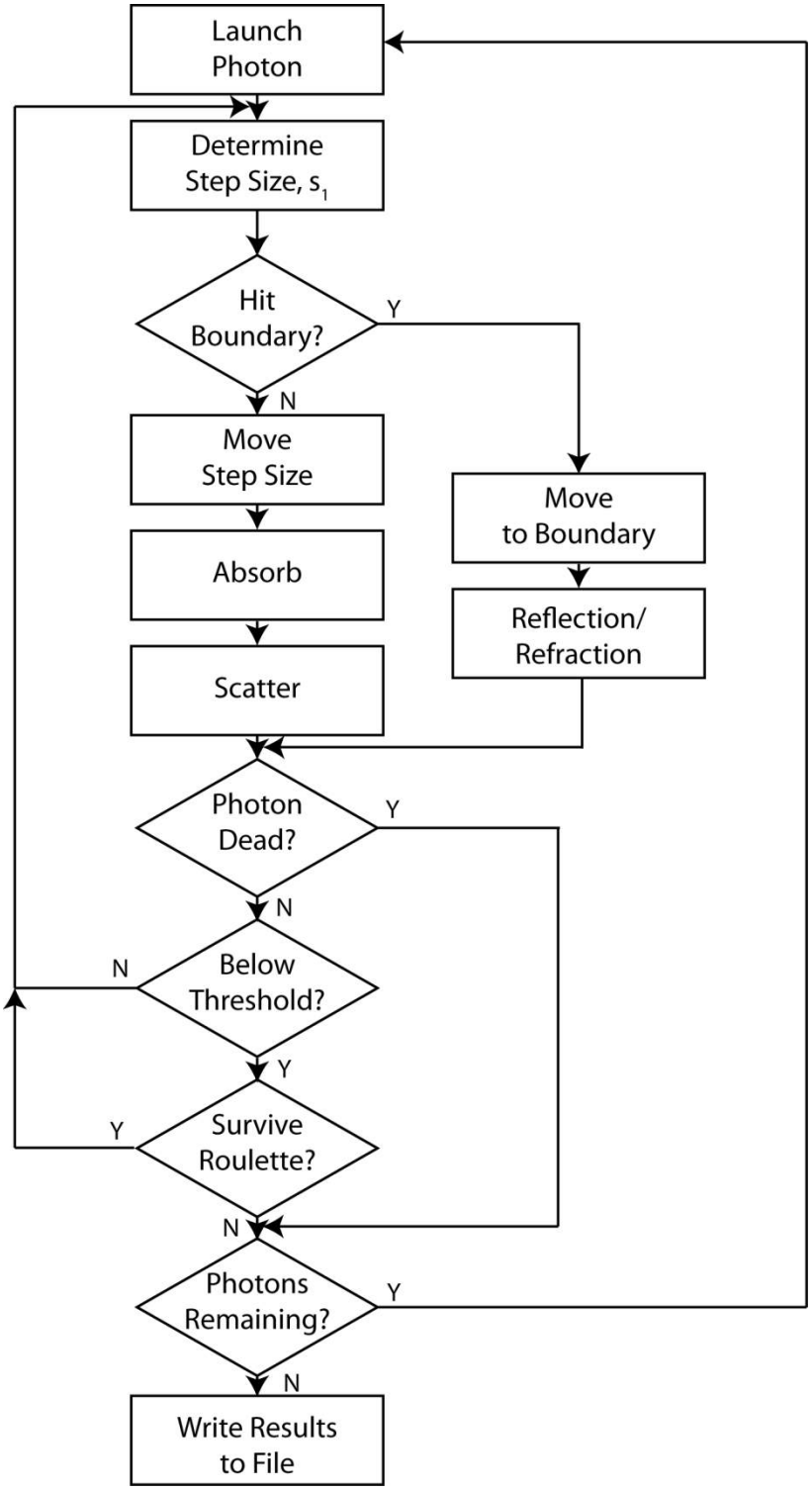


**Figure 3.1** Block diagram illustrating the general model for variance-reduction MC simulation.

The photon packet weight deposited in tissue can be converted to fluence by dividing by the local absorption coefficient. Variance reduction MC is used exclusively in all parts of this thesis.

Each photon packet begins by being launched from an appropriate source model. A number of these source models will be discussed in section 3.3. At each step of the simulation, the photon packet moves and undergoes absorption and scattering. These are referred to as Hop, Drop, and Spin, respectively, following the notation of Wang *et al*[28]. At the end of each simulation step, the current photon weight is compared to some pre-determined threshold value. If the weight is above the threshold, propagation continues to the next simulation step. If the weight is below, the photon packet is subjected to Russian roulette in order to determine its survival. In this technique, the photon packet is given a one in ten chance of survival. If the photon survives, its weight is increased ten-fold and propagation continues. Otherwise, the photon is killed and its weight is reduced to zero. This is done to prevent the propagation of a large number of photon packets with very low weight, while maintaining energy conservation[90]. After a photon is killed, another is launched until the specified number of photon packets has been launched.

Before undergoing absorption, the photon first travels a distance that is determined by the local optical properties and a random number. This pathlength is referred to as the step size, and is quantified by using the definition of the total attenuation coefficient, $\mu_t$,

$$\mu_t = \frac{-d(\ln[P\{s \geq s'\}])}{ds'} \tag{3.2}$$

where *P* represents probability and *s* represents step size[28]. If this expression is integrated over the range (0, $s_1$), we arrive at an exponential distribution for step size

$$P\{s < s_1\} = 1 - \exp(-\mu_t s_1), \tag{3.3}$$

where $s_1$ is a step size of a given length. This probability distribution can be sampled using the expression

$$s_1 = \frac{-\ln(\xi)}{\mu_t} \tag{3.4}$$

where $\xi$ is a uniformly distributed random number in the range (0,1], with square brackets indicating end inclusion on the specified range. After determination of $s_1$, the photon packet travels this distance in the direction defined by the direction cosines $u_x$, $u_y$, and $u_z$. These direction cosines are defined as the cosine of the angle between the photon trajectory and the respective Cartesian axis in the simulation space.

If the photon packet would encounter a tissue boundary during its travel, consideration of refraction and reflection is required. This is accomplished by computation of the Fresnel reflection coefficient, *R*, for the given index mismatch and angle of incidence, assuming random polarization. A uniformly distributed random number on the range [0,1] is then generated and compared to this intensity-based coefficient. If the random number is less than or equal to *R* or the angle of incidence is greater than the critical angle, the photon packet is reflected. If the random number is greater, the photon packet is refracted using Snell's law. In our MC model, we do not split photon packets at boundary interactions.

The final interaction represented in MC simulation is elastic scattering. This consists of changes in the photon packet's direction of propagation and is again represented using a combination of tissue optical properties and random number generation. The photon scattering consists of two angular components, the deflection angle, θ, and the azimuthal angle, ψ. The value of θ can be determined from a scattering phase function. In this case, we use the Henyey-Greenstein phase function[91]

$$P\{\cos\theta\} = \frac{1-g^2}{2(1+g^2-2g\cos\theta)^{3/2}}, \tag{3.5}$$

where *P* again represents probability and *g* is the average cosine of the scattering angle. This function can be sampled using the expression

$$\cos\theta = \frac{1}{2g}\left[1+g^2-\left(\frac{1-g^2}{1-g+2g\xi}\right)^2\right], \tag{3.6}$$

where ξ is again a random number on the range [0,1]. The azimuthal angle is assumed to be uniform in the range [0,2π], so its value can be sampled by $\psi = 2\pi\xi$. These expressions are then combined to determine the new direction cosines.

The code of Wang *et al* represents tissue as infinitely wide slabs of finite depth[28]. Since we are primarily interested in interstitial applications of MC in complex media, we must represent a three-dimensional tissue volume. This allows for locally varying optical properties and spatially-localized mapping of fluence deposition. Three-dimensional volumes are typically represented with either voxels or meshes. In mesh-based schemes, the sample volume is sub-divided into triangular regions that are defined by the sample geometry. This allows for finer representation of smooth boundaries, but

carries a significant computational overhead for mesh determination and collision detection. We have therefore chosen to represent 3D volumes by the use of uniform cuboid voxels, with each voxel storing the absorbed weight at that location and having independently-definable optical properties. This method has lower up-front computational cost, and allows for simpler representation of boundaries[30]. This simplification can result in slight errors close to boundaries[92], so some caution is warranted in regions that are very close to boundaries.

### 3.2.2 GPU-based implementation

As mentioned previously, MC simulation is an ideal candidate for translation to GPU. This transition is eased by the availability of tools for the creation of GPU-based code. We used NVIDIA's Compute Unified Device Architecture (CUDA) extensions to C. However, there are some concerns related to the architecture of the GPU. In order to illustrate this, we refer to the diagram shown in Figure 3.2**.**

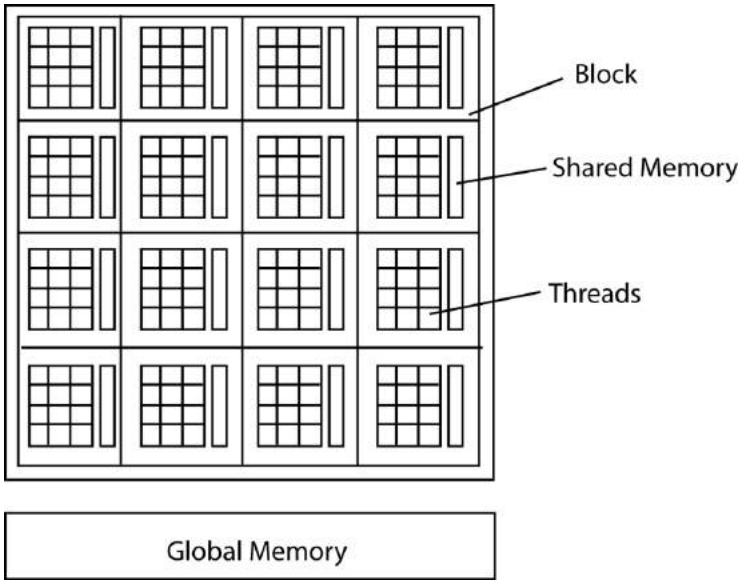


**Figure 3.2** Diagram of GPU architecture illustrating organization of individual threads into blocks. Each block contains shared memory that can only be accessed by threads in that block. Global memory is accessible by all blocks.

The GPU consists of global memory and an array of thread blocks. Each block consists of a number of individual threads, each of which is capable of running a MC simulation. The threads within a block are not completely independent, as they are collected into groups of 32 threads, called warps, at run-time. Each thread has its own local memory, and each block has shared memory that can be accessed by the threads in that block. Reads and writes within the local and shared memories are very fast, but the size of these memories is small. All blocks have access to the large global memory, but transfers between global memory and individual blocks are comparatively slow. On the GPU we use (GeForce GTX 570, NVIDIA Corporation, Santa Clara, California), the size of the global memory is 1280 MB, while the shared memory is only 48 kB. However, the latency and bandwidth are much better for operations involving the shared memory. The global memory must be populated from the system (CPU) memory, which is much

slower than the global to block transfer. Therefore, the usage of memory should be optimized to favor shared memory over global memory, while minimizing transfers between system and global memory.

The GPU architecture, while allowing for massive parallelization of the code, introduces some constraints on the program. The first of these involves branching within the code. As mentioned previously, threads are organized into warps at run-time. Each warp executes common instructions on each of the threads. If the threads diverge (i.e. threads encounter a conditional statement), the warp is paused and threads within that warp are run serially[93]. This can lead to significant slow-down if there are multiple levels of divergence. This can be problematic for MC code, as MC simulations include a large amount of branching to account for the different conditions encountered in independent photon runs. In order to alleviate this issue, we have tried to minimize branching within the code. This was done by forcing certain calculations out of branches and into the main body of the code. For example, in the case of checking for 3D boundary collisions, traditional CPU code uses multiple nested conditional statements to look for the proper collision and distance to interface. With the GPU code, all collisions are computed for each thread, with only a single branch determining which path is taken by each photon.

Another concern involves writing the results of simulations to memory. In order to output results for the entire simulation volume, each thread needs to be able to write deposited fluence to the total absorption array, which is stored in global memory. Since each thread is operating in parallel, there is no guarantee that memory access will occur

in the order in which it is desired. This becomes problematic when multiple threads wish to access the same element of the array at the same time. To ensure that only one thread writes to a specific piece of global memory at a time, atomic operations must be used. These atomic operations guarantee dedicated access to global memory by pausing other threads attempting to access the same location. This results in serial writes being guaranteed, at a significant time penalty. Therefore, writing to global memory is minimized in the code.

Use of highly parallelized GPU codes also requires specialized random number generators for MC simulation. In a traditional CPU-based quasi-random number generator, the random number generated depends upon a seed created from the current time. For the case of highly parallelized code, multiple runs could request a random number at the same time, resulting in them receiving the same number and rendering the runs identical. To avoid this, parallel number generators that do not depend upon a clock-based seed are required. Here, we use the Multiply With Carry method described by Alerstam *et al*[29]. Briefly, this method uses a large list of safeprimes (numbers $q$, where both $q$ and $(q-1)/2$ are prime) as multipliers in a modulo-division to create a large ($2^{64}$) list of quasi-random numbers for each thread[94]. This list is generated at run-time for each simulation.

## 3.3 Source and probe models

Most freely available MC codes utilize simple, off-surface source models. In order to examine problems related to interstitial PDT (iPDT), we have created a number of source and detector models for optical devices embedded in the tissue. Whenever possible, these models have been informed by the known geometry and materials of the device.

### 3.3.1 Cylindrical diffusing fibers

Cylindrical diffusing fibers (diffusers) are optical fibers in which the distal portion emits light radially along some length. They are designed to provide homogeneous irradiance along the length of the diffusing section. This irradiance is also uniform in all radial directions. These diffusers are used in a number of areas in biomedicine, such as interstitial photocoagulation and interstitial hyperthermia[95]. They are also used prominently in iPDT. However, explicit MC models of cylindrical diffusing fibers have not been created. Previous efforts have treated cylindrical diffusers as linear arrays of ideal point sources[88, 96]. While this makes computation more straightforward than in a more complex model, this description may not be fully accurate. In these linear array models, once photon packets are launched from the linear array of point sources, the effect of the diffuser on the propagation of light is neglected. The sources are treated only as launch points for photon packets, and the effect of the index mismatch between the diffuser and the surrounding tissue is ignored. Photon packets that would re-enter the diffuser are treated as still being in the surrounding tissue, which eliminates the possibility of using linear arrays of point sources to model detectors for spectroscopy. In order to model the detection of photon packets, these packets must be followed through

the diffuser to the detection point. Therefore, a more complete MC model of cylindrical diffusing fibers is desired.

Our diffuser model, based on a patent by Edward Sinofsky[97], is constructed as shown schematically in Figure 3.3.

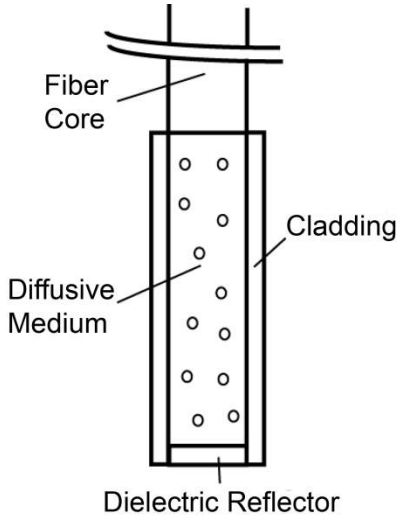


**Figure 3.3** Schematic of cylindrical diffusing fiber, showing the four regions that are modeled. Photon packets are launched from the fiber core, with the diffusive medium being treated as having negligible absorption and the cladding being treated as having negligible absorption and scattering. The dielectric reflector is treated as a perfect reflector. Reproduced from [98].

It consists of four components: a fiber core, a diffusive medium, a dielectric reflector, and cladding. The fiber core is the 400 μm diameter core of a 0.22 numerical aperture (NA) jacketed optical fiber. The diffusive medium consists of titanium dioxide ($TiO_2$) particles, with an average radius of 14.7 nm and an index of refraction of 2.488, embedded in a clear epoxy (Mastersil 151, Masterbond Inc., Hackensack, NJ) that has a density of 1 g/cm$^3$ and a refractive index of 1.43 [97]. The number density of $TiO_2$ particles providing a uniform axial fluence distribution is determined through simulation, as described below. The reflector is a dielectric stack, which is designed to provide

maximum reflection with minimal heating. The cladding is a 0.25 mm layer of Teflon® FEP (DuPont, Wilmington, DE) with an index of 1.344 that surrounds the diffusive medium and dielectric reflector.

Each of these four regions is modeled differently. The fiber core is treated as the launch point for photon packets, with packets being launched within the NA of the fiber. The face of the fiber core also serves as the detection point for fluorescence photon packets. Any fluorescence packet striking the fiber core within the NA of the fiber is recorded as being detected.

Since the diffusive medium consists only of $TiO_2$ spheres and a clear epoxy, it is treated as having negligible absorption. Photon propagation within the diffuser is therefore governed only by scattering. The bulk scattering coefficient ($\mu_s$) within the diffusive medium depends on the concentration and size of the $TiO_2$ particles and is assumed to be uniform. This scattering coefficient must be optimized to achieve axially homogeneous irradiance along the diffuser length. In order to determine the optimal scattering coefficient for each diffuser length, $\mu_s$ was varied over a series of simulations and the homogeneity of the axial fluence profile was examined. The optimal value of $\mu_s$ was found by minimizing the deviation from an axially homogeneous fluence profile along the length of the diffuser.

The cladding layer consists of clear plastic and does not contain any scatterers. It is therefore treated as having negligible absorption and scattering. Therefore, this layer only has the effect of inducing Fresnel reflection and transmission. The dielectric reflector is treated as a perfect reflector.

In simulations, diffusers are specified by their three dimensional coordinates, length and radius of the diffusive region, and the outside radius of the cladding. Also specified are the NA of the fiber core, the scattering coefficient of the diffusive region, and the refractive indices of the diffusive region and cladding. The total fluence to be delivered by the diffuser is specified in units of J/cm. An arbitrary number of these diffusers can be included in the simulation, with each diffuser able to launch photons and detect fluorescence. The diffusers can be oriented arbitrarily, with no requirement that they remain parallel.

For photon propagation, each photon packet is launched at a random location on the specified fiber core at a random angle that is within the NA of the fiber. In the diffusive region, the photon packet propagates by normal MC methods. This includes reflections off of the dielectric reflector and cladding. Since the scatterers present in the diffusive region are much smaller than a wavelength, the scattering can be treated as isotropic ($g$=0), assuming random orientations of the scatterers and random polarization of the light. Upon transmission into the cladding, propagation continues without scattering or absorption. If the photon is transmitted into the surrounding tissue, propagation is continued as normal with the specified scattering and absorption in the tissue region.

Boundary interaction with the diffuser is done by monitoring the photon position with respect to the coordinates of the diffuser axis. If the current step size of the photon would take it either into or out of a diffuser, the coordinate system is temporarily converted to cylindrical coordinates. A random number is then compared to the Fresnel

reflection coefficient for the boundary. If this random number is less than the reflection coefficient, the photon is reflected and propagation continues. Otherwise, the photon undergoes refraction and then continues propagation. If a photon makes it to the fiber core within the diffuser and is transmitted, the photon weight is recorded as detected.

A study of the detection of fluorescence by cylindrical diffusing fibers using this MC model[98] is described in chapter 5. Details are provided there on the accuracy of the model.

### 3.3.2 Encapsulated optical probe for interstitial diffuse reflectance spectroscopy

The fluence distribution generated by a cylindrical diffusing fiber is strongly dependent on the optical properties of the tissue. We would therefore like a method to determine interstitial optical properties for iPDT treatment planning. A more involved discussion of optical properties and the recovery of them from diffuse reflectance measurements is contained in chapter 4. Here we are primarily concerned with the MC model of the probe used to acquire these measurements.

The optical probe in question consists of six beveled side-firing fibers arranged helically around a central diffuser. All fibers are embedded in an encapsulant and surrounded by a clear cladding. A side-view of this probe is shown in Figure 3.4.

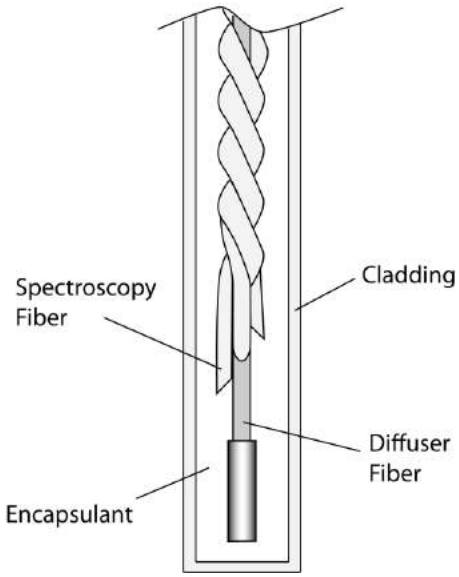


**Figure 3.4** Schematic of the custom optical probe used for diffuse reflectance measurements, showing the four regions that are modeled. Photons are launched from, and detected by, the spectroscopy fibers. The diffuser fiber, encapsulant, and cladding are treated as having negligible absorption and scattering, with refraction and reflection at interfaces being the only effects.

The probe is modeled with four different materials: the spectroscopy fibers, the encapsulant, the central diffuser, and the cladding. The spectroscopy fibers are 0.22 NA, 200 μm diameter optical fibers with a 38º bevel at the distal end and an index of refraction of 1.46. Fibers have a polyimide coating, and are silver coated over the last 3.5 mm. The emitting/detecting surface of each fiber is free of both the polyimide and silver coatings. The central diffuser is also a 200 μm diameter optical fiber with an index of refraction of 1.46. The encapsulant is a clear epoxy with negligible scattering and an index of refraction of 1.504, while the cladding has an index of 1.508. The outside diameter of the entire probe is 1.1 mm.

In the simulation space, the optical probe is defined by the Cartesian coordinates of the center of the distal end of the probe. The proximal end of the probe is assumed to extend out of the simulation space. Each of the spectroscopy fibers' position and orientation is pre-defined, based on specifications provided by the manufacturer of the probe (Pioneer Optics Company, Bloomfield, CT). These are provided in Table 3.1.

| Fiber Number | Vertical Position Relative to Diffuser (mm) | Pointing angle (degrees) |
|---|---|---|
| 1 | 1.9 | 5 |
| 2 | 3.7 | 85 |
| 3 | 5.5 | 135 |
| 4 | 7.6 | 195 |
| 5 | 9.6 | 270 |
| 6 | 10.8 | 331 |

**Table 3.1** Relative positions and angles of spectroscopy fibers in optical probe.

During launching of photons from the probe, a random position is selected within the chosen fiber radius at a height equal to the top of the bevel. A photon is then launched within the NA of the fiber, and allowed to reflect off of the beveled surface. After reflection, the photon encounters the interface between the spectroscopy fiber and the encapsulant, and is either reflected or transmitted. If the photon is transmitted, propagation continues in the encapsulant. This region is treated as being free of absorption and scattering, so photons travel in straight-line paths until they encounter the

cladding, triggering another reflection check. If the photon is transmitted, it enters the cladding and continues propagation. Otherwise, the photon continues propagating within the probe, where it can encounter interfaces with the central diffuser fiber and the individual spectroscopy fibers. The index mismatches at these interfaces can cause refraction and reflection, with the last 3.5 mm of each spectroscopy fiber being treated as a perfect reflector due to the silver coating. In the cladding layer, absorption and scattering are also treated as negligible, with boundary interactions being the only factors accounted for.

If a photon re-enters the probe during propagation, it can be scored as detected. This is done by tracking propagation as described above, noting when the photon strikes spectroscopy fibers. If the photon hits the portion of the fiber that is free of coatings within the NA of the fiber and is transmitted, its weight is recorded as detected. This un-coated portion of each fiber is defined as the distal region of the spectroscopy fiber, going from the end of the fiber to the top of the bevel. The detected weight is stored on a per-fiber basis, and written to file after the completion of the simulation. In section 3.2, the time penalty required for atomic operations was discussed. Since we are only interested in the detected fluence, the deposition of fluence within the tissue is not recorded during these simulations. This eliminates a significant number of atomic operations, improving the speed of the simulation in this case.

### 3.3.3 Isotropic source and detector

For certain applications, we do not need access to multiple source and detector positions. This is particularly true in fluorescence spectroscopy, where a detected signal can be filtered to separate excitation light from emitted fluorescence. This allows for the use of a single, small optical probe for spectroscopy, which is attractive in cases where we are not delivering illumination for PDT. This is accomplished by the use of an isotropic source/detector probe, as shown in Figure 3.5.

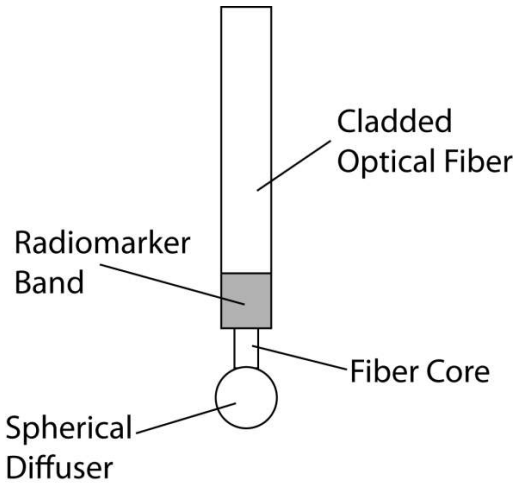


**Figure 3.5** Isotropic source and detector probe. The spherical diffuser has an outside diameter of 850 μm, and is isotropic to within 10%. The optical fiber has a 400 μm diameter core, and the radiomarker band is present for visualization with CT during insertion into a patient.

This probe consists of a 400 μm diameter core optical fiber with 0.37 NA attached to a 0.85 mm diameter spherical diffuser at the distal end. The spherical diffuser is similar in principle to the linear diffuser described previously, but is designed to detect uniformly over its surface rather than produce a homogeneous irradiance profile. This is again accomplished by the use of a scattering medium of the appropriate concentration. The probe detection profile is isotropic to within 10%. The probe also has a radiomarker band

that is visible by CT imaging. This is especially important because isotropic probes are typically used deep within the body, where they cannot be positioned visually. The probe model was designed to correspond to that used in experiments outlined in chapter 6.

Due to the low angular dependence of the isotropic detector, it is modeled more simply than the previous probes. Photons are launched from the surface of the spherical diffuser within an angular range limited by the critical angle between the probe and the surrounding tissue. The position and angle are chosen using uniformly distributed random numbers that sample the surface of the sphere and the allowed transmission angles. The weight of the photon packet is adjusted for Fresnel loss at the interface. During propagation of photons in the tissue, interaction with the un-jacketed optical fiber is possible. In this case, the optical fiber is treated as having negligible absorption and scattering, with the only effects being refraction and reflection due to index mismatches. If a photon packet strikes the surface of the spherical diffuser and is transmitted, it is scored as detected.

In the scheme eventually implemented in chapter 6, this Monte Carlo model was not utilized. This was done to reduce computation time during non-linear optimization. However, there is no reason to believe that a Monte Carlo based method could not utilized, as was previously done by Finlay *et al*[99]. In fact, such a model might be required in certain complex geometries.

# Chapter 4

# Recovery of Optical Properties from Turbid Media for PDT Treatment Planning

## 4.1 Introduction

For PDT, the main optical quantities of interest are fluence and fluence rate. Fluence corresponds to the total energy delivered to the treatment volume, while fluence rate corresponds to the amount of energy delivered per unit time. Therefore, we are generally interested in the transport of energy through a medium rather than the rigorous propagation of electromagnetic waves. This energy flow is commonly treated as depending on two factors, absorption and scattering. These factors are quantified by the absorption and scattering coefficients, $\mu_a$ and $\mu_s$, respectively. These coefficients represent the inverse of the mean free path (MFP), or the average distance over which a photon will travel before encountering an absorption or scattering event.

At wavelengths relevant to PDT, absorption in biological tissues is largely due to hemoglobin and water. There can also be contributions from lipids, melanin, and other pigments such as bilirubin[32]. In the case of PDT, the photosensitizer is also an absorber and can have absorption comparable to hemoglobin. Hemoglobin is typically present at a concentration of approximately 150 g/L in blood[100], with a hematocrit of approximately 40% and a blood volume fraction on the order of 4%[101]. Hematocrit refers to the volume fraction of red blood cells in blood, while the blood volume fraction represents the volume percentage of blood in bulk tissue. This results in tissue being

comprised of roughly 1.6% erythrocytes by volume. The absorption of hemoglobin is also dependent on the binding of oxygen, which allows for spectroscopy to determine quantities such as the oxygen saturation of the blood.

Scattering in biological tissue is due to the presence of a large number of refractive index mismatches, and accounts for much of the light-tissue interaction at wavelengths in the red portion of the visible spectrum and NIR. In this wavelength range, the value of the scattering coefficient is much larger than the absorption coefficient, which is what allows for the diffusion approximation that will be discussed later. Whereas $\mu_a$ is on the order of 0.1-10 $cm^{-1}$ for this wavelength range, the scattering coefficient is on the order of 100-1000 $cm^{-1}$[17], with both quantities being wavelength dependent. The relative contributions of scattering and absorption are quantified by the albedo, which is defined as $a = \mu_s/(\mu_a + \mu_s)$. For most biological tissues at wavelengths relevant to PDT, the value of albedo is larger than 0.99. This large albedo can make it difficult to separate the effects of absorption and scattering in the recovery of optical properties. Scattering in biological tissue is further defined by the scattering anisotropy, $g$. This value is the average value of the cosine between the photon path before scattering and the photon path after scattering, and is typically in the range of 0.8 to 0.95 in tissue[17]. The scattering anisotropy is incorporated into the fitting of optical properties by invocation of the reduced scattering coefficient, which is defined as $\mu_s' = \mu_s(1-g)$. The reduced scattering coefficient allows a medium with scattering coefficient $\mu_s$ and scattering anisotropy $g$ to be modeled as a medium with isotropic scattering and a reduced scattering coefficient of $\mu_s'$[102].

As the exact values of $\mu_a$ and $\mu_s$ can have a large effect on the illumination pattern generated by a light source, there has been a great deal of effort to extract optical properties from measurements of tissue samples. These methods rely on the detection of light injected into a sample, resolved in either the time or spatial domain. In the time domain, resolution is achieved either through usage of a pulsed source and time-gated detection or through examination of changes in frequency content. By time-gating the detection, "time of flight" for a particular set of photons can be determined, which is related to photon pathlength. This pathlength is in turn related to the scattering of the sample. For examination in the frequency domain, the phase shift and modulation of the frequency-modulated source are used to derive the scattering behavior of the sample[17]. Both of these techniques have been extensively examined, with a number of studies published showing good recovery of optical properties from time[103-105] and frequency based methods[106-108]. Time-resolved techniques suffer from increased instrumental complexity and expense, due to the need for pulsed sources and time or phase sensitive detection.

This thesis focuses on spatially resolved approaches to optical property determination from diffuse reflectance. In this scenario, broadband light is injected into the tissue at a given point on the surface and detected at one or more positions. The exact methods for extracting optical properties from these methods are covered in subsequent sections, but all rely on some model of light propagation in tissue. There has been significant work done on this topic, with numerous studies detailing recovery of optical properties from spatially resolved measurements[39, 109, 110]. Our laboratory has also

done significant work on the recovery of optical properties from surface measurements of diffuse reflectance[37, 111, 112]. The main advantage to spatially-resolved diffuse reflectance is a reduction in instrumental complexity, which can lead to easier clinical implementation. Broadband, spatially-resolved measurements also allow for the extraction of information about a larger number of absorbers.

In this chapter, the results of two studies are provided. The first involves the extraction of optical properties from diffuse reflectance measurements of freshly excised human kidneys. This utilizes the $P_3$ approximation to the radiative transport equation, which will be covered in the next section. The second study focuses on the recovery of optical properties from reflectance measurements made with a custom interstitial optical probe comprised of six fibers arranged helically around a central diffuser. A Monte Carlo model of the probe is demonstrated, and experimental verification is performed in tissue-simulating phantoms.

## 4.2 Radiative transport theory and approximate solutions

Due to the turbid nature of biological tissue, two families of approaches to the determination of light propagation through tissue have been developed: multiple scattering theory and transport theory[36]. Multiple scattering theory starts with equations governing the electromagnetic field and introduces statistical considerations to account for multiple scattering. This results in a form that is mathematically rigorous, but lacks broad applicability. We therefore focus on radiative transport theory, which is summarized in the equation

$$\nabla \cdot (L\hat{s}) + \frac{1}{c}\frac{\partial L}{\partial t} = -\mu_t L + \mu_s \int p(\hat{s}, \hat{s}')L(\vec{r}, \hat{s}')d\omega' + \varepsilon(\vec{r}, \hat{s}), \qquad (4.1)$$

where $L$ is the radiance, $\hat{s}$ is the direction of light propagation, $c$ is the speed of light, $\mu_t$ is the total attenuation coefficient ($\mu_t \equiv \mu_a + \mu_s$), $\mu_s$ is the scattering coefficient, $p$ is the scattering phase function, and $\varepsilon$ is the source function. The radiance is a scalar function defined as the average optical power flux density per unit area per unit solid angle in direction $\hat{s}$ at a position $\vec{r}$. The first term on the right side of the equation represents radiance being absorbed or scattering out of the direction $\hat{s}$[36]. The second term on the right side represents radiance scattering into the direction $\hat{s}$ and the third represents sources of radiance.

The scattering phase function, $p(\hat{s},\hat{s}')$ is defined as the probability that a photon propagating in the direction $\hat{s}'$ will be scattered into the direction $\hat{s}$. This phase function is generally assumed to be a function only of the angle between $\hat{s}$ and $\hat{s}'$. The exact form of

this phase function is an active area of research[113], but it can be characterized by the scattering anisotropy, *g*, which is defined as

$$g = \int_{4\pi} p(\hat{s}, \hat{s}')d\Omega, \tag{4.2}$$

where dΩ is the differential solid angle. This scattering anisotropy is the mean cosine of the scattering angle, and a larger value indicates that the medium is more strongly forward scattering. For the purposes of scattering in biological tissue, the scattering phase function is often assumed to have the form,

$$p(\cos\theta) = \frac{1-g^2}{(1+g^2-2g\cos\theta)^{3/2}}, \tag{4.3}$$

where *g* is the scattering anisotropy and θ is the angle between the original direction of propagation and the direction after scattering. This is known as the Henyey-Greenstein function[91]. This phase function has been shown to be applicable for light propagation in biological tissues[114], and will be used throughout this thesis.

The radiative transport equation is not directly solvable, except for a very limited set of conditions. Therefore, approximations to this equation are often made. This is commonly done by expanding the expressions for the radiance and source as summations

$$L(\vec{r}, \hat{s}, t) = \sum_{l=0}^{N} \sum_{m=-l}^{l} \left(\frac{2l+1}{4\pi}\right)^{1/2} \varphi_{lm}(\vec{r}, t) Y_{lm}(\hat{s}) \tag{4.4}$$

$$S(\vec{r}, \hat{s}, t) = \sum_{l=0}^{N} \sum_{m=-l}^{l} \left(\frac{2l+1}{4\pi}\right)^{1/2} \sigma_{lm}(\vec{r}, t) Y_{lm}(\hat{s}), \tag{4.5}$$

where $\varphi_{lm}$ and $\sigma_{lm}$ are the moments of the radiance and the source distribution, respectively, and $Y_{lm}$ are spherical harmonics[37]. The simplest of these approximations

is the $P_1$ approximation, which is equivalent to the diffusion approximation under steady-state conditions. This approximation provides accurate modeling of radiance at distances from the source that are much larger than the photon MFP. However, the diffusion approximation requires a number of limiting assumptions. The largest of these are that the source and detector must be separated by more than 1 transport MFP ($1/\mu_t$), and the albedo must be close to 1 ($\mu_s >> \mu_a$). Further discussion of these and other limitations of the first-order approximations are discussed in detail by Fishkin *et al*[115].

Due to these limitations, this thesis focuses on the $P_3$ approximation to the radiative transport equation. As stated previously, this involves expanding expressions for the radiance and source distribution to third order. It should be noted that even ordered expansions do not significantly change the degree of anisotropy in the modeled radiance, so only odd ordered expansions are considered[37]. Following the derivation of Hull and Foster[37], we can determine the Green's function for $P_3$ radiance by first considering the case of an infinite slab source in an infinite medium. This yields a set of four differential equations that can be solved directly. By taking the limit as the slab width goes to zero, the source strength goes to infinity, and the product of source strength and slab width remains constant, while imposing symmetry and continuity constraints, we can express the radiance in the $P_3$ approximation as

$$L(\vec{r},\hat{s}) = \sum_{l=0}^{3} \Psi_l(r) P_l(\vec{r}\cdot\hat{s}) , \tag{4.6}$$

where $\Psi_l(r)$ are the moments of radiance and $P_l$ are Legendre polynomials. The moments of radiance are given by

$$\Psi_l(r) = -[B^- h_l(-\upsilon^-) Q_l(-\upsilon^- r) + B^+ h_l(-\upsilon^+) Q_l(-\upsilon^+ r)], \tag{4.7}$$

where

$$\upsilon^{\pm} = \left( \frac{\beta \pm \sqrt{\beta^2 - \Gamma}}{18} \right)^{1/2} \tag{4.8}$$

$$\beta = 27\mu_a\mu_t^{(1)} + 28\mu_a\mu_t^{(2)} + 35\mu_t^{(2)}\mu_t^{(3)} \tag{4.9}$$

$$\Gamma = 3780\mu_a\mu_t^{(1)}\mu_t^{(2)}\mu_t^{(3)} \tag{4.10}$$

and $\mu_t^{(n)} = \mu_a + (1 - g^n)\mu_s$. This simplification of $\mu_t^{(n)}$ is due to the assumption of the Henyey-Greenstein phase function. $\upsilon^+$ is known as the transient solution, and only contributes significantly at source-detector separations less than approximately 2 transport MFPs. $\upsilon^-$ is known as the asymptotic solution, and dominates at larger source-detector separations. The functions $h_l$ in equation 4.7 are defined as

$$h_0 = 1 \tag{4.11}$$

$$h_1(\upsilon) = -\frac{\mu_a}{\upsilon} \tag{4.12}$$

$$h_2(\upsilon) = -\frac{1}{2} + \frac{3\mu_a\mu_t^{(1)}}{2\upsilon^2} \tag{4.13}$$

$$h_3(\upsilon) = -\frac{9\mu_a\mu_t^{(1)}}{14\mu_t^{(3)}\upsilon} + \frac{3\upsilon}{14\mu_t^{(3)}} \tag{4.14}$$

and the functions $Q_l$ are defined by the recursion relation

$$Q_l(x) = Q_{l-2}(x) - \frac{2l-1}{x} Q_{l-1}(x) \tag{4.15}$$

with the first two $Q_l$ given by

$$Q_0(x) = \frac{e^x}{x} \tag{4.16}$$

$$Q_1(x) = \left(1 - \frac{1}{x}\right)\frac{e^x}{x}. \tag{4.17}$$

The constants $B^-$ and $B^+$ in equation 4.7 are defined as

$$B^{\pm} = \frac{(\upsilon^{\pm})^5[3\mu_a\mu_t^{(1)} - (\upsilon^{\mp})^2]}{12\pi\mu_a^2\mu_t^{(1)}[(\upsilon^{\pm})^2 - (\upsilon^{\mp})^2]}. \tag{4.18}$$

For the purposes of this thesis, we are interested in two boundary scenarios. The first of these is the case of an isotropic point source in an infinite homogeneous medium. The fluence in this case (i.e. the zeroth moment of the radiance) can be found by simply evaluating equation 4.7 for the case of $l$=0. This results in the expression

$$\Psi_0(r) = B^- \frac{e^{-\upsilon^- r}}{\upsilon^- r} + B^+ \frac{e^{-\upsilon^+ r}}{\upsilon^+ r}, \tag{4.19}$$

where $B^{\pm}$ and $\upsilon^{\pm}$ are as defined in equations 4.18 and 4.8, respectively. This result will be used in chapter 6 for the recovery of intrinsic fluorescence from distorted spectra.

The other case we are interested in involves the spatially resolved detection of light injected at the surface of a tissue sample. Therefore, we would like to develop an expression for the radially resolved reflectance due to a source at the surface of a sample. In order to do this, we again follow the derivation of Hull and Foster[37]. For the $P_N$ approximation, (N+1)/2 conditions must be satisfied at each boundary. Since we are considering a single boundary between a semi-infinite medium and a non-scattering air region, the $P_3$ approximation requires 2 boundary conditions to be satisfied. Since the $P_3$ Green's function is the sum of two diffusion Green's functions, one for $\upsilon^+$ and one for $\upsilon^-$,

we can satisfy boundary conditions by treating the transient and asymptotic solutions as independent, and solve for the boundary conditions individually. This is done by using an extrapolated boundary approximation to the partial-current boundary condition. This requires that the fluence is equal to 0 at an extrapolated boundary at a height of $z = z_b$ above the sample surface. For the case of an isotropic point source at depth $z = z_0$, this condition is satisfied by inserting a negative image source at a height of $z = -(z_0 + 2z_b)$. Under the diffusion approximation, this extrapolated boundary is located at $z_b = 2AD$, where D is the diffusion coefficient defined by $D = 1/[3(\mu_a + \mu_s')]$ and A is a dimensionless parameter called the internal reflection coefficient. This coefficient represents a modification to the Marshak boundary condition to account for Fresnel reflection at the boundary[116], and is discussed in detail by Aronson[117].

Since we are treating the $P_3$ solution as the sum of two diffusion solutions, the $P_3$ boundary conditions require the insertion of two image sources in order to satisfy the extrapolated boundary conditions. This results in a point source at $z = z_0$, and image sources at $z = -(z_0 + 4AD_{trans})$ and $z = -(z_0 + 4AD_{asymp})$, where $D_{trans} = \mu_a/(\upsilon^+)^2$ and $D_{asymp} = \mu_a/(\upsilon^-)^2$. We can then apply the expression for reflectance,

$$R_{\text{det}}(\rho; z_0) = \int_{\Omega_{\text{det}}} T_{fresnel}[\cos^{-1}(\hat{s}\cdot\hat{n})]L(\vec{r},\hat{s};z_0)\hat{n}\cdot\hat{s}\,d\Omega\,, \tag{4.20}$$

in order to determine the detected radiance as a function of ρ, the radial distance from the source, and $z_0$, the depth of the buried point source. Here $T_{\text{fresnel}}$ is the Fresnel transmission coefficient, $\hat{n}$ is the outward normal, and $\Omega_{\text{det}}$ is the solid angle subtended by the detector. This expression is evaluated for each of the point and image sources

specified above by inserting equation 4.6 into equation 4.20. This yields an expression of the form

$$R(\rho; z_0) = \sum_{l=0}^{3} \frac{2l+1}{4\pi} \Psi_l(\rho; z_0) S_l(\rho; z_0) \tag{4.21}$$

for each source. The functions $S_l$ in equation 4.21 are defined as

$$S_0(\rho; z_0) = k_1 \tag{4.22}$$

$$S_1(\rho; z_0) = k_2 \left[ \frac{z_0}{(\rho^2 + z_0^2)^{1/2}} \right] \tag{4.23}$$

$$S_2(\rho; z_0) = k_3 \left[ \frac{3z_0^{\,2}}{2(\rho^2 + z_0^2)} \right] + k_5 \left[ \frac{3\rho^2}{2(\rho^2 + z_0^2)} \right] - \frac{k_1}{2} \tag{4.24}$$

$$S_3(\rho; z_0) = k_4 \left[ \frac{5z_0^{\,3}}{2(\rho^2 + z_0^2)^{3/2}} \right] + k_6 \left[ \frac{15 z_0 \rho^2}{2(\rho^2 + z_0^2)^{3/2}} \right] - k_2 \left[ \frac{3z_0}{2(\rho^2 + z_0^2)^{1/2}} \right], \tag{4.25}$$

where $k_n$ are constants that depend on the numerical aperture of the detector and the refractive-index mismatch at the boundary. Values of these constants are given for a variety of conditions in Hull and Foster[37]. In this case, we show the solution for a buried point source. For the case of the image sources, $z_0$ would be replaced by $-(z_0 + 2AD_{trans})$ or $-(z_0 + 2AD_{asymp})$.

In order to create an expression for reflectance that depends only on radial distance from the source, the beam incident on the sample surface is replaced by a point source at a depth of $z_0 = 1/(\mu_a + \mu_s')$, with its strength appropriately adjusted for the effects of Fresnel reflection[109]. This results in an expression for reflectance, $R(\rho)$, that is defined radially for a given source position and depends on the sample optical properties.

## 4.3 Optical property measurements of freshly excised human kidneys

Renal parenchymal tumors, most frequently renal cell carcinomas (RCC), represent the sixth most common malignancy diagnosed in men and the eighth most common in women in the United States. In 2012 it was estimated that there were over 64,000 new cases of renal cancer in the United States, with roughly 14,000 deaths occurring from the disease[118]. While traditionally these tumors were detected because of gross hematuria, flank pain, and an abdominal mass[119], currently fewer than 10% of patients have these symptoms or signs, and more than half are detected as incidental findings on abdominal imaging performed for unrelated symptoms such as abdominal pain. Most incidentally found renal tumors are fairly small (under 4 cm) and generally have an excellent prognosis with minimally invasive procedures. Traditionally, non-metastatic RCC's have been treated with curative intent by radical nephrectomy, a major surgery with concomitant post-operative complications and frequently accompanied by worsening overall kidney function.

Over the past 5 years there has been increasing interest in reducing morbidity by the use of minimally invasive techniques[120], particularly radiologically driven ones. These have primarily focused on thermotherapies, including radiofrequency ablation (RFA)[121] and cryotherapy[122].

Due to the success that has been achieved with minimally invasive treatments of renal cancers, we have chosen to evaluate the viability of PDT for treatment of these tumors. While it has not been used in clinical scenarios for renal parenchymal tumors, there is little reason to expect, particularly based upon the highly vascular nature of these

tumors, that they would not be amenable – indeed ideal – for PDT approaches combined with state-of-the-art imaging and percutaneous applications. In order to assess the viability of PDT for treating cancers of the kidney, particularly RCCs, we measured the optical properties of freshly excised kidney using diffuse reflectance spectroscopy[123]. These data were then incorporated into treatment planning models for interstitial PDT to assess the feasibility of PDT to treat renal cancers.

### 4.3.1 Experimental methods and data analysis

White light, steady-state diffuse reflectance spectroscopy was used to extract optical properties from kidney tissue. The system used was previously designed and built in our laboratory[111], and is shown schematically in Figure 4.1.

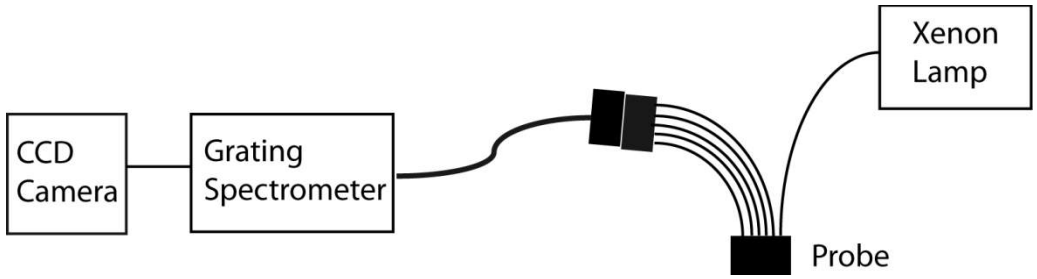


**Figure 4.1** Spectroscopy system used for diffuse reflectance measurements of freshly excised kidney tissue.

Broadband light from a xenon lamp was delivered to the surface of the tissue via a 400 μm core diameter optical fiber, which is terminated in a custom optical probe (see Figure 4.2).

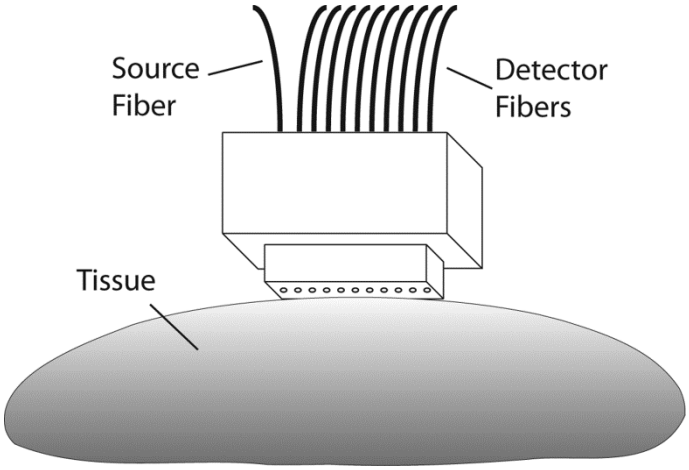


**Figure 4.2** Schematic of the optical probe used in contact with the tissue surface for diffuse reflectance measurements. The source fiber launched broadband light into the tissue, and ten detection fibers, located at distances of 1-10 mm from the source fiber, collected the diffusely reflected signal. Reproduced from [123].

In addition to the fiber for delivery of white light, the probe also contains a linear array of 20 detection fibers (200 μm core diameter) positioned at 1 mm spacings at distances of 1-20 mm from the source fiber. The distal ends of the detection fibers are gathered into a bundle that terminates in a ferrule. At the end of the ferrule, the fibers are arranged into a row and positioned in the focal plane of a 0.275-m imaging spectrograph (SpectraPro - 275, Princeton Instruments/Acton, Acton, MA). The fibers were imaged onto the surface of a thermoelectrically cooled, 512 x 512, 16-bit CCD camera (Pixis512, Princeton Instruments/Acton, Trenton, NJ). Spectral information over the range 630-800 nm was recorded along one axis of the CCD, while detector fiber position was recorded along the other. This allowed for simultaneous collection of spatially-resolved diffuse reflectance spectra from each detector position. For the studies reported here, adequate signal-to-noise was obtained from the first 10 detection fibers, corresponding to source-detector separations of 1-10 mm. We confirmed that these detector positions were sufficient by

systematically deleting data from the most remote fiber and refitting the remaining points until a change in the returned optical properties was observed. For all kidneys analyzed, 5-8 source-detector separations were adequate for accurate recovery of optical properties.

Kidneys used in this study were from patients in the Department of Urology at the University of Rochester Medical Center who were scheduled to receive surgery for kidney cancer. The study, risks, and benefits of participation were presented to subjects, and consent forms approved by the University of Rochester's Research Subject Review Board were presented to patients at the time of their office visit. Kidneys were collected during surgical nephrectomies, and were handled under the supervision of a pathologist prior to, during, and after diffuse reflectance measurements. Kidneys collected for this study were diagnosed with conventional RCC, RCC papillary type 1, RCC papillary multifocal, oncocytoma, and urothelial carcinoma.

Nephrectomy specimens were brought directly from the operating room to the laboratory for optical measurements. A pathologist performed the initial dissection of the specimen as per standard surgical pathology grossing procedures on a bench adjacent to the diffuse reflectance spectroscopy setup. This ensured a clean, flat-cut surface against which the spectroscopy probe could be positioned with good contact. By visual inspection, the pathologist then identified normal and neoplastic tissue where optical measurements were to be performed. A representative dissected kidney is shown in Figure 4.3.

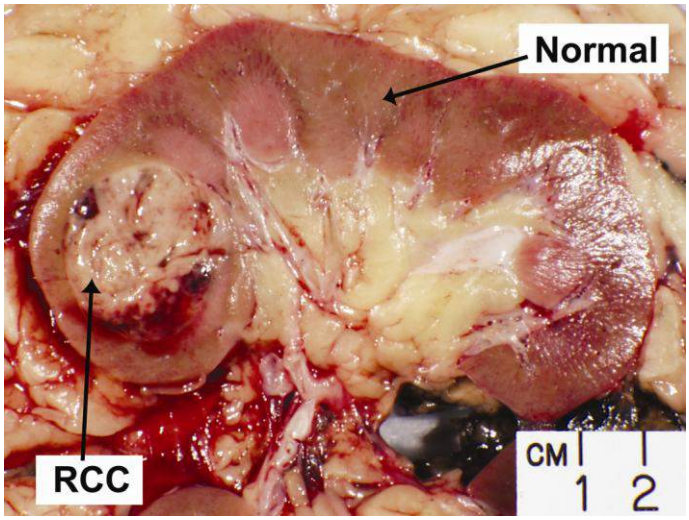


**Figure 4.3** Photograph of a sectioned kidney containing a renal cell carcinoma (RCC). Reproduced from [123].

For diffuse reflectance measurements, the spectroscopy probe was placed in gentle contact with either normal or tumor tissue. Broadband white light was then injected via the source fiber, and detected at the first 10 detector positions. Raw data were corrected for system throughput and fiber cross-talk and then processed through a Savitsky-Golay smoothing filter.

Spectra were analyzed using the $P_3$ approximation as detailed in section 4.2. The $P_3$ approximation was chosen rather than the diffusion approximation due to its validity over a wider range of potential optical properties. At each wavelength, a reflectance expression based on equation 4.21 was used to fit the measured reflectance as a function of radial distance from the source. As mentioned previously, the actual reflectance expression consisted of terms analogous to equation 4.21 for each point source and image source in order to properly fit the boundary conditions. For the measurements performed here, the index of refraction of the tissue was assumed to be 1.4 and the numerical

aperture of the detector was 0.22, resulting in a value of A = 2.95[117], and $k_1$ = 0.0775, $k_2$ = 0.0771, $k_3$ = 0.0766, $k_4$ = 0.0761, $k_5$ = 0.0005, and $k_6$ = 0.0005[37].

For fitting of optical properties, the $P_3$ model of light transport was fit to the measured, spatially-resolved diffuse reflectance using a constrained nonlinear optimization routine found in the MATLAB optimization toolbox (Mathworks, Natick, MA). The fitting function, $\chi^2$, to be minimized was the sum of the squared error between the measured dataset at each wavelength and the $P_3$ model, scaled by the measured diffuse reflectance at each source-detector separation, as shown in equation 4.26,

$$\chi^2 = \sum_{j=1}^{10} [(D(r = r_j) - R(r = r_j, \mu_a, \mu_s')) / D(r = r_j)]^2 \qquad (4.26)$$

where $D(r_j)$ are radially-resolved measurements and $R(r_j, \mu_a, \mu_s')$ are reflectance values at positions $r_j$ computed using the $P_3$ approximation with test optical properties. All 10 source-detector separations, $r_j$, were used simultaneously to compute $\chi^2$ for each set of test optical properties. Constrained minimization was performed using the interior point algorithm included in MATLAB's fmincon function, with $\mu_a$ and $\mu_s'$ extracted as free parameters. The values of $\mu_a$ and $\mu_s'$ were both constrained to be positive in the fit, and the value of the scattering anisotropy ($g$) was assumed to be 0.85[17]. The transport scattering coefficient, $\mu_s'$, was constrained to be monotonically decreasing with increasing wavelength, as this has been demonstrated experimentally[124, 125]. The values of $\mu_a$ and $\mu_s'$ corresponding to a minimized $\chi^2$ were stored in an array. The

radially-resolved measurement for each wavelength in the data set was analyzed using an identical procedure.

### 4.3.2 Experimental results

We analyzed data from 14 kidneys. Results obtained from two kidneys were not interpretable due to low signal levels. Figure 4.4 shows representative diffuse reflectance spectra acquired from the RCC region of a freshly excised human kidney. The spectra were corrected for measured system throughput, background signal, and cross-talk in the CCD. Individual traces correspond to different source-detector separations on the diffuse reflectance probe, which range from approximately 1 – 10 mm.

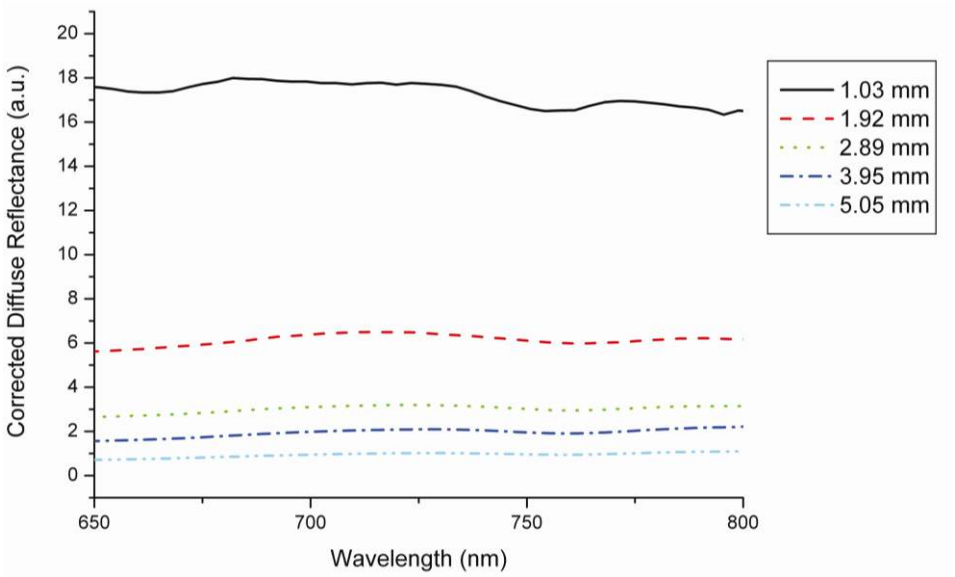


**Figure 4.4** Measured diffuse reflectance spectra at the first five source-detector separations collected from a kidney region identified as RCC. Spectra were corrected for measured optical system throughput, background, and cross-talk in the CCD. Individual traces correspond to different source-detector separations on the diffuse reflectance probe, with their locations relative to the source fiber given in the legend. Reproduced from [123].

Optical properties of tumor and normal kidney tissue were extracted at each wavelength by fitting a $P_3$ model of light transport to the measured data using a constrained nonlinear optimization routine as described in section 4.3.1. An example of such a fit is shown in Figure 4.5.

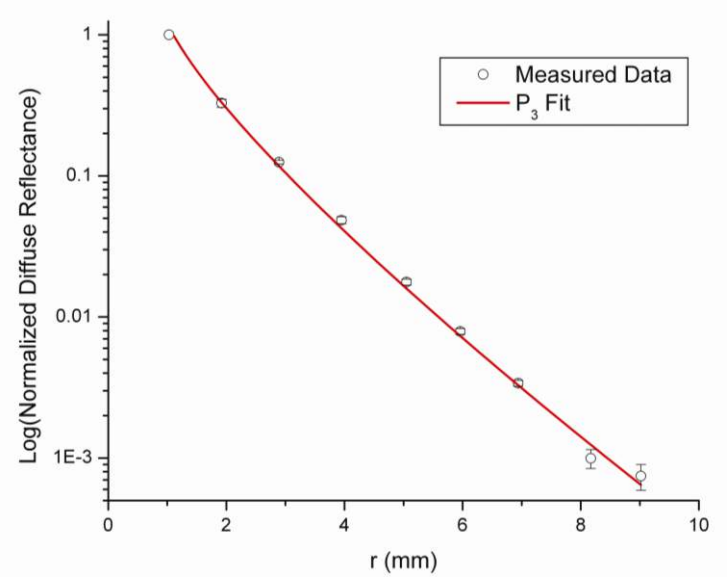


**Figure 4.5** The data points are corrected and normalized diffuse reflectance measurements made at 780 nm in a representative RCC. Each point was acquired at a different source-detector separation (r (mm)). Error bars are the standard deviations of three repeated measurements of the same sample. The fit of the $P_3$ model to these data yielded optical properties of $\mu_a = 0.072$ mm$^{-1}$ and $\mu_s' = 1.40$ mm$^{-1}$. Reproduced from [123].

The individual data points are corrected and normalized diffuse reflectance measurements made at 780 nm in a representative RCC. Each point was acquired at a different source-detector separation (r (mm)) using the probe as described above. The fit shown in Figure 4.5 yielded optical properties of $\mu_a = 0.072$ mm$^{-1}$ and $\mu_s' = 1.40$ mm$^{-1}$.

By analyzing spatially resolved reflectance at each measured wavelength, absorption and scattering spectra over the measured spectral range were determined for each kidney sample. Examples from two lesion types are shown in Figure 4.6.

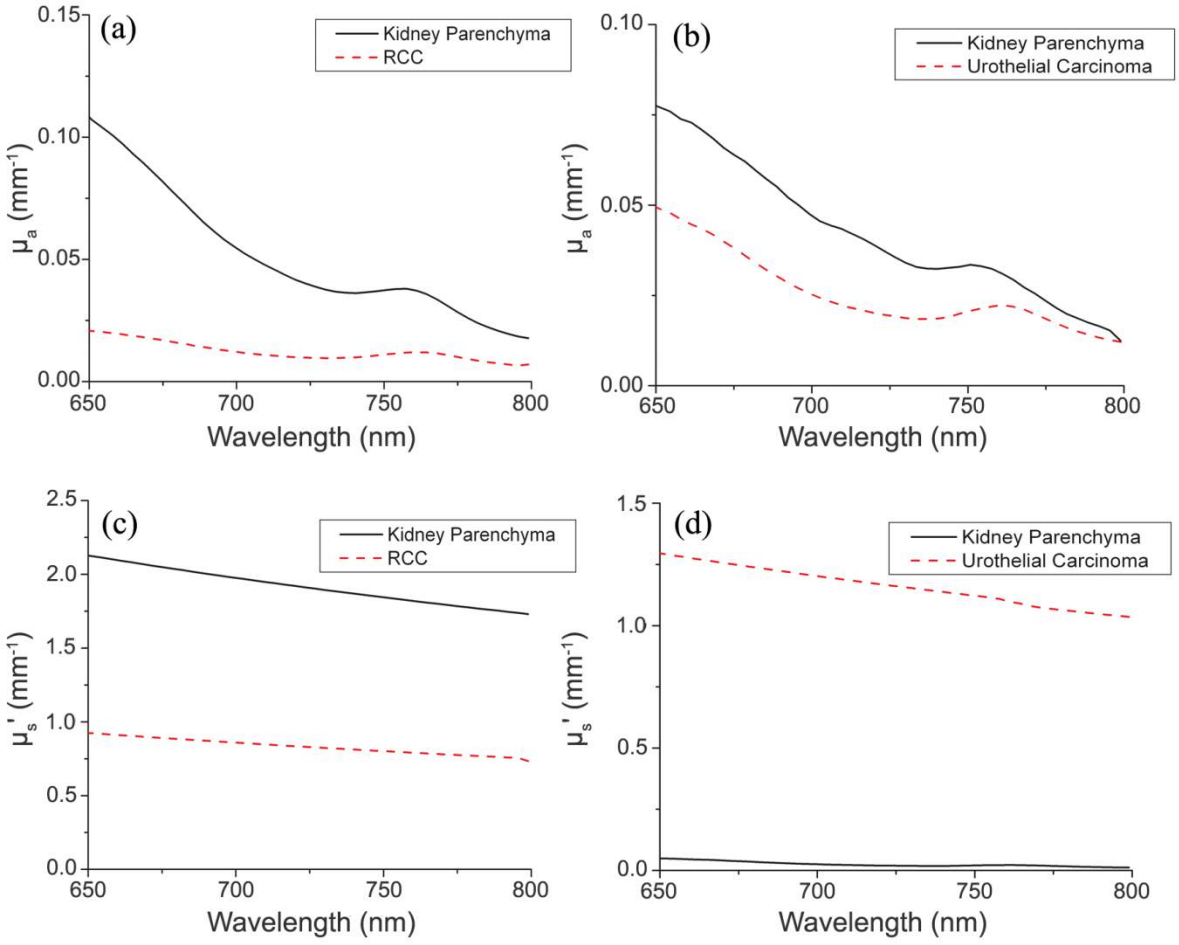


**Figure 4.6** Values of (a) $\mu_a$ and (b) $\mu_s'$ extracted from fitting the $P_3$ model to measured diffuse reflectance spectra from a kidney diagnosed with RCC. (c) and (d) are $\mu_a$ and $\mu_s'$, respectively, extracted from fitting the $P_3$ model to measured diffuse reflectance spectra from a urothelial carcinoma and adjacent normal parenchyma. Reproduced from [123].

In these two cases, $\mu_a$ was lower in the tumor than in the normal kidney tissue. However, this trend was not reproducible across all of the kidney samples (data not shown). The spectra exhibit decreased absorption and scattering with increasing wavelength, as

expected. The absorption feature near 759 nm corresponds to a peak characteristic of deoxyhemoglobin.

The recovered values of $\mu_a$ ranged from 0.016-0.14 $mm^{-1}$ for RCC conventional, 0.003-0.22 $mm^{-1}$ for oncocytoma, 0.02-0.062 $mm^{-1}$ for urothelial carcinoma, 0.14-0.31 $mm^{-1}$ for RCC, papillary type 1, 0.5-0.75 $mm^{-1}$ for RCC, papillary multifocal, and 0.017-0.13 $mm^{-1}$ for kidney parenchyma. The recovered values of $\mu_s'$ ranged from 0.48-1.92 $mm^{-1}$ for RCC conventional, 1.23-2.5 $mm^{-1}$ for oncocytoma, 1.06-1.33 $mm^{-1}$ for urothelial carcinoma, 0.25-0.3 $mm^{-1}$ for RCC, papillary type 1, 1.32-1.83 $mm^{-1}$ for RCC, papillary multifocal, and 0.11-5.51 $mm^{-1}$ for kidney parenchyma. These recovered optical properties yielded values of the transport albedo [$a' \equiv \mu_s'/(\mu_a + \mu_s')$] that ranged from 0.49-0.99. The recovery of transport albedos lower than 0.98 indicates that the $P_3$ approximation was an appropriate choice over the diffusion approximation.

### 4.3.3 Monte Carlo model

PDT of renal tumors would be performed by introducing an optical fiber or fibers directly into the tumor under image guidance. Simulations of light propagation in tissue from cylindrical diffusing tip fibers were performed using the MC code discussed in chapter 3[98].

MC simulations were used to model two scenarios. The first consisted of an ellipsoidal tumor embedded in normal kidney. The tumor had equatorial radii of 1.1 cm and a polar radius of 1.3 cm, with a semi-infinite region of normal kidney tissue surrounding it. This tumor size was determined by averaging measured tumor dimensions from clinical images, and assuming an ellipsoidal tumor shape. In this case,

optical properties used were those extracted from $P_3$ fits to measured diffuse reflectance in both normal kidney and tumor tissue, with each being assigned to the appropriate region of the sample. Based on the treatment wavelengths used for currently available and anticipated PDT photosensitizers, simulations were run at 630, 652, 670, 692 and 780 nm for each kidney sample.

The second model consisted of a homogeneous tissue sample, comprised of either normal kidney or tumor tissue. Optical properties were set uniformly to match those extracted from $P_3$ fits to measured diffuse reflectance in normal or tumor tissue. Simulations of both normal and tumor tissue were run at 50 discrete wavelengths from 630 to 800 nm for each kidney sample. This allowed for modeling of a characteristic light propagation distance at each of the measured wavelengths.

For all MC simulations, 1,000,000 photon packets were launched from a 2-cm-long diffuser. In all cases, the tissue sample was represented with a 100 x 100 x 100 grid of cuboid voxels, each with dimensions of 0.026 cm. A Henyey-Greenstein phase function with $g = 0.85$ was used for all simulations.

### 4.3.4 Monte Carlo simulation results

Monte Carlo simulations of light propagation from cylindrical diffusing fibers were run using the optical properties extracted from each of the kidney samples. A representative fluence distribution generated by the delivery of 100 J $cm^{-1}$ of 630 nm light from a 2-cm-long diffuser is shown in Figure 4.7.

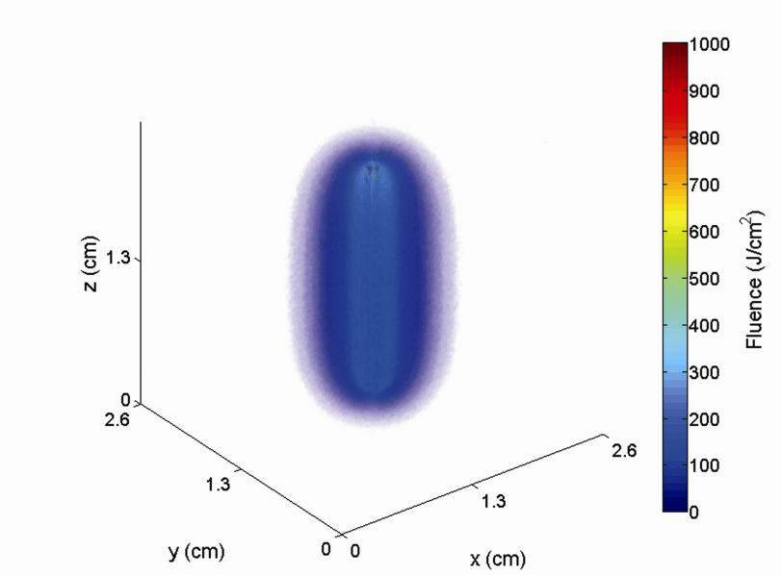


**Figure 4.7** 3D rendering of the simulated fluence distribution around an optical fiber with the proximal end of a 2-cm-long diffusing segment of the fiber positioned at z = 0.3 cm above the boundary separating the tumor and normal tissue regions. Tumor optical properties were set to $\mu_a$ = 0.062 mm$^{-1}$, $\mu_s'$ = 1.34 mm$^{-1}$, and $g$ = 0.85, which correspond to values extracted from an urothelial carcinoma at 630 nm, as shown in Figure 4.6 (c, d). Reproduced from [123].

This wavelength corresponds to the long wavelength absorption maximum of the FDA-approved photosensitizer Photofrin. The figure shows fluence deposited in the surrounding tissue using optical properties that were derived from a kidney diagnosed with urothelial carcinoma. In order to examine this fluence distribution more carefully, cuts were made through the fluence distribution perpendicular to the diffuser axis. The results of this are shown in Figure 4.8a for a 2-cm-long diffuser delivering 100 J cm$^{-1}$, with each contour line corresponding to a fluence increment of 50 J cm$^{-2}$. The outer black line in the figure represents the boundary between tumor and normal tissue, as described previously. The inner black line represents the boundary between tumor tissue and the diffuser.

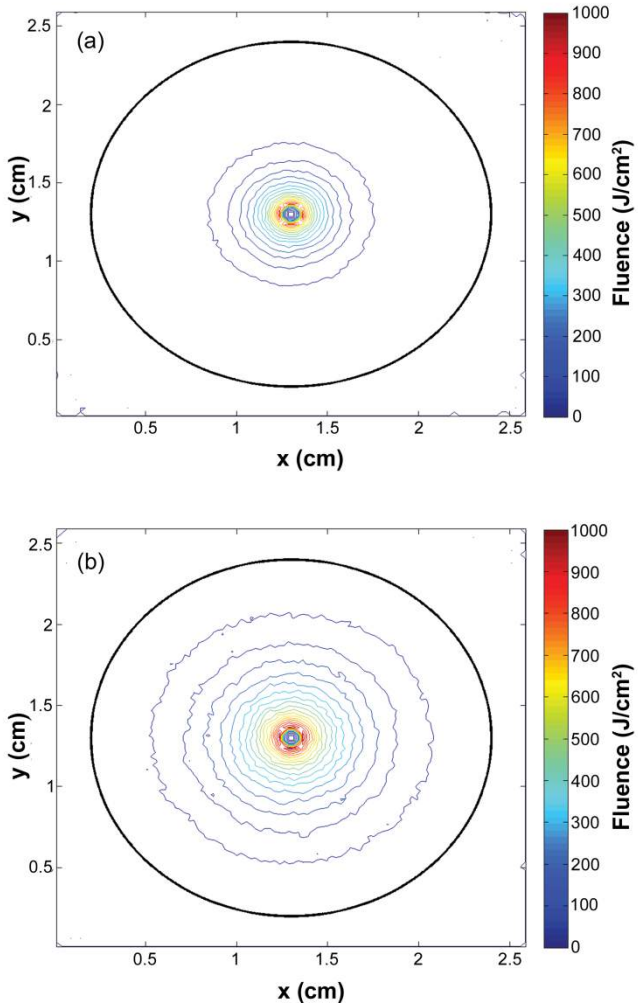


**Figure 4.8** Contour plots of cuts through simulated fluence distributions around a 2-cm-long diffusing fiber at (a) 630 nm and (b) 780 nm, with a total fluence of 100 J $cm^{-1}$ delivered. Each contour line corresponds to a fluence increment of 50 J $cm^{-2}$. The simulated volume consists of an ellipsoidal tumor region, with equatorial radii of 1.1 cm and a polar radius of 1.3 cm, surrounded by a semi-infinite region of normal tissue. The boundary between tumor and normal tissue is shown as the outer black line; the boundary with the diffuser is shown as the inner black line. The optical properties correspond to values extracted from the tumor and normal regions of a kidney diagnosed with urothelial carcinoma, as shown in Figure 4.6 (c, d). Reproduced from [123].

Figure 4.6 reproduces in human kidney the well known observation that absorption and scattering in tissue both decrease with increasing wavelength in this spectral range. It is therefore appealing to consider the use of photosensitizers with longer wavelength

absorption in iPDT of the kidney. This potential is shown in Figure 4.8, where fluence deposition is modeled at 630 and 780 nm. At the longer wavelength the penetration of light is greatly improved compared to 630 nm. For a delivered fluence of 100 J $cm^{-1}$, ~20% of the tumor volume received a light dose of at least 50 J $cm^{-2}$ at 630 nm. This increased to approximately 50% of the tumor volume at 780 nm. Additionally, nearly 30% of the tumor received a light dose of 100 J $cm^{-2}$ or more at 780, compared to ~11% at 630 nm. This trend was reproducible across all samples, with the percentage of the tumor receiving a prescribed light dose increasing by an average of 2.2-fold as a result of changing the wavelength from 630 to 780 nm. Increasing the fluence delivered by the cylindrical diffuser to 600 J $cm^{-1}$ extends the 50 J $cm^{-2}$ contour to the simulated boundary of the tumor (not shown).

In order to describe a characteristic distance of light propagation from a cylindrical diffusing fiber, MC simulations were run using homogeneous optical properties in a semi-infinite tissue volume surrounding a 2-cm-long diffuser. A zeroth order modified Bessel function of the second kind, $K_{0,}$ is a useful analytic approximation to light emitted from an infinitely long cylinder. Thus, a function of the form

$$\phi(r) = K_0(r/\delta) \tag{4.27}$$

was fit to radially averaged cuts through simulated fluence distributions at the axial midpoint of the diffuser. Here, $\phi(r)$ is the fluence at radial position $r$, $K_0$ is a zeroth order modified Bessel function of the second kind, and $\delta$ is a characteristic light propagation distance, which we define as the distance from the diffuser over which light

is attenuated to ~ 40% of its value at the fiber surface. A representative fit to a simulation run with $\mu_a$ = 0.017 mm$^{-1}$ and $\mu_s'$ = 1.55 mm$^{-1}$ is shown in Figure 4.9.

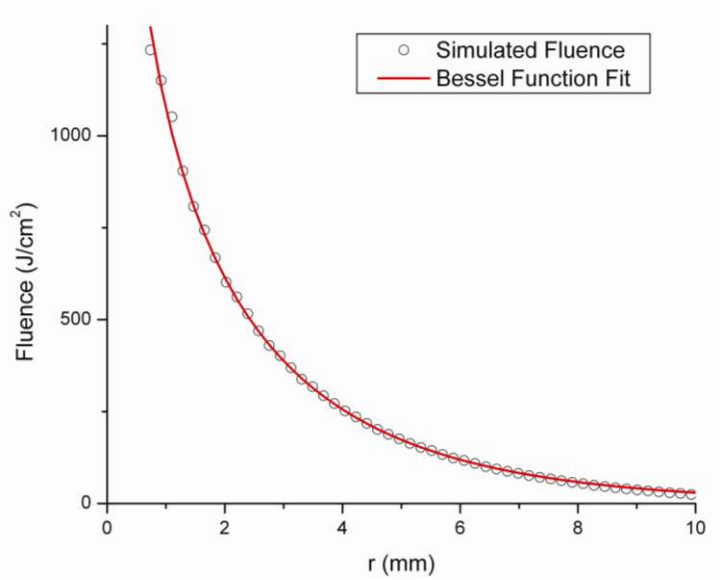


**Figure 4.9** Results of fitting a zeroth order modified Bessel function of the second kind, $K_0$ (equation 4.27), to a cut through the simulated fluence around a 2-cm-long diffuser. The fluence plotted is the radially averaged simulated fluence at the axial midpoint of the diffuser. Optical properties were set to $\mu_a$ = 0.017 mm$^{-1}$, $\mu_s'$ = 1.55 mm$^{-1}$, and $g$ = 0.85, which correspond to values extracted from a representative RCC at 780 nm. From such fits, the characteristic propagation distance, $\delta$, is obtained. Reproduced from [123].

The optical properties used correspond to values extracted from a typical RCC at 780 nm. The fit shown is typical and of good quality. The $\delta$ value extracted from this fit was 3.43 mm. The results of this are shown in Figure 4.10 for optical properties from a typical kidney diagnosed with RCC.

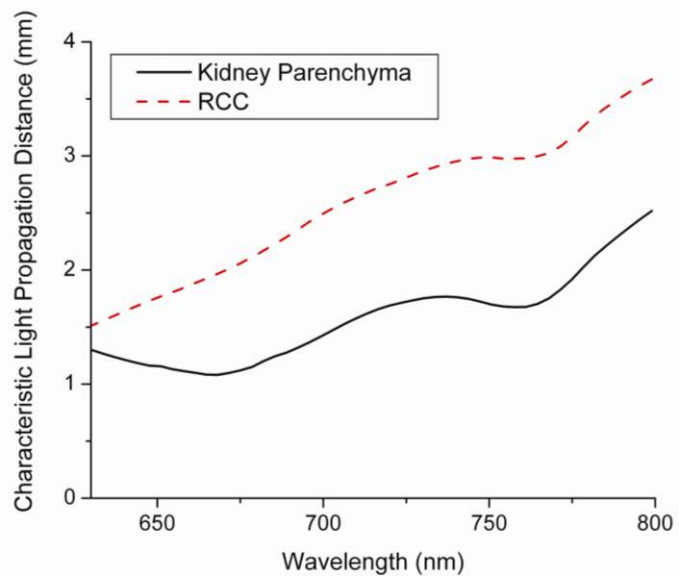


**Figure 4.10** Simulated light propagation distance, δ, based on Bessel function fit to the simulated radial distribution of fluence in Figure 4.9, for a kidney diagnosed with RCC. Reproduced from [123].

An increased penetration depth with increasing wavelength was found for all measured tumor samples. The mean penetration depths for the five tumor types in this study and for the normal kidneys are collected in Table 4.1 for five wavelengths selected for relevance to clinical PDT.

| λ (nm) | 630 (Photofrin) | 652 (Foscan) | 670 (Methylene Blue) | 692 (BPD) | 780 (Next generation) |
|---|---|---|---|---|---|
| **Diagnosis** | | | | | |
| **RCC Conventional** (n = 9) | 1.28±0.91 (0.38-2.67) | 1.77±1.04 (0.86-3.72) | 1.85±1.02 (0.97-3.83) | 2.15±1.15 (1.09-4.48) | 2.78±1.21 (1.31-5.19) |
| **Oncocytoma** (n = 2) | 1.65±1.85 (0.34-2.96) | 2.10±2.35 (0.44-3.76) | 2.30±2.60 (0.46-4.14) | 2.57±2.91 (0.51-4.63) | 3.17±3.54 (0.66-5.67) |
| **RCC, Papillary Type 1** (n = 1) | 1.11 | 1.25 | 1.32 | 1.51 | 1.84 |
| **RCC, Papillary Multifocal** (n = 1) | - | 0.49 | 0.51 | 0.56 | 0.66 |
| **Urothelial Carcinoma, Low-grade Papillary** (n = 1) | 1.95 | 2.23 | 2.43 | 2.88 | 3.68 |
| **Kidney Parenchyma** (n = 14) | 1.70±0.30 (1.47-2.29) | 1.92±0.36 (1.24-2.41) | 1.92±0.58 (1.00-2.92) | 2.49±0.78 (1.66-4.36) | 3.72±1.31 (2.15-6.73) |

**Table 4.1** Mean characteristic light propagation distances, in mm, at five selected wavelengths, separated by diagnosis. Wavelengths were selected to correspond with the absorption peaks of Photofrin (630 nm), Foscan (652 nm), methylene blue (670 nm), benzoporphyrin derivative (BPD, 692 nm), and next-generation photosensitizers (780 nm). Uncertainties shown are standard deviations over multiple samples, and values in parentheses indicate range over multiple samples. Reproduced from [123].

### 4.3.4 Discussion

Renal parenchymal tumors, most frequently renal cell carcinomas (RCC), are increasingly being detected earlier as incidental radiological findings. These tumors are often detected when they are small enough such that radical nephrectomy, either by open surgery or laparoscopy, is not necessary. Patients with only one kidney, with bilateral disease, or who are too frail to undergo surgery are not normally treated by nephrectomy. Minimally invasive, kidney sparing therapies based on percutaneous approaches such as RFA and cryotherapy have their own limitations, particularly in well perfused organs like the kidney. There is therefore a compelling rationale for considering image-guided, interstitial PDT in this context, and this motivated the study of the optical properties of RCC, other less common lesions, and normal kidney parenchyma.

The characteristic propagation distance, $\delta$, which we have defined, corresponds to the distance in the tissue at which the deposited fluence falls to ~40% of the maximum value immediately adjacent to the fiber. The propagation distances shown in Table 4.1 translate to diameters around a single diffuser of ~ 2.6 mm at 630 nm to 5.6 mm at 780 nm. It is important to emphasize that this does not define the zone that can be treated effectively. As illustrated in Figure 4.8, the area that receives a specified, clinically relevant fluence is typically larger than the characteristic propagation distance. Also, as suggested above, multiple diffuser fibers can be used to treat a larger volume. This is commonly done in PDT treatment of the prostate[126], where fibers are inserted on a grid specified by a template, with an approximate spacing of 5-7 mm between diffusers. The size and arrangement of this grid can be tailored to fit the tumor of an individual patient.

The heterogeneity in tumor optical properties reported in this study provides strong rationale for direct pre-treatment optical property determinations using interstitial optical fiber-based spectroscopy.

The wavelengths used for MC simulation were chosen to correspond to the absorption maxima of several clinically relevant PDT photosensitizers. The wavelength of 630 nm corresponds to Photofrin, a porphyrin photosensitizer, which is currently approved to treat a number of diseases, including esophageal, endobronchial, and bladder cancers and Barrett's esophagus with high grade dysplasia[1, 2]. Foscan, also known as Temoporfin or mTHPC, has an absorption maximum of 652 nm, and is approved in Europe for recurrent, inoperable head and neck cancers, and is being investigated in ongoing clinical trials for the treatment of other neoplastic conditions[2, 48]. Simulations performed at 670 nm were chosen to correspond to the absorption of photosensitizers such as HPPH or methylene blue. HPPH has been used in the treatment of thoracic malignancies[127, 128], Barrett's esophagus[129], and early cancers and precancers of the oral cavity[130]. Methylene blue is FDA-approved as a diagnostic dye and is the only known treatment for methemoglobinemia. Methylene blue has also been used successfully as a photosensitizer in a number of PDT studies[66-68]. Benzoporphyrin derivative (BPD), also known as verteporfin, has an absorption maximum of 692 nm and is approved worldwide for the treatment of age-related macular degeneration[1]. The wavelength of 780 nm was chosen to correspond to the absorption of some emerging photosensitizers, such as TOOKAD[131] and others still in preclinical development[132], which are designed to take advantage of increased penetration of light in this spectral

range. Based on our findings, these next-generation sensitizers with high absorption at 780 nm and beyond would be favorable candidates for clinical trials of interstitial PDT of renal cancers.

We conclude that image-guided, interstitial PDT in selected populations of patients with kidney tumors is feasible and should be considered a viable treatment option.

## 4.4 Determination of optical properties by interstitial spectroscopy using a custom fiber optic probe

A great deal of progress has been made on the determination of optical properties from surface measurements of diffuse reflectance. As outlined in the introduction, as well as in chapter 2 and section 4.3 of this thesis, surface spectroscopy measurements can yield accurate values for $\mu_a$ and $\mu_s'$. These techniques are limited in their applicability, however, due to the requirement that the tissue in question be accessible to surface measurements. Due to the absorptive and highly scattering nature of tissue, light propagation is limited to regions that are close to the source and detectors. An excellent analysis of the regions sampled by steady-state diffuse reflectance for a particular source-detector configuration is provided by Feng, Zeng, and Chance[133]. In the weak absorption limit, they give $z = \frac{d\sqrt{2}}{4}$ as the maximum depth of sensitivity, where *d* is the source-detector separation. In the strong absorption limit, this maximum depth changes to $z = \sqrt{\frac{d}{2\mu_{eff}}}$, where $\mu_{eff}$ is the effective attenuation coefficient and is defined as $\mu_{eff} = \sqrt{3\mu_a(\mu_a + \mu_s')}$. For a source-detector separation of 10 mm (the largest separation used in the previous section), this yields a maximum depth sensitivity of approximately 3.5 mm.

In iPDT, optical fibers are used to deliver illumination for PDT deep within the body. Therefore, a scheme for determination of optical properties deep within the body is required. There has been a good deal of work done on this topic, with solutions being

roughly separated into two categories. The first of these uses separate spectroscopy fibers that are inserted into the tumor at a prescribed spacing. Due to the relatively large separation of these spectroscopy fibers, a diffusion model of light propagation is generally used to fit optical properties based on detected light[40]. An alternative implementation of this uses the treatment fibers to deliver and collect spectroscopy light[126]. The other broad category of interstitial spectroscopy techniques uses a single encapsulated probe, but requires extensive calibration with a large library of optical phantoms[38, 39]. These techniques do not rely on models of the probe or light propagation, but instead use empirical calibrations.

We are primarily interested in treating bulky tumors deep within the body. In these scenarios, the insertion of multiple fibers can be undesirable. Even for a large tumor that is easily accessible to multiple fibers, the insertion of additional spectroscopy fibers increases clinical complexity and increases the risk of complications. For certain treatment regimes, insertion of multiple spectroscopy fibers might not be possible. One neoplasm we are considering for PDT is cholangiocarcinoma, which is a malignancy of the bile ducts. To treat this with PDT, a single fiber would be inserted into the bile duct. Therefore, we would like a spectroscopy scheme that also consists of a single probe that can be inserted along the same track as the treatment fiber.

### 4.4.1 Probe design and Monte Carlo model

The custom optical probe (Pioneer Optics Company, Bloomfield, CT) used to perform interstitial optical property recovery is shown in Figure 4.11.

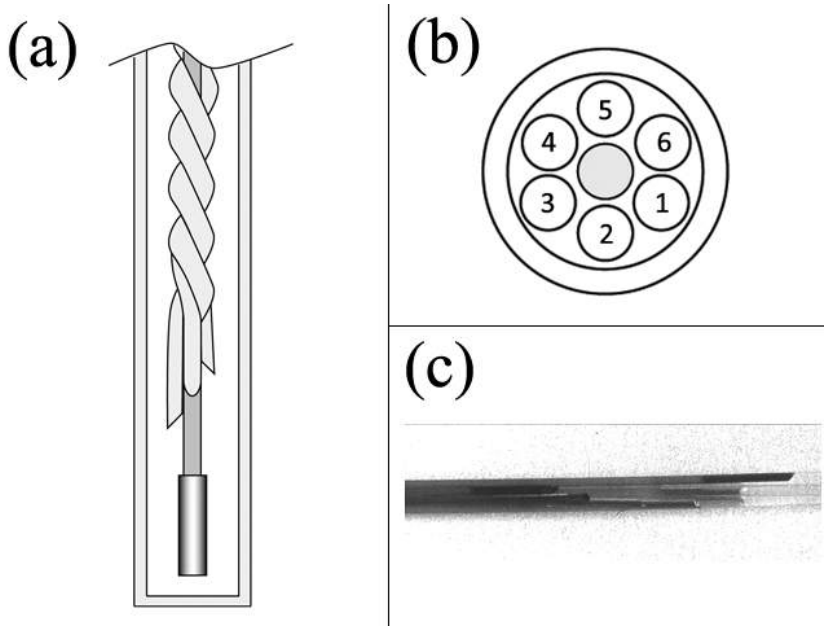


**Figure 4.11** (a) Side view of custom optical probe showing helical arrangement of spectroscopy fibers. (b) Cross-section of optical probe showing radial placement of fibers. (c) Photograph of optical probe showing fiber positions, silver coating, and central diffuser.

The probe consists of six side-firing, beveled optical fibers arranged helically around a central diffuser, surrounded by an encapsulant. Each of the fibers points in a different radial direction, and is capable of functioning as either a source or detector. Each spectroscopy fiber is beveled at a 38º angle, has a polyimide coating along its length, and silver coating at the tip. A small region at the tip of each fiber is free of both coatings to allow for transmission of light. Details on the arrangement of these fibers is given in chapter 3.

For a typical measurement, spectroscopy light is emitted from one of the fibers and detected sequentially at the other fibers. This is performed using the system shown in Figure 4.12.

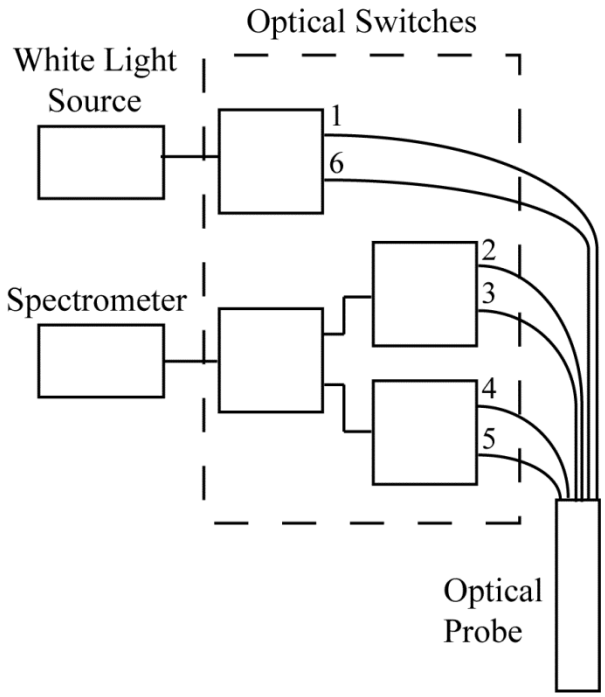


**Figure 4.12** System diagram for interstitial diffuse reflectance spectroscopy
In this arrangement, broadband white light is delivered by either fiber 1 or 6, and detected by fibers 2-5. Further details about individual components can be found in section 4.4.4.

In order to determine optical properties, a MC model of the spectroscopy probe was developed, as outlined in chapter 3. This probe model incorporates the spectroscopy fibers, the central diffuser, the encapsulant, and the cladding. Photon packets are launched from the specified spectroscopy fiber, and detected at the other fiber positions, with the detected photon weight being recorded for each detection fiber. This detected weight is then normalized to the weight detected at the fiber closest to the source.

A library of simulated detection profiles was generated for optical property recovery. The library was generated by running simulations that launched photon packets from fiber 1 and detected at fibers 2-5. This was done to match experimental conditions. The optical property library consists of simulations run at 64 values of $\mu_a$, ranging from 0.0001 – 2 $cm^{-1}$, and 60 values of $\mu_s$, ranging from 1-180 $cm^{-1}$, for a total of 3840 combinations of optical properties. For all simulations, a Henyey-Greenstein phase function was assumed, with a value of $g = 0.73$, which was chosen to match the value of the anisotropy coefficient for Intralipid at a wavelength of 630 nm[134]. All simulations were run with 10,000,000 photon packets.

### 4.4.2 Optical property recovery algorithm

The recovery of optical properties from measured data is performed in three steps: 1) constrain $\mu_{eff}$, 2) fit $\mu_a$ and $\mu_s'$ using the value of $\mu_{eff}$ determined in step 1, and 3) fit $\mu_a$ and $\mu_s'$ spectra with known absorption and scattering spectra shape. In the first step, the value of $\mu_{eff}$ is constrained by fitting the measured data at each wavelength with an expression of the form

$$\varphi(r) = e^{-\alpha r}, \tag{4.28}$$

where $\varphi$ is the normalized detected fluence, $\alpha$ is a constant related to $\mu_{eff}$ as shown in Figure 4.14, and $r$ is the distance from the source to detector fiber along the cylindrical surface of the probe. Since the fiber positions and probe diameter are known, these distances can be computed directly. A typical fit, in this case for simulated data, is shown in Figure 4.13.

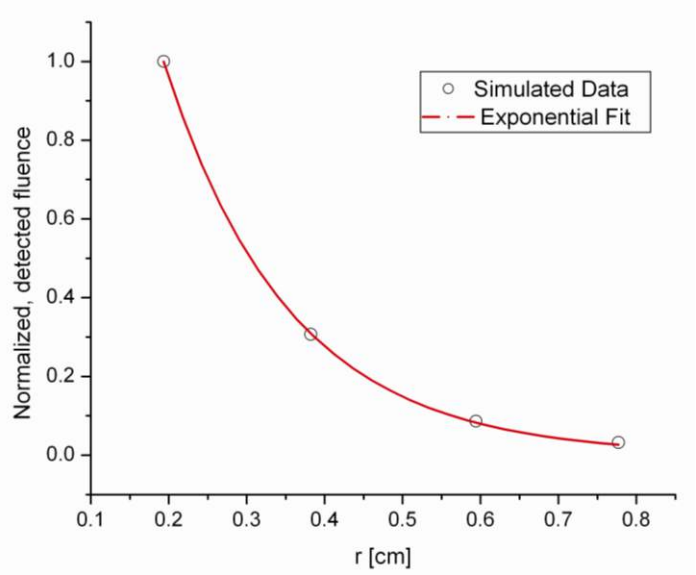


**Figure 4.13** Fitting simulated, normalized data with equation 4.28.

This value of α is then converted to $\mu_{eff}$ through a simulation library. In order to generate this library, simulations were run at a wide variety of $\mu_{eff}$ values. For each simulation of a known $\mu_{eff}$, the value of α was found by fitting equation 4.28 to the simulated data. After this was performed for all simulations, a second-order Fourier series was then fit to the relation between α and $\mu_{eff}$, as shown in Figure 4.14. The mathematical form of this fit is not of particular scientific interest, but is simply used to smooth the data.

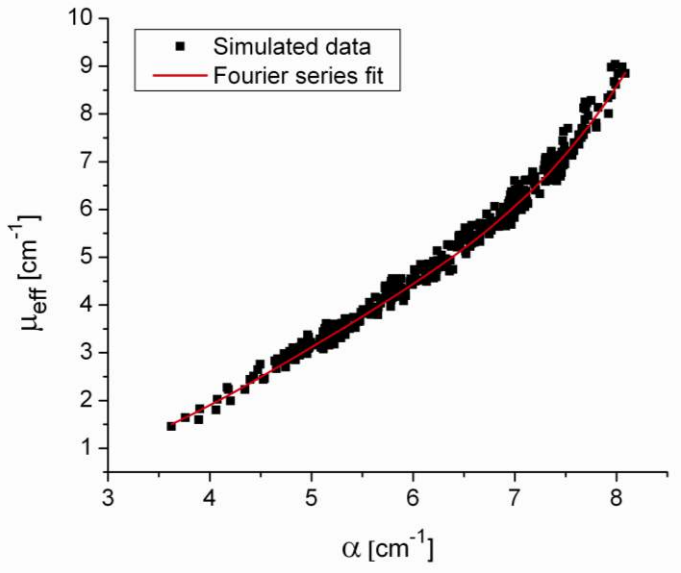


**Figure 4.14** Conversion of α to $\mu_{eff}$, determined by equation 4.28 to simulated data.

Constraining $\mu_{eff}$ is required in order to remove ambiguities in the simulation library. In order to directly fit measured data to the simulation library, one would minimize an expression of the form

$$\chi^2 = \sum_{d=2}^{5} [\varphi_m(r_d) - \varphi_{MC}(r_d, \mu_a, \mu_s')]^2 \tag{4.29}$$

at each wavelength, where $\varphi_m$ is the measured, normalized fluence detected at detector position $r_d$ and $\varphi_{MC}$ is the simulated, normalized fluence detected at detector position $r_d$ with optical properties $\mu_a$ and $\mu_s'$. Here $\mu_s'$ is used due to the relatively large source-detector separations employed. However, this results in the scenario shown in Figure 4.15.

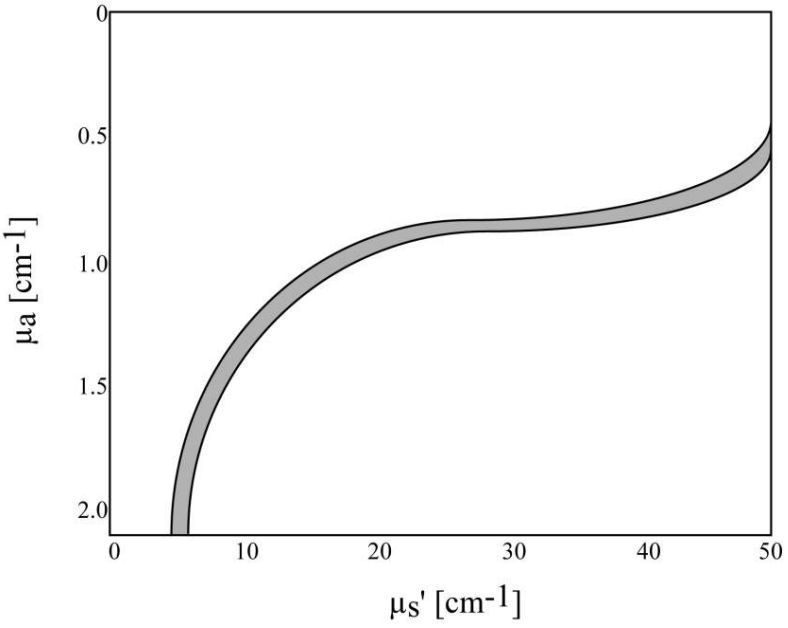


**Figure 4.15** Fitting simulated data to full simulation library. The grey region represents local minima in optimization of equation 4.29.

The grey region in the plot represents combinations of ($\mu_a$, $\mu_s'$) that generate a local minimum in equation 4.29. As can be seen, there is not one unique solution to the minimization, but a family of equally valid solutions. By inserting the constraint on $\mu_{eff}$, we can determine a unique solution to the problem, as shown in Figure 4.16.

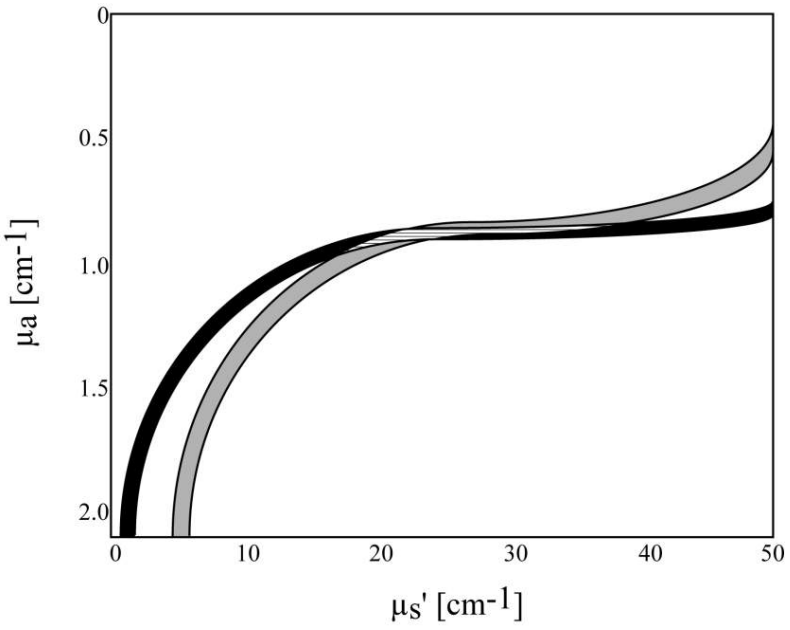


**Figure 4.16** Fit to full simulation library with $\mu_{eff}$ curve overlaid. The black region corresponds to values of $\mu_{eff}$ that are within 5% of that determined in step 1 of the algorithm. The overlapping portion of the curves is shown filled by horizontal lines.

This is done by minimizing equation 4.29 as described previously, but only considering entries in the simulation library with a $\mu_{eff}$ value that is within 5% of the $\mu_{eff}$ found in step 1 of the fitting algorithm. Doing so creates a region, composed of the overlapping portion of the black and grey curves shown filled by horizontal lines in Figure 4.16, over which we can find the optimum values of absorption and scattering coefficient. This results in plots of $\chi^2$ vs. $\mu_a$ and $\chi^2$ vs. $\mu_s'$ such as those shown in Figure 4.17.

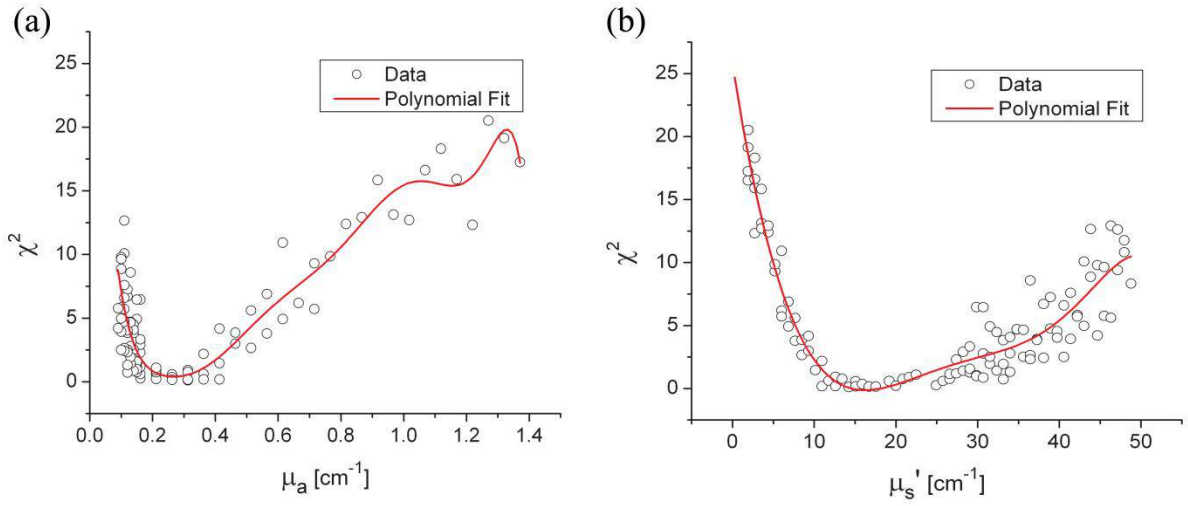


**Figure 4.17** Determination of (a) $\mu_a$ and (b) $\mu_s'$ from constrained minimization of equation 4.29. Open circles represent $\chi^2$ values for combinations of $\mu_a$ and $\mu_s'$ in the simulation, while solid lines represent a seventh-order polynomial fit to these data. The appropriate optical property combination is found by looking for the minima in these fits.

For both $\mu_a$ and $\mu_s'$, a seventh-order polynomial is fit to the curves shown in Figure 4.17 in order to determine the optimum values of the optical properties. As an error check, these determined values, $\mu_{a,fit}$ and $\mu_{s,fit}'$, are used with the value of $\mu_{eff}$ from step 1 of the algorithm to calculate

$$\mu_{a,calc} = \frac{1}{2}\left(-\mu'_{s,fit} + \sqrt{(\mu'_{s,fit})^2 + \frac{4}{3}\mu_{eff}^{\ 2}}\right), \tag{4.30}$$

$$\mu'_{s,calc} = \frac{\mu_{eff}^{\ 2}}{3\mu_{a,fit}} - \mu_{a,fit}\,. \tag{4.31}$$

If these calculated values, $\mu_{a,calc}$ and $\mu'_{s,calc}$, are different from $\mu_{a,fit}$ and $\mu'_{s,fit}$ by more than 20%, the data for this wavelength are thrown out, and fitting proceeds to the next wavelength. This is done to exclude data for which $\mu_{eff}$ is not known well enough to generate curves of comparable quality to those shown in Figure 4.17.

The final step of the algorithm involves fitting the values of $\mu_a$ and $\mu_s'$ found in step 2 with the known spectral shapes of the absorbers and scatterers present. To do this, the $\mu_s'$ spectrum is first fit with

$$\mu_s'(\lambda) = a\left(\lambda / \lambda_0\right)^{-b}, \tag{4.32}$$

where $\lambda$ is the wavelength in nm, $\lambda_0$ is a fixed normalization wavelength, and *a* and *b* are coefficients in the fit. For the results shown in this chapter, $\lambda_0$ was set to 600 nm. The values of *a* and *b* are constrained to be positive in the fit. Using the $\mu_{eff}$ spectrum found in step 1 and this fitted $\mu_s'$ spectrum, the $\mu_a$ spectrum is re-calculated using equation 4.30. This is done to remove cross-talk between absorption and scattering, since the scattering spectrum is known to be smooth. Finally, the absorption spectrum is fit with a superposition of known absorption basis spectra using a non-linear optizimation.

### 4.4.3 Recovery of optical properties from simulated data

In order to test the recovery of optical properties at single wavelengths, a series of simulations were run with 10 values of $\mu_a$ ranging from 0.1-2 $cm^{-1}$ and 7 values of $\mu_s'$ ranging from 10-80 $cm^{-1}$, with a value of $g$ = 0.73 and 10,000,000 photon packets launched per simulation. The exact values of $\mu_a$ and $\mu_s'$ were chosen so as not to correspond with any of the ($\mu_a$, $\mu_s'$) combinations in the simulation library. These simulations were then processed using the first two steps of the fitting algorithm described in the previous section. Since the simulations were run at only a single wavelength, the third step of the algorithm was not possible. The results of this are shown in Figure 4.18.

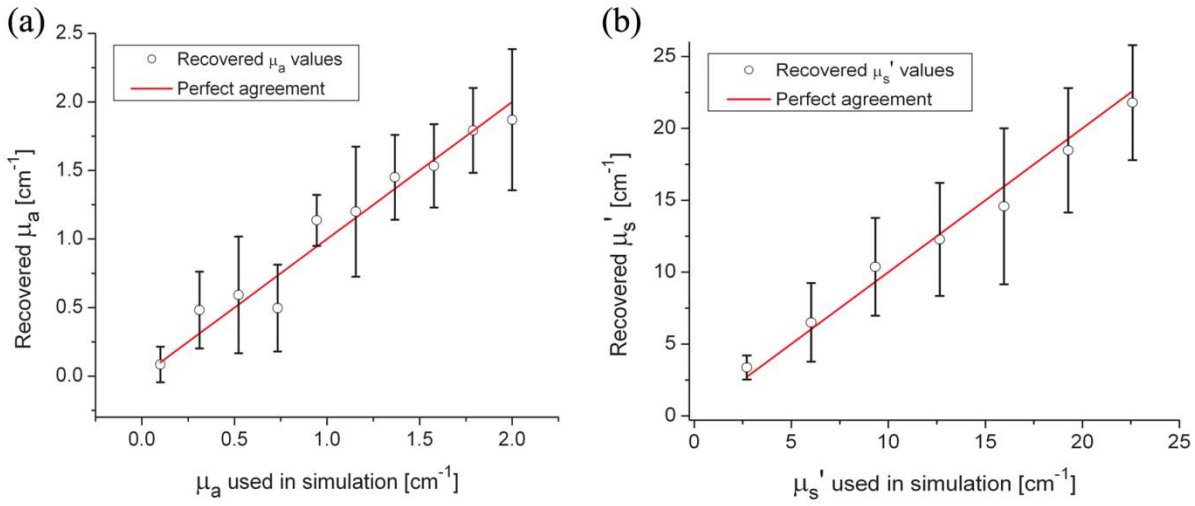


**Figure 4.18** Recovery of (a) $\mu_a$ and (b) $\mu_s'$ from MC simulations at a single wavelength.

The values shown in Figure 4.18a are averages over simulations with the same absorption coefficient, but with varying scattering coefficient. Data points in Figure 4.18b are averages over simulations with the same scattering, but differing absorption. Error bars in both figures are standard deviations over the same range. The mean error in fitting $\mu_a$ was 15.5%, with a maximum error of 54%. Mean error in fitting $\mu_s'$ was 8.9%, with a maximum error of 24%.

Simulations were then run to assess the ability of the algorithm to recover full spectra of optical properties. This was first done by simulating the propagation of light through a tissue-simulating phantom consisting of manganese meso-tetra (4-sulfanatophenyl) porphine (MnTPPS) and Intralipid. MnTPPS was chosen due to the similarity of its absorption spectrum to hemoglobin, and its negligible fluorescence in the wavelength range of interest. The absorption spectrum of MnTPPS is shown in Figure 4.19. Intralipid was chosen due to its tissue-like scattering properties.

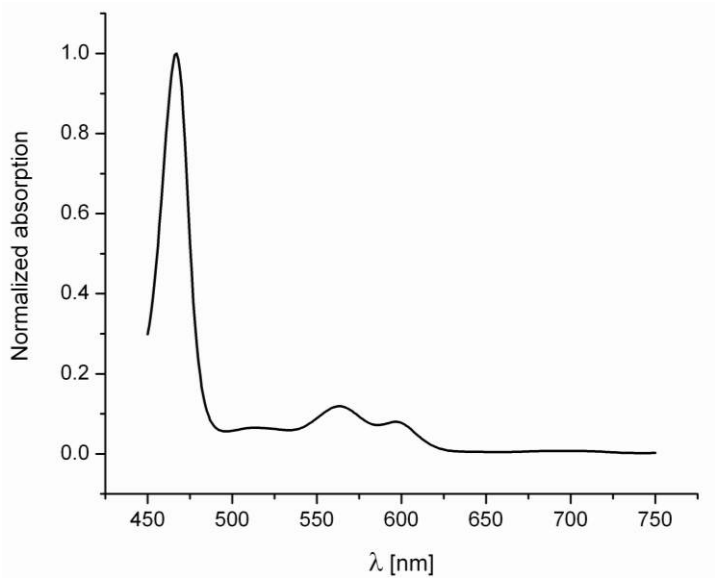


**Figure 4.19** Normalized MnTPPS absorption spectrum, measured using a commercial spectrophotometer.

The absorption spectrum used in simulations consisted of scaled versions of the spectrum shown in Figure 4.19 for MnTPPS concentrations ranging from 10-40 μM. The scattering spectrum used is given by

$$\mu_s(\lambda) = 0.16\lambda^{-2.4}, \tag{4.33}$$

$$g(\lambda) = 1.1 - 0.58\lambda, \tag{4.34}$$

where λ is the wavelength in μm, and $\mu_s$ is given in units of $mL^{-1}$ L $cm^{-1}$, where mL corresponds to mL of Intralipid-10% and L corresponds to the total volume of the tissue phantom[134]. Intralipid concentrations ranging from 55-90 mL/L were used in simulations.

Simulations were run at 44 discrete wavelengths ranging from 520-620 nm for each concentration combination of MnTPPS and Intralipid, with optical properties sampled from a scaled version of the absorption spectrum shown in Figure 4.19 and the

reduced scattering spectrum given by equations 4.33 and 4.34. The detection profiles from each of these simulations were then run through the full fitting algorithm described in section 4.4.2. Some typical results are shown in Figure 4.20.

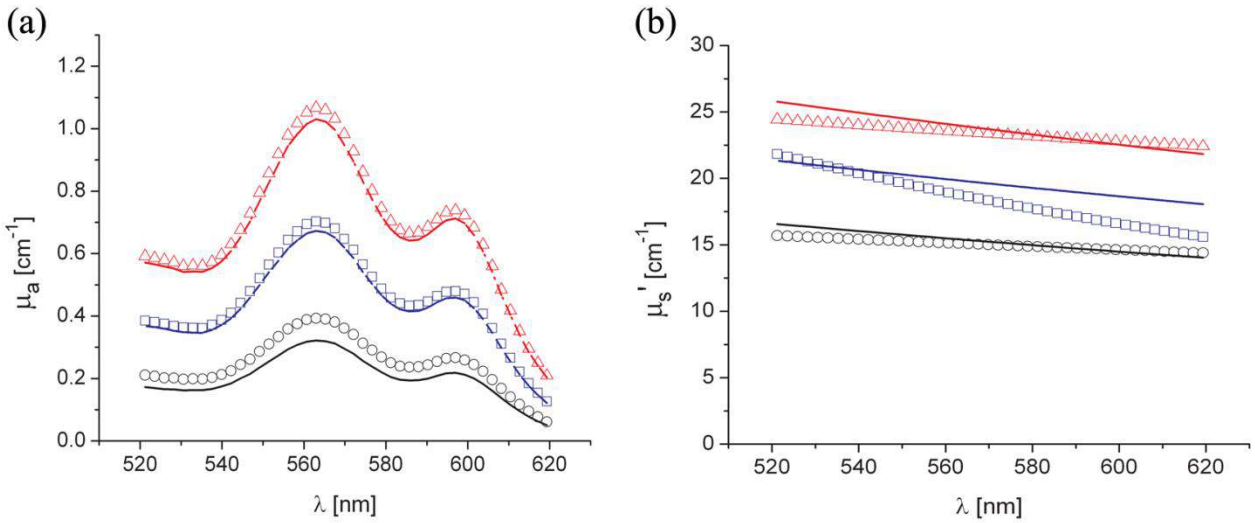


**Figure 4.20** Recovery of (a) $\mu_a$ and (b) $\mu_s'$ spectra from simulations in tissue-simulating phantoms containing MnTPPS and Intralipid. Symbols represent recovered values, while lines of the same color as the symbols represent the spectra input into the simulation.

Figure 4.20a shows the recovery of $\mu_a$ spectra at a constant Intralipid concentration of 90 mL/L and varying MnTPPS concentration, while Figure 4.20b shows the recovery of $\mu_s'$ spectra at a constant MnTPPS concentration of 25 μM and varying Intralipid concentration. Shown in Figure 4.21 is a summary of the recovery of MnTPPS concentrations from simulated data.

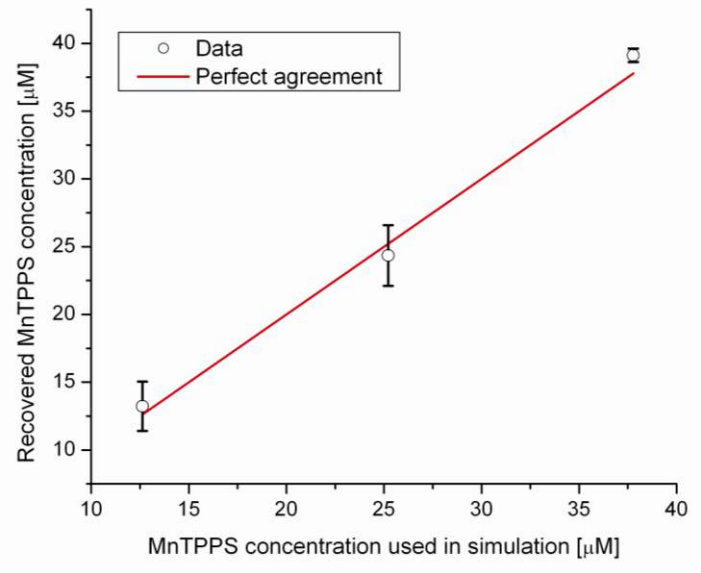


**Figure 4.21** Recovery of MnTPPS concentration from simulations in tissue-simulating phantoms. Symbols represent the mean value over three simulations performed at different Intralipid concentrations, error bars represent standard deviation over this range, and the solid line represents perfect agreement.

Data points shown are averages over simulations with the same MnTPPS concentration, and the Intralipid concentration varying. Error bars are standard deviations over these same data. As can be seen, the recovery of MnTPPS concentration tracks linearly with the actual concentration used in simulation. The mean error in the recovery of MnTPPS concentration was 6.5%, with a maximum error of 20%.

In order to test the ability of the algorithm to separate the effects of multiple absorbers, simulations were also performed with synthetic hemoglobin absorption spectra. The absorption of hemoglobin is oxygen dependent, with oxy- and deoxyhemoglobin having different absorption spectra, as shown in Figure 4.22.

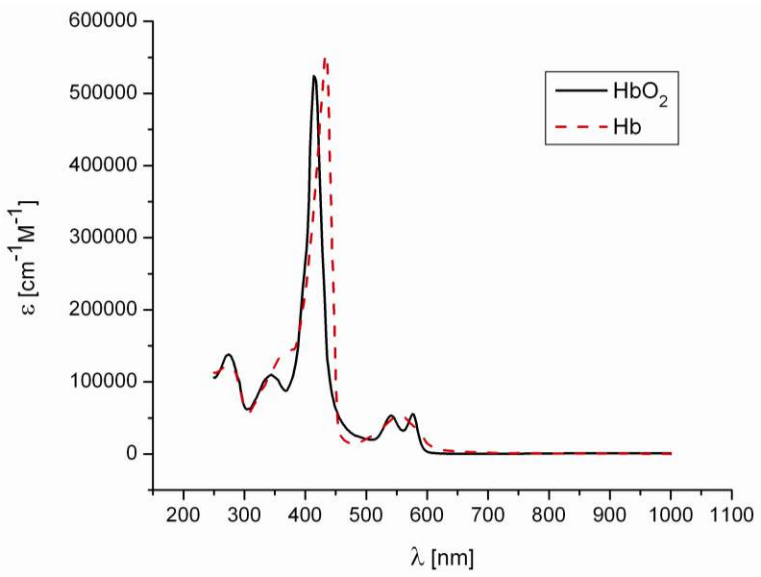


**Figure 4.22** Absorption of oxyhemoglobin ($HbO_2$) and deoxyhemoglobin (Hb) in units of molar extinction coefficient [$cm^{-1}$ $M^{-1}$].

The spectra shown are from Prahl[135]. The oxygen content of hemoglobin can be quantified by the oxygen saturation, which is defined as

$$SO_2 = \frac{[HbO_2]}{[Hb]+[HbO_2]}, \tag{4.35}$$

where $[HbO_2]$ is the concentration of oxyhemoglobin and $[Hb]$ is the concentration of deoxyhemoglobin.

The scattering spectrum used for these simulations is given by

$$\mu_s(\lambda) = a\left(\lambda / \lambda_0\right)^{-b}, \tag{4.36}$$

where $\lambda_0$ = 600 nm and $b$ = -2.4 in this case. A constant value of $g$ = 0.85 was used for all simulations.

Simulations were performed at hemoglobin concentrations of 100-200 g/L, with blood volume fraction set to 4% and oxygen saturation ranging from 0 to 1. The value of

*a* in equation 4.36 ranged from 80-120. For each combination of hemoglobin concentration, oxygen saturation, and scatterer concentration, simulations were run at 125 discrete wavelengths ranging from 500-850 nm, with 10,000,000 photon packets launched for each simulation. The wavelength range was split into two distinct regimes for fitting purposes, one ranging from 500-620 nm and the other from 620-850. This was done in order to separate the region where hemoglobin has pronounced absorption features (500-620 nm) from the smoother, lower absorption NIR region. These data were then processed using the fitting algorithm described above. The results of this are shown in Figure 4.23.

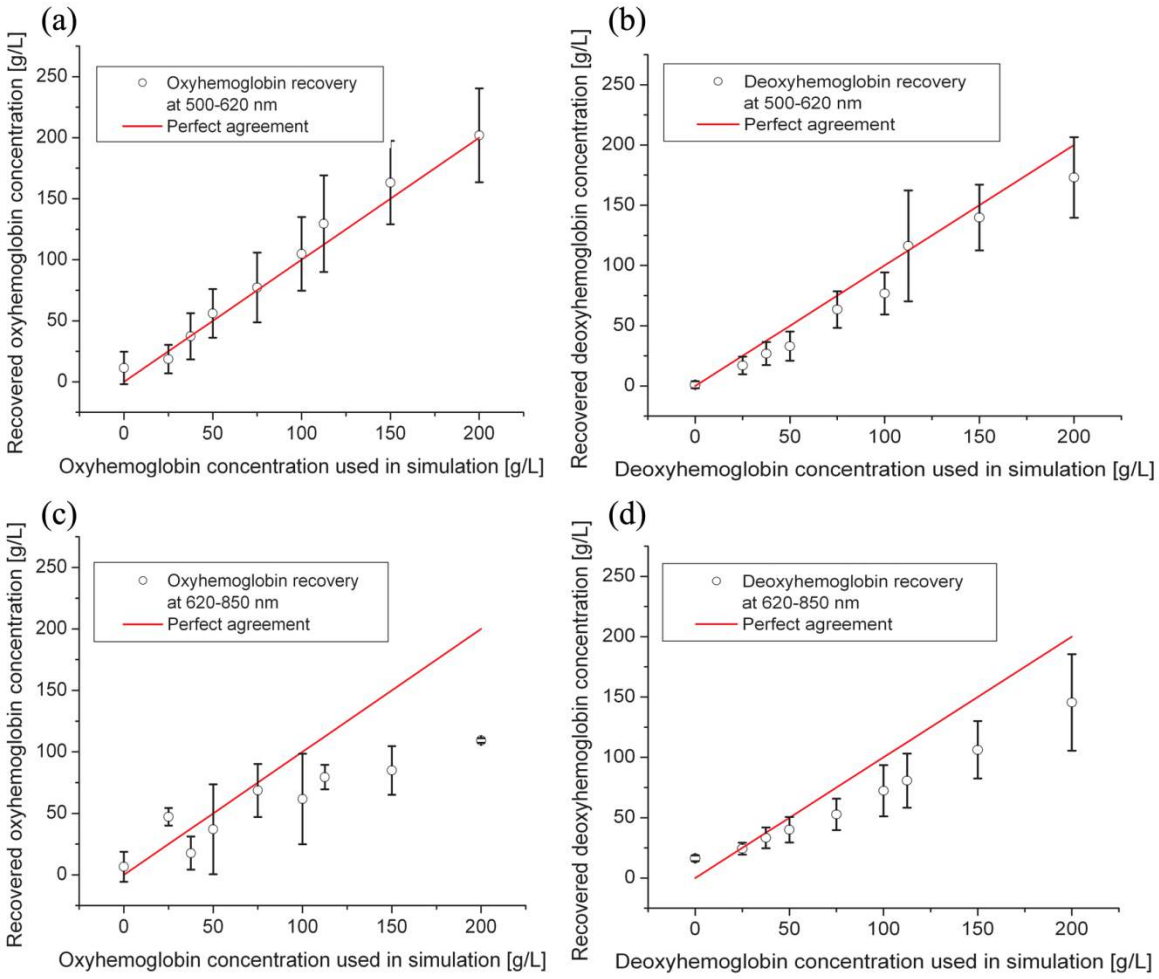


**Figure 4.23** Recovery of (a) oxy- and (b) deoxyhemoglobin concentration from simulations in the wavelength range of 500-620 nm, and (c) oxy- and (d) deoxyhemoglobin concentrations from simulations in the 620-850 nm wavelength regime. Data points represent the mean value over simulations with the same hemoglobin concentration, but varying oxygen saturation and scatterer concentration, while error bars represent standard deviations. Solid lines represent perfect agreement.

Data points are again averages of simulations run with the same value of one parameter, with other parameters varying, and error bars are standard deviations. As can be seen, the algorithm is able to discriminate between oxy- and deoxyhemoglobin well from 500-620 nm, but the fitting is poorer in the NIR regime. This appears to be due to the lower scattering present at these longer wavelengths, as shown by equation 4.36. If the value of

*a* in equation 4.36 is increased to 175, the recovery of hemoglobin concentration is improved in the NIR region, as shown in Figure 4.24. This loss of sensitivity at lower scattering coefficients is a limitation of the algorithm/probe combination, and will be discussed further in section 4.4.5. Determination of oxygen saturation is shown in Figure 4.25.

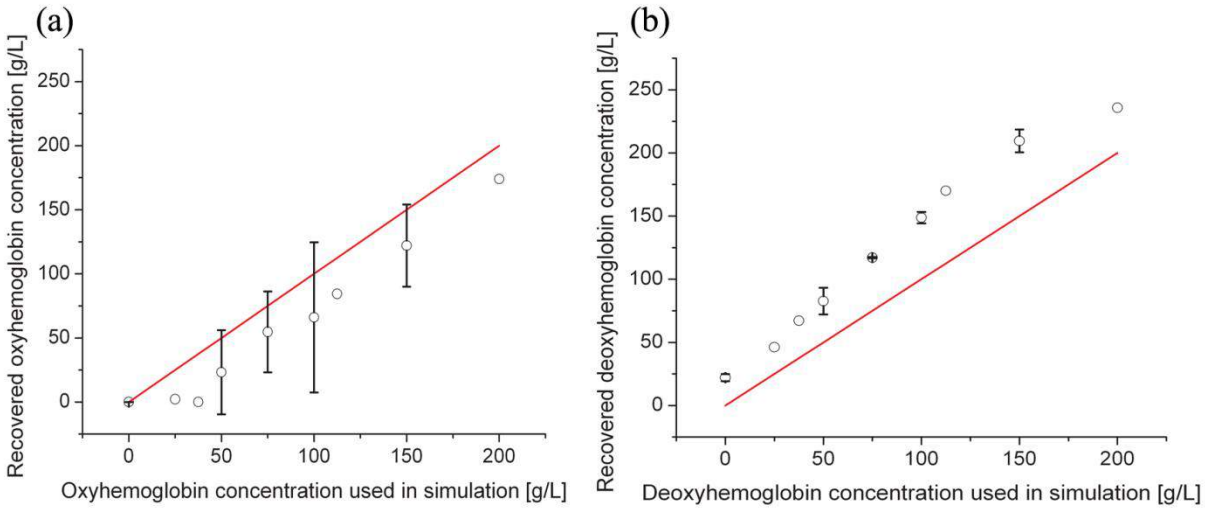


**Figure 4.24** Recovery of (a) oxy- and (b) deoxyhemoglobin concentration from simulations performed in the 620-850 nm region with the value of *a* in equation 4.36 increased to 175. Data points represent the mean value over simulations with the same hemoglobin concentration, but varying oxygen saturation and scatterer concentration, while error bars represent standard deviations. Solid lines represent perfect agreement.

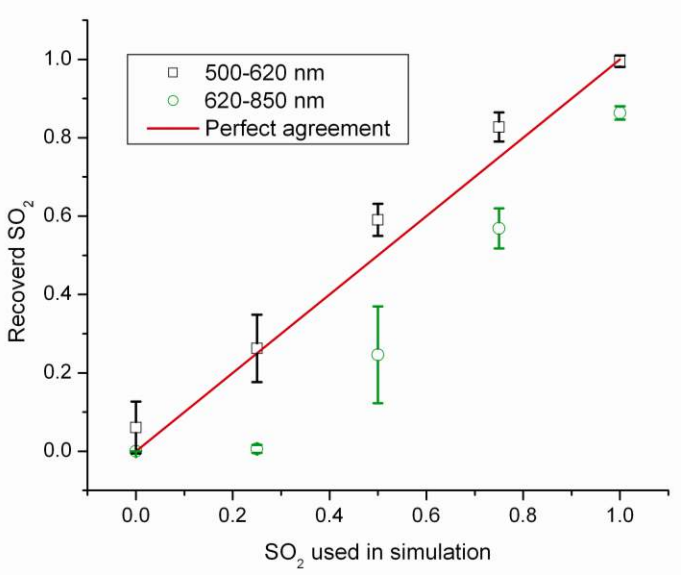


**Figure 4.25** Recovery of oxygen saturation from simulations in the 500-620 (□) and 620-850 (○) nm regions. Data points represent average values over simulations performed at the same oxygen saturation, but with varying values of hemoglobin and scatterer concentration, while error bars represent standard deviation. The solid line represents perfect agreement.

As can be seen, recovery is more accurate for the 500-620 nm regime, with mean error of 8.4% and maximum error of 18%. The recovery is less accurate in the 620-850 nm region, with mean error of 46%. This is likely due to the presence of strong, distinct hemoglobin absorption features in the 500-620 nm region, which makes separation of absorbers more straightforward.

### 4.4.4 Experimental verification

In order to verify the results obtained in simulations, measurements were performed in tissue-simulating phantoms using the system shown in Figure 4.12. These phantoms consisted of Intralipid-20% (Baxter Healthcare Corporation, Deerfield, IL) as a scatterer, and either MnTPPS (Porphyrin Products, Logan, UT) or intact human erythrocytes as absorbers. For MnTPPS phantoms, the solvent was deionized water and MnTPPS was

added to achieve concentrations of 10-50 μM. This was done by creating a stock solution of 10 mg/mL MnTPPS in deionized water, and adding the appropriate amount to 1 L of deionized water in order to achieve the desired concentration.

For phantoms containing intact human erythrocytes, whole blood was drawn from healthy, non-smoking volunteers. Blood was drawn into tubes containing sodium heparin in order to prevent clotting. The blood was transferred to centrifuge tubes, and an amount of phosphate buffered saline (PBS, Life Technologies, Grand Island, NY) at pH 7.4 equal to the blood volume was added. These were then centrifuged at 2500 rpm for five minutes. The supernatant was aspirated and the blood re-suspended in PBS, and this process was repeated until the supernatant was clear. After the clear supernatant was aspirated, approximately 1 mm of the erythrocyte layer was also removed in order to ensure removal of the white blood cells. This is vital, as white blood cells rapidly consume oxygen, which would lead to the phantom quickly becoming de-oxygenated. The remaining erythrocytes were refrigerated until use.

Basis spectra for each of the absorbers and Intralipid were generated using a commercial spectrophotometer (Varian 50 Bio, Palo Alto, CA). For the Intralipid basis, Intralipid-20% was diluted to a concentration of $10^{-6}$ mL/L and the spectrum measured in a 1 cm cuvette. Assuming negligible absorption, the optical density (OD) reported by the spectrophotometer was directly converted to a scattering spectrum. This scattering spectrum was found to agree with that of van Staveren *et al*[134], which is given in equation 4.33. The MnTPPS spectrum was found by measuring MnTPPS in deionized water at a concentration of 25 μM, and averaging the results of multiple measurements in

order to improve the signal-to-noise ratio. The spectra for oxy- and deoxyhemoglobin were obtained from Prahl[135].

For each phantom experiment, 1 L of the proper solvent (deionized water for MnTPPS phantoms and PBS for erythrocyte phantoms) and the chosen amount of Intralipid-20% were added to a 3 L container that had been spray painted black (Krylon Ultra-Flat Black, Sherwin-Williams Comopany, Solon, OH). The solution was stirred continuously during the experiment using a stir plate and a stir bar that had also been spray painted black. The probe shown in figure 4.11 was then submerged in the phantom such that the most proximal spectroscopy fiber was 3 cm below the surface. This depth was chosen to ensure that all spectroscopy fibers were sufficiently far from both the bottom of the container and the surface of the phantom, so that measurements could be treated as having been made in an infinite homogeneous medium, as was done in simulations. For MnTPPS phantoms, MnTPPS was added incrementally.

For erythrocyte phantoms, the desired amount of Intralipid was added to PBS, and the mixture was heated to 37 ºC while stirring. Since the hemoglobin-oxygen dissociation kinetics are temperature dependent, a constant temperature that corresponded to human body temperature was required during experiments. Temperature was monitored continuously using a digital thermometer and was found to vary by at most 1.5 ºC.

The oxygen partial pressure of the phantom was also monitored, using an oxygen-sensitive microelectrode (Microelectrodes Inc., Londonberry, NH). The microelectrode was calibrated using two points, air-saturation and total deoxygenation. The air-saturated

point was obtained by allowing the electrode to rest in air for 15 minutes, and noting its steady-state output voltage. The deoxygenated point was obtained by submerging the electrode in PBS, and adding $Na_2S_2O_4$. A linear response between the two calibration points was assumed, allowing for conversion of electrode voltage to oxygen partial pressure. The partial pressure was recorded at the time of each measurement made in phantom.

Erythrocytes were added to the phantom at a volume fraction of 1.6%. This is based on assumption of a 4% blood volume fraction and a hematocrit of 40%. Phantoms were deoxygenated by addition of approximately 1 g of dry baker's yeast, with total deoxygenation being achieved over a period of 20-30 minutes. At each measurement, both the phantom temperature and oxygen partial pressure were recorded.

At each increment, a spectroscopic measurement was made using fiber 1 of the probe as a source. Broadband light from a tungsten-halogen lamp (Avantes, Broomfield, CO) was delivered by fiber 1, and light was sequentially detected by fibers 2-5 using a cascade of optical switches (Piezosystem Jena, Hopedale, MA). The light from each detection fiber was routed to a TE-cooled, 16-bit spectrometer (B&W Tek, Newark, DE), and the integration time was adjusted to maximize usage of the spectrometer's dynamic range. Integration times ranged from 12-30 seconds for each detector fiber, with a total collection time of approximately one minute.

Measured spectra were background subtracted and corrected for the effects of wavelength-dependent system response and fiber throughput. The background was determined by making dark measurements with the same integration time as the light

measurement. The system response was determined by inserting the probe into a 6" integrating sphere (Labsphere, North Sutton, NH) and illuminating with fiber 1. Spectra were then detected at each of the detection fibers, with a dark background being subtracted from each. Since the lamp spectrum is known and the integrating sphere has spectrally flat reflectance in this wavelength regime, the detected signal is taken to be a result of system response. In order to determine the throughput of the individual detection fibers, the probe was inserted into a 6" integrating sphere, this time with a baffle between the probe and the sphere's detector port. A stable calibration lamp and power supply (LPS-100-167, Labsphere) were used to illuminate the sphere through the baffled detector port, providing uniform radiance. Spectra were then measured at each of the detection fibers. Given the stable power output of the calibration lamp, the differences in detected power were assumed to be due to differences in the throughputs of individual detection fibers. All other measured spectra were divided by these throughput values in order to ensure that spectra detected by different fibers were on the same scale.

For MnTPPS phantoms, three sets of experiments were performed at Intralipid-20% concentrations of 55, 75, and 90 mL/L. At each scatterer concentration, MnTPPS was added to achieve four concentrations from 10-50 μM. Typical spectra collected in such an experiment are shown in Figure 4.26.

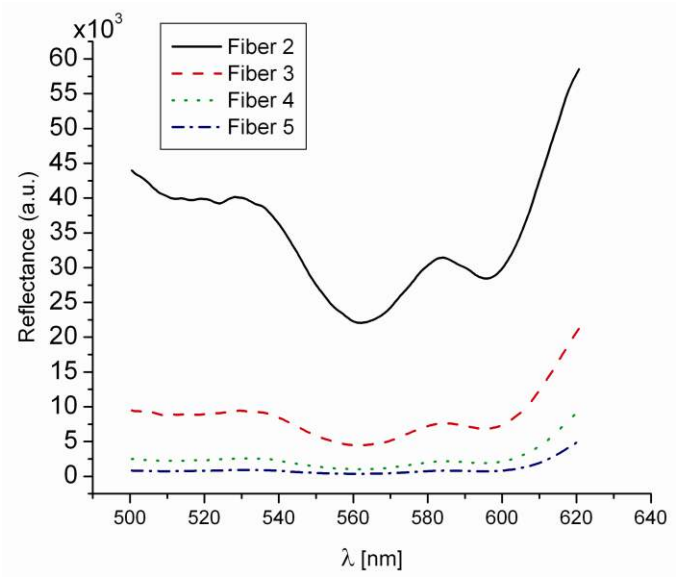


**Figure 4.26** Measured reflectance spectra, corrected for dark background, system response, and fiber throughput, in a phantom consisting of 1 L of deionized water, 40 mL of Intralipid-20%, and 280 µL of 10 mg/mL MnTPPS.

These spectra have been background subtracted, and corrected for the effects of system response and fiber throughput, as specified previously.

The spectra were then processed using the fitting algorithm described in section 4.4.2. In the first step, equation 4.28 was fit to the spatially-resolved reflectance at each wavelength, as shown in Figure 4.27a.

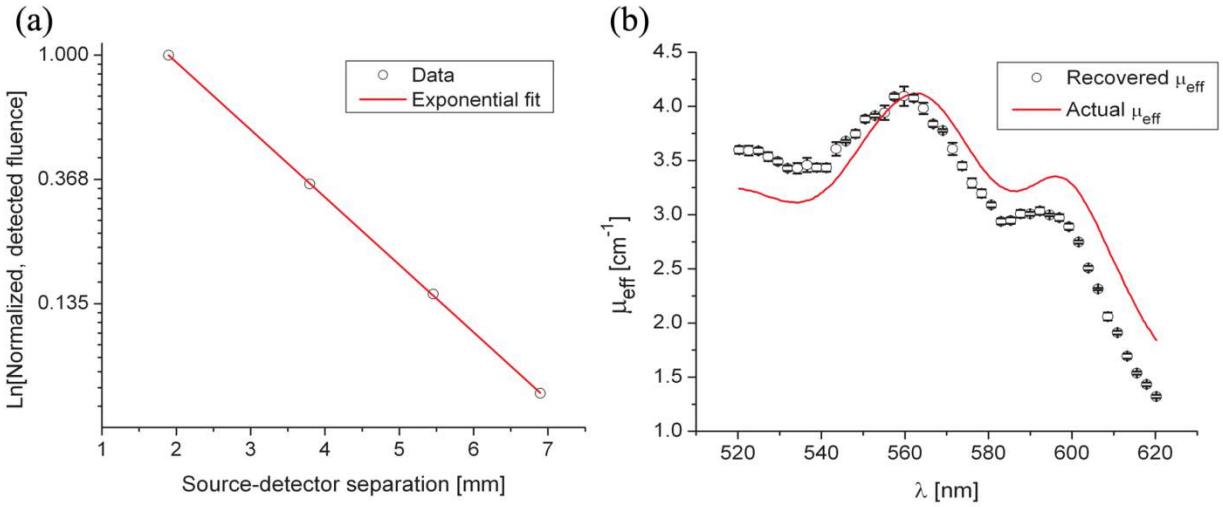


**Figure 4.27** Step 1 of optical property fitting algorithm for a phantom with a MnTPPS concentration of 12.5 μM and an Intralipid-20% concentration of 55 mL/L. (a) Fitting of φ(r) with equation 4.28, shown on a log scale, at λ = 520 nm (b) Recovered $\mu_{eff}$ values (○) found using the scheme shown in Figure 4.14. Error bars represent standard deviations over three repeated measurements of the same phantom. The actual $\mu_{eff}$ spectrum is derived from the known concentrations of MnTPPS and Intralipid.

The values of α found at each wavelength were then converted to $\mu_{eff}$, as shown in Figure 4.14. This resulted in a $\mu_{eff}$ such as the one shown in Figure 4.27b. The open circles represent fitted $\mu_{eff}$ values, and the solid line is the calculated $\mu_{eff}$ based on the known optical properties of the phantom. As can be seen, the $\mu_{eff}$ spectrum is recovered fairly well, with an average error of 10.3%.

In the second step of the fitting process, the $\mu_{eff}$ values found in step 1 are used to constrain a fit to the simulation library given by equation 4.29. This results in plots such as those shown in Figure 4.28, which are used to find the optical properties at each wavelength.

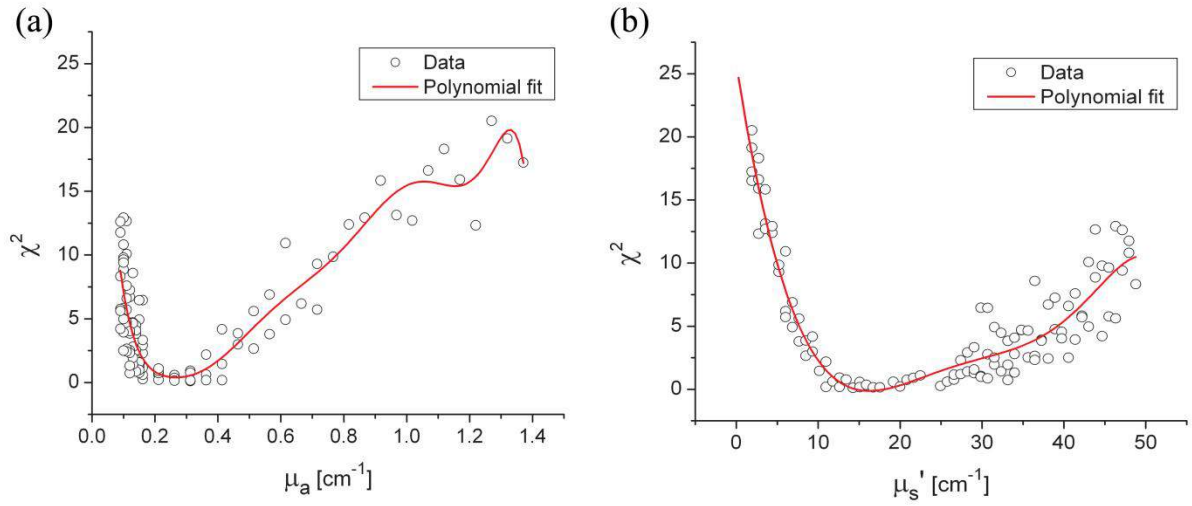


**Figure 4.28** Determination of (a) $\mu_a$ and (b) $\mu_s'$ from constrained minimization of equation 4.29 at $\lambda = 520$ nm for the same phantom as in Figure 4.27. Open circles represent $\chi^2$ values for valid combinations of $\mu_a$ and $\mu_s'$ in the simulation library compared to the measured data, while solid lines represent a seventh-order polynomial fit to these data.

This results in optical property spectra such as those shown in Figure 4.29.

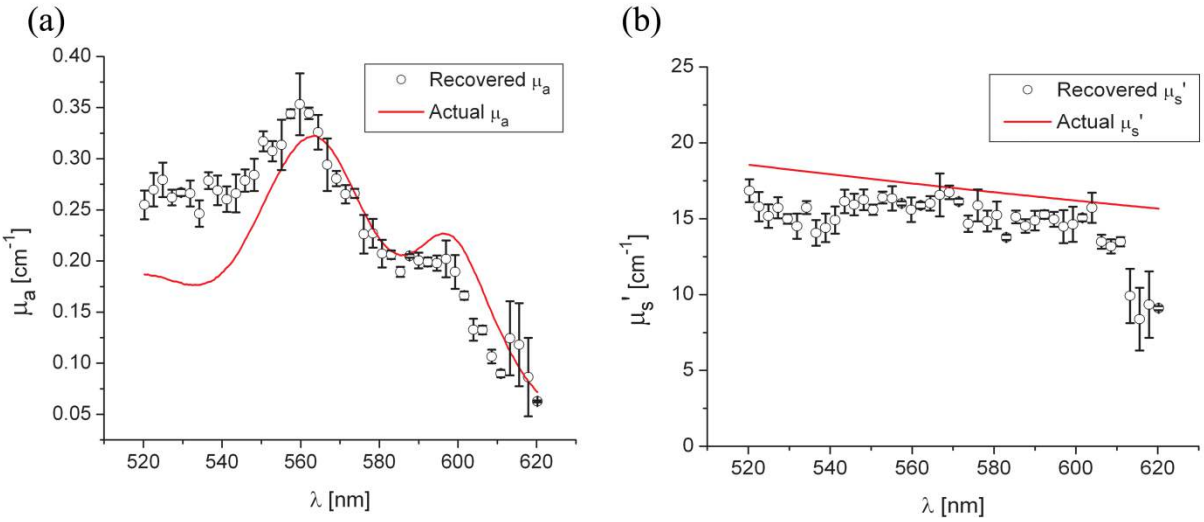


**Figure 4.29** Recovery of (a) $\mu_a$ and (b) $\mu_s'$ from measurements of the tissue-simulating phantom from Figure 4.27 and Figure 4.28. Fitting was performed by minimization of equation 4.29, constrained by the $\mu_{eff}$ spectrum shown in Figure 4.27b.

In this case, error bars are standard deviations over repeated measurements of the same phantom.

In the final step of the fitting algorithm, spectra are fitted with the absorber and scatterer spectral shapes. The results of this are shown in Figure 4.30.

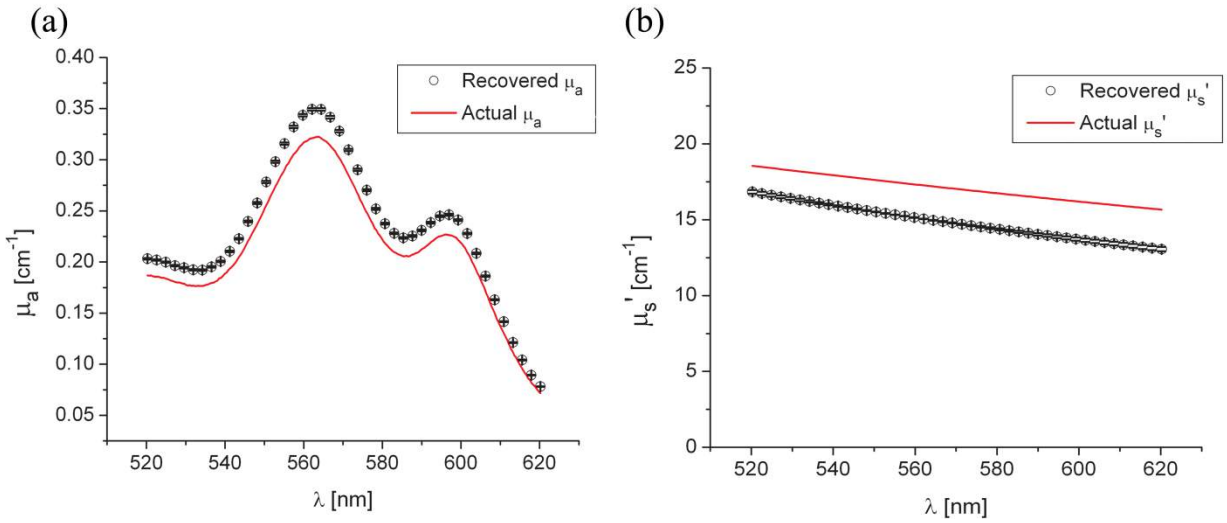


**Figure 4.30** Results of fitting the (a) $\mu_a$ and (b) $\mu_s'$ spectra shown in Figure 4.29 with the known shape of the absorption spectrum and the known form of the scattering spectrum.

Here, the open circles represent recovered optical properties and the solid lines represent known optical properties of the phantom. As can be seen, the recovery of $\mu_a$ is good, with a mean error of 8.8%. The recovery of $\mu_s'$ is also good, with a mean error of 13.3%.

The results of the three sets of MnTPPS phantom experiments are summarized in Figure 4.31. Each experiment corresponds to one particular scatterer concentration, with measurements made at four MnTPPS concentrations for each.

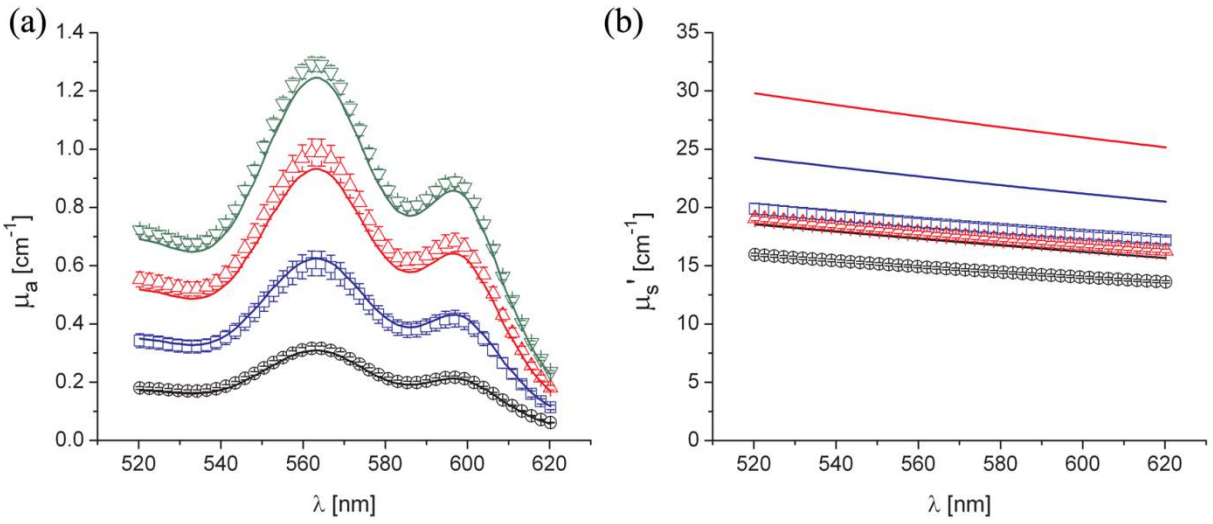


**Figure 4.31** Combined results of (a) $\mu_a$ and (b) $\mu_s'$ recovery for all three sets of experiments. Data points shown in (a) are averages over measurements made in three phantoms with varying Intralipid concentration, at MnTPPS concentrations of 12.5 μM (○, black), 25 μM (□, blue), 37.5 μM (Δ, red), and 50 μM (∇, green). Solid lines of the same color as the symbols correspond to known absorption spectra for the given MnTPPS concentrations. Data points in (b) correspond to averages over measurements made in three phantoms at Intralipid concentrations of 55 (○, black), 75 (□, blue), and 90 mL/L (Δ, red), at four MnTPPS concentrations. The solid lines of the same color as the symbols represent the known scattering spectrum for each of the three phantoms.

In Figure 4.31a, data points are averages over all three sets of experiments for the given MnTPPS concentrations, with error bars corresponding to standard deviation. Measurements were made at MnTPPS concentrations of 12.5 μM (○, black), 25 μM (□, blue), 37.5 μM (Δ, red), and 50 μM (∇, green), for each of the three scatterer concentrations. For Figure 4.31b, data points are averages over a particular experiment at a given scatterer concentration for all values of MnTPPS concentration, with error bars corresponding to standard deviation. Measurements were made at Intralipid concentrations of 55 (○, black), 75 (□, blue), and 90 mL/L (Δ, red), with four MnTPPS concentrations examined for each experiment. As can be seen, the fitting of $\mu_a$ is

consistently good, with a mean error of 9.0% and a maximum error of 38%. The fitting of $\mu_s'$ is poorer, with a mean error of 19% and a max error of 48%.

The same procedure was repeated for phantoms containing intact human erythrocytes. Typical fitted $\mu_a$ spectra are shown in Figure 4.32 for the case of fully oxygenated and fully deoxygenated hemoglobin phantoms.

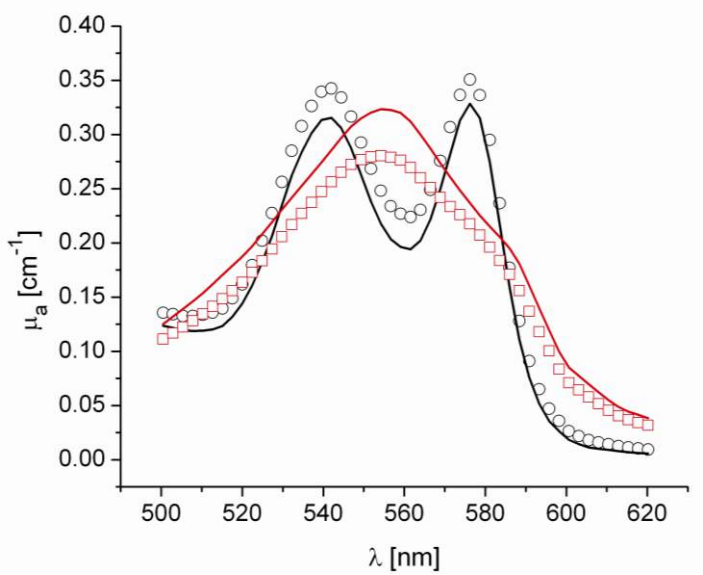


**Figure 4.32** Recovered $\mu_a$ spectra for phantom measurements with fully oxygenated (○) and fully deoxygenated (□) hemoglobin. Solid lines represent the known $\mu_a$ spectrum given the known hemoglobin concentration and oxygen saturation.

As can be seen, spectra from both oxy- and deoxyhemoglobin can be recovered from measurements made in phantoms. The algorithm tends to slightly overestimate the absorption of oxyhemoglobin, and underestimate the absorption of deoxyhemoglobin.

In addition to full oxygenation and deoxygenation, cases in which there are contributions from both oxy- and deoxyhemoglobin are interesting. The ability of the algorithm to separate the contributions of both species of hemoglobin can be assessed by examining the recovery of $SO_2$. This is shown in Figure 4.33.

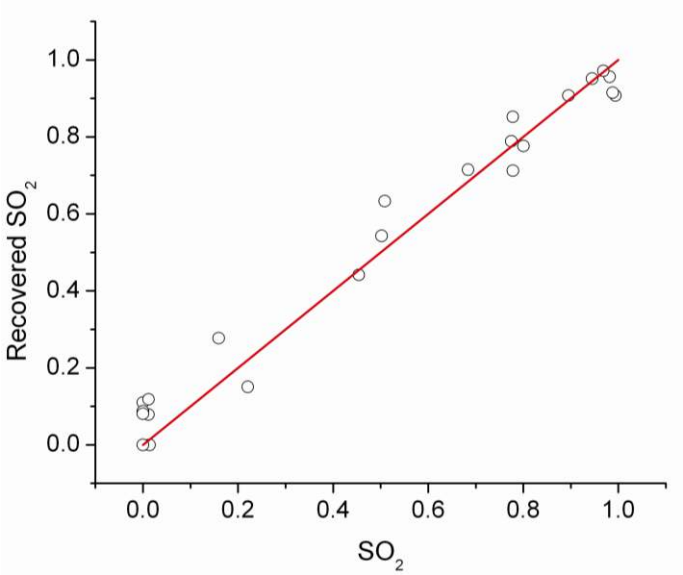


**Figure 4.33** Recovery of $SO_2$ from measurements made in phantoms containing erythrocytes. Each data point corresponds to a measurement made in a phantom at a particular oxygenation. The solid line represents perfect agreement.

$SO_2$ values are recovered well, with a mean error of 12% and a max error of 73%. As mentioned previously, the algorithm tends to overfit the contribution of oxyhemoglobin, so $SO_2$ values are slightly skewed high in the recovery. This also results in larger errors at smaller values of $SO_2$, which is the cause of the reported 73% maximum error for fully deoxygenated hemoglobin.

The measured oxygen partial pressure and $SO_2$ are related through the Hill equation, given by

$$SO_2 = \frac{pO_2^n}{pO_2^n + p50^n}, \tag{4.37}$$

where $pO_2$ is the measured oxygen partial pressure, $p50$ is the partial pressure at which hemoglobin in 50% saturated, and $n$ is a parameter known as the Hill coefficient[136]. Since we obtain $SO_2$ from spectral fitting, we can determine the values of these

coefficients by fitting equation 4.37 to the measured data. This is shown for the case of a single phantom in Figure 4.34.

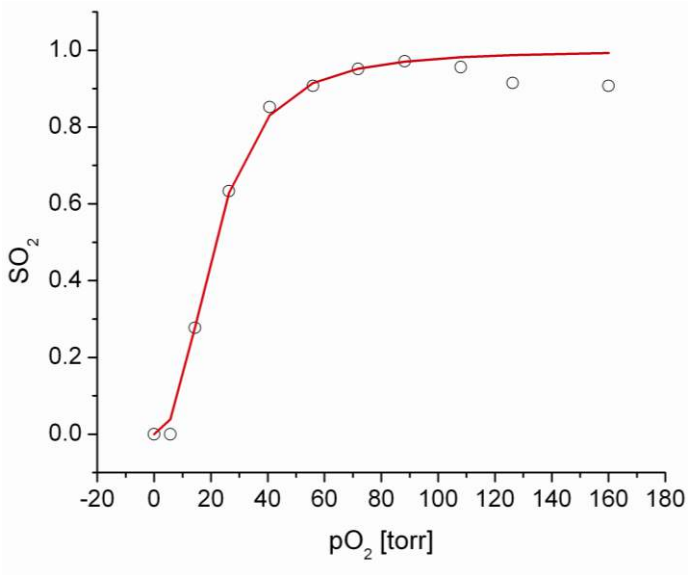


**Figure 4.34** Recovered $SO_2$ values (○) as a function of measured $pO_2$ for a single phantom, with the corresponding fit (solid line) to equation 4.37. This fit yielded values of *p50* = 21.9 and *n* = 2.44.

In this case, the parameters in equation 4.37 were found to be *p50* = 21.9 torr and *n* = 2.4. For all phantom measurements combined, these values were found to be 32.3±10 torr and 2.3±0.4. These values are close to the typical values of *p50* = 26 torr and *n* = 2.8, although the recovered *p50* are on average 24% higher than the frequently reported value of 26 torr.

### 4.4.5 Discussion

There have been many studies done on the recovery of optical properties from spatially-resolved diffuse reflectance spectroscopy. Here we present a method that utilizes a single encapsulated optical probe, and is capable of recovering optical properties over a wide range of absorption and scattering coefficients. The technique has been shown to be

valid to transport albedos as low as 0.95, which is a larger range than for the diffusion approximation. We have demonstrated recovery of $\mu_a$ with a mean error of 9% and $\mu_s'$ recovery with a mean error of 19%, which are comparable to errors found in previous studies of interstitial optical property recovery. Wang and Zhu demonstrated the recovery of interstitial optical properties using multiple isotropic detectors and a diffusion model[40]. In simulations, they were able to recover $\mu_a$ with an error of 16% and $\mu_s'$ with an error of 4%. They report the recovery of interstitial optical properties *in vivo*, but do not comment on the accuracy of the reconstruction. Chin *et al* performed recovery of optical properties using relative interstitial steady-state reflectance measurements[137]. Their method resulted in recovery of optical properties to within ~20% for measurements made in tissue-simulating phantoms containing Intralipid and Naphthol Green. Dimofte *et al* also reported a method for the determination of interstitial optical properties using point measurements made in a linear channel at a fixed distance from a point source[41]. Using a diffusion approximation, they demonstrated recovery of $\mu_a$ and $\mu_s'$ with mean errors of 8% and 18%, respectively. The errors we demonstrate for our method are comparable to these values, and are better in some cases.

A number of studies have also examined optical property recovery in the context of hemoglobin spectroscopy. Here we demonstrated recovery of $SO_2$ with an average error of 12%, and were able to recover reasonable values for the Hill parameters. Hemoglobin oxygen dynamics have been studied extensively using spatially resolved diffuse reflectance measurements made with surface-contact probes. Previous studies performed in our laboratory have demonstrated accurate recovery of $SO_2$, and have also

demonstrated recovery of the parameters in the Hill equation[99, 101]. Due to the direct applicability of analytical methods to the surface-contact geometry, these studies showed more rigorous recovery of $SO_2$ and the Hill parameters. In the case of interstitial spectroscopy, there have been fewer quantitative studies done of hemoglobin oxygen dynamics. Thompson *et al* demonstrated interstitial measurements of $SO_2$ during PDT of nodular basal cell carcinoma, with the value varying widely between patients[138]. However, they do not provide any pre-clinical evaluation of the accuracy of this recovery. Yu *et al* also demonstrated interstitial recovery of $SO_2$ and total hemoglobin concentration during motexafin lutetium PDT of the prostate[16]. They found that both values decreased during PDT. Kruijt *et al* described a similar trend in a mouse model during m-THPC PDT, using multiple isotropic probes[139]. Most of these techniques require the insertion of multiple spectroscopy fibers, which can be unattractive in certain clinical situations.

As previously mentioned, our algorithm is only valid for certain ranges of optical properties. We have not found any limits on the recovery of $\mu_a$, but the valid $\mu_s'$ range only extends over a particular range. This places limits on the values of $\mu_{eff}$ that can be recovered, due to the dependence of $\mu_{eff}$ on $\mu_s'$. This is illustrated in Figure 4.35.

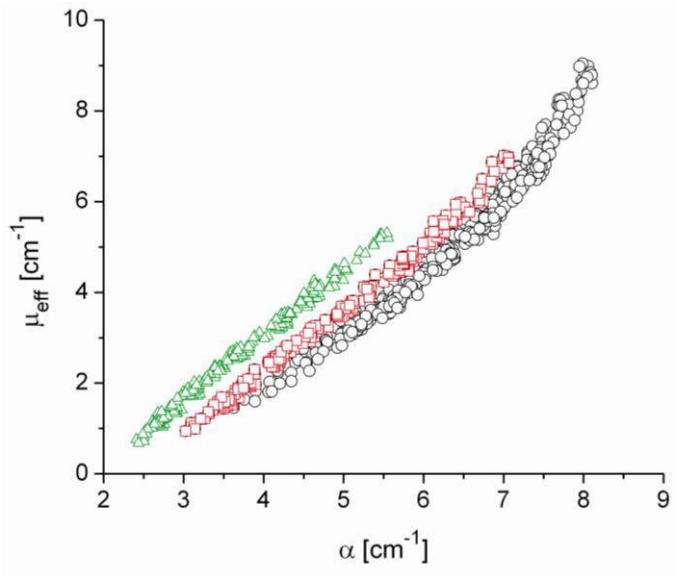


**Figure 4.35** Relationship between α and $\mu_{eff}$ for the range of scattering coefficients used in the simulation library (○), and for scattering spectra using values of 40 (□) and 20 (Δ) for *a* in equation 4.36.

As can be seen in the figure, the relationship between α and $\mu_{eff}$ described in section 4.4.2 only holds for values of $\mu_s'$ ranging from approximately 10-30 $cm^{-1}$. The open circles shown in Figure 4.35 correspond to simulations using scattering spectra with values of *a* in equation 4.36 ranging from 60-100. These were the simulations used to generate the relationship used in step one of the fitting algorithm. The other plots shown correspond to simulations run with lower values of *a* in the scattering spectrum. It is evident that the relation between α and $\mu_{eff}$ does not hold for this range of scattering coefficients.

We hypothesize that this limitation is due to the geometry of the probe and the assumptions made in step one of the fitting algorithm. Since each of the spectroscopy fibers is in a different position and orientation on the probe, some amount of scattering is required to ensure that adequate signal is detected at each of the fibers. From the simulations shown in Figure 4.35 we have determined that the technique presented here

requires a transport albedo higher than approximately 0.95, with the experiments shown having values of *a*' ranging from 0.94-0.998. This allows for recovery of a wider range of optical properties than methods using the diffusion approximation, which generally require a transport albedo of at least 0.98[115]. However, other methods such as the $P_3$ approximation allow reconstruction of much lower transport albedos, as described previously in this chapter.

In addition to the limitation on low scattering coefficients, our method also does not work well for very high scattering coefficients. This is due to the assumption of a single radial separation *r* between fibers in equation 4.28. At reasonable scattering coefficients, this assumption is valid, as photons tend to follow roughly the same path from source to detector. At higher scattering coefficients, photons can travel in both directions (i.e. clockwise and counterclockwise) around the probe from source to detector. This results in the same source-detector having multiple possible values of *r* along the surface of the probe, which causes equation 4.28 to be fit poorly.

Much of the time, we wish to know the optical properties of tissue so that we can determine the light dose that will be delivered to this tissue by a given PDT treatment. It is therefore important to consider the effects that error in recovered optical properties will have on the expected fluence distribution in tissue. To examine this, we consider the case of a 2 cm cylindrical diffusing fiber delivering a light dose of 100 J/cm embedded in tumor tissue with $\mu_{\mathbf{a}} = 0.2$ cm$^{-1}$ and $\mu_s' = 10$ cm$^{-1}$. For the true optical properties, MC simulations tell us that the characteristic light propagation distance $\delta$ will have a value of 4.1 mm. If we introduce errors in $\mu_a$ and $\mu_s'$ similar to those obtainable by our method,

the value of $\delta$ is changed to 3.7 mm. Therefore, a 9% error in $\mu_a$ and a 19% error in $\mu_s'$ lead to a 9.8% error in $\delta$.

As described previously in this section, the probe design used introduces some limitations on the ranges of optical properties that can be recovered. It is therefore interesting to think about future probe designs that could improve the robustness of the optical property recovery. One design that we have considered involves the creation of a cylindrical probe with a flat face into which spectroscopy fibers would be embedded, as shown in Figure 4.36.

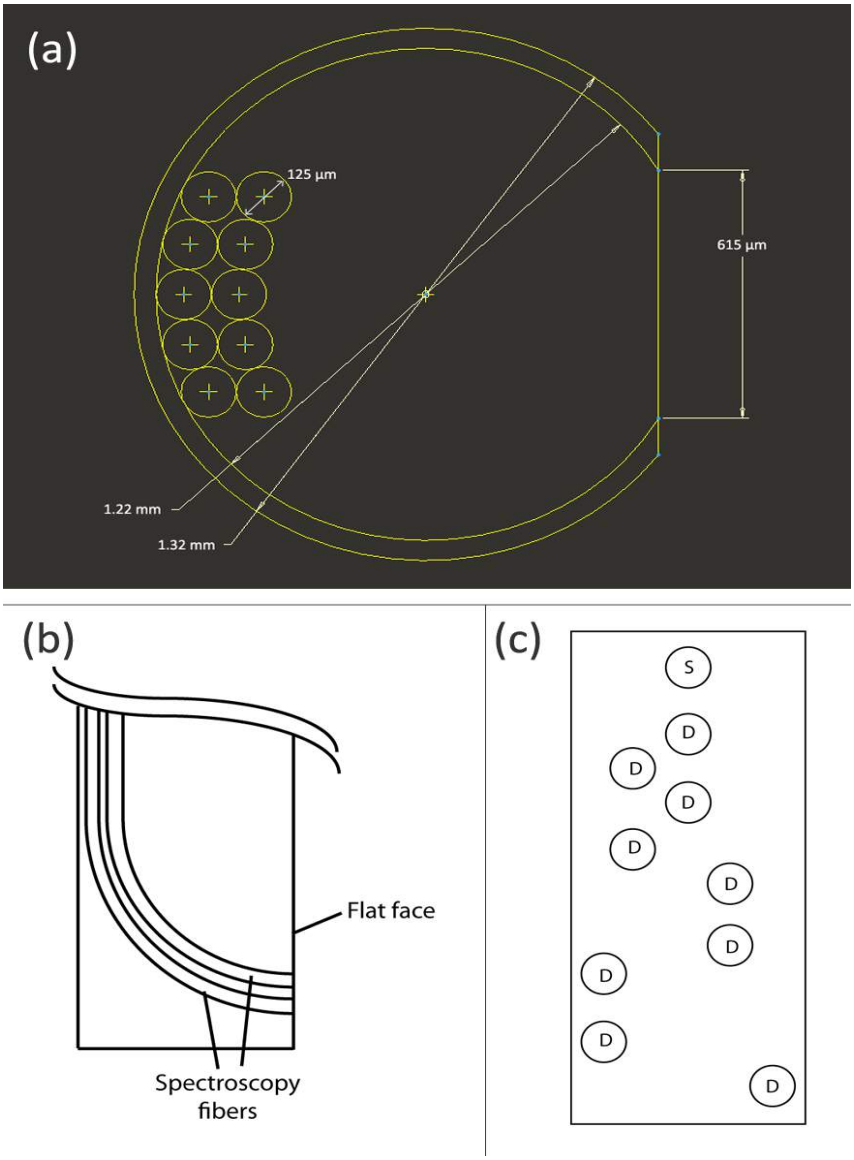


**Figure 4.36** (a) Cross-section of the proposed probe, illustrating the 125 µm spectroscopy fibers, 1.22 mm core region, 1.32 mm outside diameter, and flat face for embedding of spectroscopy fibers. (b) Side view of the design, showing the bend of the spectroscopy fibers. (c) Illustration of the flat face, showing the arrangement of the source and detector fibers (not drawn to scale).

The probe design consists of ten 125 µm diameter fibers encapsulated in a 1.22 mm clear epoxy core, surrounded by a 50 µm thick cladding. Each of the ten fibers is bent such that the distal end is flush with a face of the probe that is ground flat, with one fiber

designed to deliver light while the others detect. This design avoids some of the difficulties presented by the current probe design. First, the spectroscopy fibers are all pointed in the same direction. This reduces the probability of photons having multiple preferred paths around the probe, which complicates approximations that rely on the assumption of a unique radial separation between source and detector. This design also allows for the detector fibers to be closer to the source fiber. In the current probe design, the shortest source-detector separation is 1.9 mm, while the longest is 6.9 mm. For the design shown in Figure 4.36, source-detector separations range from 0.25-10 mm. This improved coverage of radial space could allow for the direct application of analytical approximations such as $P_3$ to measured data.

This speculative design would require the use of novel fibers in order to achieve the desired outside diameter of 1.32 mm, which would allow the probe to fit through a 17-gauge biopsy needle. Each fiber would be required to have a very tight bend radius in order to make the 90º turn from the probe axis to the flat face. We propose to use bend-insensitive multi-mode fiber to achieve this. These fibers exhibit much lower loss than traditional optical fiber under tight bend radii, and are not as prone to breakage. Preliminary testing using Corning ClearCurve VSDN optical fiber (Corning Incorporated, Corning, NY) shows approximately 30% transmission of light incident on the fiber at a bend radius of 1.25 mm, with breakage of the fiber occurring at a bend radius of roughly 0.85 mm. These fibers should therefore allow the construction of the design shown in Figure 4.36. It is hypothesized that this design could further improve the accuracy of the optical recovery method outlined in this chapter.

# Chapter 5

# Detection of Fluorescence by Cylindrical Diffusing Fibers

## 5.1 Introduction

A key part of determining the fluence distribution in interstitial PDT involves knowing the optical properties of the regions being treated. These optical properties depend on tissue properties, such as blood volume and oxygenation, as well as photosensitizer absorption. As covered in chapter 4, the values of optical properties are typically determined in a spectroscopic fashion. Most photosensitizers are naturally fluorescent, so fluorescence measurements are often used[19]. In iPDT, this typically involves the insertion of dedicated spectroscopy fibers[44]. This increases clinical complexity and can lead to increased bleeding. In some cases it would therefore be convenient to use the already inserted treatment diffusers for spectroscopic measurements, especially fluorescence measurements. This is especially true for situations in which only a single fiber can be inserted into the desired volume, such as in the treatment of cholangiocarcinoma[12].

In this study[98], we utilized the GPU-accelerated MC model of cylindrical diffusing fibers described in chapter 3. This model was used to simulate the irradiance delivered by these fibers, as well as the generation and detection of fluorescence by them. The simulation of fluorescence detection was particularly interesting, as heterogeneous detection along the length of the fiber was predicted. This heterogeneous detection

sensitivity was experimentally validated using a layered phantom, showing quantitative agreement with simulation.

## 5.2 Methods

### 5.2.1 MC model

The model used in this study was described in section 3.3.1. In addition to the details discussed there, this study also tracked the propagation of fluorescence. Whenever photon weight was absorbed, a fluorescence photon packet with a weight equal to the absorbed weight multiplied by the quantum yield of fluorescence was launched at that location. This fluorescence photon packet was immediately propagated by the above MC methods, but used optical properties specified for the fluorescence emission wavelength. If a fluorescence photon packet struck the fiber core inside the diffuser within the NA of the fiber, the photon was scored as detected fluorescence. The position of its creation was recorded, as was the detected weight. This allowed for the generation of a map of the origins of detected fluorescence photons, as well as what diffuser they were detected by in the case of an array of diffusers. This provided a description of regions that are sampled by spectroscopic measurements performed using the diffuser as a detector.

All simulations were performed on a GeForce GTX 570 GPU (NVIDIA Corporation, Santa Clara, CA), using the CUDA extensions to C. The simulation parameters were stored in shared memory for faster access, while the absorption and detected fluorescence matrices were stored in the global device memory due to their large size. Atomic operations were required to update the absorption or detected fluorescence matrices in order to eliminate race conditions in memory access. The GPU-based code

was found to execute approximately 30x faster than a CPU-based version of the same code.

### 5.2.2 Phantom preparation

In order to validate the MC results, multi-layered phantoms were created. These phantoms consisted of either two or three layers as shown in Figure 5.1.

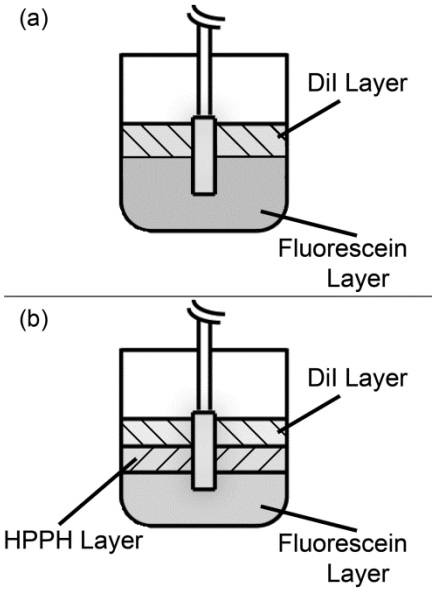


**Figure 5.1** Experimental set-up for measurement of fluorescence in (a) two-layer and (b) three-layer phantoms. The diffuser was inserted such that each layer bordered on an equal length of the diffuser. Only one diffuser is shown for clarity, but experiments used two diffusers inserted in parallel with a separation of 1 cm. One diffuser was used for delivery of an axially homogeneous fluorescence excitation profile, while the other was used for detection of fluorescence. Reproduced from [98].

In both cases, the bottom layer was a solid layer comprised of agar. 500 mg of agar (SELECT Agar®, Invitrogen Corporation, Carlsbad, CA) was added to 50 mL of deionized water and heated to 95º C while stirring. Heat was then removed and the solution was stirred until the temperature fell to 80º C. At this point, 5 mL of 10% Liposyn (Liposyn® II 10%, Abbott Laboratories, Abbott Park, IL), 14.6 µL of India ink

(Higgins No. 4418, Chartpak Incorporated, Leeds, MA), and 36.6 µL of 1 mg/mL fluorescein (Sigma-Aldrich, St. Louis, MO) were added. Stirring continued until the solution reached 60º C, at which point it was refrigerated at 5º C overnight to solidify. The addition of this concentration of Liposyn provides a scattering coefficient of ~90 $cm^{-1}$ at 488 nm[134]. Assuming a scattering anisotropy of 0.82, this produces a reduced scattering coefficient of 16.5 $cm^{-1}$. To ensure consistency, all phantoms were prepared from the same bottle of Liposyn. The addition of India ink brings the absorption coefficient to 2 $cm^{-1}$ at 488 nm. The amount of fluorescein added gives a fluorophore concentration of 2 µM. This will be referred to as the fluorescein layer.

For the two layer phantom shown in Figure 5.1a, the top layer was a liquid layer. This layer consisted of 10 mL of octanol (1-octanol, Sigma-Aldrich), 1 mL of 10% Liposyn, 2.8 µL of India ink, and 20.5 µL of 1 mg/mL 1,1'-Dioctadecyl-3,3,3',3'-tetramethylindocarbocyanine perchlorate (DiI) (Sigma-Aldrich). This was again designed to have a reduced scattering coefficient of 16.5 $cm^{-1}$, an absorption coefficient of 2 $cm^{-1}$, and a fluorophore concentration of 2 µM. This will be referred to as the DiI layer.

For the three layer phantom shown in Figure 5.1b, the top layer was the DiI layer and the bottom layer was the fluorescein layer, both of which are described above. The middle layer consisted of 10 mL of 0.9% saline, 1 mL of 10% Liposyn, 3.06 µL of India ink, and 110.4 µL of 201.3 µM 2-[1-hexyloxyethyl]-2-devinyl pyropheophorbide-a (HPPH) dissolved in 1% Tween/phosphate buffered saline (PBS). HPPH is a second generation photosensitizer[140] that is also fluorescent. It was prepared for us by

Ravindra Pandey at Roswell Park Cancer Institute in Buffalo, NY using the procedure described in Pandey *et al* [141]. This will be referred to as the HPPH layer.

Before use, each of the two liquid layers was stirred vigorously and poured on top of the fluorescein layer. Due to the immiscibility of octanol and saline solution, the DiI and HPPH layers remained distinct. HPPH is hydrophobic, but we dissolved it in Tween/PBS before diluting this solution in 0.9% saline. This keeps the HPPH confined to the saline solution, and we have seen no evidence of HPPH crossing into the DiI layer. Both liquid layers also remained distinct from the solid fluorescein layer.

### 5.2.3 Experimental validation of simulated fluorescence detection by diffusers

For fluorescence measurements two diffusers were inserted parallel into the above phantoms, with a separation of 1 cm. For two layer experiments, two 1-cm diffusers (Pioneer Optics Company, Bloomfield, CT) were inserted 0.5 cm into the fluorescein layer shown in Figure 5.1a. The DiI layer was designed to have a depth of 0.5 cm when poured into a 150 mL flask, which meant that the proximal half of the diffuser was fully in the DiI layer and the distal half was fully in the fluorescein layer. Therefore, any detected DiI fluorescence is known to have been generated along the proximal half of the diffuser, and any detected fluorescein fluorescence is known to have been generated along the distal half of the diffuser.

For three layer experiments, two 1.5-cm diffusers (PhotoGlow Inc, South Yarmouth, MA) were inserted 0.5 cm into the fluorescein layer shown in Figure 5.1b. Both the DiI and HPPH layers were designed to have a depth of 0.5 cm when poured into

a 150 mL flask, which meant that the diffuser length was divided into three equal sections.

In both cases, excitation light at 488 nm was provided by an argon-ion laser (Innova 70, Coherent, Santa Clara, CA), filtered by a band-pass filter (Z488Trans-pc-xr, Chroma Technology Corp, Bellows Falls, VT). Excitation light was delivered at 40 mW/cm for two layer experiments and at 15 mW/cm for three layer experiments. The optical power was lower for three layer experiments due to larger coupling losses in the 1.5 cm diffusers. Optical power was measured using an integrating-sphere-based laser power measurement system (LPMS-060-SF-Si, Labsphere, North Sutton, NH). Excitation light was delivered through one of the diffusers in the experiment, and fluorescence was detected by the other. This was done to ensure homogeneous excitation along the diffuser length, and to minimize the detection of auto-fluorescence generated within the fiber. Light captured by the second diffuser was filtered through a long-pass filter (HQ500LP, Chroma) before being detected by a TE-cooled, 16 bit spectrometer (Compass X, B&W Tek, Newark, DE) using an integration time of 20 seconds.

For calibration purposes, fluorescence spectra were also collected from phantoms consisting of only one of the fluorophore layers. In order to do this, larger volumes of the layers described above were created while maintaining the concentrations of each component. This allowed the diffusers to be fully submerged in each layer.

### 5.2.4 Data correction and spectral fitting

All fluorescence spectra collected were corrected for background and system response. This was done by subtracting a dark measurement from the raw fluorescence

measurement and dividing by a wavelength-dependent system response. Dark measurements were acquired by integrating dark signals for the durations described above. System responses were acquired by placing a single diffuser in the center of an integrating sphere (3P-LPM-060-SF, Labsphere) and shining a NIST-traceable lamp (Model # LS-1-CAL, Ocean Optics, Dunedin, FL) through one of the detection ports on the sphere. The measured spectrum was then background subtracted and divided by the known lamp spectrum to obtain the system response.

After fluorescence spectra were corrected, they were fit using a singular value decomposition (SVD) algorithm based on the work of Press *et al*[74]. Basis spectra for each of the fluorophores were used in the fits. These basis spectra were acquired by measuring the fluorescence emission of each layer in a commercial fluorometer (Varian Eclipse, Palo Alto, CA). In addition to the basis spectra, a series of 61 Fourier terms was also used in fitting to account for unknown possible contributions to the measured fluorescence. These Fourier terms were given a smaller weight in the fitting in order to favor the basis spectra. Fitting followed the SVD scheme found in MATLAB (Mathworks, Natick, MA).

After SVD fitting, the fit magnitudes for each fluorophore were further corrected for absorption and fluorescence yield effects. Each of the three fluorophores used has some absorption at 488 nm, and emits fluorescence beyond 500 nm. However, each fluorophore has different absorption at 488 nm and a different quantum yield of fluorescence. As mentioned previously, fluorescence spectra were acquired for each layer individually. These “pure” measurements were made using the same excitation

wavelength and power as in the layered measurements, and with the same concentrations of scatterer, absorber, and fluorophore. So any differences in absorption at 488 nm or fluorescence quantum yield were also present in the pure measurements. Therefore, any difference in magnitude between the pure and layered measurements was due to the detection capability of the diffuser at the height of the appropriate layer. To account for this, we divide the fit magnitude of the layered measurement by that of the pure measurement. This gives a relative measurement of the detected fluorescence that is weighted for absorption and fluorescence quantum yield.

## 5.3 Results

### 5.3.1 Determination of the scattering coefficient within the diffusive region

As mentioned previously, the scattering coefficient within the diffuser determines the homogeneity of the axial fluence profile at the surface of the diffuser. If the value of $\mu_s$ is too large, most of the light launched from the fiber face will scatter out of the diffuser near the proximal end. If the value is too small, then the scattering out of the diffuser will be weak, which decreases the efficiency of the device. Figure 5.2 shows the simulated degradation in axial fluence profile for a 1 cm diffuser that is induced by use of an improper scattering coefficient.

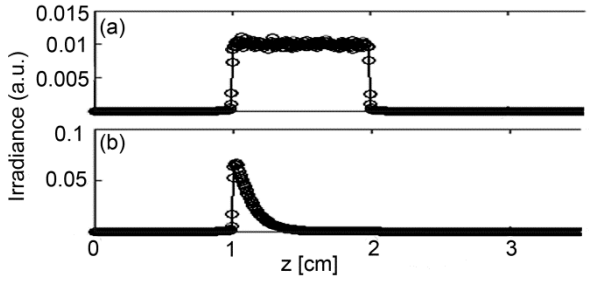


**Figure 5.2** Simulated irradiance profiles along the surface of a 1 cm diffuser, with its proximal end at z = 1 cm, illustrating the effect of changing $\mu_s$. Simulation parameters are identical in both cases except for the value of $\mu_s$ inside the diffusive region, which was (a) 0.2009 $cm^{-1}$ and (b) 10 $cm^{-1}$. Reproduced from [98].

Figure 5.2a shows the homogeneous fluence profile along the surface of a 1 cm diffuser for the determined optimal value of $\mu_s$ = 0.2009 $cm^{-1}$ inside the diffuser. Figure 5.2b shows the effect of raising the value of $\mu_s$ to 10 $cm^{-1}$ within the diffuser, which results in too much light scattering out of the diffuser near the proximal end. The value of $\mu_s$ within the diffuser is therefore crucial to the generation of a homogeneous axial fluence profile.

The optimal $\mu_s$ for homogeneous axial fluence changes with diffuser length. The optimal $\mu_s$ values computed using our MC model for diffuser lengths between 1 and 5 cm are shown in Table 5.1.

| | | | Calculated | Pioneer Diffuser |
|---|---|---|---|---|
| Diffuser Length (cm) | $\mu_s$ (cm $^{-1}$) | N (cm $^{-3}$) | N (ppm) | N (ppm) |
| 1 | 0.2009 | $7.485 \times 10^{17}$ | 99.25 | 100 |
| 1.5 | 0.119 | $4.434 \times 10^{17}$ | 58.75 | - |
| 2 | 0.0821 | $3.059 \times 10^{17}$ | 40.56 | - |
| 3 | 0.0486 | $1.811 \times 10^{17}$ | 24.01 | - |
| 4 | 0.03355 | $1.250 \times 10^{17}$ | 16.57 | - |
| 5 | 0.025 | $9.314 \times 10^{16}$ | 12.35 | 12 |

**Table 5.1** Optimal scattering coefficient ($\mu_s$) for homogeneous irradiance for multiple diffuser lengths, and the corresponding calculated number density of scatterers (N). N is given in units of $cm^{-3}$ and parts per million (ppm) by weight. Number densities in ppm by weight used in commercial diffusers manufactured by Pioneer Optics Company are shown for comparison. Reproduced from [98].

As can be seen, the required $\mu_s$ for homogeneous fluence decreases with increasing diffuser length. This corresponds to a reduced concentration of scatterers through $\mu_s=\sigma N$, where $\sigma$ is the scattering cross-section and N is the number density of scatterers[36]. The scattering cross-section can be calculated using

$$\sigma = \frac{8\pi}{3} k^4 a^6 \left| \frac{n_s^2 - n_m^2}{n_s^2 + 2n_m^2} \right|, \tag{5.1}$$

which is valid for the scatterer size and wavelength we are considering[36]. Here $k$ is the wave vector, $a$ is the scatterer radius, $n_s$ is the index of the scatterer, and $n_m$ is the index of the surrounding medium. The scatterer concentrations in Table 5.1 were calculated using $a$ =14.7 nm, $n_s$=2.488, and $n_m$=1.43. The values calculated for 1 and 5 cm diffusers match those used in commercial diffusers manufactured by Pioneer Optics Company

[142]. Number densities of scatterers were converted to parts per million (PPM) by weight using the known density and volume of the diffusive region and the molecular weight of $TiO_2$.

### 5.3.2 Fluence distributions generated by Monte Carlo model of diffuser

A typical fluence map generated by a 1 cm diffuser is shown in Figure 5.3.

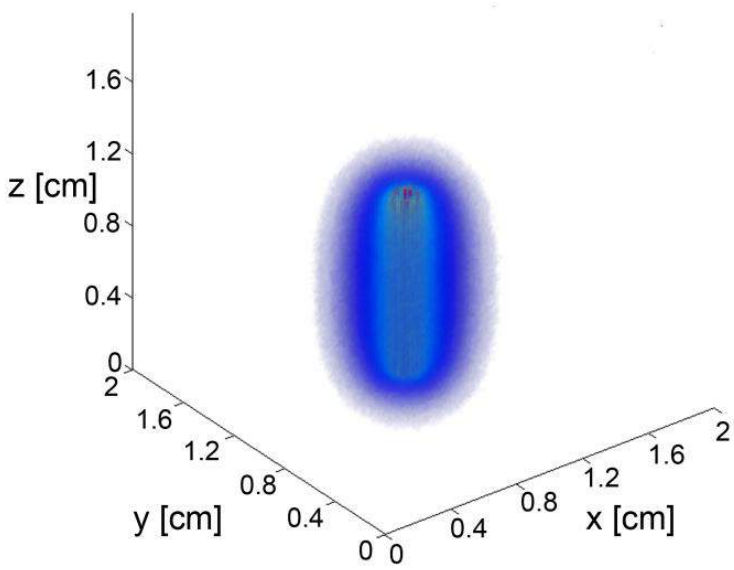


**Figure 5.3** 3D rendering of the fluence distribution around a 1 cm cylindrical diffusing fiber with its proximal end at z = 0.5 cm and an air-tissue boundary at z = 0. Tissue optical properties were set to $\mu_a$ = 2 $cm^{-1}$, $\mu_s$ = 100 $cm^{-1}$, and $g$ = 0.9. Voxel size was 0.02 cm x 0.02 cm x 0.02 cm. Reproduced from [98].

The air-tissue boundary is located at z = 0, and the proximal end of the diffuser is at z = 0.5 cm. For this particular simulation, the tissue sample is homogeneous and semi-infinite with $\mu_a$ = 2 $cm^{-1}$, $\mu_s$ = 100 $cm^{-1}$, $g$ = 0.9, and $n$ = 1.395[143].

In order to compare to a model based on a finite linear array of point sources, the radial distribution of fluence generated by the diffuser was examined for both models. In these simulations we assumed a refractive index of 1.43 for the linear array to match that

of the epoxy in the diffuser. Cuts through the fluence distribution were made radially from the axial mid-point of the diffuser for both models. The results of this are shown in Figure 5.4.

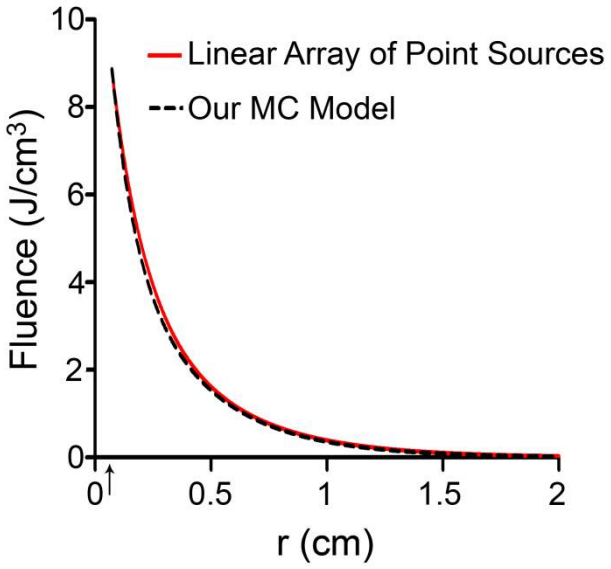


**Figure 5.4** Comparison between linear array of point sources model and our MC model in terms of radial degradation of fluence for $\mu_a$ = 2 $cm^{-1}$, showing substantial overlap between the two methods. Shown is a cut through the fluence at the axial center of a 1 cm diffuser. Simulation parameters were identical, except for the source model. The arrow indicates the position of the outer radius of the diffuser. Reproduced from [98].

As can be seen, the fluence cuts are virtually identical for the two models. Similar results were obtained for cuts at other axial positions on the diffuser, and at other angles (data not shown). This indicates that a model based on a linear array of point sources is sufficient for determination of fluence distribution.

### 5.3.3 Modeling of fluorescence generation and detection

As mentioned previously, fluorescence photon packets are generated at the location of each absorption event within the tissue medium surrounding a diffuser. Generated

fluorescence photon packet weights consist of the absorbed weight, scaled by the quantum yield of fluorescence. Therefore the distribution of generated fluorescence is a scaled version of the absorption distribution. This is shown in Figure 5.5a for a 1 cm diffuser.

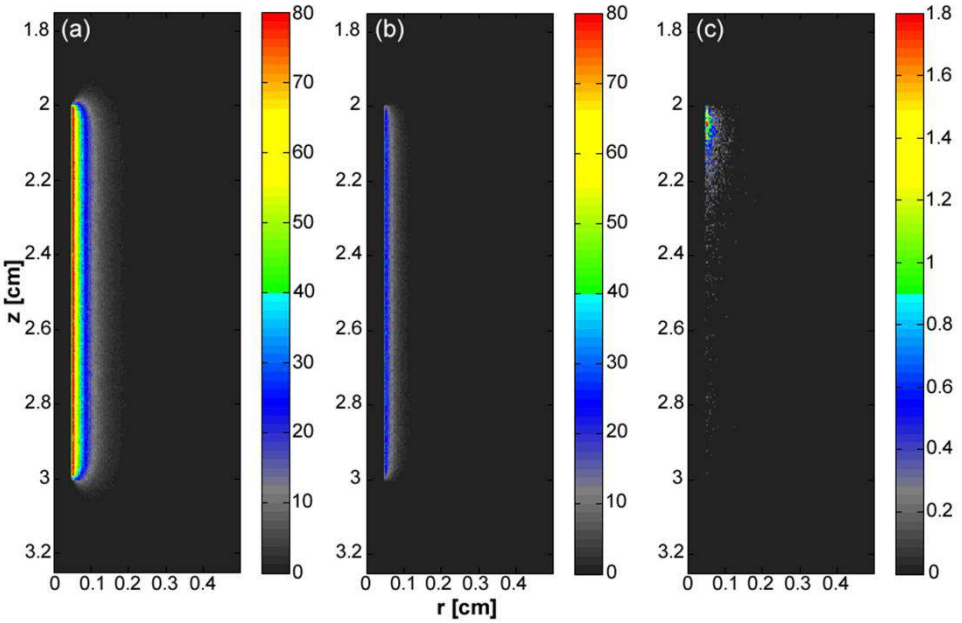


**Figure 5.5** (a) Fluorescence generated in tissue by a 1-cm diffuser with its proximal end at z = 2 cm and an outer radius of 0.05 cm. (b) Origins of fluorescence photons that crossed into the diffuser after being generated in the surrounding tissue. (c) Origins of fluorescence photons that were detected by the diffuser. $\mu_a$ was set to 2 $cm^{-1}$ in tissue. Shown are planar cuts through the simulated volume at the center of the diffuser. Only the right half of this plane is shown for clarity. The left half is identical. Reproduced from [98].

As expected, this generated fluorescence is homogeneous along the length of the diffuser. Figure 5.5b shows the origins and weights of generated fluorescence photons that cross into the diffuser. This is simply a scaled version of the generated fluorescence, and is again homogeneous along the length of the diffuser. The distribution of the origins of detected fluorescence photon packets is shown in Figure 5.5c. Each pixel magnitude is

the sum of the detected weight of fluorescence photon packets generated at that location that migrated through the diffuser, reached the fiber core, and were scored as detected. This distribution is highly heterogeneous, with a majority of the detected fluorescence being generated near the proximal end of the diffuser.

Axial profiles of the simulated detected fluorescence are shown in Figure 5.6. These profiles were created by summing the detected fluorescence at each z position within the simulated tissue volume.

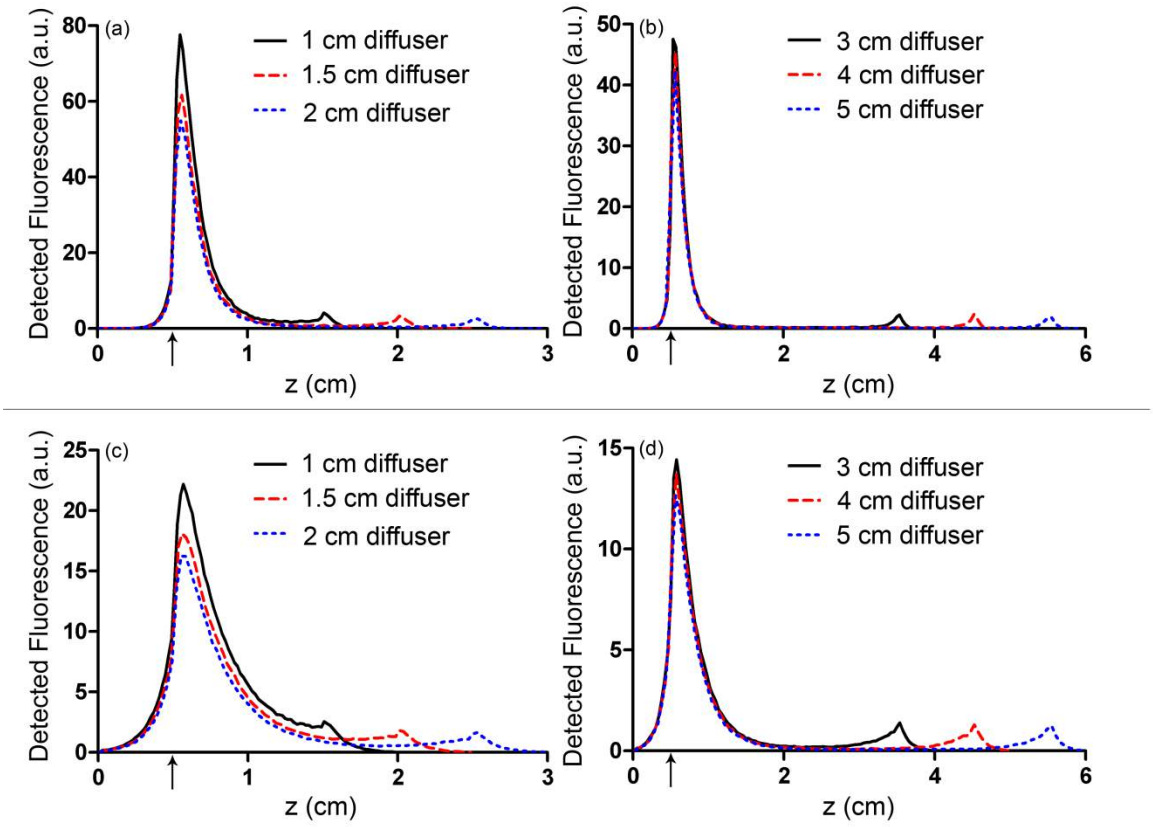


**Figure 5.6** Simulated detected fluorescence by axial position along (a) 1-2 cm diffusers with $\mu_a$=2 cm$^{-1}$, (b) 3-5 cm diffusers with $\mu_a$=2 cm$^{-1}$, (c) 1-2 cm diffusers with $\mu_a$=0.2 cm$^{-1}$, and (d) 3-5 cm diffusers with $\mu_a$=0.2 cm$^{-1}$. All simulations used $\mu_s$=90 cm$^{-1}$ and $g$=0.82, and placed the diffuser's proximal end at z = 0.5 cm. The arrows indicate the location of the proximal end of the diffusers. Reproduced from [98].

Optical properties of the tissue sample were set to $\mu_s = 90$ cm$^{-1}$, $g = 0.82$, and n = 1.395, with either $\mu_a = 2$ cm$^{-1}$ to match experimental conditions or $\mu_a = 0.2$ cm$^{-1}$ to represent a typical value in tissue[144]. As can be seen, the majority of detected fluorescence comes from the proximal portion of the diffuser, with a slightly increased contribution from the distal portion of the diffuser relative to the center. Detected fluorescence, detailed by diffuser segment, is shown in Table 5.2.

| | | Diffuser Segment (Thirds) | | | Diffuser Segment (Halves) | |
|---|---|---|---|---|---|---|
| Diffuser Length (cm) | $\mu_a$ (cm$^{-1}$) | Proximal | Middle | Distal | Proximal | Distal |
| 1 | 0.2 | 69.88±0.02 | 18.15±0.03 | 11.98±0.01 | 81.17±0.01 | 18.83±0.01 |
| | 2.0 | 86.22±0.17 | 7.76±0.08 | 6.02±0.09 | 91.54±0.15 | 8.46±0.15 |
| 1.5 | 0.2 | 77.61±0.08 | 12.76±0.01 | 9.64±0.09 | 86.06±0.04 | 13.94±0.04 |
| | 2.0 | 90.48±0.12 | 3.92±0.07 | 5.60±0.12 | 93.01±0.13 | 6.99±0.13 |
| 2 | 0.2 | 82.54±0.11 | 8.26±0.08 | 9.21±0.02 | 88.10±0.06 | 11.90±0.06 |
| | 2.0 | 92.03±0.04 | 2.58±0.07 | 5.39±0.09 | 93.52±0.07 | 6.48±0.07 |
| 3 | 0.2 | 86.77±0.04 | 4.08±0.01 | 9.16±0.03 | 89.46±0.02 | 10.54±0.02 |
| | 2.0 | 92.71±0.12 | 1.91±0.08 | 5.38±0.13 | 93.75±0.10 | 6.25±0.10 |
| 4 | 0.2 | 88.49±0.04 | 2.40±0.07 | 9.11±0.03 | 89.89±0.01 | 10.11±0.01 |
| | 2.0 | 92.92±0.04 | 1.57±0.05 | 5.50±0.04 | 93.73±0.03 | 6.27±0.03 |
| 5 | 0.2 | 88.66±0.92 | 2.03±0.01 | 9.32±0.11 | 89.73±0.13 | 10.27±0.13 |
| | 2.0 | 93.34±0.07 | 1.56±0.06 | 5.10±0.13 | 94.10±0.10 | 5.90±0.10 |

**Table 5.2** Percentage of generated fluorescence that is collected by various segments of different diffuser lengths, as determined by our MC model. Thirds correspond to the three-layer experiment, and halves correspond to the two-layer experiment. Uncertainties given are the standard deviation of three successive runs of the simulation. Reproduced from [98].

In all cases, the majority of detected fluorescence comes from the proximal third of the diffuser, with contributions ranging from 86-92% for $\mu_a = 2$ cm$^{-1}$ and from 70-88% for $\mu_a = 0.2$ cm$^{-1}$. In all but the 1 cm case for both values of $\mu_a$ and the 1.5 cm case for $\mu_a = 2$ cm$^{-1}$, the distal third of the diffuser is responsible for the next largest contribution to detected fluorescence, with the center segment having the smallest contribution. Relative fluorescence collection by the distal third ranges from 5.38-6.66% for $\mu_a = 2$ cm$^{-1}$ and

9.11-11.98% for $\mu_a = 0.2$ cm$^{-1}$, with the center section collecting 1.63-6.11% for $\mu_a = 2$ cm$^{-1}$ and 2.03-18.15% for $\mu_a = 0.2$ cm$^{-1}$.

Simulations were run with 1,000,000 photon packets on a 100x100x100 grid of voxels. Due to the statistical nature of MC modeling, simulations were repeated three times in order to evaluate reproducibility. The variation in detected fluorescence varies by at most 4% between runs, with most values varying by less than 1%. The run-times were approximately one minute for simulations of fluence distribution and approximately thirty minutes for simulations of fluorescence detection.

### 5.3.4 Experimental validation of fluorescence detection

Experiments were performed in two and three layer phantoms with 1 and 1.5 cm diffusers, respectively. Typical SVD fits to corrected fluorescence spectra are shown in Figure 5.7. The two-layer fit in Figure 5.7a shows contributions from DiI and fluorescein, while the three layer fit in Figure 5.7b shows contributions from DiI, fluorescein, and HPPH. In both cases the magnitude of the Fourier terms is relatively small, indicating a good fit to the data.

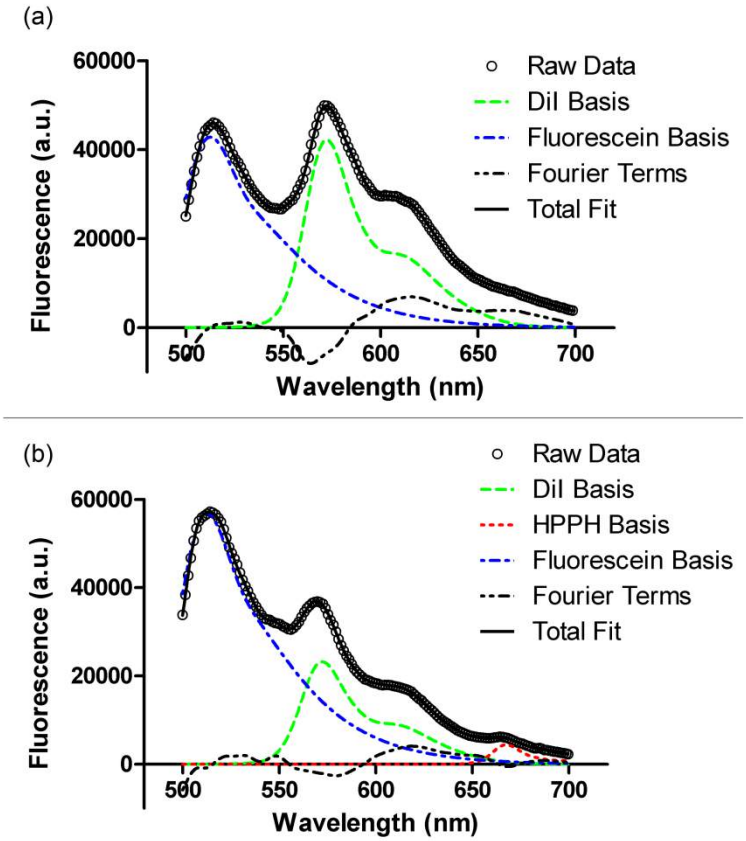


**Figure 5.7** Results of SVD fitting to representative fluorescence spectra collected from (a) two-layer and (b) three-layer phantoms, with spectra corrected for background and system response. Fit magnitudes shown are not corrected for the effects of fluorescence quantum yield and absorption at 488 nm. Reproduced from [98].

Fit coefficients for the fluorophores were further corrected for absorption and fluorescence quantum yield as described above. The corrected values were then used to determine the relative contributions of each segment of the diffuser to the overall detected fluorescence. The results of this are shown in Figure 5.8, with the simulated values shown for comparison.

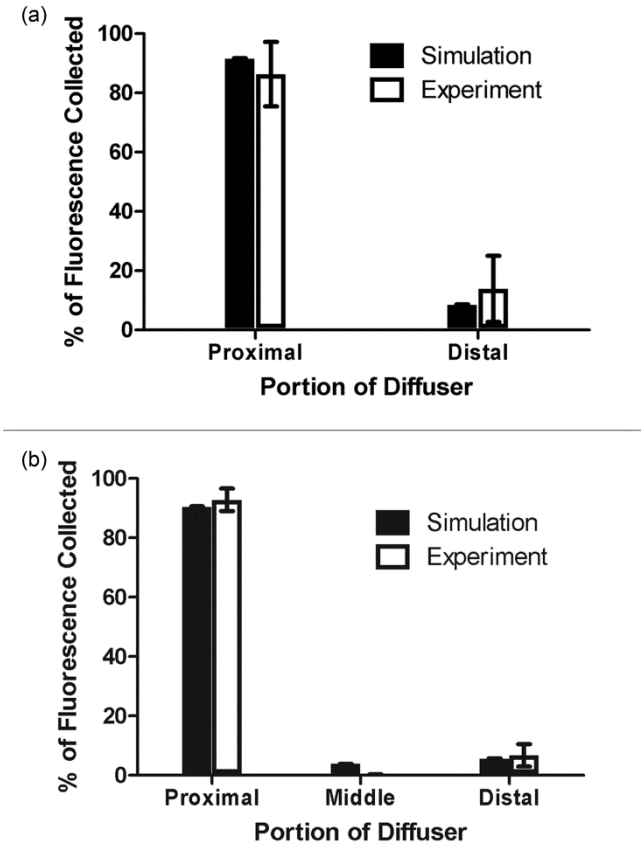


**Figure 5.8** Comparison between simulated and experimental fluorescence detection using (a) 1 cm and (b) 1.5 cm diffusers. Heights of experimental bars (□) indicate the mean value of (a) n = 6 and (b) n = 4 experiments, with error bars representing standard deviation. Values used were corrected for background, system response, fluorescence quantum yield, and absorption at 488 nm. Heights of simulated bars (■) indicate the mean value of 3 simulations, with error bars representing the standard deviation. The value of $\mu_a$ was set to 2 $cm^{-1}$ for both simulation and experiment. Reproduced from [98].

For both two and three layer experiments there is agreement between simulation and experiment to better than 6%. The results shown are for a set of 6 two layer experiments, and a set of 4 three layer experiments. Error bars are standard deviations. Error bars for simulated data are the standard deviations from three successive runs of the simulation.

## 5.4 Discussion

Simulations of both the linear array of point sources and our diffuser model show very similar results for radial fluence profiles, demonstrating that it is appropriate to use the linear array of point sources model when only the fluence distribution for a single diffuser is desired. This less complex model will run slightly faster, since the propagation of photons within the diffuser and boundary collisions with the diffuser are not computed.

To the best of our knowledge, this is the first time that heterogeneous collection of fluorescence by a cylindrical diffuser has been demonstrated, either experimentally or by simulation. As shown here, most of the fluorescence collected by a diffuser is generated near its proximal end with a relatively small spike near the distal end. Given the long scattering mean free path within the diffuser, the large contribution from the proximal end may be explained simply in terms of the diffuser geometry. The NA of the fiber core and the index mismatch between the tissue, cladding, and diffusive medium define the range of angles over which fluorescence entering the diffuser is detected. The axial-coordinate of a photon incident on the diffuser and the index mismatch combine to constrain the range of angles over which the photon can enter the diffuser and be detected. As the axial-coordinate of the incoming photon moves further from the fiber core, this range of acceptable angles decreases. Because fluorescence in the tissue is emitted isotropically, photons are incident on the diffuser at a random angle. Therefore, if the range of acceptable angles decreases with increasing distance from the fiber core and the incident angles are random, the detection of photons also decreases with

increasing distance from the fiber core. The spike in collection at the distal end can be explained by the presence of the dielectric reflector. Photons that enter the diffuser close to the distal end are more likely to strike the reflector, which directs the trajectory of a fraction of these towards the proximal end of the diffuser. Coupled with reflections off of the cladding, this can result in increased probability of detection. In geometric terms, this has the effect of increasing the range of incoming photon angles that can reach the fiber core.

It is important to note that the detection distribution of a cylindrical diffuser is sensitive to the optical properties of the tissue. In particular, the absorption of the tissue will change the axial detection profile. As we have shown, the proximal portion of the diffuser is most sensitive to the detection of fluorescence. With lower tissue absorption, the likelihood of a fluorescence photon reaching the proximal portion of the diffuser before being absorbed is increased. This allows fluorescence that is generated a larger axial distance from the fiber core to be detected. For example, a value of 2 $cm^{-1}$ for $\mu_a$ results in approximately 86% of detected fluorescence being generated along the proximal third of the diffuser. For $\mu_a = 0.2$ $cm^{-1}$, this value is reduced to 70%, with a greater proportion of the detected fluorescence being generated further from the proximal end of the diffuser. While the fluorescence detection profile is still heterogeneous, the sharp degradations shown in Figure 5.6a and Figure 5.6b are smoothed out for lower values of $\mu_a$, as seen in Figure 5.6c and Figure 5.6d.

Knowledge of the detection distribution of a cylindrical diffuser is important if these fibers are to be used for dosimetry in iPDT. Given a detected fluorescence

spectrum, spectroscopic methods can be used to estimate optical properties and photosensitizer concentrations, as will be described in chapter 6. Having a MC model of the origins of detected fluorescence photons allows for these quantities to be mapped to a specific tissue volume. However, a disadvantage of using cylindrical diffusing fibers as spectroscopy probes is that an incomplete map of optical properties would be generated. As we have shown, the detection sensitivity of a cylindrical diffuser is highly heterogeneous, with certain regions near the diffuser not being sampled by spectroscopic measurements. This means that spectroscopic data would not be available for all locations within the tissue, requiring assumptions of optical properties in un-sampled regions. In schemes that use separate spectroscopy fibers, a full map of optical properties can be generated by translating the spectroscopy fibers[145].

The use of separate spectroscopy fibers is not always an option, as in some cases only a single fiber can physically be inserted into the desired volume. This is typically the situation in iPDT for cholangiocarcinoma[12], as well as in the treatment of other hollow organs. In these cases, the only way to obtain spectroscopic information about the tissue would be to use the single treatment diffuser as both a source and detector.

Of critical importance to the clinical deployment of this technique is the speed of the MC simulation. As previously noted, traditional MC simulations can take several hours to run. With our GPU-accelerated model, we have reduced this run-time to the order of one minute. While this is a large improvement, it would be desirable to further reduce this to the order of one second. Alerstam *et al* have shown a 300x speed-up by moving to a GPU-accelerated version of MCML[29]. This would be excellent for our

model, but it is unclear whether this speed-up is achievable for our scenario. The model presented by Alerstam *et al* only allows for layered samples and does not incorporate a diffuser model or fluorescence. This eliminates the need for boundary checks at each voxel and at the diffuser boundary, and removes the need for atomic operations in the detection of fluorescence. These differences can have a significant effect on run-time due to the nature of the GPU. Each of the boundary checks requires a substantial number of conditional statements, even after the optimizations discussed in chapter 3. As mentioned there, all branches of conditionals are executed serially before converging after the conditional[93], resulting in an increase in run-time. The use of atomic operations for fluorescence detection also results in significantly increased run-time. Other studies have shown that the use of atomic operations in GPU-accelerated MC can result in a slow-down of 75%[30].

Our MC model may also be useful in the design of cylindrical diffusing fibers. As mentioned previously, the output irradiance of the diffuser is largely determined by the scattering properties of the diffusive region. These scattering properties are determined by the size and index of the scatterer used, as well as the density of the scatterer. Once a scatterer is chosen, its size and index are known. By simulating a range of $\mu_s$ values and optimizing homogeneity, the density can be computed. This can then be used to manufacture the desired diffuser. Alternatively, some other non-uniform irradiance profile along the diffuser may be desired. Our model can again be used to predict the scatterer concentration required to achieve this profile. This could be done by adjusting a uniform scatterer concentration, or by allowing a heterogeneous distribution

of scatterers. Having a non-uniform distribution of scatterers is often used in the design of two-dimensional diffusers to generate a desired illumination pattern[146], and could therefore be applied to the design of cylindrical diffusers.

# Chapter 6

# Recovery of Intrinsic Fluorescence from Single-Point Interstitial Measurements

## 6.1 Introduction

Reflectance spectroscopy can provide a great deal of information about tissue optical properties, as was outlined in chapters 2 and 4. Fluorescence spectroscopy can also be a valuable tool in the analysis of tissues. There exist a number of biologically relevant compounds that are naturally fluorescent, such as nicotinamide adenine dinucleotide (NADH) and flavin adenine dinucleotide (FAD)[147]. The fluorescence of these and other naturally occurring fluorophores has been used to differentiate between healthy and malignant tissue in the oral cavity[148], the larynx[149], and the colon[150], among others. In PDT, the use of fluorescence spectroscopy is particularly important as most photosensitizers are fluorescent[32]. As was described in chapter 2, characteristics of this photosensitizer fluorescence can be used to deduce something about the photodynamic dose being delivered. Finally, a number of drugs are fluorescent, and can be tracked and analyzed using fluorescence spectroscopy. One notable example of this is doxorubicin, which is a chemotherapeutic agent used to treat a wide variety of malignancies[151]. There have been a number of studies done to track doxorubicin concentration after injection using fluorescence *in vivo* in mouse models[152, 153] and in excised human breast cancer tissue after treatment[154].

In thin samples, collected fluorescence spectra can be analyzed directly in order to yield the concentration of the fluorophore. However, in samples with high scattering or absorption, the detected fluorescence spectrum can be heavily distorted. This is due to emitted fluorescence being absorbed and scattered within the sample. Furthermore, the propagation of the excitation light is affected by the background absorption and scattering, resulting in detected fluorescence that is not exactly proportional to fluorophore concentration or other known environmental factors. This is illustrated in Figure 6.1.

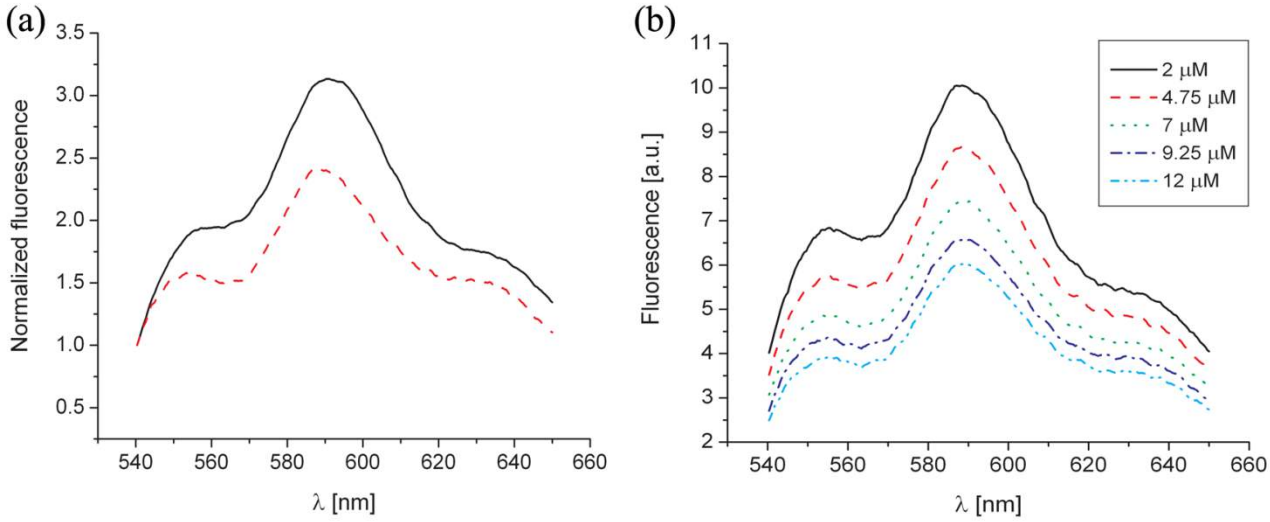


**Figure 6.1** (a) Intrinsic (solid line) and detected (dashed line) doxorubicin fluorescence spectra, normalized to their values at 540 nm, illustrating the spectral distortion induced by background absorption and scattering. The detected fluorescence spectrum was measured in a phantom consisting of 50 mL/L Intralipid and 25 μM MnTPPS. (b) Detected fluorescence spectra measured in a phantom containing doxorubicin at a concentration of 3 μM. Spectra correspond to measurements made as the concentration of the background absorber, MnTPPS, was increased from 2 μM to 12 μM.

The solid line shown in Figure 6.1a is the intrinsic fluorescence spectrum of doxorubicin, while the dashed line is a detected fluorescence spectrum in a solution consisting of 80 mL deionized water, 4 mL of Intralipid-20%, and MnTPPS at a concentration of 25 μM,

with both spectra normalized to their values at 540 nm. The MnTPPS absorption spectrum is shown in Figure 4.19. As can be seen, the shape of the fluorescence spectrum is altered by propagation through a turbid sample. The magnitude of the detected fluorescence is also sensitive to background optical properties, as shown in Figure 6.1b. If a simple correlation between fluorescence magnitude and fluorophore concentration were assumed, each of the spectra shown in Figure 6.1b would return a different doxorubicin concentration. Each of these spectra, however, has the same doxorubicin concentration, with background absorber concentration being the only difference.

Therefore, if we wish to deduce information about a fluorophore based on a distorted detected fluorescence spectrum, we need to correct for the effects of propagation through the turbid medium. This has been studied by a number of research groups. Solutions can roughly be divided into two categories: 1) techniques that rely upon knowledge of the sample's optical properties and 2) techniques that retrieve intrinsic fluorescence without pre-existing knowledge of the sample's optical properties. In the first class of techniques, the optical properties of the tissue sample are often determined using diffuse reflectance, as was discussed in chapter 4. These optical properties are then used with a model of light propagation in order to correct for their effects on the fluorescence spectrum. The model often takes the form of Monte Carlo simulation, with the optical properties determined by diffuse reflectance used as inputs to the simulation. Liu *et al* demonstrated accurate recovery of intrinsic fluorescence using an inverse Monte Carlo model driven by diffuse reflectance measurements[155]. Wang

*et al* also showed recovery of intrinsic fluorescence, but in a more complex layered model of the skin[156].

Other groups have used approximations to the radiative transport equation in order to model the propagation of fluorescence through a sample. Zhadin and Alfano used a simplified diffusion model in order to correct for distortions to intrinsic fluorescence[157]. Diamond *et al* demonstrated recovery of intrinsic fluorescence using a full diffusion model and spatially resolved reflectance and fluorescence measurements[158]. Reflectance measurements were fit using Monte Carlo simulations in order to extract optical properties. These optical properties were then used with a diffusion model of fluorescence in order to recover fluorophore concentration. A more complex method is known as the forward-adjoint model, and will be discussed in detail in the next section.

Photon migration theory can also be used to correct fluorescence spectra using measured diffuse reflectance, as was demonstrated by Wu, Feld, and Rava[73]. This can result in very simple corrections that consist of dividing the measured fluorescence by the diffuse reflectance spectrum, as was used in chapter 2. Finlay *et al* expanded this method by introducing an empirical correction to the detected fluorescence based on a measurement of the diffuse reflectance measured at the excitation wavelength[54]. A version of this, adapted to the probe geometry, was used in chapter 2 to correct detected Pc 4 fluorescence spectra.

Techniques that do not require the optical properties to be known *a priori* have not been investigated as thoroughly. Finlay and Foster used the forward-adjoint

fluorescence model in order to recover intrinsic fluorescence by assuming that the absorbers and scatterers in a sample are known, but not their concentrations[99]. This allowed for the simultaneous recovery of fluorophore concentration and background optical properties. Chang *et al* used an analytical expression based on diffusion theory in order to extract intrinsic fluorescence from a 2-layered skin model[159]. This is then used to provide possible diagnostic information on cervical dysplasia.

In this chapter, we demonstrate a method for the recovery of intrinsic fluorescence and optical properties from turbid samples using a single interstitial, isotropic source and detector. This recovery does not require a separate diffuse reflectance measurement. The forward-adjoint method is utilized, with modifications made to account for the interstitial geometry. Verification of the method is performed in tissue simulating phantoms containing doxorubicin as a fluorophore.

## 6.2 Forward-adjoint fluorescence model

As discussed previously, the absorption and scattering properties of a sample can have a significant effect on the detected fluorescence spectrum. In order to correct for these sample-induced distortions to the fluorescence, a model of fluorescence propagation and detection is required. Here, we use the forward-adjoint method, first proposed by Crilly *et al*[160].

In this method, the generation and detection of fluorescence is represented by two functions, the fluence distribution generated by the source and the positional importance. The fluence distribution can be calculated or simulated by forward-modeling techniques, such as those described in chapter 4, or Monte Carlo techniques such as those described

in chapter 3. The adjoint portion of the method is accounted for in the positional importance. Rather than represent the propagation of fluorescence as a combination of photon sources at the locations of fluorescence generation, the adjoint approach determines the locations that contribute to the detected signal as a function of the optical properties. The positional importance is therefore the probability that a given detected photon originated from a specific point in the sample.

The forward-adjoint fluorescence model is expressed mathematically as

$$F_{\text{det}} = (\lambda_x / \lambda_m)\mu_{af}\varphi_f \int \Phi_x(\vec{r})\tilde{\Phi}_m(\vec{r})dV \tag{6.1}$$

where $\lambda_x$ and $\lambda_m$ are the excitation and emission wavelengths, respectively, and $\mu_{af}$ and $\varphi_f$ are the absorption coefficient of the fluorophore at the excitation wavelength and the fluorescence quantum yield, respectively[99]. These terms combined represent the intrinsic fluorescence, $F_0$. $\Phi_x(\vec{r})$ is the fluence generated by the source, and $\tilde{\Phi}_m(\vec{r})$ is the positional importance, both of which depend on the optical properties of the sample. The subscripts *x* and *m* correspond to excitation and emission, respectively, here and in the rest of this chapter. This integral represents the propagation of excitation and emission light through the sample, and therefore accounts for the distortion of the intrinsic fluorescence spectrum.

As mentioned previously, the form of the fluence and positional importance requires the use of an approximation to the radiative transport equation. Here, we use the $P_3$ approximation, as detailed in chapter 4. We are interested in the use of an isotropic source and detector, so we consider the case of an isotropic point source in an infinite medium. The fluence is given in this case by equation 4.19. This expression for fluence

accounts for the diffuse portion of light propagation, but does not account for ballistic photons. In the limit of zero background absorption and scattering, this results in equation 6.1 predicting zero detected fluorescence, which is clearly incorrect. We therefore introduce a term to equation 4.19 to account for light that propagates along a straight-line path. This results in an expression for fluence given by

$$\Psi_0(r) = B^- \frac{e^{-\upsilon^- r}}{\upsilon^- r} + B^+ \frac{e^{-\upsilon^+ r}}{\upsilon^+ r} + \sqrt{\frac{1}{4\pi}} \frac{\exp(-\mu_t r)}{r} \tag{6.2}$$

where the definitions and values of all coefficients are given by equations 4.8 and 4.18. This results in the proper limiting behavior as the background scattering and absorption go to zero (i.e. $F_{det} = F_0$ when background absorption and scattering both go to zero), and ensures that the integral in equation 6.4 converges under these conditions. The form of the positional importance is identical, but with optical properties corresponding to the emission wavelength[160]. In order to obtain an expression for detected fluorescence, we evaluate equation 6.1 using equation 6.2 for $\Phi_x(\vec{r})$ and $\tilde{\Phi}_m(\vec{r})$. This results in an integral of the form

$$F_{\text{det}} = F_0 \int_{r_x=0}^{\infty} \int_{\theta=0}^{\pi} \int_{\phi=0}^{2\pi} \Phi_x(r_x)\tilde{\Phi}_m(r_m) r_x^{\,2} \sin(\theta) dr_x d\theta d\phi . \tag{6.3}$$

Since we are using the same isotropic probe as a source and detector, $r_x = r_m = r$, and the problem is symmetrical in $\theta$ and $\phi$. This simplifies the integral to

$$F_{\text{det}} = 4\pi F_0 \int_{r=0}^{\infty} \Phi_x(r)\tilde{\Phi}_m(r) r^2 dr . \tag{6.4}$$

With the expressions for fluence and positional importance given by equation 6.2, this results in the expression for detected fluorescence given in equation 6.5,

$$F_{\det} = 4\pi F_0 \left[ \sum_{i=(+,-)} \sum_{j=(+,-)} \frac{B_x^i B_m^j}{\upsilon_x^i \upsilon_m^j (\upsilon_x^i + \upsilon_m^j)} + \sqrt{\frac{1}{4\pi}} \left( \sum_{k=(+,-)} \frac{B_x^k}{\upsilon_x^k (\upsilon_x^k + \mu_{t,m})} + \sum_{l=(+,-)} \frac{B_m^l}{\upsilon_m^l (\upsilon_m^l + \mu_{t,x})} + \sqrt{\frac{1}{4\pi}} \frac{1}{\mu_{t,x} + \mu_{t,m}} \right) \right], \tag{6.5}$$

where the coefficients are again found in equations 4.8 and 4.18. This expression is identical to equation (5) from Finlay and Foster[99], in the limit of the source-detector separation going to zero and with the addition of terms to account for proper limiting behavior. For realistic values of $\mu_s$, the terms corresponding to this correction are negligible compared to those contained in the first line of equation 6.5.

In techniques that have access to diffuse reflectance measurements of the sample, equation 6.5 would be evaluated directly using the measured optical properties. The detected fluorescence would be divided by the distortion induced by background absorption and scattering in order to determine the intrinsic fluorescence. Here, we want to determine the intrinsic fluorescence directly without *a priori* access to the sample's optical properties. In order to do this, we invoke knowledge of the absorbers present in the sample and the scattering spectrum shape given by equation 4.36. An iterative fitting procedure can then be utilized in order to determine the intrinsic fluorescence.

In order to determine the value of the distortion to the intrinsic fluorescence, the scalar error metric

$$\chi^2 = \sum_{\lambda} [F_{\det,norm}(\lambda) - F_{calc,norm}(\lambda)]^2 \tag{6.6}$$

is minimized for the entire spectrum using a constrained non-linear optimization (fmincon, MATLAB, Mathworks, Natick, MA), with the absorber and scatterer concentrations constrained to be positive. Here $F_{det,norm}$ is the measured, detected fluorescence spectrum divided by its value at some wavelength $\lambda_0$. $F_{calc,norm}$ is a calculated detected fluorescence spectrum, computed using equation 6.5, the known shape of the intrinsic fluorescence spectrum and a trial set of absorber concentrations and scatterer parameters, divided by its value at $\lambda_0$. The absorption spectra consist of the absorption due to the background absorbers, as well as the absorption due to the fluorophore. The normalization is performed because $F_{det}$ and $F_{calc}$ are on different scales. In the computation of $F_{calc}$, $F_0$ is assumed to consist of only one fluorophore. However, the fitting procedure could be expanded to include multiple fluorophores, as described in Finlay and Foster[99].

After the optimum set of optical properties is determined, these are used to generate the distortion

$$D = 4\pi\left[\sum_{i=(+,-)}\sum_{j=(+,-)}\frac{B_x^i B_m^j}{\upsilon_x^i \upsilon_m^j(\upsilon_x^i+\upsilon_m^j)}\right.$$

$$\left.+\sqrt{\frac{1}{4\pi}}\left(\sum_{k=(+,-)}\frac{B_x^k}{\upsilon_x^k(\upsilon_x^k+\mu_{t,m})}+\sum_{l=(+,-)}\frac{B_m^l}{\upsilon_m^l(\upsilon_m^l+\mu_{t,x})}+\sqrt{\frac{1}{4\pi}}\frac{1}{\mu_{t,x}+\mu_{t,m}}\right)\right], \qquad (6.7)$$

where the coefficients correspond to the minimized set of optical properties. The intrinsic fluorescence is then found by

$$F_0 = \frac{F_{\det}}{D}. \qquad (6.8)$$

In principle, the optical properties found should correspond to the sample optical properties. However, we found that there was some cross-talk between the absorption due to the fluorophore and that due to the background absorbers. Therefore, a second fitting step is performed in order to separate these effects. In order to do this, $F_0$ is fixed at the value found in equation 6.8. As described above, this $F_0$ consists of the absorption of the fluorophore and the quantum yield. The quantum yield is assumed to be a constant value and is derived by calibration with known concentrations of the fluorophore in question. The value of $F_0$ can therefore be used to calculate $\mu_{a,f}$ and the concentration of the fluorophore. This concentration of fluorophore is then used to set the contributions of the fluorophore to the absorption at the excitation and emission wavelengths. Minimization is then performed over the error metric

$$\chi^2 = 1000\sum[F_{\text{det}} - F_{calc}]^2 \tag{6.9}$$

where $F_{det}$ is the detected fluorescence spectrum and $F_{calc}$ is the detected fluorescence spectrum calculated using equation 6.5, the known $F_0$, and a trial set of background absorber concentrations and scattering parameters. The minimization is performed with a constrained global minimizer (MultiStart, MATLAB), in order to ensure that local minima are not found. MultiStart was chosen as a global optimizer to ensure deterministic results. The absorber concentrations and scattering parameters, *a* and *b*, are constrained to be non-negative. The factor of 1000 was included to ensure that the optimization runs to completion.

## 6.3 Experimental validation

The method outlined in section 6.2 was verified by measurements in tissue-simulating phantoms.

### 6.3.1 Phantom preparation

Tissue-simulating phantoms consisted of deionized water, Intralipid-20% as a background scatterer, and MnTPPS as a background absorber. The fluorophore used was doxorubicin hydrochloride. Phantoms were prepared with 80 mL of deionized water and 4 mL of Intralipid-20%, to which varying concentrations of MnTPPS and doxorubicin were added. MnTPPS was prepared at a stock solution of 10 mg/mL by dissolving powdered MnTPPS in deionized water.

Absorption basis spectra for MnTPPS and doxorubicin were measured using a commercial spectrophotometer (Varian 50 Bio, Palo Alto, CA). The MnTPPS spectrum was found by measuring MnTPPS in deionized water at a concentration of 25 μM, and averaging the results of multiple measurements in order to improve the signal-to-noise ratio. The doxorubicin basis spectrum was found by measuring doxorubicin HCl in deionized water at a concentration of 85 μM. Normalized versions of these spectra are shown in Figure 6.2.

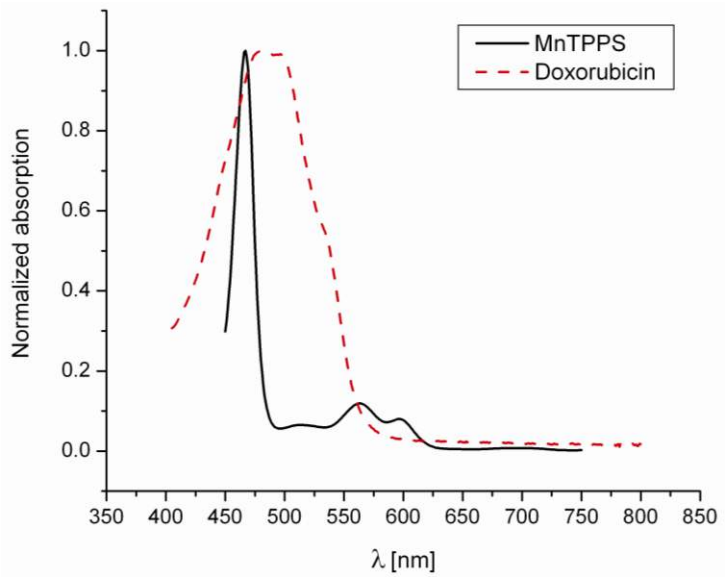


**Figure 6.2** Normalized absorption spectra of MnTPPS (solid line) and doxorubicin (dashed line) in deionized water. Spectra were measured using a commercial spectrophotometer.

The fluorescence basis function for doxorubicin was found by making measurements, as described in the next section, of doxorubicin fluorescence in a phantom consisting of 80 mL of deionized water, 0-4 mL of Intralipid-20%, and doxorubicin at concentrations of 1.5-15 μM. These spectra were then divided by $4\pi D$, calculated using equation 6.7 and the known scatterer and doxorubicin concentration, in order to retrieve the intrinsic doxorubicin fluorescence. These spectra were normalized and averaged over all measured data in order to create the basis spectrum shown in Figure 6.1.

### 6.3.2 Data collection and correction

Spectra were collected using the system shown in Figure 6.3.

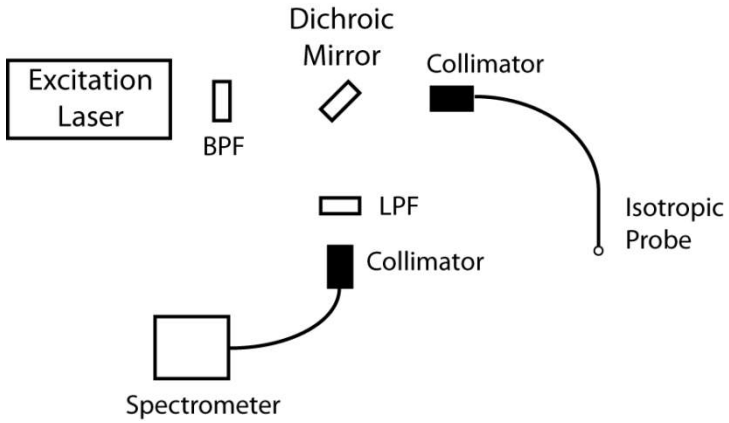


**Figure 6.3** System used for collection of fluorescence spectra. BPF and LPF refer to band-pass and long-pass filters, respectively.

Fluorescence was excited by a 488 nm laser diode (iBeam Smart 488-S, Toptica Photonics, Victor, NY), filtered by a bandpass filter (model 52650, Oriel Instruments, Stratford, CT). This excitation light was passed through a dichroic mirror (488trans-Pc-xr, Chroma Technology Corporation, Bellows Falls, VT), and focused into a fiber-coupled isotropic probe (model IP85, Medlight SA, Switzerland). The emitted fluorescence was collected by the isotropic probe, collimated, reflected off of the dichroic mirror, and filtered with a long-pass filter (HQ500LP, Chroma Technology Corporation). This was then focused into an optical fiber and detected by a TE-cooled, 16-bit spectrometer (B&W Tek, Newark, DE). Integration times varied by experiment, but were generally in the range of 50-500 ms. Data collection and instrument control were performed with a laptop computer through a custom LabVIEW interface (National Instruments, Austin, TX).

After data collection, raw fluorescence spectra were corrected for dark background, system response, integrating time, and excitation power. Dark spectra collected without excitation light were subtracted from each measured fluorescence spectrum. After dark subtraction, each spectrum was divided by a wavelength-dependent system response. This was found by placing the isotropic probe into a 6" integrating sphere, with a baffle between the detector port and the probe (Labsphere, North Sutton, NH). A NIST-traceable lamp (model LS-1-CAL, Ocean Optics, Dunedin, FL) was then used to illuminate the sphere through the baffled detector port, and the spectrum detected. This detected spectrum was divided by the known lamp spectrum to get the system response. All spectra were also divided by the integration time and excitation power, in order to get all measured spectra on the same scale. Excitation power was measured using the integrating sphere mentioned previously with a silicon photodiode (SDA-050-U, Labsphere) and calibrated radiometer (SC-6000, Labsphere). Excitation power was typically on the order of 5 mW.

Spectra were also corrected for fluorescence created within the spectroscopy system, as shown in Figure 6.4. The spectrum shown by the solid line was measured in a phantom containing doxorubicin, with the large features at wavelengths longer than 660 nm coming from the spectroscopy system.

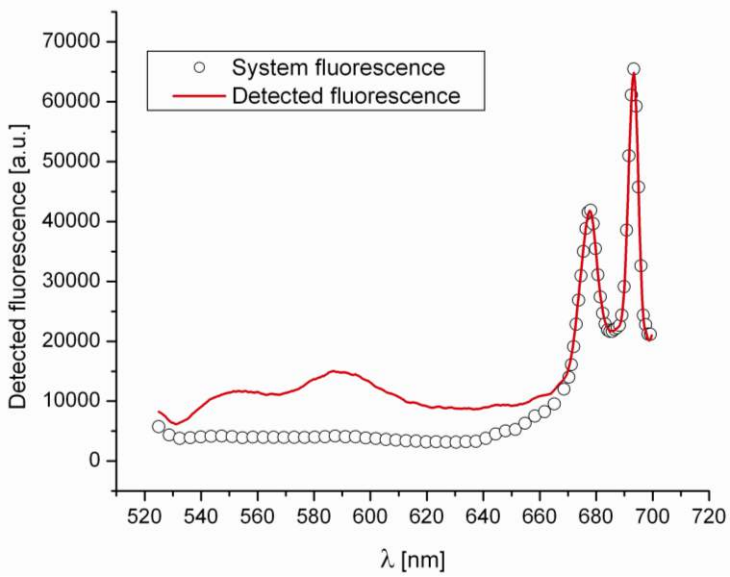


**Figure 6.4** Detected fluorescence spectrum showing contributions from the desired doxorubicin fluorescence and the system fluorescence. The solid line represents a detected fluorescence spectrum measured in a phantom containing doxorubicin with evidence of system fluorescence. The open circles represent a fit of the system fluorescence in the range of 665-700 nm to the measured data. This fit is used to remove the effects of system fluorescence.

In order to correct for this, spectra were measured in either 80 mL of water or 80 mL of water with 1-4 mL of Intralipid-20%. The spectra taken in phantoms containing Intralipid were then corrected for scattering-induced distortion using equation 6.7. The resulting spectra were then normalized and averaged to produce the spectrum shown by the open circles in Figure 6.4. System fluorescence was found to come largely from the isotropic probe. This system fluorescence spectrum had two peaks at 678 and 693 nm, which were outside the range used for fluorescence measurement and in a region of low absorption and scattering. Therefore, this region could be fit using a non-linear optimization from 665-700 nm, as shown in Figure 6.4, to determine the contribution of system fluorescence to the detected signal. For each fluorescence spectrum collected,

two measurements were made. One was at low integration time (40-50 ms) in order to capture the system fluorescence peaks without saturating the detector. This spectrum was used for the fitting procedure shown in Figure 6.4. Another spectrum was then taken at a higher integration time (typically 100-500 ms), in order to use the full dynamic range of the spectrometer in the 500-650 spectral window. The system fluorescence fit from the first spectrum was then scaled to the integration time of the second spectrum, and subtracted off. The fitting could not be performed directly on the spectrum measured at higher integration time because the integration times used caused the system fluorescence to saturate the detector.

### 6.3.3 Results

Experimental verification of the technique was performed in tissue-simulating phantoms as described above, at doxorubicin concentrations ranging from 1.5-50 μM. At each doxorubicin concentration, spectra were collected for 5 MnTPPS concentrations from 2-12 μM. For each phantom, fluorescence measurements were made, as described previously, and corrected for dark background, system response, and system fluorescence.

After correction, fluorescence spectra were analyzed using the fitting algorithm described in section 6.2. The results for a particular experiment are shown in Figure 6.5.

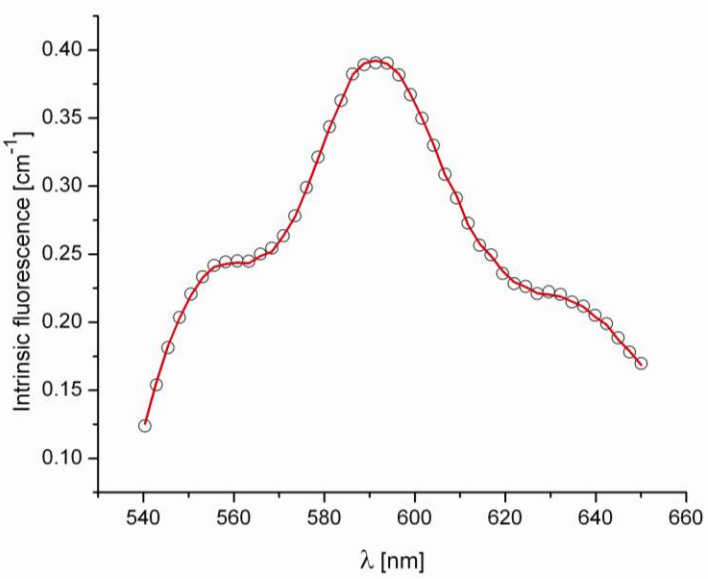


**Figure 6.5** Recovered intrinsic fluorescence spectrum (○) using the forward-adjoint model, compared to the known intrinsic fluorescence spectrum (solid line) for a doxorubicin concentration of 12 μM.

The open circles correspond to the recovered intrinsic fluorescence spectrum, while the solid line represents the known intrinsic fluorescence spectrum, based on the doxorubicin concentration in the phantom. For this experiment, the doxorubicin concentration was 12 μM and the MnTPPS concentration was 4.75 μM.

A summary of doxorubicin concentration recovery over all measured phantoms is shown in Figure 6.6a.

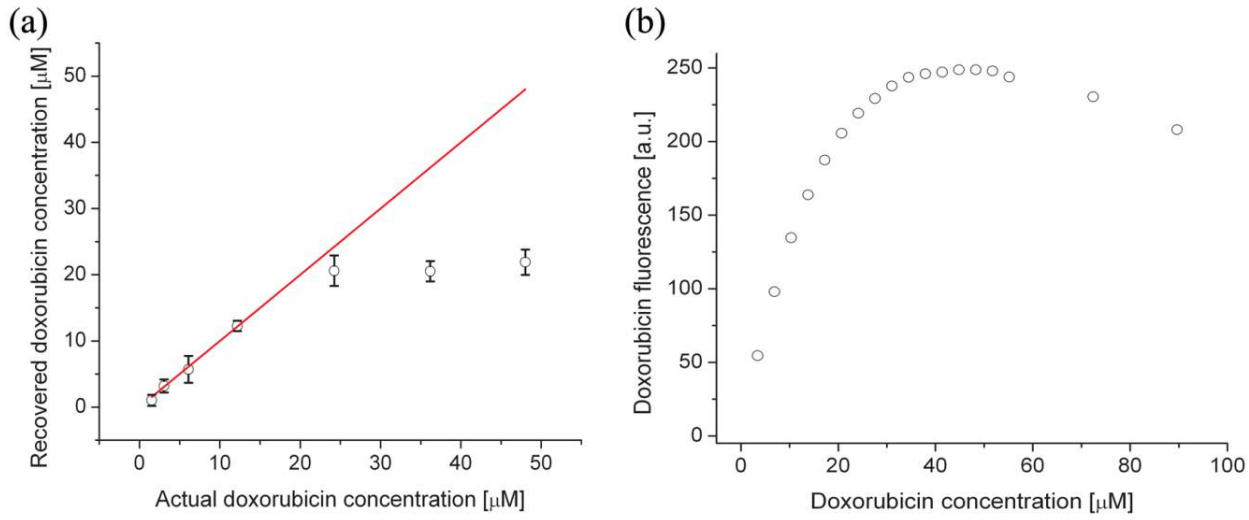


**Figure 6.6** (a) Recovery of doxorubicin concentration using the forward-adjoint fluorescence model in tissue-simulating phantoms containing Intralipid-20% and MnTPPS. The accuracy of concentration recovery breaks down beyond a doxorubicin concentration of approximately 25 μM, due to self-quenching. The solid line represents perfect agreement. (b) Fitted magnitude of doxorubicin fluorescence with increasing doxorubicin concentration, measured using a commercial fluorometer.

In Figure 6.6a, data points represent the average recovered doxorubicin concentration for an experiment consisting of measurements at five MnTPPS concentrations, with error bars representing standard deviation. As can be seen the recovery is good up to a doxorubicin concentration of approximately 25 μM. Beyond this point, self-quenching of the doxorubicin fluorescence occurs. In this process, there is direct energy transfer between adjacent fluorophores[161]. Unlike inner filtering, which is re-absorption of fluorescence by the fluorophore, self-quenching does not have an appreciable effect on the shape of the detected fluorescence spectrum. The only effect is a reduction in overall fluorescence magnitude. Therefore, this method cannot correct for the effects of self-quenching, meaning that a doxorubicin concentration of 25 μM represents a fundamental upper limit for recovery. This value is comparable to the results of fitting doxorubicin

fluorescence spectra measured in a commercial fluorometer, as shown in Figure 6.6b. Here doxorubicin fluorescence was measured in a 1 cm quartz cuvette with increasing fluorophore concentration. The results were then fit using non-linear least squares and the doxorubicin fluorescence basis function in order to determine the magnitude of the fluorescence. In clinical studies, the maximum doxorubicin concentration in tumor tissue was found to be 819 ng per g of tumor tissue[162]. Assuming a tumor density of 0.95 g/mL[163], this translates to a doxorubicin concentration of 1.3 μM, which is well below the 25 μM threshold.

If only the range of doxorubicin concentrations below 25 μM is considered, the recovery is as shown in Figure 6.7.

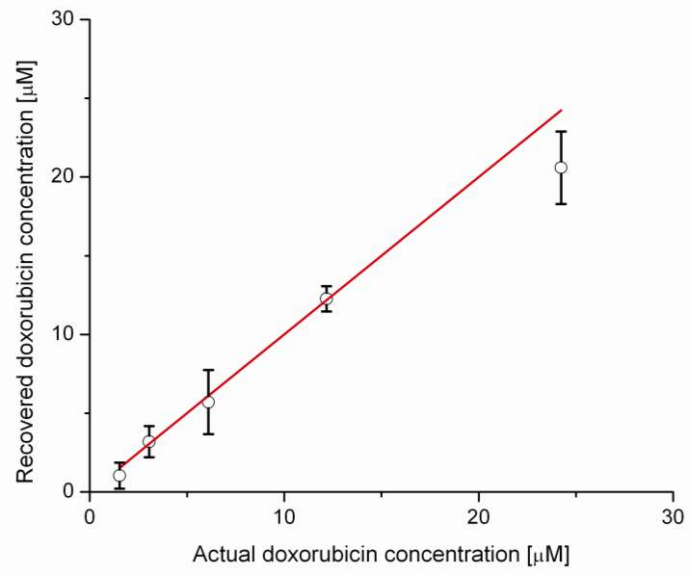


**Figure 6.7** Recovery of doxorubicin concentration using the forward-adjoint fluorescence model in the concentration regime not affected by self-quenching. The solid line represents perfect agreement.

In this regime, the recovery of doxorubicin concentration is good. The mean error in recovery is 11.8%, with a maximum error of 30%.

After determination of doxorubicin concentration, the second step of the fitting algorithm is run in order to determine the background optical properties. While the primary goal of this method is to recover intrinsic fluorescence, recovery of optical properties can be considered as a secondary benefit of the technique. The results of this for an individual experiment are shown in Figure 6.8.

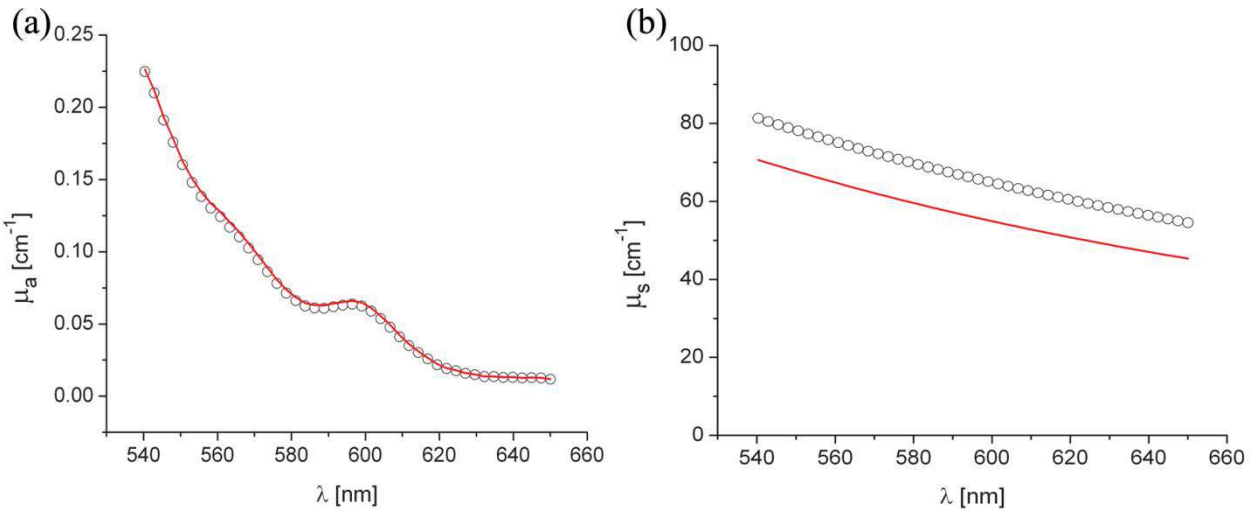


**Figure 6.8** Recovery of (a) $\mu_a$ and (b) $\mu_s$ using the forward-adjoint fluorescence model. In both cases, open circles are recovered optical properties and solid lines are known optical properties. The absorption spectrum contains contributions from 12 μM doxorubicin and 4.75 μM MnTPPS.

Here the open circles represent recovered values, while solid lines represent the known optical properties of the phantom. These are derived from the same measurements that were used to determine the intrinsic fluorescence shown in Figure 6.5.

The recovered absorption of MnTPPS can then be used to calculate concentration, based on the known molar extinction of MnTPPS. A summary of this is shown in Figure 6.9.

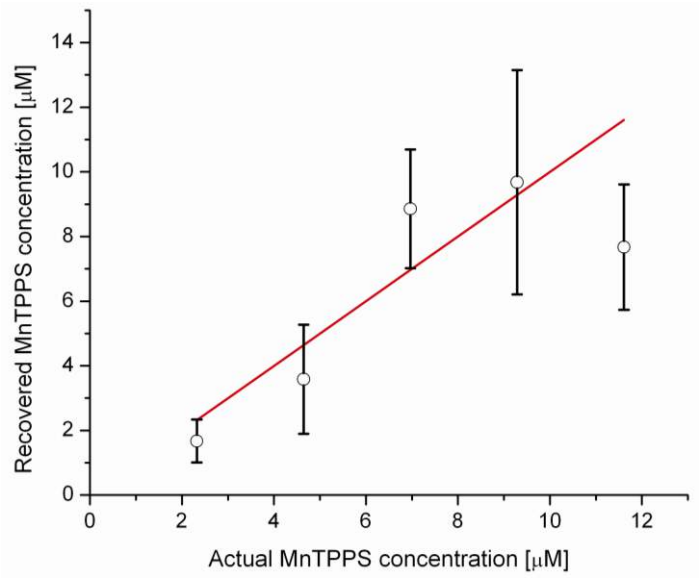


**Figure 6.9** Recovery of MnTPPS concentration from fluorescence measurements analyzed using the forward-adjoint model. The solid line represents perfect agreement. The data points represent the average recovered MnTPPS concentration over four experiments at doxorubicin concentrations of 1.5-25 μM, with error bars corresponding to standard deviation. The recovery of background absorption tracks linearly with increasing MnTPPS concentration, but is not as accurate as the recovery of fluorophore concentration. The mean error in recovery of MnTPPS concentration was 23.2%, with a maximum error of 33.9%. As previously stated, recovery of doxorubicin concentration is of primary importance, so the seemingly large errors in MnTPPS concentration recovery are not of deep concern.

The recovery of the scattering parameters shown in equation 4.36 is summarized in Figure 6.10. Here, the value of $\lambda_0$ was set to 488 nm so that the value of $a$ was equal to the scattering coefficient at the excitation wavelength.

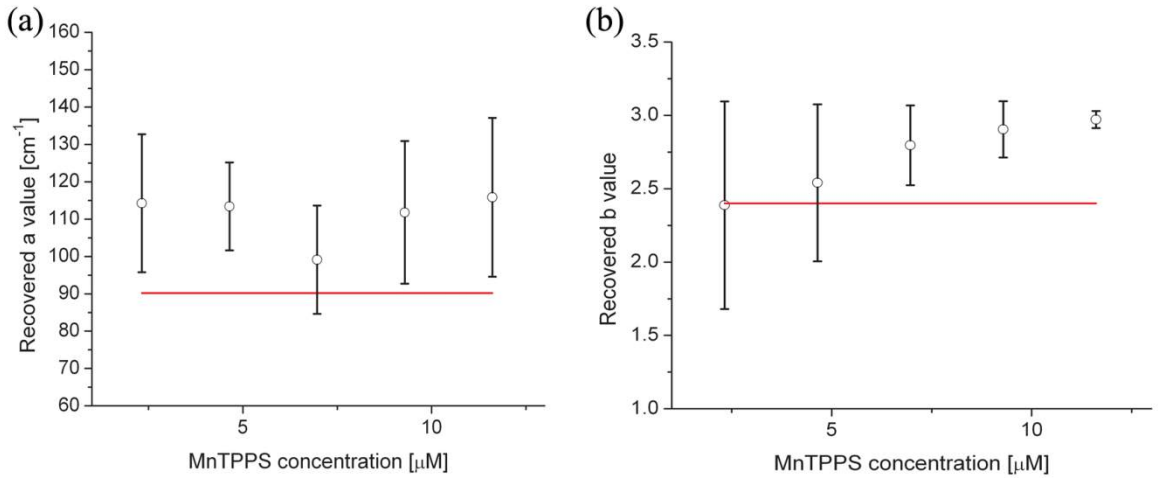


**Figure 6.10** Recovery of scattering parameters (a) *a* and (b) *b*, according to equation 4.36, using the forward-adjoint fluorescence method. Solid lines represent known values, while data points represent averages over measurements made in phantoms with the same MnTPPS concentration and varying doxorubicin concentration.

Here the solid lines represent the actual value computed for the phantom, while data points represent averages over measurements made in phantoms with the same MnTPPS concentration, but varying doxorubicin concentration. Error bars again represent standard deviation. The values of scattering parameters were chronically over-predicted, with mean errors of 24.4% and 21.2% in *a* and *b*, respectively. The mean error in the recovery of the overall $\mu_s$ spectrum was found to be 19.8%.

## 6.4 Discussion

To the best of our knowledge, this is the first time that intrinsic fluorescence has been recovered from point fluorescence measurements made in a turbid medium without *a priori* knowledge of the optical properties. As mentioned in the introduction to this chapter, there has been a great deal of work done on the recovery of intrinsic fluorescence informed by diffuse reflectance measurements of optical properties made at the surface of the sample, with comparatively little done without *a priori* knowledge of the optical

properties. In the interstitial regime, there has also been some work done on the recovery of intrinsic fluorescence. Finlay *et al* demonstrated recovery of motexafin lutetium fluorescence in the human prostate using a single side-firing optical fiber to excite and detect fluorescence[19]. This recovery utilized the forward-adjoint model, but required a separate measurement of the tissue optical properties.

Compared to schemes that employ a separate determination of optical properties, the accuracy of fluorophore concentration that we demonstrate here is similar. Weersink *et al* demonstrated recovery of fluorophore concentration with a root mean square error of 14.6%, using a ratio of detected fluorescence to reflectance as a metric of fluorophore concentration[164]. Diamond *et al* demonstrated recovery with error of 8%, using a diffusion model of fluorescence informed by reflectance measurements to determine optical properties[158], and Müller demonstrated accuracy of approximately 90%, using a method based on photon migration theory[165]. Given that these techniques employ external knowledge of optical properties, the 11.8% error for the technique described here compares favorably with these estimates.

The method presented here is also capable of extracting optical properties. As mentioned previously, this has been previously performed in surface geometry. Chang *et al* claimed that their method was capable of providing good recovery of optical properties, but did not provide any data to substantiate this claim[159, 166]. However, their recovery of fluorescence is quite robust, so it can be surmised that the recovery of optical properties is of good quality as well. Finlay and Foster demonstrated recovery of absorption from hemoglobin that was approximately 20% lower than the value

determined by diffuse reflectance[99]. They were able to recover oxygen saturation and the Hill parameters very accurately, though, which is often the goal of tissue spectroscopy. The 23.2% mean error in the recovery of absorption reported here is therefore comparable to previously reported results.

The technique described in this chapter does not require a separate measurement in order to determine the tissue optical properties before recovery of intrinsic fluorescence. This represents a significant reduction in clinical complexity, as illustrated in the simple system diagram depicted in Figure 6.3. Simplified instrumentation should ease the transition of the technique in the clinic, where it can be used to examine a number of medically relevant fluorophores.

This method also has some limitations. Since the determination of fluorescence distortion requires the background absorbers to induce a shape change in the detected spectrum, the technique will only work in the presence of absorbers with distinct absorption features. This is why the technique works well in the 500-620 nm region, where both MnTPPS and hemoglobin have strong absorption features with distinct shapes. In the NIR region, the absorption of hemoglobin is much lower and lacks strong features. This was evident in a study done by Cottrell *et al*[55]. The authors employed a divide-by-reflectance method for correction based on Wu *et al*[73], and found that the measured reflectance spectrum was featureless and stable. This division was therefore omitted. The method presented here will also not be as strong for fluorophores with a large Stokes shift. Currently, the absorption at the excitation wavelength can be determined because the effects of this absorption are also apparent in the emission

spectrum. For fluorophores with large Stokes shifts, the absorbers in the excitation and emission windows may be different, making it impossible to determine the effects of excitation attenuation from detected fluorescence spectra. This would require a separate measurement at the excitation wavelength, as was employed by Finlay *et al*[54]. Fortunately, the fluorophores we are currently interested in have emission around 550-600 nm and do not possess overly large Stokes shifts.

One fluorescent compound that we are particularly interested in examining clinically is doxorubicin. As mentioned previously, doxorubicin is a potent chemotherapeutic agent used to treat a number of malignancies. We are particularly interested in the determination of doxorubicin concentration in the liver after transcatheter arterial chemoembolization (TACE). In this therapy a chemotherapeutic agent, in this case doxorubicin, is selectively delivered to the arteries feeding a tumor. Embolization beads are delivered either simultaneously with the drug or directly afterwards in order to occlude the blood vessels feeding the tumor. This leads to higher drug concentration in the tumor, lower drug concentration in systemic circulation, and reduced blood-flow to the tumor. TACE has been used successfully as a palliative therapy for a number of liver cancers, with significantly improved survival times[167, 168].

The concentration of doxorubicin delivered to a tumor can have a significant impact on the tumor outcome[162]. However, in TACE the doxorubicin concentration delivered to the tumor is not known exactly, or routinely measured. In a typical TACE procedure, the physician injects doxorubicin embedded in embolization beads until there

is stasis of blood flow into the tumor. This can result in individual patients receiving differing concentrations of doxorubicin, which could have implications for the outcome of the treatment. Measurements of doxorubicin concentration in systemic circulation after TACE have been made[169], but there have not been measurements made of the local doxorubicin concentration in the tumor after TACE. Fluorescence-based recovery of intrinsic doxorubicin fluorescence has previously been demonstrated in mouse models[153], but this again requires a separate measure of tissue optical properties and is performed at the tissue surface.

We are actively pursuing a clinical trial in order to determine the concentration of doxorubicin present in liver tumors, specifically hepatocellular carcinoma, after TACE using the forward-adjoint method presented here. In order to do this, a 19-gauge biopsy needle will be inserted percutaneously into the tumor mass under image guidance, directly after the TACE procedure. Upon insertion, the core of the needle will be removed and the sterile, single-use isotropic optical probe will be inserted into the tumor. The detected fluorescence will then be analyzed using the method outlined in this chapter. We have secured grant funding for this project[170], and are currently writing clinical protocols for submission to the University of Rochester Research Subject Review Board. We hope to analyze the correlation between doxorubicin concentration in the tumor after TACE treatment and tumor outcome.

# Chapter 7

# Treatment Planning for Interstitial PDT

## 7.1 Introduction

As has been discussed extensively in this thesis, the optical properties of a patient's tumor and surrounding normal tissues can have a large impact on the volume treated in PDT. This can influence the segment of the tumor that receives a prescribed light dose, as well as affect the dose delivered to healthy tissues surrounding the tumor. In a typical PDT treatment, a physician will prescribe a certain threshold dose that tumor tissues must receive and a maximum permissible dose to adjacent normal tissue. This threshold dose is often determined empirically, using experiments in animal models[171] and informed by dose escalations performed in clinical trials[44]. Given varying optical properties and photosensitizer concentrations between patients, a treatment plan must seek to achieve this threshold dose on a patient by patient basis.

This is similar to the planning process for ionizing radiation. For radiation treatment planning, CT or MR images of the patient are taken, a target dose is prescribed, and the source distribution is designed such that this dose is achieved. Treatment planning is a mature field for ionizing radiation, and there are a number of commercial treatment planning packages available. These packages allow for accurate computation of dose, with 88% of patients receiving a median dose within 5% of the prescribed dose[172]. We therefore seek to provide an optical analog to this procedure for PDT.

In treatment planning for ionizing radiation, the electron densities obtained from CT imaging can be used to compute dose. In the optical regime, we do not have access to comparable information from imaging. Optical properties must therefore be determined by alternative means, as discussed in chapter 4. This is particularly pressing because of the wide inter- and intra-patient variability in optical properties that can occur. A number of studies have demonstrated this variability[173]. In particular, Simpson *et al* demonstrated that the magnitude of variation in the absorption coefficient of excised human skin was of the same order as the value of the absorption coefficient[124]. We have also shown this in freshly excised human kidneys, with values of the absorption and scattering coefficients varying over more than an order of magnitude for the same tissue type[123].

The patient's anatomy can also have a large effect on the propagation of light through the tumor and surrounding healthy tissue. This can be due to index of refraction mismatches within the patient, which can lead to fluence distributions that are different from those expected in uniform tissue volumes. At air interfaces, index mismatches can cause a greater deposition of fluence close to the boundary. In the case of interstitial PDT for tumors deep within the body, air interfaces are not as common, but there can still be significant index mismatches. Imaging also allows for differentiation between diseased and healthy tissue. As mentioned previously, the physician will often prescribe a threshold dose for diseased tissue. A maximum dose for surrounding healthy tissue will generally also be prescribed. This is especially important in organs such as the prostate, where there a number of critically important anatomical components nearby.

There have been a number of previous efforts to integrate optical spectroscopy and models of light propagation for rigorous planning of PDT treatments. These schemes typically utilize CT or ultrasound images in order to identify diseased and healthy tissue, and then use patient-specific optical properties in order to determine the treated region. Many of these treatment planning efforts for interstitial PDT have focused on the prostate, due to the risk of undesirable side effects from other treatment modalities[42]. Altschuler *et al* demonstrated the optimization of source position, length, and strength in order to plan PDT of the prostate[45]. Their optimization was based on the Cimmino feasibility algorithm, which has been used extensively in radiotherapy and guarantees convergence on a solution. Swartling *et al* used ultrasound images to define their treatment volume, and diffuse reflectance measurements coupled with a diffusion approximation in order to create treatment plans for PDT of prostate cancer[43]. Their computation of source strength was based on delivery of a threshold dose to the tumor region while minimizing exposure to surrounding organs, and also used the Cimmino algorithm. Their threshold dose was based on previous studies of PDT in prostate cancer[11]. Davdison *et al* also demonstrated a treatment planning system for PDT of the prostate, again based on ultrasound imaging and a diffusion approximation for light propagation[44]. However, their calculations of light dose were based on an assumption of uniform optical properties throughout the prostate. They achieved good results, with a correlation shown between calculated light dose and tumor response.

In this chapter, we seek to integrate the optical spectroscopy developed in chapter 4 with MC models demonstrated in chapters 3 and 5 in order to create treatment plans for

interstitial PDT. Coupled with clinical CT images, this allows for individualized treatment plans to be created. We demonstrate the method by which optical and anatomical information are combined, provide an algorithm for the placement of diffusers, and demonstrate the results of treatment planning.

## 7.2 Integration of clinical imaging and spectroscopy

Before radiotherapy, patients are typically imaged with CT or MRI. Since this is standard clinical practice, we seek to utilize this information for PDT treatment planning. Clinical CT data sets were provided by Daryl Nazareth of the Roswell Park Cancer Institute in Buffalo, NY. These data sets were in the Digital Imaging and Communications in Medicine (DICOM) standard, and contained the image slices as well as information about the imaging equipment and conditions. For the data we were provided, the pixel size was 1.27 x 1.27 mm, with a slice thickness of 2.5 mm. The image stack consisted of 165 512x512 CT images. A 3D rendering of a typical image stack is shown in Figure 7.1.

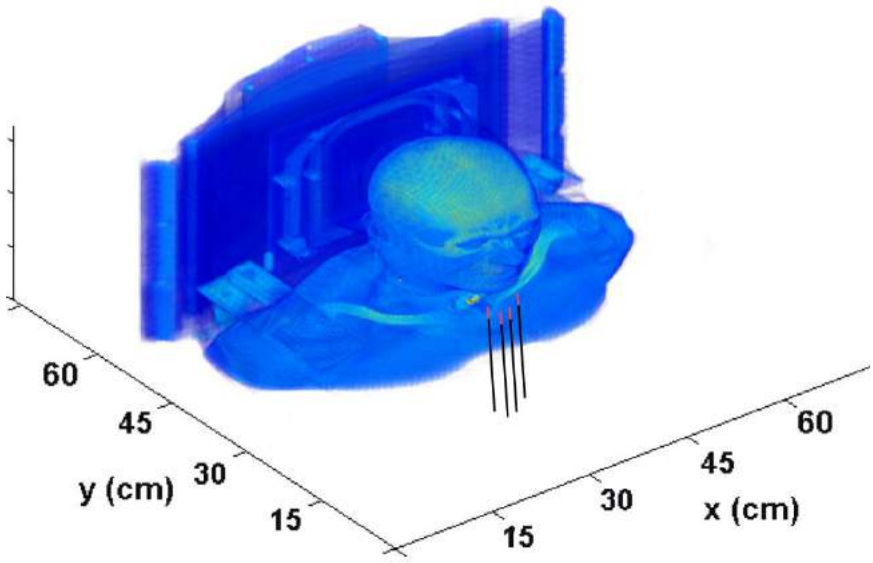


**Figure 7.1** 3D rendering of a CT stack taken from a head and neck cancer patient, illustrating the insertion of cylindrical diffusing fibers for PDT.

This data set comes from a head and neck cancer patient that received radiotherapy at Roswell Park, with the insertion of cylindrical diffusing fibers shown for reference. A cut through this stack is shown in Figure 7.2a.

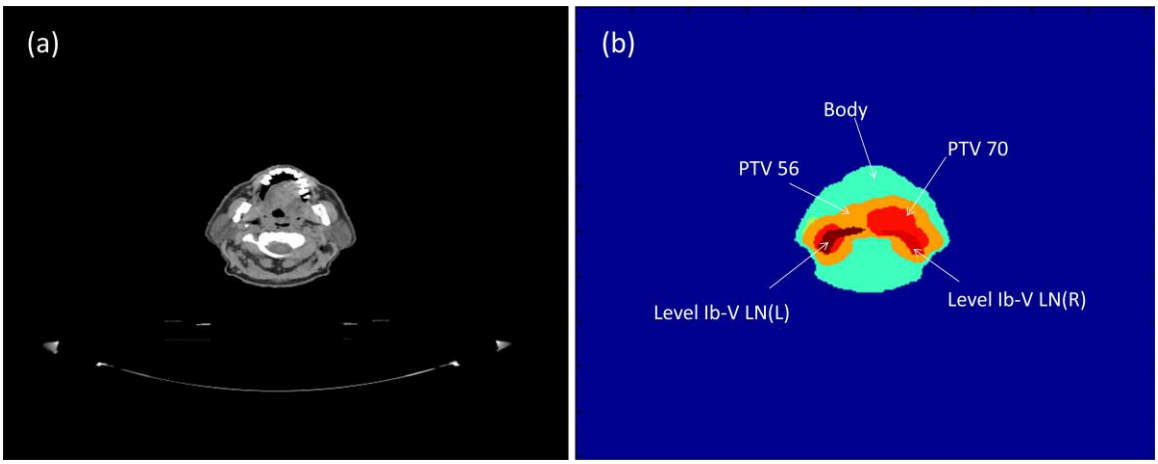


**Figure 7.2** Cut through the CT data stack showing (a) CT image data, using a soft tissue window, and (b) regions of interest as prescribed by the physician. In this case, ROIs are derived from radiotherapy treatment planning, so planning target volume (PTV) values correspond to radiation dose in Gray. The other structures visible are lymph nodes (LN).

The patient was lying on their back, with this image slice coming at the level of the mouth. Here the tumor and surrounding healthy tissue are visible, along with teeth and bones.

This anatomical information is imported into the MC simulation space by accessing the MATLAB engine from C code. This is done to take advantage of DICOM interpretation routines available in MATLAB, while still allowing for the simulation to be run in C. Initially, each voxel in the CT data stack is represented by a single voxel in the MC simulation space. The initial voxel size in the MC simulation is therefore defined by the voxel size in the CT data set, which is specified in the DICOM file. At run-time, however, the MC voxel size is re-scaled to fit a user-defined volume of interest. For example, if the user were only interested in a 2 cm cuboid region around the treatment fiber, the MC voxels would be scaled to uniformly cover this region. This allows for determination of deposited light dose at higher resolutions than are possible in CT images.

In addition to anatomical information, the DICOM file for the CT stack also contains regions of interest (ROIs), as specified by the physician. These ROIs designate whether a certain area is tumor or healthy tissue, and what dose the region should receive. A depiction of this is shown in Figure 7.2b. In this case, the ROIs are derived from a radiotherapy treatment plan, so the planning target volume (PTV) values shown correspond to planned radiation doses, in Gray. For a PDT treatment, these values would be specified as a given light dose in units of $J/cm^2$. The other structures visible are lymph

nodes (LN). These ROIs are used to inform optimization of the treatment fiber placement, as will be described in the next section.

The CT images and ROIs discussed above define the patient's anatomy. In order to make an individualized treatment plan, we also require knowledge of the patient's optical properties. In a typical case, optical property measurements are made before or during the PDT treatment. In our case, the interstitial optical probe described in chapter 4 is used. While this provides reasonably accurate values of the optical properties, it does not sample the entire treatment volume, with the optical properties determined from an interstitial spectroscopy measurement only known rigorously in a specific region. A larger volume can be sampled by translating the optical probe along the path of insertion, but this still only samples a region confined along this path. Therefore, we must make some assumption about the optical properties of tissues not sampled spectroscopically. This could potentially be done by assuming typical values of optical properties taken from the literature. Cheong *et al* provide a compilation of tissue optical properties for a variety of tissue types at a number of clinically relevant wavelengths[173]. Another option, which we have chosen to implement, is to assume that the optical properties in remote regions are homogeneous and equal to the sampled optical properties. This has been done previously in treatment planning for PDT of the prostate, with optical properties at 763 nm shown not to vary significantly within a particular prostate in the majority of patients[44]. These optical properties are imported into the simulation space using MATLAB, and are used to drive subsequent MC simulations and treatment planning.

## 7.3 Optimization of diffuser placement

After the patient's anatomy and optical properties are determined and imported into the simulation space, the placement of the treatment fibers must be determined. As mentioned previously, the treatment fibers typically used for interstitial PDT are cylindrical diffusers. In order to define a treatment plan, we must therefore specify the number and the placement of diffusers required to achieve the prescribed light dose.

Determination of these values is achieved through the use of non-linear optimization, with the metric to be minimized defined as

$$\chi^2 = 1 - \frac{T_{thresh}}{T} + C\frac{H_{thresh}}{H}, \tag{7.1}$$

where $T_{\text{thresh}}$ is the number of voxels in the tumor with a deposited dose equal to or greater than the prescribed dose, $T$ is the total number of voxels in the tumor, $H_{\text{thresh}}$ is the number of healthy voxels equal to or greater than the maximum tolerated healthy dose, and $H$ is the total number of healthy voxels. $C$ is a scaling factor that can be adjusted, based on the vulnerability of surrounding healthy tissue. If the surrounding healthy tissue were functionally vital, the value of $C$ would be large. In cases where the surrounding healthy tissue is not of critical importance, this value would be lower or zero.

Optimization begins by placing a single diffuser at roughly the center of the tumor volume. The fluence distribution created by this source is defined by equation 4.27, with the value of $\delta$ determined by running a MC simulation at the specified optical properties. An approximation to the fluence distribution is used rather than a MC simulation at each step in order to speed up the optimization process. Even though we are using GPU-

accelerated MC simulations that can be run in approximately 30 seconds, a non-linear optimization requires the objective function to be evaluated a large number of times. This would translate to unreasonably long execution times for determination of fluence distributions, particularly in the case of multiple treatment fibers.

At each step of the optimization, the diffuser position is moved and the objective function shown in equation 7.1 is evaluated for the fluence distribution specified by equation 4.27. If a specified fraction of the tumor receives the prescribed light dose, the optimization is terminated and the diffuser position is recorded and provided to the user. If this is not achieved, an additional diffuser is added and the optimization is repeated. This process continues until the tumor volume receives the prescribed light dose, or the addition of another diffuser would result in a source separation of less than $1/\delta$. This is done to ensure that diffusers are not placed unreasonably close to another, as this can be clinically challenging to achieve or may cause unacceptable injury.

An example of this process is shown in Figure 7.3 for the case of an elliptical tumor embedded in healthy tissue. The tumor has equatorial radii of 1.1 cm and a polar radius of 1.3 cm, and is surrounded by a cuboid volume of normal tissue that is 3.8 x 3.8 x 4.6 cm. This normal tissue volume was designed to be 1 cm larger than the maximum tumor dimension in each Cartesian direction.

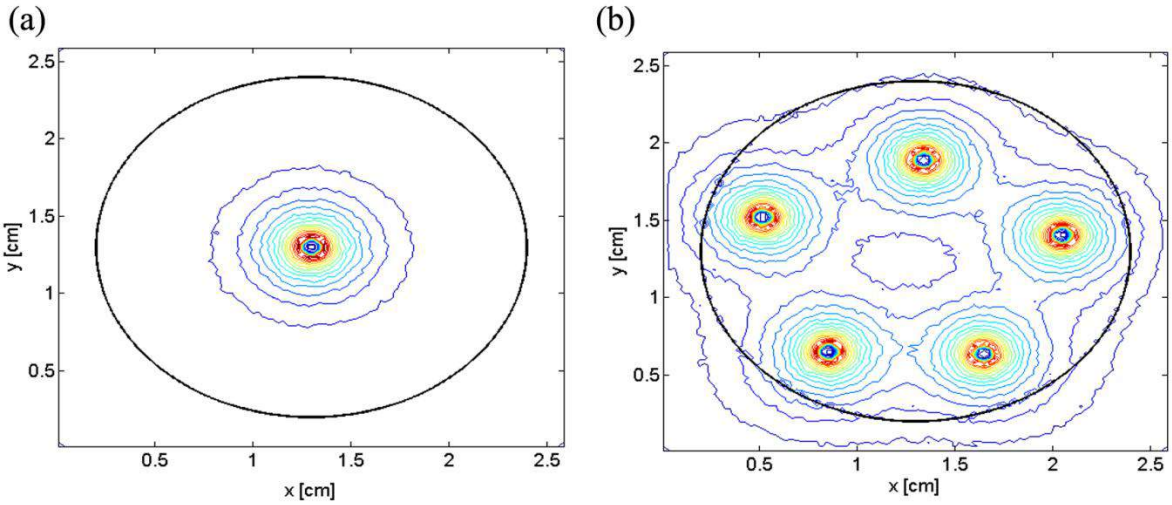


**Figure 7.3** Contour plots showing the results of source optimization for the case of (a) one cylindrical diffuser and (b) five cylindrical diffusers. In this case, the use of five diffusers was found to be optimal. Each contour line represents an increment of 100 J/cm$^2$ in the delivered dose, and the thick black line represents the boundary between tumor and healthy tissue. Each diffuser delivered 200 J/cm of fluence.

In this case, the tumor and healthy tissue optical properties are derived from measurements made of excised human kidneys, as described in chapter 4. Figure 7.3a shows the results of optimization for a single diffuser, while Figure 7.3b shows the final results of the optimization. The optimization was run with a target tumor light dose of 100 J/cm$^2$, and each diffuser delivering 200 J/cm of fluence. Here, a total of 5 diffusers was found to achieve the desired light dose in 95% of the tumor volume. Further details of the results of this optimization are presented in the following section.

## 7.4 Treatment planning

The treatment planning software consists of a MATLAB framework and the simulation space in C. The patient's anatomy and optical properties are read in through the MATLAB interface. These parameters are then used to drive an initial MC simulation with a single diffuser placed at the center of the tumor volume. The results of this

simulation are used to find the value of $\delta$ by fitting equation 4.27 to the simulated data, which is then used in the optimization of diffuser number and placement. Once these are determined, a MC simulation is run with the determined diffuser positions. The results of this simulation can then be analyzed in order to ensure that the target light dose is achieved in the specified volume of tumor, and the placements can be adjusted in order to give the desired behavior.

Results of treatment planning are typically expressed using dose-volume histograms. These histograms illustrate the portion of the tumor and healthy regions that received at least a certain light dose. These are used to evaluate whether tumor regions are receiving the prescribed dose, and whether healthy regions are being over-treated. The dose-volume histogram for the scenario depicted in Figure 7.3b is shown in Figure 7.4. As can be seen, the tumor received a significantly higher light dose than the surrounding normal tissue. 94% of the tumor received a dose of at least the prescribed 100 J/cm$^2$ dose, while only 5.7% of the healthy tissue received a dose greater than 100 J/cm$^2$. In treatment planning for radiotherapy, a therapy is typically prescribed such that 95% of the tumor receives at least 95% of the desired dose[174]. In our case, 95.3% of the tumor volume received a dose of 95 J/cm$^2$.

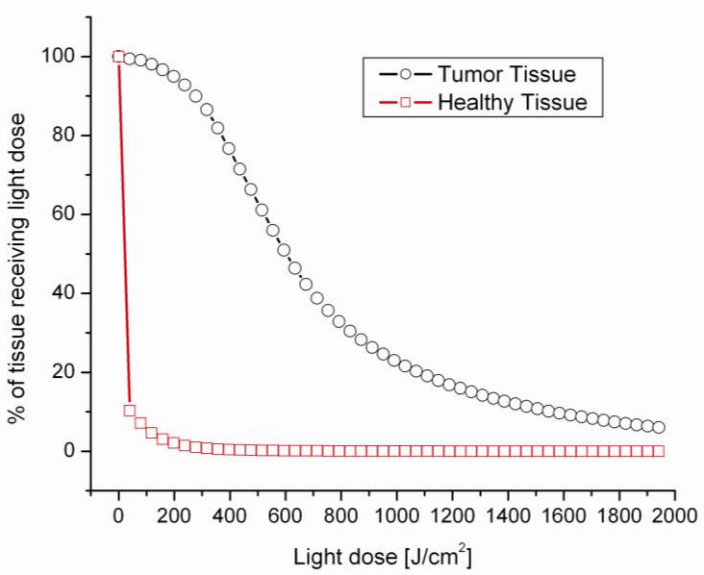


**Figure 7.4** Dose-volume histogram for the case of five diffusers inserted into an elliptical tumor embedded in healthy tissue, as shown in Figure 7.3b. Prescribed light dose was 100 J/cm$^2$, with 200 J/cm delivered by five 2 cm diffusers.

The fluence distribution generated can be dependent upon the materials surrounding the tumor volume. In the situation shown in Figure 7.3b and Figure 7.4, the tumor was surrounded by a healthy tissue volume with an index of refraction equal to that of the tumor tissue. This is not always the case. One application in which we are interested is PDT treatment of large tumors at the base of the tongue. In this case, part of the tumor is in contact with air rather than other tissue. This can result in changes to the placement of diffusers, and the fluence distribution generated. To examine this, we used the elliptical tumor specified previously half submerged in healthy tissue and half in air. This interface results in a concentration of fluence at the tissue-air interface, and leads to a different dose-volume histogram, as shown in Figure 7.5.

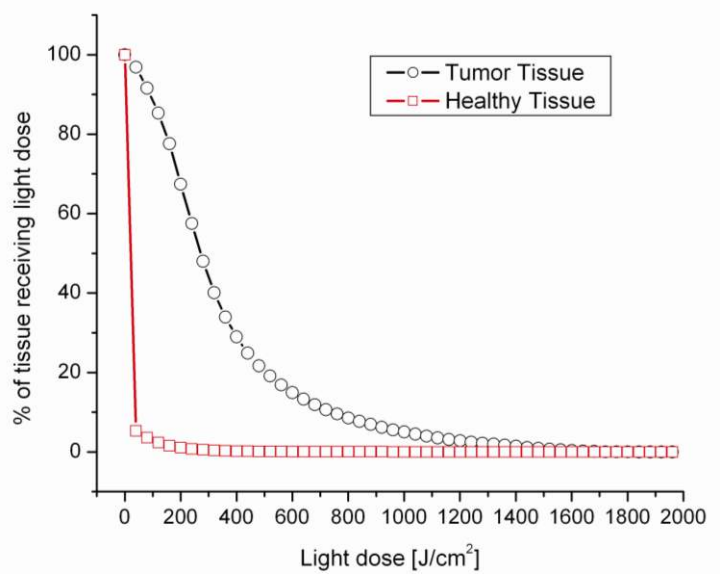


**Figure 7.5** Dose-volume histogram for the case of five diffusers inserted into an elliptical embedded half in air and half in healthy tissue. The prescribed light dose was 100 J/cm$^2$, with 350 J/cm delivered by each diffuser.

In this case, each fiber was required to deliver a total light dose of 350 J/cm in order to achieve 95% of the prescribed light dose in 95% of the tumor. 94.8% of the tumor volume received a dose of at least 100 J/cm$^2$, with 95.1% of tumor receiving a dose of 95 J/cm$^2$. We observed that the dose deposited close to the air-tumor interface was increased compared to a tumor-healthy interface due to total internal reflection, but that the overall dose deposited was reduced. This is likely due to fluence escaping the tumor at the air interface, rather than scattering back in from the healthy region. The volume of healthy tissue that received a dose greater than 100 J/cm$^2$ decreased to 2.6%. The optimal diffuser positions were found to change by an average of 0.7 mm when the air interface was added. It is therefore important to understand the effects of interfaces on the light dose in the tumor and surrounding healthy tissue.

The placement of diffusers can also have an effect on the deposited dose. In many interstitial PDT trials, the diffusers are placed uniformly in a grid pattern with typical spacings of approximately 1 cm[10, 16]. While this is more straightforward clinically, it can lead to certain regions of the tumor being undertreated. This is illustrated in Figure 7.6.

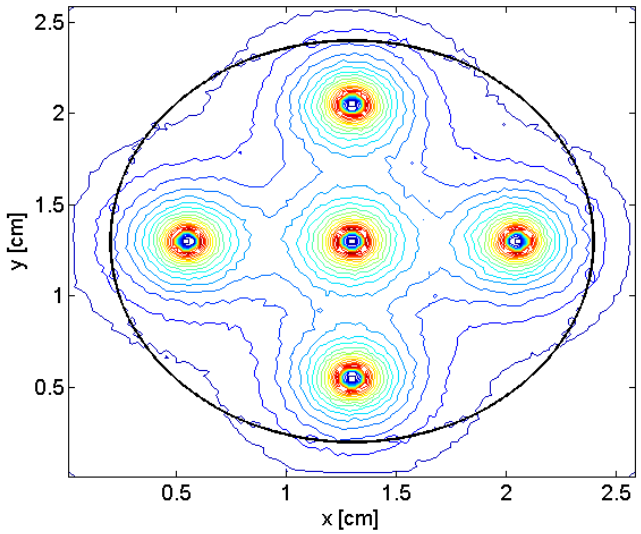


**Figure 7.6** Contour plot showing the dose distribution created by five diffusers placed in a pre-defined grid pattern, with 7.5 mm separations. Each contour line represents an increment of 100 J/cm$^2$ in the delivered dose, and the thick black line represents the boundary between tumor and healthy tissue.

Shown here is the dose distribution achieved using diffusers placed uniformly at 7.5 mm separations. While the total dose delivered to the tumor is comparable to the case of optimized diffuser positions, there are regions that are under-treated in this case. These regions are evident in the corners of the tumor region in Figure 7.6, as compared to Figure 7.3b. In this case 91% of the tumor volume received a light dose of 95 J/cm$^2$, compared to 95.3% for the optimized diffuser placement. While this difference may not

seem large, it can result in expanded viable tumor regions after treatment, potentially leading to a greater rate of tumor regrowth.

After demonstrating the viability of the treatment planning software in an idealized tumor case, we created a treatment plan using CT images and ROIs from a radiotherapy treatment plan that was carried out at Roswell Park Cancer Institute. The patient, shown in Figure 7.1 and Figure 7.2, had a primary laryngeal tumor with tumor tissue also present in the lymph nodes. In our treatment planning, we used PTV 56 (see Figure 7.2b) as our region over which to optimize the dose, with a desired light dose of 100 J/cm$^2$. Due to the tumor size, 5 cm diffusers were used in the treatment plan, with each diffuser delivering 400 J/cm. Since we did not have optical measurements of the patient, we needed to assume optical properties. In this case, we used $\mu_a$ = 0.5 cm$^{-1}$ and $\mu_s$ = 74 cm$^{-1}$ for tumor tissue, and $\mu_a$ = 0.2 cm$^{-1}$ and $\mu_s$ = 84 cm$^{-1}$ for all other soft tissues. These values were derived from those measured in kidney tissue in chapter 4. A value of $g$ = 0.9 was used for all tissue types.

A total of 15 diffusers were found to provide an adequate light dose to the desired treatment volume. The optimized locations of the diffusers are shown in Figure 7.7.

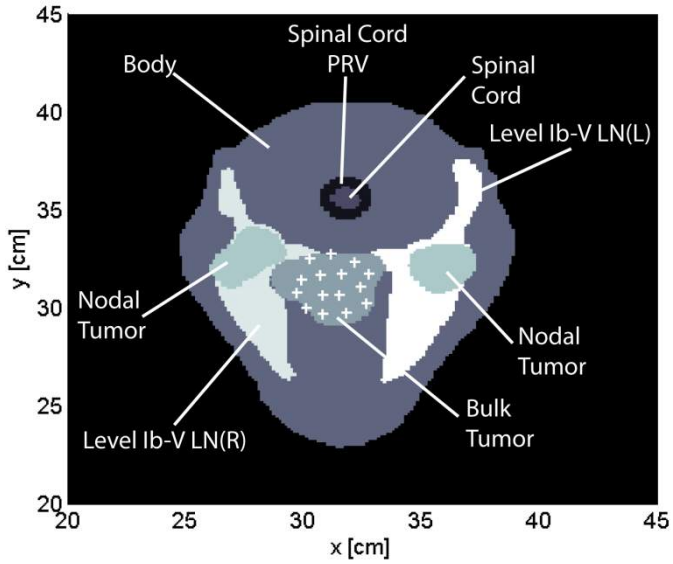


**Figure 7.7** Placement of 15 5-cm diffusers (+) in patient volume after optimization of number and placement of sources. Also shown are lymph nodes (LN) with nodal tumors, the surrounding bulk body tissue, the spinal cord, and the spinal cord planning risk volume (PRV).

After optimization of sources, 15 diffusers were spaced by an average of 8 mm to deliver the desired dose. All of the identified diffuser positions were inside the bulk tumor volume, with some placed close to the tumor boundary. These diffuser positions generated the dose-volume histogram shown in Figure 7.8. 96.4% of the tumor volume was found to receive a light dose of 100 J/cm$^2$, with 96.7% of the tumor receiving a dose of 95 J/cm$^2$. The only healthy tissues that received any light dose were the bulk body tissue and the left lymph node. 2.7% of the bulk body tissue was found to receive a light dose of greater than 100 J/cm$^2$, while 11.6% of the left lymph node was found to receive this dose.

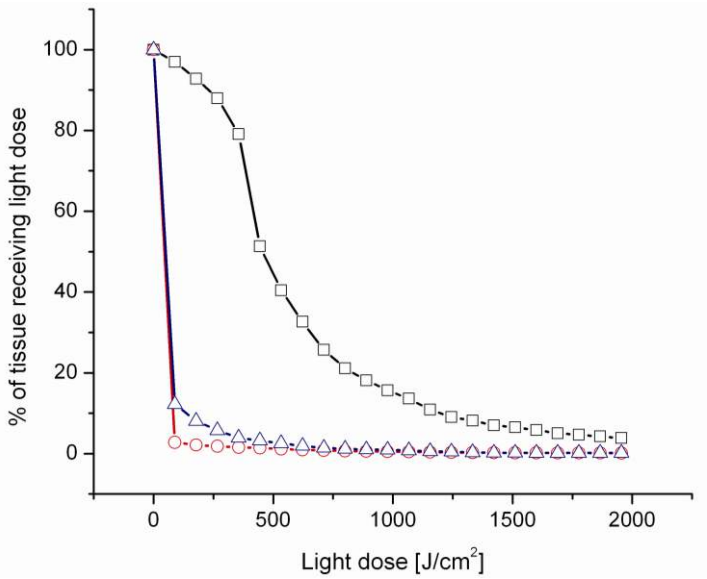


**Figure 7.8** Dose-volume histogram for 15 5-cm diffusers inserted into a treatment volume derived from CT images. Shown are the dose to tumor tissue (□), bulk body tissue (○), and the left lymph node (Δ).

Specification of precise diffuser positions can be difficult to achieve clinically, due to uncertainty in fiber placement. There may also be intervening anatomy, such as major blood vessels or bones, that does not allow placement of the diffusers at the positions specified by the treatment planning software. This can result in fiber placements that deviate from the prescribed plan. Fortunately, each of the cylindrical diffusers contains a radiomarker band that is visible by CT. After the fibers are inserted, their exact positions can be determined by imaging in the operating room. These positions can then be used to run MC simulations to determine the predicted dose. This allows the physician to have knowledge of tumor regions that may be under-treated or healthy regions that may be over-treated. The relative treatment times of the individual fibers can then be adjusted to alleviate these concerns.

## 7.5 Discussion

There is a need for treatment planning in PDT, especially in the case of interstitial PDT. Unlike in treatment modalities such as radiotherapy, the dose in PDT is often not well-defined and the same treatment regimen is often given to all patients in a trial. For example, Lightdale *et al* delivered a uniform 300 J/cm dose to all patients in a Phase III trial of PDT for esophageal cancer[8]. Similarly, Biel describes a series of clinical trials using uniform irradiation for cancers of the larynx[15]. This administration of a uniform treatment to patients with optical properties that are potentially highly variable can lead to differing tumor responses. This seems to be one of the major factors impeding the progress of PDT in clinical applications. While PDT offers a number of advantages over other treatment modalities, the results are often too unpredictable to be clinically viable. With attention to inter-patient variability and careful treatment planning, it is hoped that the results of PDT treatment will become more reproducible across patients, resulting in increased use of PDT as a treatment for a number of diseases.

The treatment planning process presented in this chapter combines a number of techniques developed previously in this thesis. We have demonstrated the creation of treatment plans that improve on the placement of diffusers on a uniform grid and assuming typical optical properties. To the best of our knowledge, this is the first time that radiotherapy treatment plans have been used to inform treatment planning for PDT. However, there is certainly still room for improvement in the method. The first area in which this is possible is in the optimization of the diffuser number and placement. Here we use a relatively simple non-linear optimization based on the coverage of tumor and

healthy volumes. Other groups have previously used the Cimmino block algorithm to optimize the placement of treatment fibers, with good results[45]. This algorithm is an iterative technique for the solution of systems of linear inequalities[175]. In the case of PDT treatment planning, the inequalities to be solved involve the light dose delivered to tumor and healthy tissues at pre-defined constraint points. The Cimmino algorithm is typically used in situations in which the dose to the surrounding healthy tissue is a critical treatment parameter, such as in the prostate. For our purposes, we have chosen to use a less complex optimization algorithm. Since a number of research groups have worked with the Cimmino algorithm, it could be productive to compare it quantitatively with our algorithm in the future.

The algorithm presented here also assumes homogeneous optical properties during the optimization. This ignores local variance in optical properties, and could result in the diffuser placement being sub-optimal. The running of a simulation using the optimized diffuser positions and full optical properties and anatomy alleviates this problem, but corrections to the treatment plan are computationally expensive at this point. For example, re-running a five diffuser treatment plan with new diffuser positions for the full optical property map takes approximately 6-10 minutes. With the assumption of homogeneous optical properties and a fluence distribution given by equation 4.27, this computation is reduced to approximately 100 ms. This computation can potentially be done using finite element models of light propagation, as has been shown by Davidson *et al*[44] and Thompson *et al*[138]. These finite element models allow for modeling of heterogeneous optical properties, and generally assume diffusion-based light propagation.

However, there can be significant computational overhead for the creation of the meshes used in the finite element calculations.

As discussed in section 7.2, the optical properties measured by spectroscopy are only known rigorously in a limited volume. Assumptions can be made about homogeneity, but these assumptions ignore small-scale changes in the local optical properties that can have a large effect on the deposited dose. It would therefore be desirable to have a map of the optical properties at high resolution over the entire treatment volume. Since the main absorber in bulk tissue is hemoglobin, a determination of the hemoglobin concentration would provide a great deal of this information. This determination may be possible using MRI. Using changes in the spin-echo signal, determinations of total blood volume have been demonstrated[176]. Techniques based on imaging of contrast media in blood vessels have also been used to determine blood volumes[177].

An MRI-based technique does not take into account the effects of oxygenation on the absorption of hemoglobin. While there have been a number of studies on determination of blood oxygenation from MRI, the results are generally qualitative[178], although there have recently been some studies done on quantitative determination of blood oxygenation based on $T_2$-relaxation-under-spin-tagging[179]. We are hoping to investigate the effects of oxygen status on the deposited dose, given total hemoglobin concentration. The tissue scattering can also have a large effect, so this relationship will also need to be examined carefully. If the errors determined are comparable to those inherent in spectroscopic determinations of optical properties, such a MRI-based scheme

could prove highly valuable. In addition to the resolution and coverage advantages, an MRI-based scheme would reduce clinical complexity. Patients routinely receive MR imaging before treatment, so no additional procedures would be required. Additionally, this would not require the addition of separate spectroscopy fibers, each of which increases the risks of bleeding and infection.

# Chapter 8

# Conclusion

In this thesis, we have covered a number of topics related to optical monitoring and treatment planning for PDT. We began with an examination of two studies of optical monitoring of PDT. In the first study, reflectance and fluorescence spectroscopy were used to inform the optimization of treatment parameters for methylene blue mediated PDT. To the best of our knowledge, this represented the first study that examined the efficacy of short drug light intervals for methylene blue mediated PDT. This short drug-light interval was informed by observation of MB fluorescence reduction during longer drug-light intervals, and was shown to improve tumor response. The *in vivo* reflectance and fluorescence spectra shown in this study also represented the first reported instances of these data in the literature.

The encouraging results obtained from this study have been used to motivate further examinations of the efficacy of MB-PDT, particularly in the treatment of infection. Using MB-PDT, Haidaris *et al* demonstrated effective killing of bacterial and fungal species obtained from patients undergoing percutaneous drainage of the abscess cavity[180]. Due to the results shown in this paper, we are actively pursuing a clinical trial to treat patients with MB-PDT following draining of infected abscesses. In these patients, methylene blue will be delivered at the time of draining and treatment light will be delivered using the laser system outlined in Appendix A. We hypothesize that PDT at the time of draining will reduce the recurrence of infection, and result in fewer surgical

procedures for patients. PDT may also reduce the reliance on prolonged antibiotic regimens that can accelerate the development of antibiotic-resistant bacteria.

We are also pursuing a clinical trial of MB-PDT in the context of cholangiocarcinoma, a malignancy of the bile ducts. Due to the generally delayed detection of this malignancy, most diagnosed patients are not eligible for surgery. Treatment usually takes the form of palliative biliary stenting to allow for drainage. These stents can often become occluded by regrowth of tumor tissue, and therefore require regular replacement. PDT at the time of stenting has been examined previously as a means of delaying this tumor regrowth[12]. Using the photosensitizer Photofrin, Ortner *et al* showed a five-fold improvement in survival for stenting with PDT versus stenting alone. Due to our success with MB-PDT and the diminished side effects associated with MB compared to Photofrin, we plan on collaborating with colleagues in interventional radiology to perform MD-PDT at the time of stenting for patients with cholangiocarcinoma. Since patients receive clinical imaging prior to stenting and the treatment fiber will be inserted under image guidance, this procedure would benefit from application of the treatment planning framework described in chapter 7.

In the second study described in chapter 2, we examined the fluorescence photobleaching of the photosensitizer Pc 4. This examination was performed at two fluence rates, and the rate of photobleaching was shown to be dependent on the fluence rate. This is the first time that fluence rate dependent photobleaching has been shown for Pc 4. Also, the photobleaching was shown to be more rapid at higher fluence rates, which has not been previously demonstrated for any photosensitizer. For other

photosensitizers, the photobleaching is either not fluence-rate dependent[85] or is more rapid at lower fluence rates[54, 55, 86, 87]. The photobleaching of Pc 4 fluorescence was shown not to correlate to tumor response, which seems to indicate that it is not a potent dosimeter for Pc 4 PDT under the conditions of our experiment. To clarify, this was shown for a Pc 4 concentration that did not demonstrate any tumor cures. In order to demonstrate this effect conclusively, the study would have to be repeated at a Pc 4 concentration that results in a significant number of tumor cures, which we are considering.

This study underscores the challenges of using photobleaching measurements to predict the outcome of PDT. While there have been a number of studies that have shown correlations between photosensitizer fluorescence photobleaching and tumor response, particularly for PpIX[21-23], measurements of individual patients were not used to predict the response for a particular patient. Correlations were only shown for groups of responders vs. groups of non-responders. Additionally, photobleaching is only useful for photosensitizers in which bleaching is strongly mediated by singlet oxygen. Finlay *et al* showed that photobleaching of Photofrin is dependent on both singlet oxygen and triplet interactions[85]. This leads to photosensitizer concentration-dependent bleaching mechanisms, which could result in photobleaching data being misinterpreted. Therefore, some caution is merited in the pursuit of photobleaching-based dosimetry schemes.

In chapter 3, we demonstrated a GPU-enhanced MC simulation framework and a number of source and detector models. These models are more accurate physical representations than have been used previously, and allow for the simulation of light

delivery and detection in complex geometries. The GPU-based nature allows for rapid simulation, which makes the creation of large MC libraries feasible. These MC models were used extensively throughout the thesis, and drove much of the work presented. One of these source models, the cylindrical diffusing fiber, was examined in further detail in chapter 5. Our model predicted heterogeneous detection of fluorescence by these fibers, which was verified experimentally. This represents the first time that the detection of fluorescence by cylindrical diffusers has been examined rigorously, and has implications for the use of these devices for the monitoring of PDT. In future clinical applications of cylindrical diffusers in treatment planning, their detection pattern will need to be carefully considered.

Chapter 4 covered two methods for optical property extraction from diffuse reflectance measurements, both in surface-contact and interstitial geometries. In the surface geometry we examined the optical properties of excised human kidneys. These extracted optical properties were similar to those previously reported for the kidney[173], and allowed us to examine the possibility of interstitial PDT in this area. We determined that PDT was indeed feasible, given the recovered optical properties, and provided evidence for the advantage of photosensitizers that absorb at longer wavelengths. A number of these longer wavelength photosensitizers are being developed[132]. We are pursuing a collaboration with Photolitec, a company founded out of Roswell Park Cancer Institute in Buffalo, NY, in order to explore the treatment of tumors with these longer wavelength photosensitizers. This motivates the potential use of PDT as another treatment option for renal cancers. We are currently considering a clinical trial of PDT

for the treatment of renal cell carcinoma, with clinical collaborators in Urology expressing great interest.

A new method for the determination of optical properties from interstitial spectroscopy measurements was also demonstrated in this chapter. We used a custom, encapsulated optical probe to make spatially resolved diffuse reflectance measurements. Using the MC model detailed in chapter 3, we were able to accurately recover absorption and scattering coefficients over a variety of absorber and scatterer concentrations. This was demonstrated in phantoms containing MnTPPS and intact human erythrocytes. The accuracy of the method is comparable to surface-contact techniques, which can rely on mathematical models that utilize the simpler boundary conditions present in that scenario. Our method has the advantage of using a single probe, with an outside diameter of 1.1 mm. This means that multiple spectroscopy fibers do not need to be inserted, reducing clinical complexity and risks to the patient. The probe can also be inserted along the same track as the treatment fiber, allowing for spectroscopy to sample approximately the same volume that will be treated by PDT. This allows for integration of the determined optical properties with treatment planning software. Our method also does not require extensive calibration with reference phantoms. Since we have a rigorous MC model of the probe, the training of the fitting algorithm could be performed automatically in the simulation space. Publication of these results is planned in the near future.

As mentioned in chapter 4, our model is only valid for transport albedos of greater than 0.95. While this covers the bulk of optical properties found in tissue, there may be some scenarios in which our model will not provide meaningful results. Another concern

with the use of interstitial probes is blood pooling around the probe. Finlay *et al* described blood pooling around reflectance probes leading to some data being uninterpretable[19]. Johansson *et al* also described blood pooling at detector fibers causing dramatically reduced signal at certain locations, leading to data being excluded[181]. If data corrupted by blood pooling are not manually excluded, this can lead to determinations of hemoglobin concentration that are higher than those present in bulk tissue.

Our spectroscopy measurements also require approximately one minute of total integration time to collect light sequentially at each of the detector fibers. If the optical properties are changing rapidly the measurements at each of the detector fibers could be made under different conditions, which could lead to transient phenemona being inaccurately represented. This problem could be alleviated by reducing integration time through the use of a brighter lamp, or by collecting the spectra at each of the detection fibers simultaneously. Our research group has previously shown simultaneous detection of broadband spectra from many fibers using a CCD[111]. This would increase the complexity of the instrumentation, which could lead to reduced clinical opportunities.

In chapter 6, a method for the determination of intrinsic fluorescence from point, interstitial measurements was demonstrated. This technique relies on a $P_3$ approximation to forward-adjoint fluorescence theory, and was able to give accurate estimations of the fluorophore concentration. The method was also capable of determining the concentrations of background absorbers, although with lower accuracy than the fluorophore concentration. To the best of our knowledge, this represents the first

demonstration of the recovery of intrinsic fluorescence from point, interstitial measurements without *a priori* knowledge of the optical properties. We are planning to publish these results in the near future.

These results have also led to the pursuit of a clinical trial for measurement of intrinsic fluorescence *in vivo*. We are planning to investigate the concentration of doxorubicin in liver tumors following the administration of this drug via TACE. While doxorubicin concentration has been measured using fluorescence in excised tissue[154], this quantity has never been measured *in vivo*. Clinical protocols are currently being prepared, with submission to the University of Rochester Research Subjects Review Board and the FDA anticipated in the near future. We have secured funding for this project[170], and plan to collect data from five patients as an initial prospective study.

Chapter 7 was the result of the integration of a number of components previously demonstrated in this thesis. Optical property recovery schemes outlined in chapter 4 were combined with the MC models described in chapter 3 in order to create a framework for interstitial PDT treatment planning. Clinical CT images were combined with an optimization algorithm in order to design PDT treatments for theoretical tumor volumes, with improved light dose distributions demonstrated for optimized source placements. To the best of our knowledge, this is the first time that radiotherapy treatment plans have been used to inform treatment planning for PDT. As a next step, we are planning to test the treatment planning framework in mouse models to examine its relation to tumor response. We are also planning to refine the algorithm for optimization of source placement to account for tissue interfaces. A fully formed treatment planning

package will allow for the creation of individualized PDT treatments, which should improve the efficacy of such treatments. It is hoped that this will reduce the variability in tumor response, and result in the increased deployment of PDT in the treatment of cancer.

This thesis has focused on the use of PDT for the treatment of bulky tumors deep within the body. While PDT offers a number of advantages, including reduced scarring and systemic side effects, it is important to acknowledge other therapies that exist. Perhaps the most well known of these is radiotherapy. In this modality, ionizing radiation is used to induce DNA damage that leads to cell death in the treated volume. This therapy is the standard of care for a number of cancers, and has shown excellent results. Radiotherapy also allows for the treatment of large volumes, and can therefore treat tumors that may not be feasible for PDT. However, radiotherapy can also have significant side effects. For the case of head and neck cancers, radiation delivered to surrounding healthy tissues can result in reductions in muscle mass[182], difficulty swallowing[183], impaired speech[184], and can lead to dependence on tracheotomy or a percutaneous gastrostomy tube[185].

Another treatment modality that is widely used in the treatment of bulky tumors is radio-frequency ablation (RFA). In this technique, tumor tissue is subjected to high-frequency alternating current. This causes a temperature increase, leading to cell death[186]. RFA has been used extensively in the treatment of liver tumors[187, 188]. As with PDT, RFA is often used in patients that are not eligible for surgery. Unlike PDT, RFA requires significant heating of the tumor tissue to achieve the desired response. In well-perfused tumors, the rapid out flux of blood can lead to reduced heating in the tumor

tissue. Therefore, RFA may not be a viable therapy for tumors in which there is significant blood flow.

Another treatment that relies on changing the temperature of tissue to cause cell death is cryotherapy. This therapy relies on dramatic reduction of temperature to kill tumor tissue. Cryotherapy has been used in the treatment of a number of malignancies, with success shown particularly in the cases of prostate[189] and lung cancers[190]. Cryotherapy has also been compared with PDT for the cases of actinic keratosis and Bowen's disease. Szeimies *at al* showed comparable response rates for PDT and cryotherapy in the treatment of actinic keratosis[191]. However, PDT provided better cosmetic results and higher patient satisfaction. In another study of actinic keratosis, Freeman *et al* showed significantly higher tumor response rate for PDT compared to cryotherapy[192]. For Bowen's disease, Morton *et al* showed comparable results between cryotherapy and PDT[193].

One major shortcoming of PDT is its inability to treat broadly metastasized tumors. Due to the relatively short penetration depth of treatment light, PDT can only be used to treat localized tumors. It is therefore best suited for applications in which malignancy has been detected early, or where side effects of more systemic treatments will be too severe. There has also been some investigation of the use of PDT to trigger systemic anti-tumor immunity. Gollnick *et al* showed an increase in the presence of antigen presenting cells at sites remote from PDT, which can lead to increased recruitment of T cells[194]. This has led to the proposal of PDT-generated antitumor vaccines, as demonstrated by Korbelik *et al*[195].

Despite its localized nature, PDT is an attractive option for the treatment of bulky tumors. The decreased damage to surrounding normal tissue provides a strong motivator for the use of PDT, particularly in regions where traditional therapies cannot be applied. With careful attention to dosimetry and treatment planning, it is entirely possible that PDT could become another viable treatment option for clinical oncologists.

# References

1. Agostinis, P., K. Berg, K. A. Cengel, T. H. Foster, A. W. Girotti, S. O. Gollnick, S. M. Hahn, M. R. Hamblin, A. Juzeniene, D. Kessel, M. Korbelik, J. Moan, P. Mroz, D. Nowis, J. Piette, B. C. Wilson and J. Golab. Photodynamic therapy of cancer: an update. *CA: A Cancer Journal for Clinicians* **61**, 250-281 (2011).

2. O'Connor, A. E., W. M. Gallagher and A. T. Byrne. Porphyrin and nonporphyrin photosensitizers in oncology: preclinical and clinical advances in photodynamic therapy. *Photochem Photobiol* **85**, 1053-1074 (2009).

3. Laubach, H.-J., S. K. Chang, S. Lee, I. Rizvi, D. Zurakowski, S. J. Davis, C. R. Taylor and T. Hasan. In-vivo singlet oxygen dosimetry of clinical 5-aminolevulinic acid photodynamic therapy. *J Biomed Opt* **13** (5), 050504 (2008).

4. Ochsner, M. Photophysical and photobiological processes in the photodynamic therapy of tumours. *J Photochem Photobiol B* **39**, 1-18 (1997).

5. Dougherty, T. J., C. J. Gomer, B. W. Henderson, G. Jori, D. Kessel, M. Korbelik, J. Moan and Q. Peng. Photodynamic therapy. *J Natl Cancer Inst* **90** (12), 889-905 (1998).

6. Hampton, J. A., D. Skalkos, P. M. Taylor and S. H. Selman. Iminum salt of copper benzochlorin (CDS1), a novel photosensitizer for photodynamic therapy: mechanism of cell killing. *Photochem Photobiol* **58** (1), 100-105 (1993).

7. Hopper, C. Photodynamic therapy: a clinical reality in the treatment of cancer. *The Lancet* **1**, 212-219 (2000).

8. Lightdale, C. J., S. K. Heier, N. E. Marcon, J. James S. McCaughan, H. Gerdes, B. F. Overholt, J. Michael V. Sivak, G. V. Stiegmann and H. R. Nava. Photodynamic therapy with porfimer sodium versus thermal ablation therapy with Nd:YAG laser for palliation of esophageal cancer: a multicenter randomized trial. *Gastrointest Endosc* **42** (6), 507-512 (1995).

9. Moghissi, K., K. Dixon, M. Stringer, T. Freeman, A. Thorpe and S. Brown. The place of bronchoscopic photodynamic therapy in advanced unresectable lung cancer: experience of 100 cases. *Eur J Cardiothorac Surg* **15**, 1-6 (1999).

10. Patel, H., R. Mick, J. Finlay, T. C. Zhu, E. Rickter, K. A. Cengel, S. B. Malkowicz, S. M. Hahn and T. M. Busch. Motexafin lutetium-photodynamic therapy of prostate cancer: short- and long-term effects on prostate-specific antigen. *Clin Cancer Res* **14** (15), 4869-4876 (2008).

11. Moore, C. M., T. R. Nathan, W. R. Lees, C. A. Mosse, A. Freeman, M. Emberton and S. G. Brown. Photodynamic therapy using meso tetra hydroxy phenyl chlorin (mTHPC) in early prostate cancer. *Lasers Surg Med* **38**, 356-363 (2006).

12. Ortner, M. E. J., K. Caca, F. Berr, J. Liebetruth, U. Mansmann, D. Huster, W. Voderholzer, G. Schachschal, J. Mossner and H. Lochs. Successful photodynamic therapy for nonresectable cholangiocarcinoma: a randomized prospective study. *Gastroenterology* **125** (5), 1355-1363 (2003).

13. Beck, T. J., F. W. Kreth, W. Beyer, J. H. Mehrkens, A. Obermeier, H. Stepp, W. Stummer and R. Baumgartner. Interstitial photodynamic therapy of nonresectable malignant glioma recurrences using 5-aminolevulinic acid induced protoporphyrin IX. *Lasers Surg Med* **39**, 386-393 (2007).

14. Lou, P.-J., H. Jager, L. Jones, T. Theodossy, S. Brown and C. Hopper. Interstitial photodynamic therapy as salvage treatment for recurrent head and neck cancer. *Br J Cancer* **91**, 441-446 (2004).

15. Biel, M. A. Photodynamic therapy treatment of early oral and laryngeal cancers. *Photochem Photobiol* **83**, 1-6 (2007).

16. Yu, G., T. Durduran, C. Zhou, T. C. Zhu, J. C. Finlay, T. M. Busch, S. B. Malkowicz, S. M. Hahn and A. G. Yodh. Real-time *in situ* monitoring of human prostate photodynamic therapy with diffuse light. *Photochem Photobiol* **82**, 1279-1284 (2006).

17. Wilson, B. C. and S. L. Jacques. Optical reflectance and transmittance of tissues: principles and applications. *IEEE J Quantum Electron* **26** (12), 2186-2199 (1990).

18. Busch, T. M., X. Xing, G. Yu, A. Yodh, E. P. Wileyto, H.-W. Wang, T. Durduran, T. C. Zhu and K. K.-H. Wang. Fluence rate-dependent intratumor heterogeneity in physiologic and cytotoxic responses to Photofrin photodynamic therapy. *Photochem Photobiol Sci* **8**, 1683-1693 (2009).

19. Finlay, J. C., T. C. Zhu, A. Dimofte, D. Stripp, S. B. Malkowicz, T. M. Busch and S. M. Hahn. Interstitial fluorescence spectroscopy in the human prostate duing motexafin lutetium-mediated photodynamic therapy. *Photochem Photobiol* **82**, 1270-1278 (2006).

20. Bonnett, R. and G. Martínez. Photobleaching of sensitisers used in photodynamic therapy. *Tetrahedron* **57**, 9513-9547 (2001).

21. Boere, I. A., D. J. Robinson, H. S. d. Bruijn, J. Kluin, H. W. Tilanus, H. J. C. M. Sterenborg and R. W. F. d. Bruin. Protoporphyrin IX fluorescence photobleaching and the response of rat Barrett's esophagus following 5-aminolevulinic acid photodynamic therapy. *Photochem Photobiol* **82**, 1638-1644 (2006).

22. Ascencio, M., P. Collinet, M. O. Farine and S. Mordon. Protoporphyrin IX fluorescence photobleaching is a useful tool to predict the response of rat ovarian cancer following hexaminolevulinate photodynamic therapy. *Lasers Surg Med* **40**, 332-341 (2008).

23. Tyrrell, J. S., S. M. Campbell and A. Curnow. The relationship between protoporphyrin IX photobleaching during real-time dermatological methyl-aminolevulinate photodynamic therapy (MAL-PDT) and subsequent clinical outcome. *Lasers Surg Med* **42**, 613-619 (2010).

24. Bai, L., J. Guo, F. A. B. III and J. L. Eiseman. The relationship of phthalocyanine 4 (Pc 4) concentrations measured noninvasively to outcome of Pc 4 photodynamic therapy in mice. *Photochem Photobiol* **85**, 1011-1019 (2009).

25. Gate, L. F. Comparison of the photon diffusion model and Kubelka-Munk equation with the exact solution of the radiative transport equation. *Appl Opt* **13** (2), 236-238 (1974).

26. Murrer, L. H. P., J. P. A. Marijnissen and W. M. Star. *Ex vivo* light dosimetry and Monte Carlo simulations for endobronchial photodynamic therapy. *Phys Med Biol* **40**, 1807-1817 (1995).

27. Liu, Q., C. Zhu and N. Ramanujam. Experimental validation of Monte Carlo modeling of fluorescence in tissues in the UV-visible spectrum. *J Biomed Opt* **8** (2), 223-236 (2003).

28. Wang, L., S. L. Jacques and L. Zheng. MCML - Monte Carlo modeling of light transport in multi-layered tissues. *Comput Methods Programs Biomed* **47**, 131-146 (1995).

29. Alerstam, E., T. Svensson and S. Andersson-Engels. Parallel computing graphics processing units for high-speed Monte Carlo simulation of photon migration. *J Biomed Opt* **13** (6), 060504 (2008).

30. Fang, Q. and D. A. Boas. Monte Carlo simulation of photon migration in 3D turbid media accelerated by graphics processing units. *Opt Express* **17** (22), 20178 (2009).

31. Ren, N., J. Liang, X. Qu, J. Li, B. Lu and J. Tian. GPU-based Monte Carlo simulation for light propagation in complex heterogeneous tissues. *Opt Express* **18** (7), 6811 (2010).

32. Wilson, B. C. and M. S. Patterson. The physics, biophysics and technology of photodynamic therapy. *Phys Med Biol* **53**, R61-R109 (2008).

33. Kienle, A. and M. S. Patterson. Determination of the optical properties of turbid media from a single Monte Carlo simulation. *Phys Med Biol* **41**, 2221-2227 (1996).

34. Palmer, G. M. and N. Ramanujam. Monte Carlo-based inverse model for calculating tissue optical properties. Part I: theory and validation on synthetic phantoms. *Appl Opt* **45** (5), 1062-1071 (2006).

35. Kumar, Y. P. and R. M. Vasu. Reconstruction of optical properties of low-scattering tissue using derivative estimated through perturbation Monte-Carlo method. *J Biomed Opt* **9** (5), 1002-1012 (2004).

36. Ishimaru, A., Wave Propagation and Scattering in Random Media, IEEE Press, New York, NY (1997).

37. Hull, E. L. and T. H. Foster. Steady-state reflectance spectroscopy in the $P_3$ approximation. *J Opt Soc Am A* **18** (3), 584-599 (2001).

38. Bargo, P. R., S. A. Prahl, T. T. Goodell, R. A. Sleven, G. Koval, G. Blair and S. L. Jacques. *In vivo* determination of optical properties of normal and tumor tissue with white light reflectance and an empirical light transport model during endoscopy. *J Biomed Opt* **10** (3), 034018 (2005).

39. Rajaram, N., T. H. Nguyen and J. W. Tunnell. Lookup table-based inverse model for determining optical properties of turbid media. *J Biomed Opt* **13** (5), 050501 (2008).

40. Wang, K. K.-H. and T. C. Zhu. Reconstruction of *in-vivo* optical properties for human prostate using interstitial diffuse optical tomography. *Opt Express* **17** (14), 11665-11672 (2009).

41. Dimofte, A., J. C. Finlay and T. C. Zhu. A method for determination of the absorption and scattering properties interstitially in turbid media. *Phys Med Biol* **50**, 2291-2311 (2005).

42. Svanberg, K., N. Bendsoe, J. Axelsson, S. Andersson-Engels and S. Svanberg. Photodynamic therapy: superficial and interstitial illumination. *J Biomed Opt* **15** (4), 041502 (2010).

43. Swartling, J., J. Axelsson, G. Ahlgren, K. M. Kälkner, S. Nilsson, S. Svanberg, K. Svanberg and S. Andersson-Engels. System for interstitial photodynamic therapy with online dosimetry: first clinical experiences of prostate cancer. *J Biomed Opt* **15** (5), 058003 (2010).

44. Davidson, S. R. H., R. A. Weersink, M. A. Haider, M. R. Gertner, A. Bogaards, D. Giewercer, A. Scherz, M. D. Sherar, M. Elhilali, J. L. Chin, J. Trachtenberg and B. C. Wilson. Treatment planning and dose analysis for interstitial photodynamic therapy of prostate cancer. *Phys Med Biol* **54**, 2293-2313 (2009).

45. Altschuler, M. D., T. C. Zhu, J. Li and S. M. Hahn. Optimized interstitial PDT prostate treatment planning with the Cimmino feasibility algorithm. *Med Phys* **32** (12), 3524-3536 (2005).

46. Mang, T. S. Dosimetric concepts for PDT. *Photodiagnosis Photodyn Ther* **5**, 217-223 (2008).

47. Veen, R. L. P. v., H. Nyst, S. R. Indrasari, M. A. Yudharto, D. J. Robinson, I. B. Tan, C. Meewis, R. Peters, S. Spaniol, F. A. Stewart, P. C. Levendag and H. J. C. M. Sterenborg. *In vivo* fluence rate measurements during Foscan®-mediated photodynamic therapy of persistent and recurrent nasopharyngeal carcinomas using a dedicated light applicator. *J Biomed Opt* **11** (4), 041107 (2006).

48. Brown, S. B., E. A. Brown and I. Walker. The present and future role of photodynamic therapy in cancer treatment. *Lancet Oncology* **5**, 497-508 (2004).

49. Wang, H.-W., T. C. Zhu, M. E. Putt, M. Solonenko, J. Metz, A. Dimofte, J. Miles, D. L. Fraker, E. Glatstein, S. M. Hahn and A. G. Yodh. Broadband reflectance measurements of light penetration, blood oxygenation, hemoglobin concentration, and drug concentration in human intraperitoneal tissues before and after photodynamic therapy. *J Biomed Opt* **10** (1), 014004 (2005).

50. Patterson, M. S., E. Schwartz and B. C. Wilson. Quantitative reflectance spectrophotometry for the noninvasive measurement of photosensitizer concentration in tissue during photodynamic therapy, in Proc. SPIE **1065**, 115-122 (1989).

51. Weersink, R. A., J. E. Hayward, K. R. Diamond and M. S. Patterson. Accuracy of noninvasive *in vivo* measurements of photosensitizer uptake based on a diffusion model of reflectance spectroscopy. *Photochem Photobiol* **66** (3), 326-335 (1997).

52. Niedre, M. J., C. S. Yu, M. S. Patterson and B. C. Wilson. Singlet oxygen luminescence as an *in vivo* photodynamic therapy dose metric: validation in normal mouse skin with topical amino-levulinic acid. *Br J Cancer* **92**, 298-304 (2005).

53. Yamamoto, J., S. Yamamoto, T. Hirano, S. Li, M. Koide, E. Kohno, M. Okada, C. Inenaga, T. Tokuyama, N. Yokota, S. Terakawa and H. Namba. Monitoring of singlet oxygen is useful for predicting the photodynamic effects in the treatment for experimental glioma. *Clin Cancer Res* **12** (7132-7139), (2006).

54. Finlay, J. C., D. L. Conover, E. L. Hull and T. H. Foster. Porphyrin bleaching and PDT-induced spectral changes are irradiance dependent in ALA-sensitized normal rat skin *in vivo*. *Photochem Photobiol* **73** (1), 54-63 (2001).

55. Cottrell, W. J., A. D. Paquette, K. R. Keymel, T. H. Foster and A. R. Oseroff. Irradiance-dependent photobleaching and pain in d-aminolevulinic acid-photodynamic therapy of superficial basal cell carcinomas. *Clin Cancer Res* **14** (14), 4475-4483 (2008).

56. Wang, H.-W., M. E. Putt, M. J. Emanuele, D. B. Shin, E. Glatstein, A. G. Yodh and T. M. Busch. Treatment-induced changes in tumor oxygenation predict photodynamic therapy outcome. *Cancer Res* **64**, 7553-7561 (2004).

57. Baran, T. M., B. R. Giesselman, R. Hu, M. A. Biel and T. H. Foster. Factors influencing tumor response to photodynamic therapy sensitized by intratumor administration of methylene blue. *Lasers Surg Med* **42** (8), 728-735 (2010).

58. II, J. C. and J. B. Leikin. Methylene Blue. *Am J Ther* **10**, 289-291 (2003).

59. Canto, M. I. F., S. Setrakian, R. E. Petras, E. Blades, A. Chak and M. V. Sivak. Methylene blue selectively stains intestinal metaplasia in Barrett's esophagus. *Gastrointest Endosc* **44** (1), 1-7 (1996).

60. Fennerty, M. B., R. E. Sampliner, D. L. McGee, L. J. Hixson and H. S. Garewal. Intestinal metaplasia of the stomach: identification by a selective mucosal staining technique. *Gastrointest Endosc* **38** (6), 696-698 (1992).

61. Jockusch, S., D. Lee, N. J. Turro and E. F. Leonard. Photo-induced inactivation of viruses: adsorption of methylene blue, thionine, and thiopyronine on Qb bacteriophage. *Proc Natl Acad Sci USA* **93** (15), 7446-7451 (1996).

62. Usacheva, M. N., M. C. Teichert and M. A. Biel. The role of the methylene blue and toluidine blue monomers and dimers in the photoinactivation of bacteria. *J Photochem Photobiol B* **71** (2), 87-98 (2003).

63. Orth, K., D. Russ, G. Beck, A. Rück and H. G. Beger. Photochemotherapy of experimental colonic tumors with intra-tumorally applied methylene blue. *Langenbck Arch Surg* **383** (3), 276-281 (1998).

64. König, K., V. Bockhorn, W. Dietel and H. Schubert. Photochemotherapy of animal tumors with photosensitizer methylene blue using a krypton laser. *J Cancer Res Clin Oncol* **113** (3), 301-303 (1987).

65. Orth, K., G. Beck, F. Genze and A. Rück. Methylene blue mediated photodynamic therapy in experimental colorectal tumors in mice. *J Photochem Photobiol B* **57** (3), 186-192 (2000).

66. Williams, J. L., J. Stamp, R. Devonshire and G. J. S. Fowler. Methylene blue and the photodynamic therapy of superficial bladder cancer. *J Photochem Photobiol B* **4** (2), 229-232 (1989).

67. Orth, K., A. Ruck, A. Stanescu and H. G. Beger. Intraluminal treatment of inoperable oesophagael tumours by intralesional photodynamic therapy with methylene blue. *The Lancet* **345**, 519-520 (1995).

68. Tardivo, J. P., A. D. Giglio, L. H. C. Paschoal, A. S. Ito and M. S. Baptista. Treatment of melanoma lesions using methylene blue and RL50 light source. *Photodiagnosic Photodyn Ther* **1**, 345-346 (2004).

69. Tardivo, J. P., A. D. Giglio, L. H. Pashoal and M. S. Baptista. New photodynamic protocol to treat AIDS-related Kaposi's sarcoma. *Photomed Laser Surg* **24** (4), 528-531 (2006).

70. Wagner, A. R. D. J. G. Pharmokinetics of highly ionized drug III: Methylene blue - blood levels in the dog and tissue levels in the rat following intravenous administration. *J Pharm Sci* **61** (7), 1090-1094 (1972).

71. Foster, T. H., B. R. Giesselman, R. Hu, M. E. Kenney and S. Mitra. Intratumor administration of the photosensitizer Pc 4 affords photodynamic therapy efficacy and selectivity at short drug-light intervals. *Transl Oncol* **3** (2), 135-141 (2010).

72. Holmes, H. J., J. C. Kennedy, R. Pottier, R. Rossi and G. Weagle. A recipe for the preparation of a rodent food that eliminates chlorophyll-based tissue fluorescence. *J Photochem Photobiol B* **29** (2), 199 (1995).

73. Wu, J., M. S. Feld and R. P. Rava. Analytical model for extracting intrinsic fluorescence in turbid media. *Appl Opt* **32** (19), 3585-3595 (1993).

74. Press, W. H., S. A. Teukolsky, W. T. Vetterling and B. P. Flannery, Numerical Recipes in C: The Art of Scientific Computing, Cambridge University Press, New York, NY (1992).

75. Junqueira, H. C., D. Severino, L. G. Dias, M. S. Gugliotti and M. S. Baptista. Modulation of methylene blue photochemical properties based on adsorption at aqueous micelle interfaces. *Phys Chem Chem Phys* **4** (11), 2320-2328 (2002).

76. Oleinick, N. L., A. R. Antunez, M. E. Clay, B. D. Rihter and M. E. Kenney. New phthalocyanine photosensitizers for photodynamic therapy. *Photochem Photobiol* **57**, 242-247 (1993).

77. Miller, J. D., E. D. Baron, H. Scull, A. Hsia, J. C. Berlin, T. McCormick, V. Colussi, M. E. Kenney, K. D. Cooper and N. L. Oleinick. Photodynamic therapy with the phthalocyanine photosensitizer Pc 4: the case experience with preclinical mechanistic and early clinical-translational studies. *Toxicol Appl Pharmacol* **224**, 290-299 (2007).

78. Baron, E. D., C. L. Malbasa, D. Santo-Domingo, P. Fu, J. D. Miller, K. K. Hanneman, A. H. Hsia, N. L. Oleinick, V. C. Colussi and K. D. Cooper. Silicon phthalocyanine (pc 4) photodynamic therapy is a safe modality for cutaneous neoplasms: results of a phase 1 clinical trial. *Lasers Surg Med* **42** (10), 728-735 (2010).

79. Kinsella, T. J., E. D. Baron, V. C. Colussi, K. D. Cooper, C. L. Hoppel, S. T. Ingalls, M. E. Kenney, X. Li, N. L. Oleinick, S. R. Stevens and S. C. Remick. Preliminary clinical and pharmacologic investigation of photodynamic therapy with the silicon phthalocyanine photosensitizer Pc 4 for primary or metastatic cutaneous cancers. *Front Oncol* **1**, 14 (2011).

80. Wang, K. K.-H., J. D. Wilson, M. E. Kenney, S. Mitra and T. H. Foster. Irradiation-induced enhancement of Pc 4 fluorescence and changes in light scattering are potential dosimeters for Pc 4-PDT. *Photochem Photobiol* **83**, 1056-1062 (2007).

81. Lee, T. K., E. D. Baron and T. H. Foster. Monitoring Pc 4 photodynamic therapy in clinical trials of cutaneous T-cell lymphoma using noninvasive spectroscopy. *J Biomed Opt* **13** (3), 030507 (2008).

82. Baran, T. M. and T. H. Foster. Fluence rate-dependent photobleaching of intratumorally administered Pc 4 does not predict tumor growth delay. *Photochem Photobiol* **88**, 1273-1279 (2012).

83. Anula, H. M., J. C. Berlin, H. Wu, Y. S. Li, X. Peng, M. E. Kenney and M. A. J. Rodgers. Synthesis and photophysical properties of slicion phthalocyanines with axial siloxy ligands bearing alkylamine termini. *J Phys Chem A* **110**, 5215-5223 (2006).

84. Sheng, C., P. J. Hoopes, T. Hassan and B. W. Pogue. Photobleaching-based dosimetry predicts deposited dose in ALA-PpIX PDT of rodent esophagus. *Photochem Photobiol* **83**, 738-748 (2007).

85. Finlay, J. C., S. Mitra, M. S. Patterson and T. H. Foster. Photobleaching kinetics of Photofrin *in vivo* and in multicell tumour spheroids indicate two simultaneous bleaching mechanisms. *Phys Med Biol* **49**, 4837-4860 (2004).

86. Robinson, D. J., H. S. d. Bruijn, N. v. d. Veen, M. R. Stringer, S. B. Brown and W. M. Star. Fluorescence photobleaching of ALA-induced protoporphyrin IX during photodynamic therapy of normal hairless mouse skin: the effect of light dose and irradiance and the resulting biological effect. *Photochem Photobiol* **67** (1), 140-149 (1998).

87. Ericson, M. B., C. Sandberg, B. Stenquist, F. Gudmundson, M. Karlsson, A.-M. Ros, A. Rosén, O. Larkö, A.-M. Wennberg and I. Rosdahl. Photodynamic therapy of actinic keratosis at varying fluence rates: assessment of photobleaching, pain and primary clinical outcome. *Br J Dermatol* **151**, 1204-1212 (2004).

88. Murrer, L. H., H. P. Marijnissen and W. M. Star. Monte Carlo simulations for endobronchial photodynamic therapy: the influence of variations in optical and geometrical properties and of realistic and eccentric light sources. *Lasers Surg Med* **22**, 193-206 (1998).

89. Boas, D. A., J. P. Culver, J. J. Stott and A. K. Dunn. Three dimensional Monte Carlo code for photon migration through complex heterogeneous media including the adult human head. *Opt Express* **10** (3), 159-170 (2002).

90. Arvo, J. and D. Kirk. Particle transport and image synthesis. *Computer Graphics* **24** (4), 63-66 (1990).

91. Henyey, L. G. and J. L. Greenstein. Diffuse radiation in the galaxy. *Astrophys J* **93**, 70-83 (1941).

92. Binzoni, T., T. S. Leung, R. Giust, D. Rüfenacht and A. H. Gandjbakhche. Light transport in tissue by 3D Monte Carlo: influence of boundary voxelization. *Comput Methods Programs Biomed* **89**, 14-23 (2008).

93. "NVIDIA CUDA C Programming Guide," NVIDIA Corporation (2010).

94. Marsaglia, G. Random number generators. *J Mod Appl Stat Meth* **2** (1), 2-13 (2003).

95. Vesselov, L. M., W. Whittington and L. Lilge. Performance evaluation of cylindrical fiber optic light diffusers for biomedical applications. *Lasers Surg Med* **34**, 348-351 (2004).

96. Farina, B., S. Saponaro, E. Pignoli, S. Tomatis and R. Marchesini. Monte Carlo simulation of light fluence in tissue in a cylindrical diffusing fibre geometry. *Phys Med Biol* **44**, 1-11 (1999).

97. Sinofsky, E. L., "Phototherapeutic Apparatus with Diffusive Tip Assembly," U.S. Patent Number 5947959 (1999).

98. Baran, T. M. and T. H. Foster. New Monte Carlo model of cylindrical diffusing fibers illustrates axially heterogeneous fluorescence detection: simulation and experimental validation. *J Biomed Opt* **16** (8), 085003 (2011).

99. Finlay, J. C. and T. H. Foster. Recovery of hemoglobin oxygen saturation and intrinsic fluorescence with a forward-adjoint model. *Appl Opt* **44** (10), 1917-1933 (2005).

100. Beutler, E. and J. Waalen. The definition of anemia: what *is* the lower limit of normal of the blood hemoglobin concentration. *Blood* **107** (5), 1747-1750 (2006).

101. Hull, E. L., M. G. Nichols and T. H. Foster. Quantitative broadband near-infrared spectroscopy of tissue-simulating phantoms containing erythrocytes. *Phys Med Biol* **43**, 3381-3404 (1998).

102. Bevilacqua, F. and C. Depeursinge. Monte Carlo study of diffuse reflectance at source-detector separations close to one transport mean free path. *J Opt Soc Am A* **16** (12), 2935-2945 (1999).

103. Patterson, M. S., B. Chance and B. C. Wilson. Time resolved reflectance and transmittance for the non-invasive measurement of tissue optical properties. *Appl Opt* **28** (12), 2331-2336 (1989).

104. Liebert, A., H. Wabnitz, J. Steinbrink, M. Möller, R. Macdonald, H. Rinneberg, A. Villringer and H. Obrig. Bed-side assessment of cerebral perfusion in stroke patients based on optical monitoring of a dye bolus by time-resolved diffuse reflectance. *NeuroImage* **24**, 426-435 (2005).

105. Mazurenka, M., A. Jelzow, H. Wabnitz, D. Contini, L. Spinelli, A. Pifferi, R. Cubeddu, A. D. Mora, A. Tosi, F. Zappa and R. Macdonald. Non-contact time-resolved diffuse reflectance imaging at null source-detector separation. *Opt Express* **20** (1), 283-290 (2012).

106. Chance, B., M. Cope, E. Gratton, N. Ramanujam and B. Tromberg. Phase measurement of light absorption and scatter in human tissue. *Rev Sci Instrum* **69** (10), 3457-3481 (1998).

107. Pham, T. H., R. Hornung, M. W. Berns, Y. Tadir and B. J. Tromberg. Monitoring tumor response during photodynamic therapy using near-infrared photon-migration spectroscopy. *Photochem Photobiol* **73** (6), 669-677 (2001).

108. Cuccia, D. J., F. Bevilacqua, F. R. Ayers and B. J. Tromberg. Quantitation and mapping of tissue optical properties using modulated imaging. *J Biomed Opt* **14** (2), 024012 (2009).

109. Farrell, T. J., M. S. Patterson and B. Wilson. A diffusion theory model of spatially resolved, steady-state diffuse reflectance for the noninvasive determination of tissue optical properties *in vivo*. *Med Phys* **19** (4), 879-888 (1992).

110. Wang, Q., D. Le, J. Ramella-Roman and J. Pfefer. Broadband ultraviolet-visible optical property measurement in layered turbid media. *Biomed Opt Express* **3** (6), 1226-1240 (2012).

111. Nichols, M. G., E. L. Hull and T. H. Foster. Design and testing of a white-light, steady-state diffuse reflectance spectrometer for determination of optical properties of highly scattering systems. *Appl Opt* **36** (1), 93-104 (1997).

112. Finlay, J. C. and T. H. Foster. Hemoglobin oxygen saturations in phantoms and *in vivo* from measurements of steady-state diffuse reflectance at a single, short source-detector separation. *Med Phys* **31** (7), 1949-1959 (2004).

113. Kanick, S. C., U. A. Gamm, M. Schouten, H. J. C. M. Sterenborg, D. J. Robinson and A. Amelink. Measurement of the reduced scattering coefficient of turbid media using single fiber reflectance spectroscopy: fiber diameter and phase function dependence. *Biomed Opt Express* **2** (1), 1687-1702 (2011).

114. Jacques, S. L., C. A. Alter and S. A. Prahl. Angular dependence of HeNe laser light scattering by human dermis. *Lasers Life Sci* **1**, 309-333 (1987).

115. Fishkin, J. B., S. Fantini, M. J. vandeVen and E. Gratton. Gigahertz photon density waves in a turbid medium: theory and experiments. *Phys Rev E* **53** (3), 2307-2319 (1996).

116. Haskell, R. C., L. O. Svaasand, T.-T. Tsay, T.-C. Feng, M. S. McAdams and B. J. Tromberg. Boundary conditions for the diffusion equation in radiative transfer. *J Opt Soc Am A* **11** (10), 2727-2741 (1994).

117. Aronson, R. Boundary conditions for diffusion of light. *J Opt Soc Am A* **12** (11), 2532-2539 (1995).

118. Siegel, R., D. Naishadham and A. Jemal. Cancer Statistics, 2012. *CA Cancer J Clin* **62**, 10-29 (2012).

119. Cohen, H. T. and F. J. McGovern. Renal-cell carcinoma. *N Engl J Med* **353** (23), 2477-2490 (2005).

120. Olweny, E. O., S. K. Park, Y. K. Tan, S. L. Best, C. Trimmer and J. A. Cadeddu. Radiofrequency ablation versus partial nephrectomy in patients with solitary clinical T1a renal cell carcinoma: comparable oncologic outcomes at a minimum of 5 year of follow-up. *Eur Urol* **61** (6), 1156-1161 (2012).

121. Zagoria, R. J. Percutaneous image-guided radiofrequency ablation of renal malignancies. *Radiol Clin North Am* **41** (5), 1067-1075 (2003).

122. Powell, T., C. Whelan and B. F. Schwartz. Laparoscopic renal cryotherapy: biology, techniques and outcomes. *Minera Urol Nefrol* **57** (2), 109-118 (2005).

123. Baran, T. M., J. D. Wilson, S. Mitra, J. L. Yao, E. M. Messing, D. L. Waldman and T. H. Foster. Optical property measurements establish the feasibility of photodynamic therapy as a minimally invasive intervention for tumors of the kidney. *J Biomed Opt* **17** (9), 098002 (2012).

124. Simpson, C. R., M. Kohl, M. Essenpreis and M. Cope. Near-infrared optical properties of *ex vivo* human skin and subcutaneous tissue measured using the Monte Carlo inversion technique. *Phys Med Biol* **43**, 2465-2478 (1998).

125. Honda, N., K. Ishii, T. Terada, T. Nanjo and K. Awazu. Determination of the tumor tissue optical properties during and after photodynamic therapy using inverse Monte Carlo method and double integrating sphere between 350 and 1000 nm. *J Biomed Opt* **16** (5), 058003 (2011).

126. Johansson, A., J. Axelsson, S. Andersson-Engels and J. Swartling. Realtime light dosimetry software tools for interstitial photodynamic therapy of the human prostate. *Med Phys* **34** (11), 4309-4321 (2007).

127. Loewen, G. M., R. Pandey, D. Bellnier, B. Henderson and T. Dougherty. Endobronchial photodynamic therapy for lung cancer. *Lasers Surg Med* **38**, 364-370 (2006).

128. Simone, C. B., J. S. Friedberg, E. Glatstein, J. P. Stevenson, D. H. Sterman, S. M. Hahn and K. A. Cengel. Photodynamic therapy for the treatment of non-small cell lung cancer. *J Thorac Dis* **4**, 63-75 (2011).

129. Nava, H. R., S. S. Allamaneni, T. J. Dougherty, M. T. Cooper, W. Tan, G. Wilding and B. W. Henderson. Photodynamic therapy (PDT) using HPPH for the treatment of precancerous lesions associated with barrett's esophagus. *Lasers Surg Med* **43** (7), 705-712 (2011).

130. Sunar, U., D. Rohrbach, N. Rigual, E. Tracy, K. Keymel, M. T. Cooper, H. Baumann and B. H. Henderson. Monitoring photobleaching and hemodynamic responses to HPPH-mediated photodynamic therapy of head and neck cancer: a case report. *Opt Express* **18** (14), 14969-14978 (2010).

131. Framme, C., H. G. Sachs, B. Flucke, D. Theisen-Kunde and R. Birngruber. Evaluation of the new photosensitizer Tookad (WST09) for photodynamic vessel occlusion of the choroidal tissue in rabbits. *Invest Ophthalmol Vis Sci* **47**, 5437-5446 (2006).

132. Li, G., A. Graham, Y. Chen, M. P. Dobhal, J. Morgan, G. Zheng, A. Kozyrev, A. Oseroff, T. J. Dougherty and R. K. Pandey. Synthesis, comparative photosensitizing efficacy, human serum albumin (site II) binding ability, and intracellular localization characteristics of novel benzobacteriochlorins derive from *vic*-Dihydroxybacteriochlorins. *J Med Chem* **46**, 5349-5359 (2003).

133. Feng, S., F.-A. Zeng and B. Chance. Photon migration in the presence of a single defect: a perturbation analysis. *Appl Opt* **34** (19), 3826-3837 (1995).

134. Staveren, H. J. v., C. J. M. Moes, J. v. Marle, S. A. Prahl and M. J. C. v. Gemert. Light scattering in Intralipid-10% in the wavelength range of 400-1100 nm. *Appl Opt* **30** (31), 4507-4514 (1991).

135. Prahl, S., "Optical Absorption of Hemoglobin," http://omlc.ogi.edu/spectra/hemoglobin/ (1999).

136. Brown, W. E. L. and A. V. Hill. The oxygen-dissociation curve of blood, and its thermodynamical basis. *Proc R Soc Lond* **94**, 297-334 (1923).

137. Chin, L. C. L., A. E. Worthington, W. M. Whelan and I. A. Vitkin. Determination of the optical properties of turbid media using relative interstitial radiance measurements: Monte Carlo study, experimental validation, and sensitivity analysis. *J Biomed Opt* **12** (6), 064027 (2007).

138. Thompson, M. S., A. Johansson, T. Johansson, S. Andersson-Engels, S. Svanberg, N. Bendsoe and K. Svanberg. Clinical system for interstitial photodynamic therapy with combined on-line dosimetry measurements. *Appl Opt* **44** (19), 4023-4031 (2005).

139. Kruijt, B., A. v. d. P.-v. d. Heuvel, H. S. d. Bruijn, H. J. C. M. Sterenborg, A. Amelink and D. J. Robinson. Monitoring interstitial m-THPC-PDT *in vivo* using fluorescence and reflectance spectroscopy. *Lasers Surg Med* **41**, 653-664 (2009).

140. Bellnier, D. A., W. R. Greco, H. Nava, G. M. Loewen, A. R. Oseroff and T. J. Dougherty. Mild skin photosensitivity in cancer patients following injection of Photochlor (2-[1-hexyloxyethyl]-2-devinyl pyropheophorbide-a; HPPH) for photodynamic therapy. *Cancer Chemother Pharmacol* **57**, 40-45 (2005).

141. Pandey, R. K., F.-Y. Shiau, A. B. Sumlin, T. J. Dougherty and K. M. Smith. Structure/activity relationships among photosensitizers related to pheophorbides and bacteriopheophorbides. *Bioorg Med Chem Lett* **2** (5), 491-496 (1992).

142. Hille, R., Personal Communication (2010).

143. Bolin, F. P., L. E. Preuss, R. C. Taylor and R. J. Ference. Refractive index of some mammalian tissues using a fiber optic cladding method. *Appl Opt* **28** (12), 2297-2303 (1989).

144. Hull, E., D. Conover and T. Foster. Carbogen-induced changes in rat mammary tumor oxygenation reported by near infrared spectroscopy. *Br J Cancer* **79**, 1709-1716 (1999).

145. Zhu, T. C., J. C. Finlay and S. M. Hahn. Determination of the distribution of light, optical properties, drug concentration, and tissue oxygenation in-vivo in human prostate during motexafin lutetium-mediated photodynamic therapy. *J Photochem Photobiol B* **79**, 231-241 (2005).

146. Tagaya, A., M. Nagai, Y. Koike and K. Yokoyama. Thin liquid-crystal display backlight system with highly scattering optical transmission polymers. *Appl Opt* **40** (34), 6274-6280 (2001).

147. Pavlova, I., M. Williams, A. El-Naggar, R. Richards-Kortum and A. Gillenwater. Understanding the biological basis of autofluorescence imaging for oral cancer detection: high-resolution fluorescence microscopy in viable tissue. *Clin Cancer Res* **14** (8), 2396-2404 (2008).

148. Roblyer, D., C. Kurachi, V. Stempanek, M. D. Williams, A. K. El-Naggar, J. J. Lee, A. M. Gillenwater and R. Richards-Kortum. Objective detection and delineation of oral neoplasia using autofluorescence imaging. *Cancer Prev Res* **2**, 423-431 (2009).

149. Malzahn, K., T. Dreyer, H. Glanz and C. Arens. Autofluorescence endoscopy in the diagnosis of early laryngeal cancer and its precursor lesions. *Laryngoscope* **112** (3), 488-493 (2009).

150. Shao, X., W. Zheng and Z. Huang. Near-infrared autofluorescence spectroscopy for *in vivo* identification of hyperplastic and adenomatous polyps in the colon. *Biosens Bioelectron* **30** (1), 118-122 (2011).

151. Wood, J., "Doxorubicin," in The Cytotoxics Handbook, Fourth Edition M. Allwood, A. Stanley and P. Wright, Eds., Radcliffe Medical Press Ltd, Oxford (2002).

152. Sepaniak, M. J., B. J. Tromberg and J. F. Eastham. Optical fiber fluoroprobes in clinical analysis. *Clin Chem* **29** (9), 1678-1682 (1983).

153. Palmer, G. M., R. J. Boruta, B. L. Viglianti, L. Lan, I. Spasojevic and M. W. Dewhirst. Non-invasive monitoring of intra-tumor drug concentration and therapeutic response using optical spectroscopy. *J Control Release* **142**, 457-464 (2010).

154. Lankelma, J., H. Dekker, R. F. Luque, S. Luykx, K. Hoekman, P. v. d. Valk, P. J. v. Diest and H. M. Pinedo. Doxorubicin gradients in human breast cancer. *Clin Cancer Res* **5**, 1703-1707 (1999).

155. Liu, C., N. Rajaram, K. Vishwanath, T. Jiang, G. M. Palmer and N. Ramanujam. Experimental validation of an inverse fluorescence Monte Carlo model to extract concentration of metabolically relevant fluorophores from turbid phantoms and a murine tumor model. *J Biomed Opt* **17** (7), 077012 (2012).

156. Wang, S., J. Zhao, H. Lui, Q. He and H. Zeng. Monte Carlo simulation of near infrared autofluorescence measurements of *in vivo* skin. *J Photochem Photobiol B* **105** (3), 183-189 (2011).

157. Zhadin, N. N. and R. R. Alfano. Correction of the internal absorption effect in fluorescence emission and exciation spectra from absorbing and highly scattering media: theory and experiment. *J Biomed Opt* **3** (2), 171-186 (1998).

158. Diamond, K. R., T. J. Farrell and M. S. Patterson. Measurement of fluorophore concentrations and fluorescence quantum yield in tissue-simulating phantoms using three diffusion models of steady-state spatially resolved fluorescence. *Phys Med Biol* **48**, 4135-4149 (2003).

159. Chang, S. K., N. Marin, M. Follen and R. Richards-Kortum. Model-based analysis of clinical fluorescence spectroscopy for *in vivo* detection of cervical intraepithelial dysplasia. *J Biomed Opt* **11** (2), 024008 (2006).

160. Crilly, R. J., W.-F. Cheong, B. Wilson and J. R. Spears. Forward-adjoint fluorescence model: Monte Carlo integration and experimental validation. *Appl Opt* **36** (25), 6513-6519 (1997).

161. Lakowicz, J. R., Principles of Fluorescence Spectroscopy, Springer Science+Business Media, LLC, New York, NY (2006).

162. Cummings, J. and C. S. McArdle. Studies on the *in vivo* disposition of adriamycin in human tumours which exhibit different responses to the drug. *Br J Cancer* **53**, 835-838 (1986).

163. Martin, A. D., M. Z. Daniel, D. T. Drinkwater and J. P. Clarys. Adipose tissue density, estimated adipose lipid fraction and whole body adiposity in male cadavers. *Int J Obes Relat Metab Disord* **18** (2), 79-83 (1994).

164. Weersink, R., M. S. Patterson, K. Diamond, S. Silver and N. Padgett. Noninvasive measurement of fluorophore concentration in turbid media with a simple fluorescence/reflectance ratio technique. *Appl Opt* **40** (34), 6389-6395 (2001).

165. Müller, M. G., I. Georgakoudi, Q. Zhang, J. Wu and M. S. Feld. Intrinsic fluorescence spectroscopy in turbid media: disentangling effects of scattering and absorption. *Appl Opt* **40** (25), 4633-4646 (2001).

166. Chang, S. K., D. Arifler, R. Drezek, M. Follen and R. Richards-Kortum. Analytical model to describe fluorescence spectra of normal and preneoplastic epithelial tissue: comparison with Monte Carlo simulations and clinical measurements. *J Biomed Opt* **9** (3), 511-522 (2004).

167. Aliberti, C., G. Benea, M. Tilli and G. Fiorentini. Chemoembolizaiton (TACE) of unresectable intrahepatic cholangiocarcinoma with slow-release doxorubicin-eluting beads: preliminary results. *Cardiovasc Intervent Radiol* **31**, 883-888 (2008).

168. Poggi, G., A. Amatu, B. Montagna, P. Quaretti, C. Minoia, C. Sottani, L. Villani, B. Tagliaferri, F. Sottotetti, O. Rossi, E. Pozzi, F. Zappoli, A. Riccardi and G. Bernardo. OEM-TACE: A new therapeutic approach in unresectable intrahepatic cholangiocarcinoma. *Cardiovasc Intervent Radiol* **32**, 1187-1192 (2009).

169. Varela, M., M. I. Real, M. Burrel, A. Forner, M. Sala, M. Brunet, C. Ayuso, L. Castells, X. Montañá, J. M. Llovet and J. Bruix. Chemoembolization of hepatocellular carcinoma with drug eluting bead: efficacy and doxorubicin pharmacokinetics. *J Hepatol* **46**, 474-481 (2007).

170. Baran, T. M., "Determination of doxorubicin concentration in TACE treatment of primary liver cancers by fluorescence spectroscopy," American Society for Laser Medicine & Surgery, Inc. (2012).

171. Farrell, T. J., B. C. Wilson, M. S. Patterson and M. C. Olivo. Comparison of the *in vivo* photodynamic threshold dose for Photofrin, mono- and tetrasulfonated aluminum phthalocyanine using a rat liver model. *Photochem Photobiol* **68** (3), 394-399 (1998).

172. Das, I. J., C.-W. Cheng, K. L. Chopra, R. K. Mitra, S. P. Srivastava and E. Glatstein. Intensity-modulated radiation therapy dose prescription, recording, and delivery: patterns of variability among institutions and treatment planning systems. *J Natl Cancer Inst* **100**, 300-307 (2008).

173. Cheong, W.-F., S. A. Prahl and A. J. Welch. A review of the optical properties of biological tissues. *IEEE J Quantum Electron* **26** (12), 2166-2185 (1990).

174. Bratengeier, K., M. Oechsner, M. Gainey and M. Flentje. Remarks on reporting and recording consistent with the ICRU reference dose. *Radiat Oncol* **4**, 44 (2009).

175. Censor, Y., M. D. Altschuler and W. D. Powlis. On the use of Cimmino's simultaneous projections method for computing a solution of the inverse problem in radiation therapy treatment planning. *Inverse Probl* **4**, 607-623 (1988).

176. Zijl, P. C. M. v., S. M. Eleff, J. A. Ulatowski, J. M. E. Oja, A. M. Uluğ, R. J. Traystman and R. A. Kauppinen. Quantitative assessment of blood flow, blood volume and blood oxygenation effects in functional magnetic resonance imaging. *Nat Med* **4** (2), 159-167 (1998).

177. Demsar, F., T. P. L. Roberts, H. C. Schwickert, D. M. Shames, C. F. v. Dijke, J. S. Mann, M. Saeed and R. C. Brasch. A MRI spatial mapping technique for microvascular permeability and tissue blood volume based on macromolecular contrast agent distribution. *Magn Reson Med* **37**, 236-242 (1997).

178. Ogawa, S., T. M. Lee, A. R. Kay and D. W. Tank. Brain magnetic resonance imaging with contrast dependent on blood oxygenation. *Proc Natl Acad Sci USA* **87**, 9868-9872 (1990).

179. Lu, H., F. Xu, K. Grgac, P. Liu, Q. Qin and P. v. Zijl. Calibration and validation of TRUST MRI for the estimation of cerebral blood oxygenation. *Magn Reson Med* **67**, 42-49 (2012).

180. Haidaris, C. G., T. H. Foster, D. L. Waldman, E. J. Mathes, J. McNamara, S. R. Gill and T. Curran. Effective photodynamic therapy against microbial populations in human deep tissue abscess aspirates. *Antimicrob Agents Chemother*, in review (2013).

181. Johansson, A., T. Johansson, M. S. Thompson, N. Bendsoe, K. Svanberg, S. Svanberg and S. Andersson-Engels. *In vivo* measurement of parameters of dosimetric importance during interstitial photodynamic therapy of thick skin tumors. *J Biomed Opt* **11** (3), 034029 (2006).

182. Tedla, M., M. Valach, R. L. Carrau, I. Varga, M. Profant, P. Mráz and P. Weismann. Impact of radiotherapy on laryngeal intrinsic muscles. *Eur Arch Otorhinolaryngol* **269**, 953-958 (2012).

183. Caglar, H. B., R. B. Tishler, M. Othus, E. Burke, Y. Li, L. Goguen, L. J. Wirth, R. I. Haddad, C. M. Norris, L. E. Court, D. J. Aninno, M. R. Posner and A. M. Allen. Dose to larynx predicts for swallowing complications after intensity-modulated radiotherapy. *Int J Radiat Oncol Biol Phys* **72** (4), 1110-1118 (2008).

184. Rancati, T., M. Schwarz, A. M. Allen, F. Feng, A. Popovtzer, B. Mittal and A. Eisbruch. Radiation dose volume effects in the larynx and pharynx. *Int J Radiat Oncol Biol Phys* **76** (3), S64-S69 (2010).

185. Tulunay-Ugur, O. E., C. McClinton, Z. Young, J. A. Penagaricano, A.-M. Maddox and E. Vural. Functional outcomes of chemoradiation in patients with head and neck cancer. *Otolaryngol Head Neck Surg* **148** (1), 64-68 (2013).

186. Curley, S. A. Radiofrequency ablation of malignant liver tumors. *Oncologist* **6**, 14-23 (2001).

187. Sutherland, L. M., J. A. R. Williams, R. T. A. Padbury, D. C. Gotley, B. Stokes and G. J. Maddern. Radiofrequency ablation of liver tumors: a systemic review. *Arch Surg* **141**, 181-190 (2006).

188. Decadt, B. and A. K. Siriwardena. Radiofrequency ablation of liver tumours: systemic review. *Lancet Oncol* **5**, 550-560 (2004).

189. Hou, A. H., K. F. Sullivan and E. D. Crawford. Targeted focal therapy for prostate cancer: a review. *Curr Opin Urol* **19** (3), 283-289 (2009).

190. Lee, S.-H., W.-J. Choi, S.-W. Sung, Y.-K. Kim, C.-H. Kim, J.-I. Zo and K.-J. Park. Endoscopic cryotherapy of lung and bronchial tumors: a systemic review. *Korean J Intern Med* **26** (2), 137-144 (2011).

191. Szeimies, R. M., S. Karrer, S. Radakovic-Fijan, A. Tanew, P. G. Calzavara-Pinton, C. Zane, A. Sidoroff, M. Hempel, J. Ulrich, T. Proebstle, H. Meffert, M. Mulder, D. Salomon, H. C. Dittmar, J. W. Bauer, K. Kernland and L. Braathen. Photodynamic therapy using topical methyl 5-aminolevulinate compared with cryotherapy for actinic keratosis: a prospective, randomized study. *J Am Acad Dermatol* **47** (2), 258-262 (2002).

192. Freeman, M., C. Vinciullo, D. Francis, L. Spelman, R. Nguyen, P. Fergin, K.-E. Thai, D. Murrel, W. Weightman, C. Anderson, C. Reid, A. Watson and P. Foley. A comparison of photodynamic therapy using topical methyl aminolevulinate (Metvix) with single cycle cryotherapy in patients with actinic keratosis: a prospective, randomized study. *J Dermatolog Treat* **14** (2), 99-106 (2003).

193. Morton, C. A., C. Whitehurst, H. Moseley, J. H. McColl, J. V. Moore and R. M. Mackie. Comparison of photodynamic therapy with cryotherapy in the treatment of Bowen's disease. *Br J Dermatol* **135** (5), 766-771 (1996).

194. Gollnick, S. O., B. Owczarczak and P. Maier. Photodynamic therapy and anti-tumor immunity. *Lasers Surg Med* **38**, 509-515 (2006).

195. Korbelik, M. and J. Sun. Photodynamic therapy-generated vaccine for cancer therapy. *Cancer Immunol Immunother* **55** (8), 900-909 (2006).

196. Foster, T. H. and T. M. Baran, "A Modular Laser System for Photodynamic Therapy," International Application Number PCT/US12/58459 (2012).

# Appendix A

# A Custom, Modular Laser System for Interventional Radiology Applications of Photodynamic Therapy

## A.1 Introduction

A major impediment to the widespread clinical application of PDT is the availability of FDA-approved, commercially available laser systems. There is currently only one FDA-approved PDT laser, and it is designed to work solely with Photofrin, which has peak absorption at 630 nm. The system is also expensive, with a price of approximately $100,000. As more photosensitizers are developed and approved that absorb at different wavelengths, hospitals would be required to buy multiple expensive laser systems to treat with each individual drug. These lasers are not FDA-approved, so each new wavelength would also require a separate FDA approval. This leads to the regulatory process becoming prohibitive to the adoption of newer, potentially more beneficial photosensitizers. It would therefore be desirable to have a less expensive laser system with multiple available output wavelengths and a common framework that could more easily be approved.

## A.2 Proposed design

We have proposed a design that attempts to alleviate these concerns[196], as shown in Figure A.1.

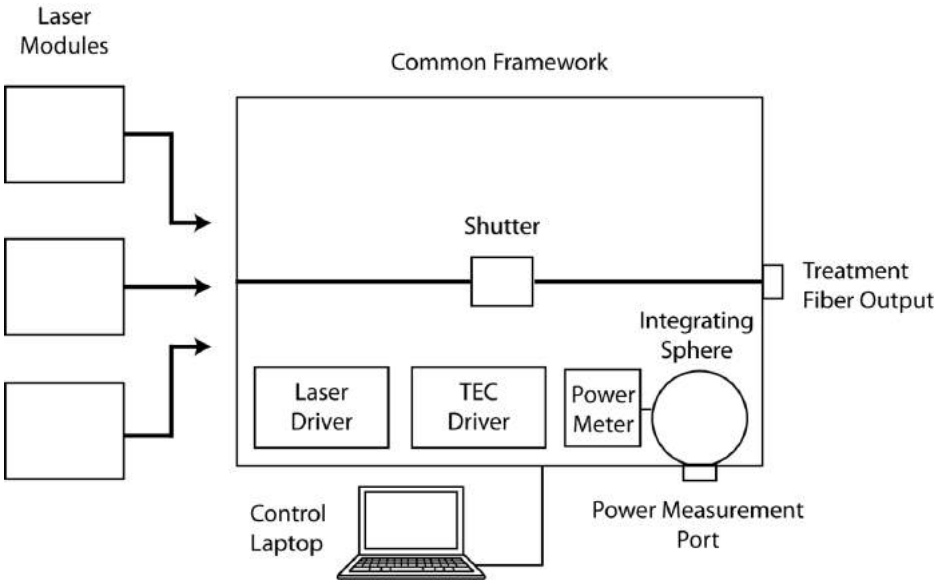


**Figure A.1** Proposed laser system design, including laser modules, drivers, laser power measurement system, shutter, and control laptop. All pieces, except the individual laser modules, are part of a common control and measurement framework that is constant for all laser modules.

The system consists of a common control and measurement framework, with swappable laser modules for excitation of multiple wavelengths. The common framework consists of laser and thermo-electric cooling (TEC) drivers, a laser power measurement system, a shutter, and a computer for control. The laser and TEC drivers are of sufficient voltage and current to drive high-power diode lasers (1-2 W) at a variety of wavelengths. This laser output power will be sufficient to drive multiple treatment fibers simultaneously. The laser power measurement system consists of an integrating sphere, detector, and power meter. The system would be calibrated at each of the desired output wavelengths

in order to ensure the delivered fluence rate at the fiber output matches the desired value. The shutter is present as an additional fail-safe, should the communication between the computer and laser somehow be interrupted. All of these components would be controlled and monitored by custom software on the laptop computer. The only pieces available to the end-user would be the SMA connector for treatment fiber attachment, and the integrating sphere port for measurement of output power. The user could then select the desired fluence rate and total fluence, insert the treatment fiber into the integrating sphere port, and the system would set the laser power and treatment time.

A more complex version of the system could also incorporate visible steering beams and fluorescence excitation sources. For certain photosensitizers, the absorption can extend into the NIR[131, 132], where the treatment field would not be visible by eye. A low-output visible wavelength would therefore need to be piped into the treatment fibers for alignment. This could be accomplished using either bifurcated fibers or optical switches. For some cases, it would also be desirable to excite fluorescence for visualization of the photosensitizer distribution by the physician. This would require a separate, low-power fluorescence excitation source to be present in the system. This could again be coupled into the treatment fibers using bifurcated fibers or optical switches.

This proposed design should help reduce the administrative and financial burdens currently present in the acquisition of clinical PDT laser systems. Since the system consists of modular laser diodes, the design could first receive approval for a given wavelength laser. Approval of additional wavelengths would then be relatively

straightforward, since the control and safety elements would already be approved. The addition of subsequent laser modules would only require the approval of the laser diode itself. Alternatively, the system could be approved for a number of clinically relevant wavelengths simultaneously.

The cost of this system would also be significantly less than the currently available FDA-approved laser system. Whereas that system costs approximately $100,000, we have built a first-generation prototype of our design for approximately $10,000, as will be described in the next section. Even with profit margins and manufacturing overheads factored in, our design would cost significantly less. Furthermore, the addition of other wavelengths would not require the purchase of a separate laser system. It would only require the purchase of additional laser modules, which cost approximately $3000-$5000. This would remove one of the impediments of transitioning into the use of newer photosensitizers.

## A.3 Laser system for methylene blue mediated PDT

In order to demonstrate this design we have constructed a prototype with a laser module aimed at the photosensitizer methylene blue. The current status of this prototype is depicted in Figure A.2.

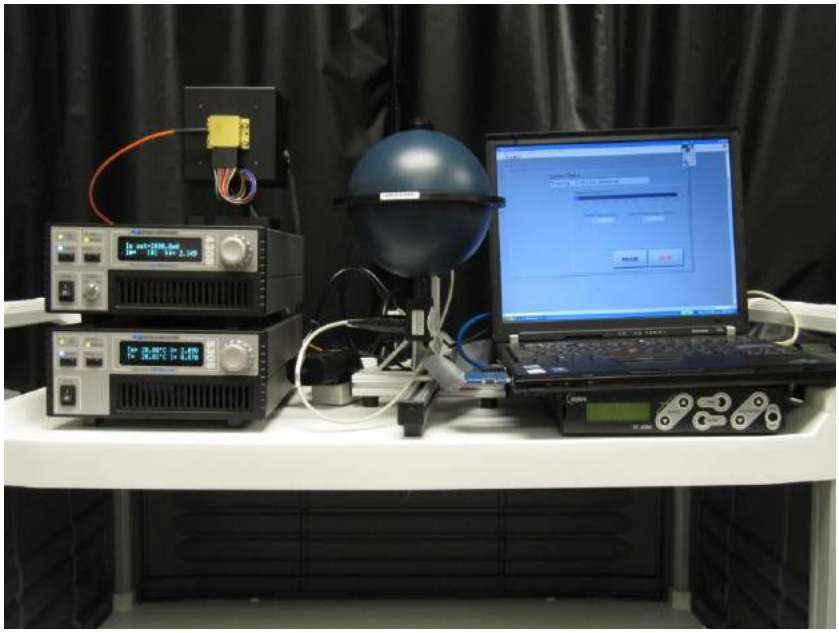

**Figure A.2** Current status of laser system for excitation of the photosensitizer methylene blue, including laser diode, drivers, laser power measurement system, and laptop computer for control.

The system consists of a 1.2 W diode laser operating at 665 nm (LDX-3230-665-HHL, LDX Optronics, Maryville, TN), mounted on an Arroyo 244 HHL laser mount (Arroyo Instruments, San Luis Obispo, CA). The laser is driven by an Arroyo 4308 Laser Source Driver and cooled by an Arroyo 5305 TEC Source Controller. The system also includes an integrating sphere based power measurement system (STM-LPMS-060-SI, Labsphere, North Sutton, NH) for determination of output power from treatment fibers. The power measurement system was re-calibrated by Labsphere for the sphere and detector shown

above. All components of the system are monitored and controlled by a custom LabVIEW interface (National Instruments, Austin, TX), run from a laptop computer. The system will be packaged into a single box, with only the output fiber connector and integrating sphere port accessible to the user. The LabVIEW interface will also be compiled into an executable, so that the code cannot be modified by the end user. We are hoping to use this completed system in a clinical trial exploring MB-PDT of infected abscesses, as discussed previously.

Future iterations of the design will focus on improved modularity of the laser diodes, ease of user interface, and packaging. Currently the laser diode is attached to the laser mount and must be screwed to connectors from the laser and TEC drivers. In the future, these connections could be made to slide or click into place, allowing new modules to be easily installed. We would also like to transition the user interface from a separate computer to an integrated touch-screen. The control software only requires 3 serial port connections, which is easily achievable with a number of commercial touch-screen packages. This would result in an interface that is similar to that already used by technicians in the interventional radiology department at the University of Rochester Medical Center. Finally, we would like to improve the packaging and appearance of the laser system. Towards this end, we have been consulting with Toptica Photonics in Victor, NY. Toptica has a wealth of experience in the design of laser systems, and they are interested in working with us on this design. We hope to have the components enclosed in small, stable package that looks similar to existing medical instruments used in the clinic.